

**Soft-Templated Synthesis of Multicomponent
Nanoporous Noble Metallic Materials as
Electrocatalysts**

February 2017

**Waseda University
Graduate School of
Advanced Science and Engineering**

**Department of Nanoscience and Nanoengineering
Research on Synthetic Chemistry of Nanomaterials**

Bo JIANG

蔣 波

Preface

Noble metal materials such as platinum (Pt), palladium (Pd), silver (Ag), and gold (Au), as one kind of the most important materials, have received much attention because of their broad applications in hydrogenation reactions, coupling reactions, fuel cells, and sensors, *etc.* Specifically, mesoporous noble metal materials have sparked increasing research in catalysis due to many advantages such as high surface areas, abundant active sites, excellent conductivity, chemical inertness, stable metallic frameworks as well as the accessible porous structure. Taking electrochemical catalysis as an example, the porous architectures in metal electrocatalysts are able to provide abundant active sites and high specific surface areas, not only maximizing the availability of electron transfer within nanosized framework, but also facilitating mass transfer from the outer surface to the inner structure. Generally, mesoporous metals are synthesized by the soft-templating and hard-templating methods, leading to the dendritic porous structure. In my thesis, I focus on the soft-templating approach based on diluted surfactant/polymer solutions for preparation of mesoporous metals with large-porous structure.

Chapter 1 introduces the historical background of the mesoporous materials and mesoporous metals. The synthetic methods of porous metals with various compositions, pore structures are reviewed with emphasis on the recent important progress. **Chapter 2** demonstrates a novel strategy for large-scale synthesis of shape- and size-controlled mesoporous Pt nanospheres (MPNs) through a slow reduction reaction in the presence of triblock copolymer Pluronic F127. **Chapter 3** shows that a facile and one-step polymeric micelle approach is demonstrated for the synthesis of Pt nanoparticles with continuously tunable porous structures and particle sizes. In **Chapter 4**, we describe two strategies for preparing mesoporous core-shell Pd@Pt nanoparticles by manipulating of reduction rate. One method is that hydrochloric acid is used as reduction inhibitor for formation of mesoporous structure. On the other hand, the ligand effect induced by bromide ions is used to manipulate the reduction rate for preparation of pseudo mesoporous core-shell Pd@Pt nanoparticles with different shapes. To further improve the electrocatalytic performance, trimetallic PtPdCu, PtPdRu nanospheres with uniform pore size and particle size were successfully obtained, as describe in **Chapter 5**.

As is well known, Pt is the most expensive and scarce element in nature. Although I have demonstrated that the mesoporous Pt, bimetallic core-shell Pd@Pt nanoparticles, and trimetallic Pt-based alloys with porous structure can effectively decrease the usage of Pt at the same time maintain the possibility to enhance the performance (**Chapter 2-5**), these approaches only reduce the usage of Pt, and do not fully solve the

problem of Pt requirements. Therefore, the development of less expensive and more abundant Pt-free electrocatalysts with improved catalytic activity and durability is still an urgent matter to address. In **Chapter 6**, Pd films with perpendicularly aligned mesochannels and branched PdCu alloy prepared are fabricated and expected to provide fascinating electrocatalytic properties due to their low diffusion resistance and the full utilization of their large surface area.

Table of Contents

Chapter 1. Introduction to Controlled Synthesis of Mesoporous Metals	1
1.1. General Introduction	2
1.2. Hard-templating Method.....	3
1.3. Soft-templating Method	5
1.3.1. Lyotropic Liquid Crystals (LLCs)	5
1.3.2. Micelle Assembly	8
1.4. Solution Phase Approach	9
1.4.1. Monocomponent Porous Metals	10
1.4.2. Core@shell Structured Porous Metals	12
1.4.3. Multicomponent Porous Alloys.....	15
1.5. Motivation and Purpose of This Study.....	17
References	19
Chapter 2. Mesoporous Pt Nanospheres with Designed Pore Surface as Highly Active Electrocatalyst	23
2.1. Introduction.....	24
2.2. Experimental Sections.....	25
2.2.1. Materials.....	25
2.2.2. Preparation of Mesoporous Pt Nanospheres	25
2.2.3. Characterization	25
2.2.4. Electrochemical Test	26
2.3. Results and Discussion.....	27
2.4. Conclusion	37
References	38
Chapter 3. Tunable-Sized Polymeric Micelles and Their Assembly for Preparation of Large Mesoporous Pt Nanoparticles	41
3.1. Introduction.....	42
3.2. Experimental Sections.....	43
3.2.1. Materials.....	43
3.2.2. Preparation of the Materials.....	43
3.2.3. Characterization	44
3.2.4. Electrochemical Test	44

3.3. Results and Discussion.....	45
3.4. Conclusion	58
References	59
Chapter 4. Surfactant-Directed Synthesis of Bimetallic Mesoporous Pt-based Electrocatalysts	62
4.1. Bimetallic Mesoporous PtPd Spheres through Surfactant-Directed Synthesis	63
4.1.1. Introduction.....	64
4.1.2. Experimental Sections.....	65
4.1.2.1. Materials.....	65
4.1.2.2. Preparation of Mesoporous Bimetallic PdPt Spheres	65
4.1.2.3. Characterization	65
4.1.2.4. Electrochemical Test	65
4.1.3. Results and Discussion.....	66
4.1.4. Conclusion	74
References	75
4.2. Morphosynthesis of Nanoporous Pseudo Pd@Pt Bimetallic Particles with Controlled Electrocatalytic Activity	77
4.2.1. Introduction.....	78
4.2.2. Experimental Sections.....	79
4.2.2.1. Materials.....	79
4.2.2.2. Preparation of Nanoporous Pd@Pt Nanospheres.....	79
4.2.2.3. Characterization	80
4.2.2.4. Electrochemical Test	80
4.2.3. Results and Discussion.....	80
4.2.4. Conclusion	91
References	92
Chapter 5. Trimetallic Mesoporous Spheres through Surfactant-Directed Synthesis	95
5.1. Mesoporous Trimetallic PtPdRu Spheres as Superior Electrocatalysts	96
5.1.1. Introduction.....	97
5.1.2. Experimental Sections.....	98
5.1.2.1. Materials	98
5.1.2.2. Preparation of Mesoporous Trimetallic PtPdRu Spheres.....	98

5.1.2.3. Characterization	99
5.1.2.4. Electrochemical Test	99
5.1.3. Results and Discussion.....	99
5.1.4. Conclusion	104
References	105
5.2. Synthesis of Ternary PtPdCu Spheres with Three-Dimensional Nanoporous Architectures toward Superior Electrochemical Catalysts.....	108
5.2.1. Introduction.....	109
5.2.2. Experimental Sections.....	110
5.2.2.1. Materials.....	110
5.2.2.2. Preparation of Materials.....	110
5.2.2.3. Characterization	111
5.2.2.4. Electrochemical Test	112
5.2.3. Results and Discussion.....	112
5.2.4. Conclusion	119
References	120
Chapter 6. Synthesis of Pt-free Metallic Electrochemical Catalysts for Electrochemical Application.....	122
6.1. Surfactant-Directed Synthesis of Mesoporous Pd Films with Perpendicular Mesochannels as Efficient Electrochemical Catalysts.....	123
6.1.1. Introduction.....	124
6.1.2. Experimental Sections.....	125
6.1.2.1. Materials.....	125
6.1.2.2. Preparation of Mesoporous Pd Films with Perpendicular Channels.....	125
6.1.2.3. Characterization	125
6.1.2.4. Electrochemical Test	126
6.1.3. Results and Discussion.....	126
6.1.4. Conclusion	134
References	135
6.2. Three-Dimensional Hyperbranched PdCu Nanostructures with High Electrochemical Activity.....	137
6.2.1. Introduction.....	138
6.2.2. Experimental Sections.....	139

6.2.2.1. Materials.....	139
6.2.2.2. Preparation of the Branched PdCu Nanostructures.....	140
6.2.2.3. Characterization	140
6.2.2.4. Electrochemical Test	140
6.2.3. Results and Discussion.....	141
6.2.4. Conclusion	148
References	149
Chapter 7. General Conclusions and Future Perspective	151
7.1. Overview of the Achievements	152
7.2. Future Prospects.....	155
List of Publications	157
Acknowledgements	160

Chapter 1. Introduction to Controlled Synthesis of Mesoporous Metals

1.1. General Introduction

Nowadays, porous structures (including zeolites and coordination polymers) cover a wide range of dimensions (**Figure 1.1**).^[1] Even though they show excellent selectivity and considerable adsorptive capacity due to their high porosity, the pore size, which is limited to less than 2 nm (microporosity), has restricted their range of applications. In the early 1990s, great progress was achieved following the synthesis of ordered mesoporous silica.^[2] The discovery of mesoporous materials was a breakthrough that has attracted a great deal of attention due to their unique properties, such as their ultra-high surface area, tunable pore size, and narrow pore size distribution. Up to now, much effort has been devoted to the synthesis and applications of mesoporous materials, which, in contrast to traditional industrial microporous materials with a pore size limited to < 2 nm, can provide large accessible spaces for guest species, thereby increasing the feasibility of a wide range of applications, such as in adsorption,^[3] separation of large molecules,^[4] catalysis,^[5] drug and DNA delivery,^[6] sensors,^[7] functional devices,^[8] Li-ion batteries, and fuel cells.^[9] Large-sized mesopores in particular greatly facilitate the transportation of guest species and thus enhance the accessibility of reaction sites.

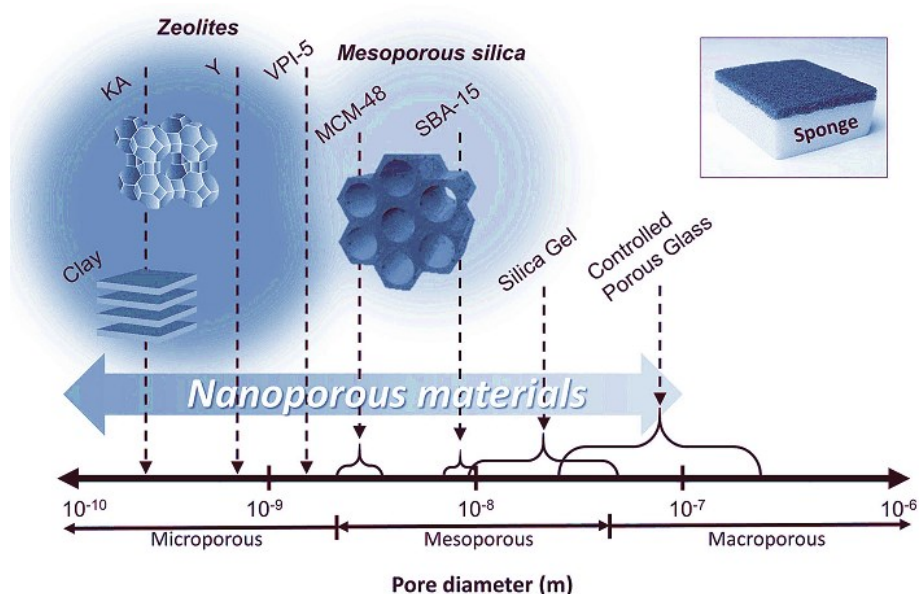


Figure 1.1 Classification of porous materials depending on their pore size. Reproduced with permission^[1] Copyright 2016, Wiley-VCH.

These recent research activities were rapidly extended to various non-siliceous mesoporous materials with different framework compositions, such as carbons, metals, metal oxides, sulfides, inorganic-organic hybrid materials, and polymers. Even though there have been many reports on the successful preparation of non-siliceous mesoporous materials, keeping the integrity of the structure stable is still a challenging issue because the mesopores tend to collapse during the crystallization of the pore walls and/or the template removal

process. Among these materials, mesoporous metals have attracted a great deal of attention. Owing to their fascinating physicochemical properties, including high electrical and thermal conductance, mesoporous metals offer a wide range of promising applications which cannot be achieved by other mesoporous materials. It has been experimentally and theoretically demonstrated that the morphology and the structure of mesoporous metals strongly affect their physical and chemical properties, which can be useful in applications such as bio-sensors, surface-enhanced Raman scattering, surface plasmon resonance, hydrogen storage, and catalysis.

Rationally designing mesoporous metals is therefore required to precisely tune their properties. By simply engineering the shape and morphology of a material, various novel porous nanostructures with specific properties can be created. Among them, dendritic metals, unlike the aforementioned oriented mesoporous materials, are generally composed of randomly oriented nanopores. Mesoporous structures are normally synthesized by templating methods (hard or soft), while dendritic nanostructures are fabricated by wet chemical methods. In this section, we cover recent progress related to this emerging field.

1.2. Hard-templating Method

In the hard-template method, targeted materials are deposited into the confined spaces of a robust mesoporous template (**Figure 1.2a**). In most cases, mesoporous silica with a robust framework and high thermal stability is used as a hard template to synthesize the metal replicas. This method can be rapidly extended to the synthesis of various mesoporous materials such as carbons, metals, and metal oxides. In contrast to the one-pot soft-templating route, the hard-templating approach usually involves several steps, including: 1) the preparation of the original template, 2) the deposition of inorganic substances, and 3) the removal of the template. The structure of the final product is generally an inverted replica of the original template. This process was firstly applied to the preparation of mesoporous carbon. Ryoo and co-workers reported the synthesis of ordered mesoporous carbons, namely, CMK-1^[10] and CMK-3^[11], obtained by using MCM-48 and SBA-15 silica templates, respectively. Following these pioneering works, large numbers of related materials with different components, mainly including metals, metal oxides, and metal sulfides, have been successfully synthesized. Ryoo and co-workers extended the hard template route to the synthesis of metallic systems. Asymmetrically mesostructured Pt networks with interconnected Pt nanowires 3 nm in diameter was obtained through flowing H₂ to reduce tetraammine platinum(II) nitrate (Pt(NH₃)₄(NO₃)₂) impregnated into MCM-48 silica, followed by their release from the template, which was removed by HF treatment.^[12] Ye et al. synthesized highly ordered mesoporous Pd by using face-centered-cubic silica supercrystals (with a pore diameter of 40 nm) as a template.^[13] With this method the mesopore sizes of the products can be precisely controlled by changing the diameters of the silica nanoparticles. Recently, Yang *et al.* prepared self-supported mesoporous Pt nanospheres from single-crystal-like MCM-48 nanospheres.^[14]

The impregnation of the template with molten salts followed by hydrogen reduction is a promising strategy to replicate both the mesostructure and the morphology of the original hard template. Interestingly, mesoporous Pt nanoparticles are thermally stable in air up to 300 °C, resist any significant metal sintering, maintain a high surface area, and exhibit high catalytic activity during the oxygen reduction reaction (ORR). The latter can be attributed to the facet-dependent reactivity as well as the presence of 3D interconnected mesopores facilitating mass transport.

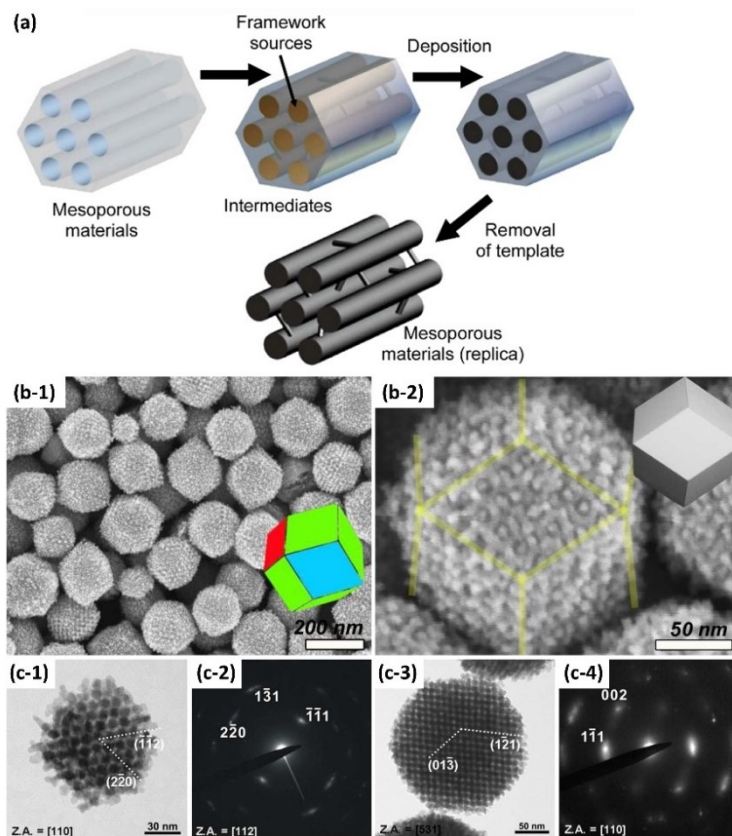


Figure 1.2 (a) Schematic illustration presenting the formation steps for synthesizing mesoporous materials through the hard-templating method. (b-1) Low- and (b-2) high-magnification SEM images of mesoporous Pt nanoparticles prepared with mesoporous silica KIT-6 templates. (c-1, c-3) Low-magnification bright-field transmission electron microscope (TEM) images of mesoporous Pt and (c-2, c-4) the corresponding electron diffraction patterns. Reproduced with permission.^[15a] Copyright 2011, American Chemical Society.

In the aforementioned hard-templating methods, it is difficult to control the metal deposition process inside the template, and thus, the shape and particle size of the product is not easy to tune, generally leading to the formation of irregularly shaped mesoporous metals. In order to improve the hard-templating route, Yamauchi and co-workers focused on the particular mechanisms responsible for the nanoscale deposition inside the mesoporous silica template (**Figure 1.2b,c**). By controlling the reductive strength of the reduction agents, they successfully synthesized monodisperse polyhedral- and olive-shaped mesoporous Pt nanoparticles with a uniform size distribution by using KIT-6 (*Ia-3d*) and SBA-15 (*p6mm*) templates,

respectively.^[15] The reduction and growth kinetics play a critical role in the rational design of mesoporous crystals. Using a mild reducing agent such as ascorbic acid (AA) provides enough time for the reductant to access the inner parts of the mesoporous silica, allowing the nucleation and growth of Pt to take place slowly in the confined mesoporous silica channels. Therefore, the Pt source material introduced into the mesopores is entirely reduced inside the hard templates without any residual deposition occurring outside the channels. By increasing the deposition time, the particle size is gradually increased. The obtained particles are isolated from each other inside the mesoporous templates, and their size distribution is narrow. Compared to other previous methods, such as H₂ reduction, this strategy does not require any complex apparatus, is simple, and is highly reproducible, showcasing its potential for large-scale production. A variety of compositions, including Pt-Ru, Pt-Co, and Pt-Ni, have also been prepared by using this strategy.^[16] Control over a well-defined morphology and a narrow size distribution will become the decisive aspect for the future use of mesoporous metals in a wide range of applications such as electrodes, sensors, catalysts, and drug delivery systems.

1.3. Soft-templating Method

Nanostructured metals and semiconductors have many important technological uses. They are commonly produced by using soft templates such as lyotropic liquid crystals (LLCs) or block copolymer micelles. Generally, the soft-templating route is accomplished through the cooperative assembly of inorganic precursor and the surfactant/block polymer via electrostatic interaction, hydrogen bonding, or Van der Waals' force *etc.* Such systems have been extensively studied for producing various nanostructures, such as nanoparticles, nanowires, nanorods, nanotubes, and two-dimensional (2D) nanoplates. The current section is focused on ordered mesoporous metals synthesized from LLC or block copolymer micelle templates.

1.3.1. Lyotropic Liquid Crystals (LLCs)

LLCs are formed by the self-assembly of surfactant micelles and can be directly employed as a structure-directing agent for the synthesis of mesoporous metals. There are two main steps: 1) the formation of the LLC and 2) the formation of the mesoporous structure by reducing metal complexes in the presence of the LLC (**Figure 1.3**). To prepare LLCs, a highly concentrated surfactant solution (around 30 wt% or more) is required. Since the first report on the preparation of mesoporous Pt particles by Attard and co-workers,^[17] the soft-templating method has been employed with various compositions. Electrochemically depositing mesoporous metallic films on a conductive substrate (*e.g.*, Au-coated substrate, indium tin oxide (ITO) substrate) generally involves a three-electrode cell, consisting of a working electrode, a reference electrode, and a counter electrode. Attard and co-workers introduced this method for the synthesis of mesoporous Pt films by electrochemical deposition^[18] In most cases, alkyl(polyethylene oxide) (C_mEO_n)-type surfactants

have been utilized for the formation of LLCs. Bartlett *et al.* successfully synthesized a mesoporous Pd film by electrochemical deposition of Pd salts in a hexagonal (H_1) LLC made of non-ionic octaethyleneglycol mono-hexadecyl ether ($C_{16}EO_8$) and decaethylene glycol hexadecyl ether ($C_{16}EO_{10}$; Brij 56) surfactants.^[19]

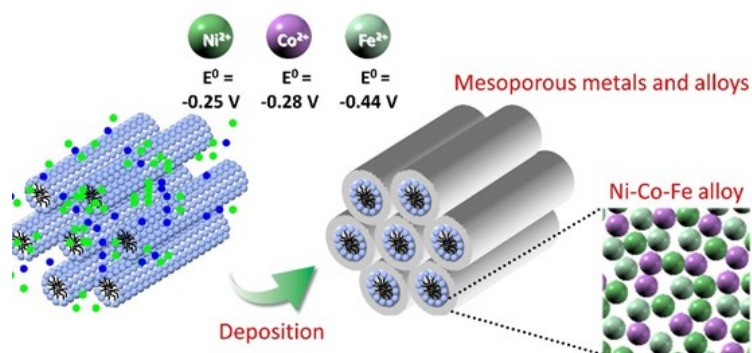


Figure 1.3 Schematic illustration of a typical formation method for mesoporous metals and alloys.

During the metal deposition, many parameters, such as temperature, deposition potential, and electrode material and geometry, surfactant and precursor, strongly affect the final structural properties. Elliott *et al.* systematically investigated the effects of deposition conditions during the synthesis of mesoporous Pt films from hexagonally ordered LLCs.^[20] In particular, the temperature and the deposition potential are found to have a critical effect on the surface area and roughness of the films. Increasing the temperature during the electrodeposition leads to a significant increase in the surface area and pore-to-pore distance, due to a gradual distortion of the mesopore arrangement. Selecting the electrode materials and geometries is also critical for increasing the surface area. When mesoporous Pt films were electrodeposited onto microelectrodes from hexagonally ordered LLCs, the resulting films showed high surface areas with efficient mass transport characteristics.^[21]

Until now, various organic templates, based on surfactants or amphiphilic block copolymers, have been utilized to synthesize mesoporous metals. The pore size depends mostly on the hydrophobic volume of the micelles. Hence, using LLCs composed of high molecular weight polymers with long hydrophobic chains, such as poly(ethylene oxide)-*b*-polystyrene (PEO-*b*-PS), enables one to make mesostructures with larger pores. Novel mesoporous Pt with closely connected giant mesocages can be obtained by using LLCs consisting of amphiphilic diblock copolymers. Increasing the pore size makes the inner parts of the mesoporous structure more accessible to guest species, a critical factor for further implementing such materials in catalytic applications.^[22] Several mesostructures (*i.e.*, lamellar, 2D hexagonal ($p6mm$), 3D cubic ($Ia-3d$), and 3D cage-type) can be easily controlled by changing the type and composition of the LLCs. Various mesostructures, including 2D-hexagonal, lamellar, and cage-type, can be obtained during the synthesis of mesoporous Pt by simply varying the composition ratio of the Pt salt to the block copolymer.^[23] The dissolved Pt aqua complexes link onto the PEO groups through hydrogen bonding, and increasing the

volume ratio of hydrophilic head groups (PEO groups) to hydrophobic tail groups (PS groups) induces a transition from lamellar to 2D hexagonal, and further to cage-type.

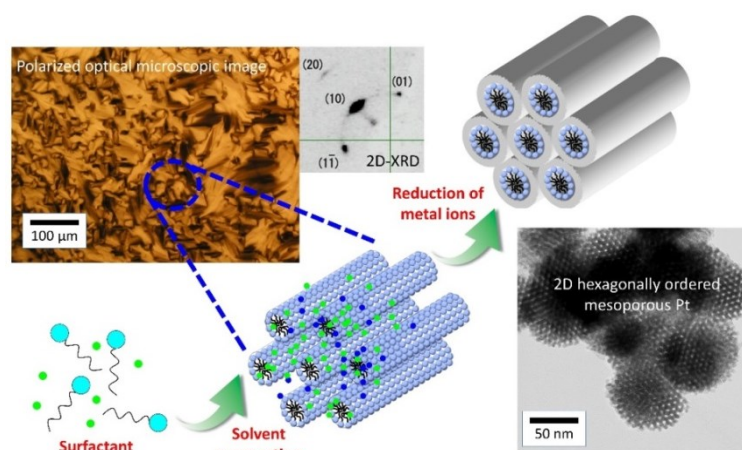


Figure 1.4 Schematic illustration of the formation of mesoporous metals by using LLCs prepared through solvent evaporation. A polarized optical microscope image, a 2D XRD pattern of the as-prepared LLCs, and a TEM image of 2D hexagonally ordered mesoporous Pt are also shown.

As previously mentioned, LLCs made of highly concentrated surfactants or block copolymers have been utilized as soft templates. Through chemical or electrochemical reduction, ordered mesoporous metal powders or films can be respectively synthesized. A large amount of surfactant is necessary to form LLCs, in which the close proximity of the molecules is mainly responsible for the self-arrangement (with concentrations above 30 wt%). After determining the ternary components (including surfactants, water, and metal species) and their respective proportions, the mixture is heated and stirred vigorously. This process is repeated until a homogeneous mixture is obtained. The formation of LLCs can be altered through solvent evaporation (**Figure 1.4**),^[24] where a volatile solvent, such as ethanol or tetrahydrofuran (THF), is added to the initial LLC precursor solution. The preferential evaporation in the homogeneous precursor solution leads to the formation of a stable LLC containing the metal complexes. Even though this method is mostly used for the synthesis of mesoporous Pt films, a wide range of mesoporous metals and alloys have been obtained by selecting the appropriate metal precursors.^[25] Pt and Pt-based alloys from LLC films with 2D hexagonal symmetry were deposited via vapor infiltration of dimethylaminoborane (DMAB).^[26] The as-prepared LLC films containing the metal ions were placed in a sealed container together with DMAB as a reducing agent, and mesoporous metal was deposited through vapor infiltration of the reducing agent. This method can also be combined with a hard template (such as porous anodic alumina, PAA) to synthesize nanorods with a mesoporous structure. Furthermore, mesoporous Pt nanotubes can be successfully prepared according to a similar system in which a moderate pressure is applied before metal deposition.^[27]

A comparable concept has been proposed by other groups such as Zhang *et al.*, who reported the fabrication of

ordered hierarchical porous Pt membranes utilizing C₁₆EO₈ as the LLC former and reverse porous poly(methyl methacrylate) (PMMA) cast from PAA as the hard template.^[28] The obtained Pt membranes have ordered mesopores and tunable large macropore channels, as well as a continuous framework similar to that of the PAA template. The mesostructure in the Pt membranes can be tailored by controlling the concentration of C₁₆EO₈ solution: 55 wt % and 70 wt % lead to the formation of hexagonal and lamellar liquid crystal phases, respectively. The same group also reported the synthesis of Pt with a geometric mesostructure, which can be controlled by confining the reduction to the cylindrical nanochannels of the PAA. Interestingly, the obtained single crystal hexagonal mesostructured Pt nanowires show dominant {110} facets, which are known to provide the highest activity towards the ORR among low-index crystallographic planes. Such single crystal surface can offer ideal model systems for reliable studies on their material properties.^[29] As another example, hierarchical Pt monoliths were prepared by chemical reduction using an opal silica hard template and LLC formed from nonionic Brij 56 surfactant (C₁₆EO₁₀) as soft template.^[30] The obtained Pt catalyst showed a larger electrochemically active surface area, as well as higher activity and tolerance to CO poisoning during the methanol oxidation reaction (MOR), compared to the commercial Pt black catalyst.

1.3.2. Micelle Assembly

In general, mesoporous metals are deposited as films on conductive substrates which act as working electrodes. It is difficult, however, to set up and operate a three-electrode cell apparatus due to the high viscosity of the LLC, in contrast to the conventional electrodeposition system for metals using an aqueous solution. Therefore, a new simpler and more sophisticated synthetic route is needed. In contrast to the LLC method, which requires high surfactant concentrations (over 30 wt %), Yamauchi and co-workers have recently proposed a micelle assembly approach using diluted surfactant solutions for the preparation of mesoporous metal films with accessible mesopores tunable over a wide range of sizes by selecting various surfactants and adding organic expanders (**Figure 1.5**). Mesoporous Pt films can be electrodeposited by the assembly of surfactant micelles with metal species. In the plating solution, dissolved Pt species are coordinated by water molecules to form metal-aqua complexes which adsorb on the external ethylene oxide (EO) moieties of the surfactant micelles. Therefore, during the electrochemical deposition, the Pt species are thought to move towards the working electrode together with the surfactant micelles which act as structure-directing agents. The plating solutions can be reused several times, showcasing the high repeatability of this method. This method was also applied to the fabrication of alternating layer-by-layer electrodeposited mesoporous Pt and Pd films.^[31] The linear relationship between the electrodeposition time and the metal layer thickness allows precise control over the film configuration. Because of the high surface area and the accessible heterometallic interfacial contacts between the Pt and Pd layers, enhanced electrocatalytic activity towards the MOR was achieved. Such a simple electrochemical design for mesoporous metals and alloys should greatly contribute to future

applications, such as in microsensors, microbatteries, micro-bioactive materials, miniaturized devices, and beyond. Furthermore, this synthetic approach is expected to generate other metallic and semiconducting nanostructured films with architectures of technological importance.

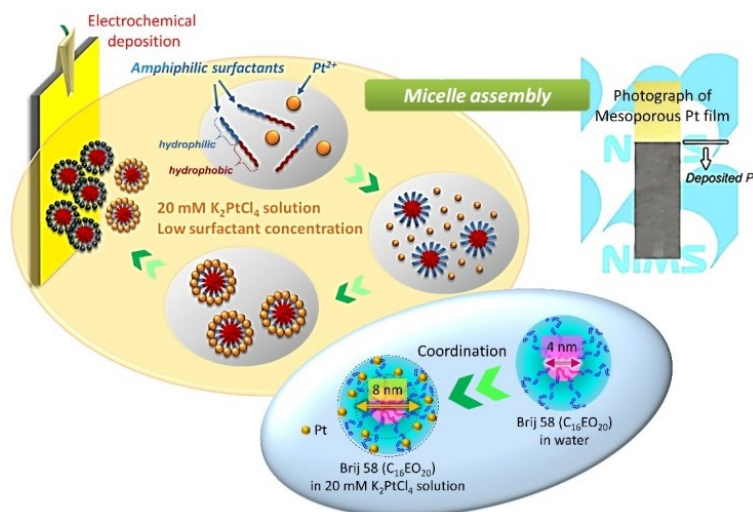


Figure 1.5 Schematic illustration of a novel micelle assembly strategy for the preparation of mesoporous metals. The dissolved metal species are coordinated on the hydrophilic shell domains of the micelles, due to hydrogen bonding. A photograph of the obtained mesoporous Pt film is also shown.

The essence of this method is to exploit the self-assembly of surfactant molecules into micelles at the solid-liquid interfaces for the synthesis of mesoporous metallic nanoparticles. Mesoporous bimetallic PdPt nanoparticles with a Pd core were successfully synthesized by combining this approach with a self-seeding process.^[32] Because the Pd species tend to be reduced faster, the spontaneous reaction of a mixture of the metal salts leads to the formation of Pd rich seeds, which can then be capped by the self-assembly of surfactant micelles. Then, the subsequent deposition of Pt over the preformed Pd seeds triggers the growth of the mesoporous Pt shell. Ascorbic acid (AA) was used as reductant because of its reducing capacity, which can be adjusted by precisely controlling the acidity of the precursor solution. This one-step synthesis procedure was carried out under highly acidic conditions to decrease the reduction rate of the metal ions providing enough time for the micelles to adhere to the Pd-rich seeds and act as a template for the subsequent growth of the mesoporous shells. The obtained mesoporous nanoparticles are strikingly uniform in size and morphology, and show greatly enhanced electrocatalytic activity, which can be attributed to the synergetic effect between the two metals, as well as the nanoporous structure, which provides a high surface area and abundant catalytically active sites.

1.4. Solution Phase Approach

In solution phase synthesis, nanocrystals of face-centered-cubic (*fcc*) metals usually tend to take on a polyhedral shape, such as a truncated octahedron, cube, octahedron, icosahedron, or decahedron, because the

overall surface energy is lower for these shapes, thereby making the nanoparticles thermodynamically more stable.^[33] Currently, however, rational synthesis by solution phase methods of dendritic metal particles with superior properties has been developed to the point where it is now possible to form nanoporous particles for a wide spectrum of metals.^[34] The synthesis of dendritic metals can be carried out through different growth mechanisms, such as kinetically controlled overgrowth, aggregation-based growth (**Figure 1.6a**), selective oxidative etching, and template-mediated methods.^[35] Nanoporous metal colloids, especially metals with dendritic morphology, are among the most complicated structures to be synthesized by solution phase routes. Therefore, understanding the nucleation and growth mechanisms of such nano-objects will enable the rational design of hierarchical porous nanostructures with superior properties.^[33b] Besides the nucleation and growth of seed structures, surfactant molecules can sometimes adsorb selectively on certain facets, which prevents the metal atoms from being deposited on these crystal planes, thus inducing dendritic/anisotropic growth of noble metal nanoparticles.^[35b,35e,36]

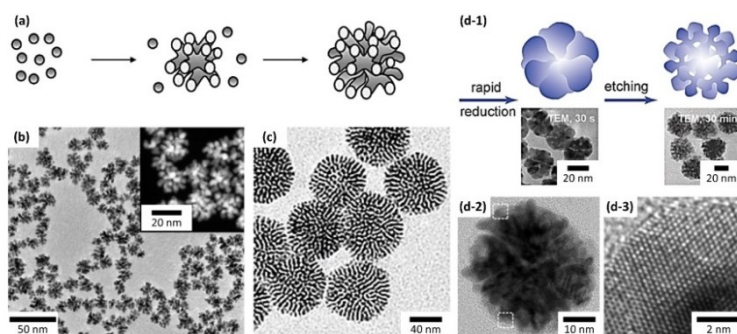


Figure 1.6 (a) Formation mechanism of branched metal nanocrystals through aggregation-based growth into nanodendrites. Reproduced with permission.^[33b] Copyright 2011, Wiley-VCH. (b) TEM image of dendritic Pt nanoparticles synthesized via a one-step aqueous-phase reaction mediated by block copolymer under mild conditions, with the inset showing higher magnification. Reproduced with permission.^[35e] Copyright 2009, American Chemical Society. (c) TEM image of dendritic Pd nanoparticles prepared with hexadecylpyridinium chloride (HDPC) as a shape-directing agent. Reproduced with permission.^[44] Copyright 2013, Wiley-VCH. (d-1) Schematic illustration of the proposed growth mechanism of the porous single-crystalline Pd nanoparticles, with the TEM images showing the products obtained after growth for 30 s and 30 min, respectively. (d-2, d-3) Low- and high-magnification TEM images of a single porous Pd nanoparticle 53 nm in size. Reproduced with permission.^[45] Copyright 2012, Wiley-VCH.

1.4.1. Monocomponent Porous Metals

There have been recent reports on surfactant-mediated synthesis which could be exploited for the fabrication of dendritic Pt nanoparticles with a narrow size distribution and large surface area (**Figure 1.6b**).^[52,53,56] Since the kinetics of the reduction reaction in this method is critical, adopting mild reducing agents (*e.g.*, ascorbic acid, formic acid) is important for producing branched nanostructures.^[37] Recently, the role of the reductant in the synthesis of dendritic Pt nanoparticles was studied by Yamauchi and co-workers.^[38] Various

agents with different reducing capabilities were used to achieve different reduction rates. The addition of AA, commonly used for the synthesis of dendritic Pt, sodium borohydride (SBH), or hydrazine monohydrate was also studied under identical experimental conditions. The reduction potentials of AA, SBH, and hydrazine in acidic solution are +0.17 V, -1.48 V, and -0.23 V, respectively. Compared to a mild reducing agent such as AA, using strongly reducing agents such as SBH and hydrazine leads to a burst of nucleation, followed by the formation of highly aggregated spherical Pt particles within a short period of time. Another key factor in the synthesis of dendritic nanostructures is the presence of surfactants or capping agents in the precursor solution. Capping agents such as polyvinyl pyrrolidone (PVP), triblock copolymers (*e.g.*, Pluronic® F127 and P123), tetradecyltrimethylammonium bromide, or sodium dodecyl sulfate are known to carry out two main functions. One is to protect the particles from agglomeration, and the second is to direct the formation of branched particles. Hence, the particle size and the length of the branches can be tuned by changing the type and the concentration of the capping agent,^[35d,39,40] although the complete role of the surfactants and other additives in the final morphology of the nanoparticles has not been clearly ascertained as yet.

In order to better understand the mechanisms involved in the formation of Pt nanocolloids, their growth was monitored in detail by *in situ* transmission electron microscopy.^[41] Besides the growth through the addition of Pt atoms, the coalescence of metal nanocrystals was also observed by tracking the metal nanocolloids in solution. Based on these observations, the formation of dendritic structures was mainly attributed to the self-assembly of tiny metal seeds.^[37,42] In this approach, the instantaneous nucleation of metal seeds within a short period of time originated from the high reduction rate of metal ions, thus leading to the rapid formation of large numbers of small seeds with a high surface to volume ratio. Following the continuous reduction of metal ions, more metal seeds can also be formed. In order to diminish their considerably high surface energy, the seeds start to coalesce in an oriented fashion instead of further growing individually.^[36b] Because of the difference in the strength of interaction between the structure-directing agents and different crystallographic surfaces of the nanocrystals, the attachment of metal seeds preferentially occurs on the surfaces with lower energy barriers. The diffusion of metal atoms across the interface between the surface and the attached seeds aids in merging the crystallites together. Other works reported dendritic particles with a polycrystalline structure, which could be attributed to a misorientation at the interface caused by the coalescence of the seeds.^[33b] The morphology of the final product greatly depends on the concentration of the seeds as well as their size and mobility in solution. A high mobility in colloidal suspension accelerates their coalescence.^[36b,37,43] On further increasing the reaction time, the dendrites are gradually transformed through coalescence into larger bundles with long branches. The formation mechanism of similar Pd dendritic nanoparticles was also proposed by Skrabalak and co-workers.^[37] In this report, the effects of the local ligand environment of the metal precursors on the rational design of nanodendrites were also

demonstrated. It was found that the addition of ligands, such as trioctylphosphine, that have a strong affinity with Pd ions and Pd seeds, leads to a decreased nucleation rate and the suppression of metal seed aggregation.

In contrast, weakly ligated agents, such as acetylacetonate, acetate, hexafluoroacetylacetonate, or chloride, facilitate the aggregation and self-assembly of metal nanoparticles, leading to the formation of dendritic structures.^[37] Recently, Huang *et al.* reported novel dendritic Pd nanoparticles with perpendicular pore channels prepared in aqueous solution at ambient temperature (**Figure 1.6c**).^[44] In this study, it was found that the reduction agent, the surfactant, and the solvent were all responsible for the formation of perpendicular channels. In a similar way to the self-assembly of metal seeds, single-crystal Pd nanoparticles with porous structure were produced by the formation of small Pd nanocrystals followed by their oriented integration (**Figure 1.6d**).^[45] Here, the reduction rate and the oxidative etching process play key roles in the formation of the porous structure. The oxidative etching, occurring preferentially at the highly active sites located in the crevices, is responsible for the porosity, while the different reduction rates of the halide ions lead to the formation of porous Pd nanoparticles. In this case, when Br⁻ ions are present or the concentration of Cl⁻ ions is high, the growth process drastically slows down and forms solid Pd nanoparticles. Yuan and co-workers successfully synthesized Rh nanodendrites in a water-based solution containing PVP, sodium lauryl sulfate (SLS), and sodium fluoride (NaF).^[46] It was demonstrated that SLS and NaF can tune the nucleation and growth rate of the Rh crystals. These results are evidence of the key role played by the synergetic effects taking place between fluoride anions and SLS in contributing to the formation of dendritic structure. Interestingly, different Rh nanostructures such as horned and cubic particles, as well as Rh networks, were produced by replacing F⁻ by Cl⁻, Br⁻, and I⁻ ions, respectively.

1.4.2. Core@shell Structured Porous Metals

Core@shell nanoparticles can exhibit interesting physical and chemical properties that have important technological outcomes.^[47] Efficient core@shell catalysts with nanoporous/dendritic shells allow outside chemical species to access the core easily.

1.4.2.1. Two-step Method

In this approach, the surfaces of the preformed metal seeds present a large number of nucleation sites for the overgrowth of different metals (**Figure 1.7a**).^[48] The seed-mediated method is well known as an effective route for the rational design of convex plain and core@shell nanoparticles.^[49] Seeded growth also offers a simple and powerful approach to prepare concave or branched multi-metallic nanospheres. In the case of branched core@shell nanoparticles, in addition to the heterogeneous nucleation of a second metal on the preformed cores, the homogeneous nucleation of small metal seeds occurs at an early stage of the reaction.

This is then followed by further growth of the dendritic shell via attachment of the metal seeds, which can be guided by various capping agents.^[36b,50] Dendritic Au@Pt nanoparticles were prepared by the deposition of a dense array of Pt nanowires on Au preformed seeds in an organic precursor solution.^[51]

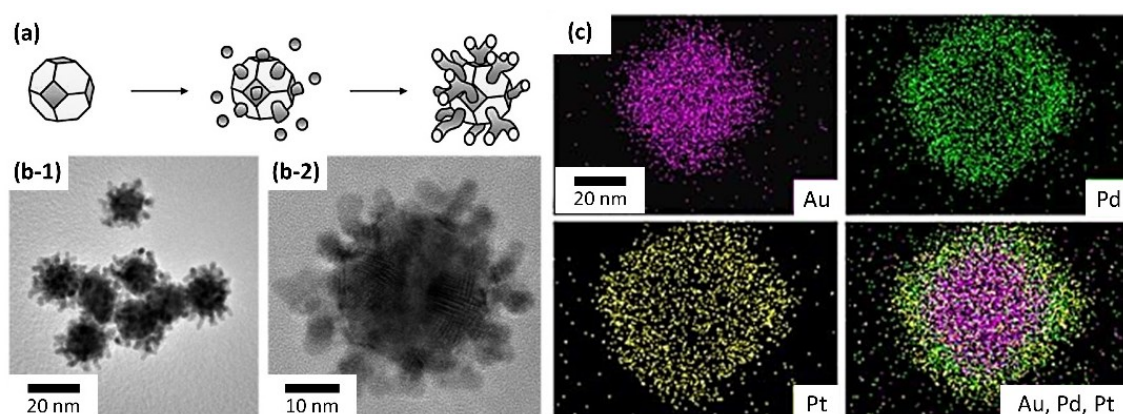


Figure 1.7 (a) Formation mechanism for aggregation-based growth in the presence of a foreign nanocrystal seed and formation of bimetallic nanodendrites. Reproduced with permission.^[33b] Copyright 2011, Wiley-VCH. (b) Low- and high-magnification TEM images of Au@Pt nanocolloids prepared from a typical solution with a Pt/Au molar ratio of 1.0. Reproduced with permission.^[60a] Copyright 2010, American Chemical Society. (c) Elemental mapping images of an Au_{oct}@PdPt nanoparticle. Reproduced with permission.^[61] Copyright 2013, American Chemical Society.

Xia and co-workers studied the synthesis of Pd@Rh nanocrystals consisting of a dense array of Rh branches supported on a Pd core and grown via a seed-mediated method. Truncated octahedral Pd nanoparticles with an average size of 9 nm were used as seeds to grow Rh branches via the reduction of Rh salts (Na₃RhCl₆) with AA. High resolution transmission electron microscope (TEM) images of the Pd@Rh nanodendrites clearly showed that Rh branches, with an average size of 3 nm, entirely covered the surface of the Pd core. Continuity of the lattice fringes extending from the Pd core to the Rh branches was also observed, suggesting that the Rh nuclei were grown epitaxially on the Pd nanocrystals (Pd and Rh have a lattice mismatch of only 2.3%).^[52] The formation mechanism was carefully investigated through TEM observations of the Pd@Rh samples at various stages of the reaction. At the early stage, along with the Rh-decorated Pd nanoparticles, small Rh seeds with less than 3 nm in size were observed, suggesting that both homogeneous and heterogeneous nucleation of Rh in the solution and on the surface of the Pd cores, respectively, occurred simultaneously. On increasing the reaction time, the number of small Rh seeds rapidly decreased, while the number of Rh branches on each Pd nanocrystal increased suggesting that the Rh branches were mainly formed through the attachment of the Rh seeds. Finally, the Pd@Rh particles were transformed into highly branched structures through the self-assembly of the Rh seeds.

Xia *et al.* also reported the synthesis of bimetallic Pd@Pt nanospheres, in which truncated Pd nanocrystals were used as seeds to guide the growth of dendritic Pt.^[33b,53] Because of the small lattice mismatch between

the two metals, the deposited Pt shell and Pd core showed an epitaxial relationship at the interface. The epitaxial growth of Pt on Pd was also reported elsewhere.^[42,54] The dendritic structure of the core@shell nanoparticles originates from the self-assembly of metal seeds, which is strongly affected by the availability of isolated sites on the preformed metal cores for the particles to attach, thus preventing an overlap between the neighboring branches.^[33b,42,53,55]

In spite of the successful synthesis of a branched network of nanocrystals, most of them do not possess well-defined symmetries.^[56] Recently, Skrabalak and co-workers have developed a new method, a seed-mediated co-reduction, for the deposition of symmetrically branched nanostructures on preformed seeds.^[57] Different concave and symmetrically branched Au/Pd nanocrystals were synthesized by coupling the co-reductions of the Au and Pd precursors. In this method, the simultaneous addition of Pd and Au precursor solutions to an aqueous suspension containing the Au cores and CTAB is followed by the addition of AA as reductant.^[58] The co-reduction of metal ions enables control over the final morphology of the binary nanocrystals by manipulating the growth kinetics of the seeds. The kinetics of overgrowth can be modulated by changing the molar ratio of metal ions or the pH in the precursor solutions. It should be mentioned that the shape and structure of the initial seeds play a key role in determining the final symmetrical dendritic shell by providing preferential sites for the growth of branches.^[56] The seed-mediated co-reduction method was also employed for the synthesis of convex polyhedral Au@Pd nanocrystals using octahedral Au nanocrystals as initial seeds.^[59]

1.4.2.2. One-step Method

In this approach, the step-by-step reduction of metal ions spontaneously occurs in a single step. The differences in the reduction potential of different metal ions play a key role in the separation of metal phases in the obtained nanospheres (*i.e.*, formation of core@shell structure). Recently, a facile synthesis route was successfully elaborated for the preparation of double- and triple-layered metallic nanoparticles, including Au@Pt, Pd@Pt, and Au@Pd@Pt, by a one-step method (**Figure 1.7b**).^[55,60] The Au@Pt core@shell nanocolloids with a Au core and a dendritic Pt shell were successfully synthesized by chemical co-reduction of H_2PtCl_6 and HAuCl_4 , in the presence of F127 under ultrasonic treatment.^[60a] Because of the large difference in their respective reduction potentials, the reduction of Au ions preferentially occurs in a short time to produce the Au cores. During this first process, the F127 cannot effectively interact with the Au nanoparticles and act as a structure-directing agent. Therefore, the Au cores in the Au@Pt possess no structural porosity. As the reduction reaction proceeds, the dendritic Pt structure overgrows on the Au nanoparticles to form dendritic Au@Pt nanocolloids.

In this synthetic procedure, the size and morphology of the initially formed metallic cores are critical for obtaining uniformly distributed core@shell nanoparticles with a controllable size. Ultrasonic irradiation is

employed to accelerate the reduction of metal ions. This phenomenon changes the nucleation kinetics from progressive to instantaneous (*i.e.*, the critical concentration of nuclei is reached immediately and further seeding is suppressed after a short period). Hence, small-sized metallic cores with a narrow size distribution can be obtained. These uniform metal cores can then serve as nucleation centers for the overgrowth of porous shells. This method was successfully extended to the synthesis of triple-layered Au@Pd@Pt core@shell structures by adding Na₂PdCl₄ to the initial precursor solution, resulting in nanoparticles consisting of an Au core, an intermediate Pd layer, and a dendritic Pt shell. Through adding the Pd intermediate layer to the Au@Pt structure, the catalytic activity could be enhanced significantly.^[60b,60c] Similar trimetallic Au@PdPt nanoparticles with a well-defined octahedral Au core and a dendritic PdPt alloy shell (Au_{oct}@PdPt) were produced by Han and co-workers (**Figure 1.7c**).^[61] The co-reduction of multiple metal precursors with dual reducing agents (AA and hydrazine) gave fine control over the nucleation and growth kinetics of the nanoparticles.

1.4.3. Multicomponent Porous Alloys

Previous computational and experimental investigations have revealed that alloy nanoparticles can exhibit a dramatic enhancement in their electrochemical activity, which is believed to originate from the synergetic effect on the electronic properties of the alloy structure. It is therefore important to synthesize alloy nanoparticles with dendritic nanostructure to further improve their electrochemical activity. A key factor in the success of solution-phase synthesis of alloy is to control the nucleation and growth of different metals with different redox properties. Under normal reduction conditions, metal salts with different reduction potentials tend to be reduced in a step-by-step fashion, thus leading to the formation of core@shell structures or phase separation. This problem can be overcome by controlling the reducing agent, surfactant binder, and temperature.

In a recent report, a very simple, one-step, and efficient route was proposed to directly produce dendritic Pt-Pd alloy nanoparticles with high surface area, carried out by simply stirring an aqueous solution containing K₂PtCl₄ and Na₂PdCl₄ binary precursors in the presence of F127 triblock copolymer and AA at room temperature for 30 min, with no need for any template, seed-mediated growth, or other additives. By simply changing the compositional ratios of the Pt and Pd sources in the precursor solutions, Pt-Pd nanodendrites with various compositions can be easily produced. Because of its unique simplicity, the proposed approach can be considered as a powerful strategy for producing Pt-Pd alloy nanoparticles with unique nanoarchitectures for commercial devices.^[62] As another interesting example, the synthesis of well-defined Pt-Pd alloy nanoflowers with dominant {111} facets was reported through a chemical reduction method in a poly(allylamine hydrochloride) (PAH) based aqueous solution. The {111}-enclosed Pt-Pd nanoflowers exhibit superior ORR activity, along with satisfactory stability and methanol tolerance under acidic conditions,

showcasing them as promising electrocatalysts for the future.^[63] Alloying Pt with a second metal (*e.g.*, Ru, Pd, and Ni) plays a key role in reducing CO poisoning and improving the catalytic activity. Among all of these alloys, Pt-Ru catalysts, where the co-reduction of Pt and Ru salts in the presence of F127 leads to the formation of Pt-Ru nanoparticles with a dendritic structure, exhibit a high tolerance to CO poisoning and enhanced catalytic activity during the MOR. This improvement is caused by the bi-functional effect of Ru on the overall electronic structure of the Pt atoms.^[64]

Zhang *et al.* reported a similar approach to prepare bimetallic Au-Pd nanocrystals with a well-defined dendritic morphology.^[65] Here, AA is used as a reductant, while P123 triblock copolymer is used as a stabilizing agent. The Au/Pd atomic ratios can be tuned over a wide range without degrading the nanodendritic morphology. The as-prepared Au-Pd nanodendrites exhibit excellent catalytic activities toward electro-oxidation of methanol and reduction of 2-nitrophenol, and the catalytic performances could be effectively tuned by varying the Au/Pd ratio. Dendritic Au-Pd alloy nanoparticles, synthesized through the co-reduction of HAuCl₄ and K₂PdCl₄ in a PVP aqueous solution by using hydrazine as a reducing agent, also show efficient electrocatalytic activity and stability towards ethanol oxidation in alkaline media.^[66] The enhanced electrocatalytic properties of dendritic particles can be attributed to the presence of a large number of active sites on their surfaces.

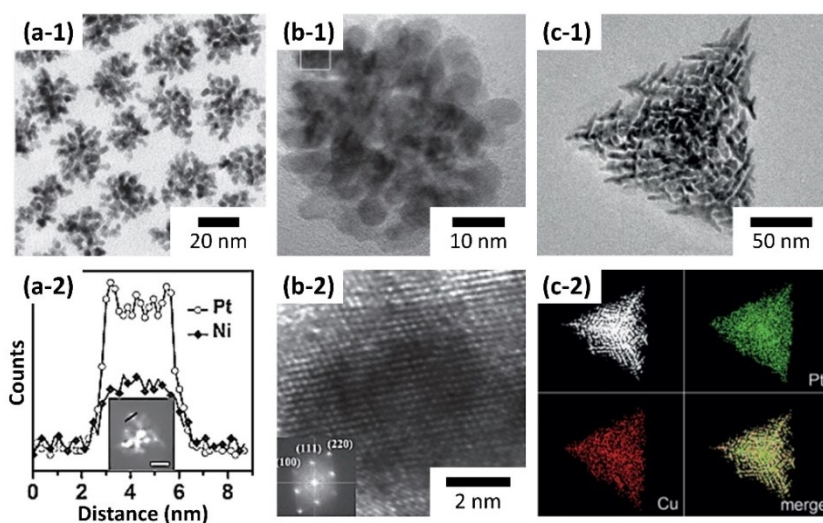


Figure 1.8 (a-1) TEM image, high-angle annular dark field-scanning TEM (HAADF-STEM) image, and (a-2) energy dispersive X-ray spectroscopy (EDX) line profiles of porous Pt₃Ni nanocrystals. Reproduced with permission.^[68] Copyright 2013, Wiley-VCH. (b) Low-magnification TEM image (b-1) and highly magnified TEM image (b-2) taken from the selected area marked by the rectangle in (b-1). The inset in (b-2) is the corresponding fast Fourier transform (FFT) pattern. Reproduced with permission.^[70] Copyright 2013, Wiley-VCH. (c) TEM image (c-1) and corresponding elemental mapping images (c-2) of Pt-Cu hierarchical trigonal bipyramid nanoframes. Reproduced with permission.^[71] Copyright 2015, Wiley-VCH.

Among the various reported Pt-based bimetallic nanostructures, intermetallic Pt₃Ni nanocrystals represent an emerging class of newly discovered electrocatalysts that exhibit exciting performance. It has been reported that the (111) surface of Pt₃Ni exhibits extremely high ORR activity, about 10-fold higher than Pt(111) and 90-fold higher than the commercial Pt/C catalysts.^[67] Nanoporous dendritic Pt₃Ni particles were prepared by simultaneous reduction of platinum(II) acetylacetonate and nickel(II) acetylacetonate by using N,N-dimethylformamide (DMF) as both solvent and reducing agent, as well as PVP and phenol as structure-directing agents (**Figure 1.8a**).^[68] The obtained dendritic Pt₃Ni nanocrystals can serve as highly efficient catalysts in the ORR with good durability. In contrast, Li *et al.* reported using the same metal precursors stirred in a mixture of octadecene, oleylamine, oleic acid, and didodecyldimethylammonium bromide, resulting in the formation of Pt-Ni nanodendrites with a homogeneously alloyed structure (non-intermetallic structure), uniform shape, and controllable size. Taking advantage of the properties of 3d-transition-metal-modified components, the highly branched Pt-Ni nanocrystals displayed excellent activity towards the hydrogenation of nitrobenzene. The self-supported dendritic structure prevents the nanocrystals from agglomerating and shows high stability.^[69]

Considering the high cost of noble metal catalysts, their substitution by inexpensive metals (e.g., Cu, Fe, Co, Ni) has been extensively studied. Zhang and co-workers reported the synthesis of Pt–Cu alloy nanocrystals with controlled morphologies by using glycine to mediate the sequential reduction kinetics in an aqueous solution (**Figure 1.8b**).^[70] Glycine plays a decisive role in altering the reduction kinetics of the metal precursors and therefore determines the final morphologies of the Pt-Cu alloy nanocrystals. By simply varying the concentration of glycine in the growth solution, dendritic Pt-Cu alloy nanocrystals could be prepared. Gong and co-workers reported the synthesis of Pt-Cu bimetallic alloy nanodendrites by a facile, one-pot, template-free, and seed-free hydrothermal method in the presence of PAH.^[35c] The autocatalytic growth and interdiffusion are responsible for the formation of the Pt-Cu alloy, whereas *in-situ* selective oxidative etching results in dendritic morphology of the Pt-Cu alloy nanostructures. Recently, Chen *et al.* reported the size-controlled synthesis of unique Pt-Cu hierarchical trigonal bipyramid nanoframes composed of similar ordered structural units (**Figure 1.8c**).^[71] Small monopods, bipods, and tripods form in the early stage, followed by the growth of secondary, tertiary, and higher-order branches, and ultimately, the formation of Pt-Cu hierarchical trigonal bipyramid structures. The as-prepared electrocatalysts exhibit enhanced electrocatalytic activity towards the formic acid oxidation reaction, owing to their unique hierarchical structure and the synergetic effects occurring between Pt and Cu.

1.5. Motivation and Purpose of This Study

Over the last few decades, nanoporous noble metals have provoked ever-increasing attention in the field of

catalysis owing to their unique physical and chemical properties. Although some strategies have been made toward to the fabrication of nanoporous noble metals with tunable structures and compositions, most of them require complex/multistep procedures and take specialized synthetic techniques, which make them challenging to scale up. From a green chemistry and sustainable development perspective, it is highly needed to develop facile and efficient approaches to fabrication of the nanoporous noble metals. Therefore, the purpose in my PhD study is to develop facile and straight soft-templating methods, based on the diluted concentration of surfactants or block polymers for controlled synthesis of nanoporous metals.

On the other hand, electrocatalytic reaction can occur only when the reactants are adsorbed onto catalyst surfaces. Nanoporous metals with an accessible surface area may result in enhancements in the electrocatalytic performances owing to the high surface areas and abundant active sites. It is note that the porous architectures of metals obtained in previous reports are mainly limited to dendritic and small-sized pores, leading to the less accessibility. Recently, nanoporous materials with large-sized pores have become a subject of extensive research because they can facilitate a smooth and efficient transport of reactants or effectively adsorb large molecules. Because the pore sizes and pore structures for metals are more difficult to control compared to general mesoporous systems such as silica, very few examples of large-sized nanoporous metals have been reported. Therefore, it is of great importance and interest to synthesize nanoporous metals with large-pore to improve the electrochemical activity, as shown in **Figure 1.9**.

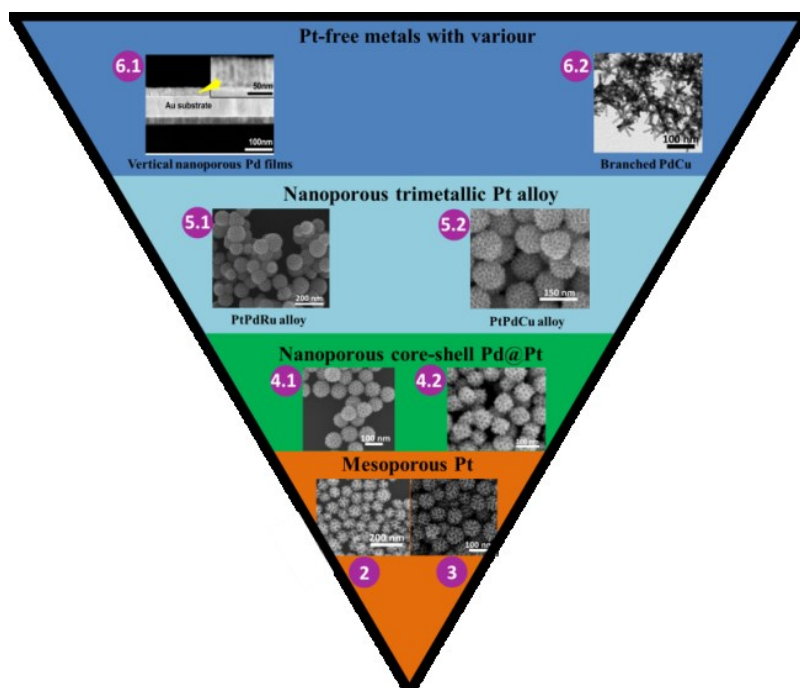


Figure 1.9 Summary of my works in this thesis

References

- [1] V. Malgras, H. Ataee-Esfahani, H. Wang, B. Jiang, C. Li, K. C-W Wu, J. H. Kim, Y. Yamauchi, *Adv. Mater.*, 2016, **28**, 993.
- [2] (a) J. Beck, J. Vartuli, W. Roth, M. Leonowicz, C. Kresge, K. Schmitt, C. Chu, D. Olson, E. Sheppard, *J. Am. Chem. Soc.*, 1992, **114**, 10834; (b) C. Kresge, M. Leonowicz, W. Roth, J. Vartuli, J. Beck, *Nature*, 1992, **359**, 710.
- [3] Y. Deng, D. Qi, C. Deng, X. Zhang, D. Zhao, *J. Am. Chem. Soc.*, 2008, **130**, 28.
- [4] A. Yamaguchi, F. Uejo, T. Yoda, T. Uchida, Y. Tanamura, T. Yamashita, N. Teramae, *Nat. Mater.*, 2004, **3**, 337.
- [5] (a) Y. Deng, Y. Cai, Z. Sun, J. Liu, C. Liu, J. Wei, W. Li, C. Liu, Y. Wang, D. Zhao, *J. Am. Chem. Soc.*, 2010, **132**, 8466; (b) M. Vallet-Regi, A. Ramila, R. Del Real, J. Pérez-Pariente, *Chem. Mater.*, 2001, **13**, 308; (c) G. Ma, X. Yan, Y. Li, L. Xiao, Z. Huang, Y. Lu, J. Fan, *J. Am. Chem. Soc.*, 2010, **132**, 9596.
- [6] (a) C.-Y. Lai, B. G. Trewyn, D. M. Jeftinija, K. Jeftinija, S. Xu, S. Jeftinija, V. S.-Y. Lin, *J. Am. Chem. Soc.*, 2003, **125**, 4451; (b) J. L. Vivero-Escoto, I. I. Slowing, C.-W. Wu, V. S.-Y. Lin, *J. Am. Chem. Soc.*, 2009, **131**, 3462; (c) R. Liu, Y. Zhang, X. Zhao, A. Agarwal, L. J. Mueller, P. Feng, *J. Am. Chem. Soc.*, 2010, **132**, 1500; (d) D. R. Radu, C.-Y. Lai, K. Jeftinija, E. W. Rowe, S. Jeftinija, V. S.-Y. Lin, *J. Am. Chem. Soc.*, 2004, **126**, 13216.
- [7] F. Jiao, P. G. Bruce, *Adv. Mater.*, 2007, **19**, 657.
- [8] (a) Y. Shi, B. Guo, S. A. Corr, Q. Shi, Y.-S. Hu, K. R. Heier, L. Chen, R. Seshadri, G. D. Stucky, *Nano Lett.*, 2009, **9**, 4215; (b) E. Rossinyol, A. Prim, E. Pellicer, J. Arbiol, F. Hernández - Ramírez, F. Peiro, A. Cornet, J. R. Morante, L. A. Solovyov, B. Tian, *Adv. Funct. Mater.*, 2007, **17**, 1801.
- [9] F. Pereira, K. Vallé, P. Belleville, A. Morin, S. Lambert, C. Sanchez, *Chem. Mater.*, 2008, **20**, 1710.
- [10] R. Ryoo, S. H. Joo, S. Jun, *J. Phys. Chem. B*, 1999, **103**, 7743.
- [11] S. Jun, S. H. Joo, R. Ryoo, M. Kruk, M. Jaroniec, Z. Liu, T. Ohsuna, O. Terasaki, *J. Am. Chem. Soc.*, 2000, **122**, 10712.
- [12] H. J. Shin, R. Ryoo, Z. Liu, O. Terasaki, *J. Am. Chem. Soc.*, 2001, **123**, 1246.
- [13] L. Ye, Y. Wang, X. Chen, B. Yue, S. Chi Tsang, H. He, *Chem. Commun.*, 2011, **47**, 7389.
- [14] P.-K. Chen, N.-C. Lai, C.-H. Ho, Y.-W. Hu, J.-F. Lee, C.-M. Yang, *Chem. Mater.*, 2013, **25**, 4269.
- [15] (a) H. Wang, H. Y. Jeong, M. Imura, L. Wang, L. Radhakrishnan, N. Fujita, T. Castle, O. Terasaki, Y. Yamauchi, *J. Am. Chem. Soc.*, 2011, **133**, 14526; (b) H. Wang, M. Imura, Y. Nemoto, S. E. Park, Y. Yamauchi, *Chem. - Asian J.*, 2012, **7**, 802.
- [16] (a) P. Karthika, H. Ataee-Esfahani, H. Wang, M. A. Francis, H. Abe, N. Rajalakshmi, K. S. Dhathathreyan, D. Arivuoli, Y. Yamauchi, *Chem. - Asian J.*, 2013, **8**, 902; (b) P. Karthika, H. Ataee-Esfahani, Y.-H. Deng, K. C.-W. Wu,

- N. Rajalakshmi, K. S. Dhathathreyan, D. Arivuoli, K. Ariga, Y. Yamauchi, *Chem. Lett.*, 2013, **42**, 447.
- [17] G. S. Attard, J. M. Corker, C. G. Göltner, S. Henke, R. H. Templer, *Angew. Chem. Int. Ed.*, 1997, **36**, 1315.
- [18] G. S. Attard, P. N. Bartlett, N. R. Coleman, J. M. Elliott, J. R. Owen, J. H. Wang, *Science*, 1997, **278**, 838.
- [19] P. Bartlett, B. Gollas, S. Guerin, J. Marwan, *Phys. Chem. Chem. Phys.*, 2002, **4**, 3835.
- [20] J. M. Elliott, G. S. Attard, P. N. Bartlett, N. R. Coleman, D. A. Merckel, J. R. Owen, *Chem. Mater.*, 1999, **11**, 3602.
- [21] J. M. Elliott, P. R. Birkin, P. N. Bartlett, G. S. Attard, *Langmuir*, 1999, **15**, 7411.
- [22] Y. Yamauchi, A. Sugiyama, R. Morimoto, A. Takai, K. Kuroda, *Angew. Chem. Int. Ed.*, 2008, **47**, 5371.
- [23] A. Takai, Y. Yamauchi, K. Kuroda, *J. Am. Chem. Soc.*, 2009, **132**, 208.
- [24] (a) Y. Yamauchi, T. Momma, H. Kitoh, T. Osaka, K. Kuroda, *Electrochem. Commun.*, 2005, **7**, 1364; (b) Y. Yamauchi, H. Kitoh, T. Momma, T. Osaka, K. Kuroda, *Sci. Technol. Adv. Mater.*, 2006, **7**, 438.
- [25] Y. Yamauchi, T. Ohsuna, K. Kuroda, *Chem. Mater.*, 2007, **19**, 1335.
- [26] Y. Yamauchi, A. Takai, M. Komatsu, M. Sawada, T. Ohsuna, K. Kuroda, *Chem. Mater.*, 2007, **20**, 1004.
- [27] A. Takai, Y. Yamauchi, K. Kuroda, *Chem. Commun.*, 2008, 4171.
- [28] X. Zhang, W. Lu, J. Dai, L. Bourgeois, N. Hao, H. Wang, D. Zhao, P. A. Webley, *Angew. Chem. Int. Ed.*, 2010, **49**, 10101.
- [29] X. Zhang, W. Lu, J. Dai, L. Bourgeois, J. Yao, H. Wang, J. R. Friend, D. Zhao, D. R. MacFarlane, *Sci. Rep.*, 2014, **4**, 7420.
- [30] C. Zhang, H. Yang, T. Sun, N. Shan, J. Chen, L. Xu, Y. Yan, *J. Power Sources*, 2014, **245**, 579.
- [31] H. Wang, S. Ishihara, K. Ariga, Y. Yamauchi, *J. Am. Chem. Soc.*, 2012, **134**, 10819.
- [32] H. Atae-Esfahani, M. Imura, Y. Yamauchi, *Angew. Chem. Int. Ed.*, 2013, **52**, 13611.
- [33] (a) S. Guo, S. Zhang, S. Sun, *Angew. Chem. Int. Ed.*, 2013, **52**, 8526; (b) B. Lim, Y. Xia, *Angew. Chem. Int. Ed.*, 2011, **50**, 76.
- [34] (a) X. Teng, X. Liang, S. Maksimuk, H. Yang, *Small*, 2006, **2**, 249; (b) J. D. Hoefelmeyer, K. Niesz, G. A. Somorjai, T. D. Tilley, *Nano Lett.*, 2005, **5**, 435, (c) H. Kim, N. T. Khi, J. Yoon, H. Yang, Y. Chae, H. Baik, H. Lee, J. H. Sohn, K. Lee, *Chem. Commun.*, 2013, **49**, 2225; (d) J. Watt, S. Cheong, M. F. Toney, B. Ingham, J. Cookson, P. T. Bishop, R. D. Tilley, *ACS Nano*, 2009, **4**, 396.
- [35] (a) S. Yang, X. Luo, *Nanoscale*, 2014, **6**, 4438; (b) Y. Song, Y. Yang, C. J. Medforth, E. Pereira, A. K. Singh, H. Xu, Y. Jiang, C. J. Brinker, F. Swol, J. A. Shelnett, *J. Am. Chem. Soc.*, 2004, **126**, 635; (c) M. Gong, G. Fu, Y. Chen, Y. Tang, T. Lu, *ACS Appl. Mater. Interfaces*, 2014, **6**, 7301; (d) L. Wang, H. Wang, Y. Nemoto, Y. Yamauchi, *Chem.*

Mater., 2010, **22**, 2835; (e) L. Wang, Y. Yamauchi, *J. Am. Chem. Soc.*, 2009, **131**, 9152; (f) S. Wang, L. P. Xu, Y. Wen, H. Du, S. Wang, X. Zhang, *Nanoscale*, 2013, **5**, 4284; (g) J. J. Lv, J. N. Zheng, S. S. Li, L. L. Chen, A. J. Wang, J. J. Feng, *J. Mater. Chem. A*, 2014, **2**, 4384.

[36] (a) L. Wang, Y. Yamauchi, *Chem. Mater.*, 2009, **21**, 3562; (b) J. Gu, Y. W. Zhang, F. Tao, *Chem. Soc. Rev.*, 2012, **41**, 8050; (c) H. Lee, S. E. Habas, S. Kweskin, D. Butcher, G. A. Somorjai, P. Yang, *Angew. Chem. Int. Ed.*, 2006, **45**, 7824.

[37] N. Ortiz, S. E. Skrabalak, *Angew. Chem. Int. Ed.*, 2012, **51**, 11757.

[38] L. Wang, C. Hu, Y. Nemoto, Y. Tateyama, Y. Yamauchi, *Cryst. Growth Des.*, 2010, **10**, 3454.

[39] H. Atae-Esfahani, L. Wang, Y. Yamauchi, *Chem. Commun.*, 2010, **46**, 3684.

[40] C. Li, M. Imura, Y. Yamauchi, *Phys. Chem. Chem. Phys.*, 2014, **16**, 8787.

[41] (a) C. B. Murray, *Science*, 2009, **324**, 1276; (b) H. Zheng, R. K. Smith, Y. W. Jun, C. Kisielowski, U. Dahmen, A. P. Alivisatos, *Science*, 2009, **324**, 1309.

[42] B. Lim, M. Jiang, T. Yu, P. H. Camargo, Y. Xia, *Nano Res.*, 2010, **3**, 69.

[43] K. Qi, Q. Wang, W. Zheng, W. Zhang, X. Cui, *Nanoscale*, 2014, **6**, 15090.

[44] X. Huang, Y. Li, Y. Chen, E. Zhou, Y. Xu, H. Zhou, X. Duan, Y. Huang, *Angew. Chem. Int. Ed.*, 2013, **52**, 2520.

[45] F. Wang, C. Li, L. D. Sun, C. H. Xu, J. Wang, J. C. Yu, C. H. Yan, *Angew. Chem. Int. Ed.*, 2012, **51**, 4872.

[46] Q. Yuan, Z. Zhou, J. Zhuang, X. Wang, *Inorg. Chem.*, 2010, **49**, 5515.

[47] (a) H. Kobayashi, M. Yamauchi, H. Kitagawa, Y. Kubota, K. Kato, M. Takata, *J. Am. Chem. Soc.*, 2008, **130**, 1818; (b) W. R. Lee, M. G. Kim, J. R. Choi, J. I. Park, S. J. Ko, S. J. Oh, J. Cheon, *J. Am. Chem. Soc.*, 2005, **127**, 16090.

[48] (a) H. Zhang, M. Jin, Y. Xia, *Angew. Chem. Int. Ed.*, 2012, **51**, 7656; (b) S. Xie, S. I. Choi, N. Lu, L. T. Roling, J. A. Herron, L. Zhang, J. Park, J. Wang, M. J. Kim, Z. Xie, M. Mavrikakis, Y. Xia, *Nano Lett.*, 2014, **14**, 3570; (c) Y. Feng, H. Liu, J. Yang, *J. Mater. Chem. A*, 2014, **2**, 6130; (d) R. Choi, S. I. Choi, C. H. Choi, K. M. Nam, S. I. Woo, J. T. Park, S. W. Han, *Chem. Eur. J.*, 2013, **19**, 8190; (e) X. Wang, B. Wu, G. Chen, Y. Zhao, P. Liu, Y. Dai, N. Zheng, *Nanoscale*, 2014, **6**, 6798.

[49] Y. Xia, Y. Xiong, B. Lim, S. E. Skrabalak, *Angew. Chem. Int. Ed.*, 2009, **48**, 60.

[50] C. Li, Y. Yamauchi, *Phys. Chem. Chem. Phys.*, 2013, **15**, 3490.

[51] (a) Z. Peng, H. Yang, *Nano Res.*, 2009, **2**, 406; (b) S. Zhou, K. McIlwrath, G. Jackson, B. Eichhorn, *J. Am. Chem. Soc.*, 2006, **128**, 1780;

[52] H. Kobayashi, B. Lim, J. Wang, P. H. Camargo, T. Yu, M. J. Kim, Y. Xia, *Chem. Phys. Lett.*, 2010, **494**, 249.

- [53] B. Lim, M. Jiang, P. H. Camargo, E. C. Cho, J. Tao, X. Lu, Y. Zhu, Y. Xia, *Science*, 2009, **324**, 1302.
- [54] Z. Peng, H. Yang, *J. Am. Chem. Soc.*, 2009, **131**, 7542.
- [55] L. Wang, Y. Nemoto, Y. Yamauchi, *J. Am. Chem. Soc.*, 2011, **133**, 9674.
- [56] C. J. DeSantis, S. E. Skrabalak, *J. Am. Chem. Soc.*, 2012, **135**, 10.
- [57] (a) C. J. DeSantis, S. E. Skrabalak, *Langmuir*, 2012, **28**, 9055; (b) C. J. DeSantis, A. C. Sue, M. M. Bower, S. E. Skrabalak, *ACS Nano*, 2012, **6**, 2617.
- [58] C. J. DeSantis, A. A. Peverly, D. G. Peters, S. E. Skrabalak, *Nano Lett.*, 2011, **11**, 2164.
- [59] D. Kim, Y. W. Lee, S. B. Lee, S. W. Han, *Angew. Chem. Int. Ed.*, 2012, **51**, 159.
- [60] (a) H. Ataee-Esfahani, L. Wang, Y. Nemoto, Y. Yamauchi, *Chem. Mater.*, 2010, **22**, 6310; (b) L. Wang, Y. Yamauchi, *J. Am. Chem. Soc.*, 2010, **132**, 13636; (c) L. Wang, Y. Yamauchi, *Chem. Mater.*, 2011, **23**, 2457.
- [61] S. W. Kang, Y. W. Lee, Y. Park, B. S. Choi, J. W. Hong, K. H. Park, S. W. Han, *ACS Nano*, 2013, **7**, 7945.
- [62] L. Wang, Y. Yamauchi, *Chem. Asian J.*, 2010, **5**, 2493.
- [63] G. Fu, K. Wu, J. Lin, Y. Tang, Y. Chen, Y. Zhou, T. Lu, *J. Phys. Chem. C*, 2013, **117**, 9826.
- [64] H. Ataee-Esfahani, Y. Nemoto, M. Imura, Y. Yamauchi, *Chem. Asian J.*, 2012, **7**, 876.
- [65] L. Shi, A. Wang, T. Zhang, B. Zhang, D. Su, H. Li, Y. Song, *J. Phys. Chem. C*, 2013, **117**, 12526.
- [66] Y. W. Lee, M. Kim, Y. Kim, S. W. Kang, J. H. Lee, S. W. Han, *J. Phys. Chem. C*, 2010, **114**, 7689.
- [67] V. R. Stamenkovic, B. Fowler, B. S. Mun, G. Wang, P. N. Ross, C. A. Lucas, N. M. Marković, *Science*, 2007, **315**, 493.
- [68] X. Huang, E. Zhu, Y. Chen, Y. Li, C. Y. Chiu, Y. Xu, Z. Lin, X. Duan, Y. Huang, *Adv. Mater.*, 2013, **25**, 2974.
- [69] W. Wang, D. Wang, X. Liu, Q. Peng, Y. Li, *Chem. Commun.*, 2013, **49**, 2903.
- [70] Z. Zhang, Y. Yang, F. Nosheen, P. Wang, J. Zhang, J. Zhuang, X. Wang, *Small*, 2013, **9**, 3063.
- [71] S. Chen, H. Su, Y. Wang, W. Wu, J. Zeng, *Angew. Chem. Int. Ed.*, 2015, **54**, 108.

Chapter 2. Mesoporous Pt Nanospheres with Designed Pore Surface as Highly Active Electrocatalyst

2.1. Introduction

Metallic nanomaterials with open curved surfaces having low-coordinated atomic sites, such as nanoporous/mesoporous structures,^[1] nanoframes,^[2] dendritic structures,^[3] and polyhedra/nanowires/nanorods,^[4] have attracted fast-growing attention in catalysis applications owing to their fascinating performance. In particular, metals with mesoporous structures possess a high surface area, three-dimensional molecular accessibility and can facilitate mass transfer from the outer surface to the inner structure.^[5] In addition, both inner and outer surfaces are composed of atoms with unsaturated valence, thus dramatically enhancing the electrocatalytic performance.^[6] Therefore, mesoporous metals offer a wide range of promising applications which cannot be satisfied by other silica-based mesoporous materials.

Currently, mesoporous metals have become a subject of extensive research as pores allow a fast and efficient transport of reactants.^[7] In order to precisely tune the properties of these materials, it is required to design their porous architecture. Several strategies, including dealloying techniques, galvanic replacement reactions, electrochemical depositions, and soft- and hard-templating methods, have been developed.^[8] Especially, soft-templating approach based on a simple chemical reduction has been considered as a more versatile, flexible, and effective strategy, which would be easily applicable to a large-scale production in the future. Until now, it should be noted that most of the studies have been reported that mesoporous metals limited to particles with irregular shape or to continuous films. The lack of control over the particle size and morphology is a serious problem, which needs to be overcome in order to further develop and implement mesoporous metals in electrocatalytic applications. My target in this study is to design mesoporous Pt nanospheres (MPNs) with a narrow size distribution by a versatile chemical reduction approach.

To further enhance the catalytic performance of MPNs, here I focus on the design of “true” mesoporous structure as well as abundant active sites on the mesoporous surfaces. Although several solution phase approaches have been attempted to prepare Pt electrocatalysts, the obtained architectures are limited to only dendritic Pt nanoparticles possessing tiny and random interspaces (less than 5 nm).^[9] Mesoporous Pt nanoparticles/nanospheres are ideal to realize beneficial mass transport.^[10] Some effective additives have been utilized to create abundant catalytically active sites on the noble metal surfaces^[11], because such additives are competent in tailoring the reaction kinetics of the precursors during the crystal growth. Therefore, in this study, I propose to prepare the “true” mesoporous Pt nanospheres with abundant active sites on the porous surface by using a kinetically controlled chemical reduction, which has never been exploited in the synthesis of

mesoporous metals. I strongly believe that it will be a promising strategy to produce performant electrocatalytic materials.

In this paper, I report the synthesis of MPNs with interconnected mesopores by a controlled chemical reduction in aqueous solution without the necessity of any seeds or organic solvents. In brief, MPNs are synthesized by reducing H_2PtCl_6 with ascorbic acid in the presence of a Pluronic F127 surfactant and KBr. It is found that F127 acts as a pore-directing agent, while the combination of bromide ions and dioxygen pairs allows the porous structure to become interconnected and the surface to become catalytically active. Compared to commercial Pt black (PtB) and PtC-20% catalysts, my MPNs exhibit an enhanced electrocatalytic activity and structural thermostability.

2.2. Experimental Sections

2.2.1. Materials

All chemicals and solvents were used as received without further purification. H_2PtCl_6 , ascorbic acid (AA), H_2SO_4 , HClO_4 and methanol were purchased from Nacalai Tesque, Inc. (Kyoto, Japan). Commercial Pt black, PtC-20%, Pluronic F127 and potassium bromide (KBr) were obtained from Sigma-Aldrich. All solutions were prepared with deionized water treated with a Millipore water purification system (Millipore Corp.).

2.2.2. Preparation of Mesoporous Pt Nanospheres

In a typical synthesis of mesoporous Pt nanospheres (MPNs), 200 mg KBr and 30 mg Pluronic F127 were dissolved in 2 mL deionized water. After complete dissolution, 0.75 mL H_2PtCl_6 solution (40 mM) and 2 mL ascorbic acid (AA) solution (0.1 M) were added. The mixed solution was then kept in a water bath for 12 hours at 70 °C. Finally, the sample was collected by centrifugation at 14,000 rpm for 20 min and the residual Pluronic F127 was removed by three consecutive washing/centrifugation cycles with ethanol and water.

2.2.3. Characterization

Scanning electron microscopy (SEM) imaging was carried out using a Hitachi SU-8000 microscope operated at 5 kV. Transmission electron microscopy (TEM) and high-angle annular dark-field scanning TEM (HAADF-STEM) observations were performed using a JEOL JEM-2100F operated at 200 kV equipped with an energy-dispersive spectrometry analyzer. The samples for TEM characterizations were prepared by depositing a drop of the diluted colloidal suspension on a grid. Wide-angle powder X-ray diffraction (XRD) patterns were acquired with a Rigaku Rint 2500 diffractometer with monochromated Cu K α radiation. Low-angle XRD patterns were obtained by using a NANO VIEWER (Rigaku, Japan) equipped with a Micro

Max-007 HF high-intensity micro-focus rotating anode X-ray generator. X-ray photoelectronic spectroscopy (XPS) spectra were obtained at room temperature by using a JPS-9010TR (JEOL) instrument with an Mg K α X-ray source. All the binding energies were calibrated via referencing to C 1 s binding energy (284.6eV).

2.2.4. Electrochemical Test

Electrochemical Measurement of Methanol Oxidation Reaction (MOR)

Cyclic voltammograms (CV) and chronoamperometric (CA) experiments were performed using a CHI 842B electrochemical analyzer (CHI Instruments, USA). A conventional three-electrode cell was used, including an Ag/AgCl (saturated KCl) reference electrode, a platinum wire as a counter electrode, and a modified glassy carbon electrode (GCE, 3 mm in diameter) as a working electrode. The modified GCE was coated with the sample (5.0 μ g) and dried at room temperature. Then, 5.0 μ L of Nafion (0.05 wt %) was coated on the surface of the modified GCE and dried before electrochemical experiments. Prior to the electrochemical measurements, the GCE modified with the as-prepared sample was electrochemically activated by a potential cycling between -0.2 V and +1.5 V (vs. Ag/AgCl) in 0.5 M H₂SO₄ until the obtained CVs became characteristic of a clean Pt electrode. Methanol electro-oxidation measurements were performed in a solution of 0.5 M H₂SO₄ containing 0.5 M methanol at a scan rate of 50 mV s⁻¹. The chronoamperometric measurement was carried out at a constant potential of 0.6 V for 3000 s.

Electrochemical Measurement of Oxygen Reduction Reaction (ORR)

CV measurements were obtained from a similar setup to the MOR measurement. A conventional three-electrode cell was used, including an Ag/AgCl (saturated KCl) reference electrode, a platinum wire as a counter electrode, and a modified rotating ring-disk electrode (RRDE, 4 mm in diameter) as a working electrode. The working electrode was prepared as follows. 2 mg of catalyst (MPNs, shallow concave Pt nanoparticles Pt, commercial Pt normally 20% on carbon (abbreviated as PtC-20%), or platinum black (abbreviated as PtB)) was dispersed in the mixture of water (0.4 mL) and Nafion (5 wt%, 10 μ L) under ultra-sonication for 30 min to get a uniform suspension of the catalysts. Then, 5 μ L of the above suspension was dropped on the disk electrode surface of the RRDE and dried at room temperature. The electrochemical measurements were performed in 0.1 M HClO₄ saturated with O₂ at a potential range between -0.2 V and 1.0 V (vs. Ag/AgCl) with a scan rate of 10 mV s⁻¹ and a typical rotating speed of 1600 rpm. In this work, electrochemical tests for different electrocatalysts were repeated for three times.

The rotating ring-disk electrode (RRDE) was used to study the reduction pathway of oxygen. The ring electrode current, which corresponds to the oxidation of intermediate (hydrogen peroxide ions, HO_2^-), was recorded together with the disk electrode current. The electron number (n) transferred per oxygen molecule involved in the ORR was calculated from RRDE voltammograms according to the following equation:

$$n=4 \times I_d/(I_d + I_r/N)$$

where I_d is the disk current, I_r is the ring current and $N = 0.4$ is the current collection efficiency of Pt ring electrode.

2.3. Results and Discussion

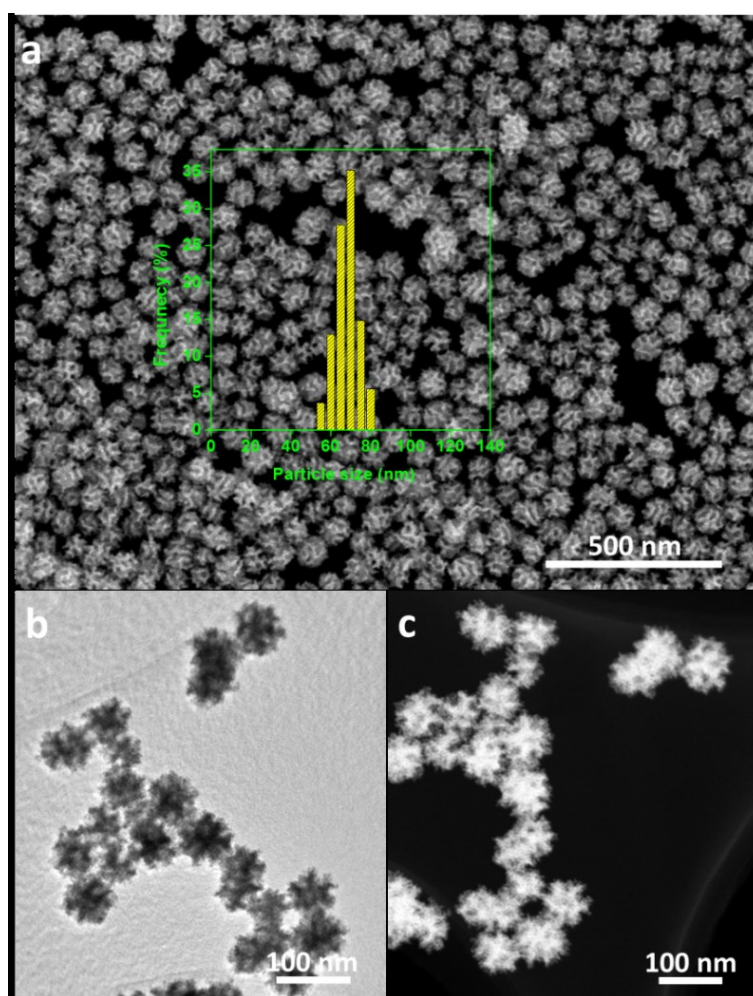


Figure 2.1 (a) Low-magnification SEM, (b) TEM, and (c) HAADF-STEM images of the MPNs prepared under the typical condition. Inset image in (a) shows particle size distribution of the MPNs.

Scanning electron microscope (SEM) and transmission electron microscopy (TEM) were employed to characterize the structures of the product. The nanospheres are well-dispersed and highly uniform in shape and

size (**Figure 2.1a**). An average size of around 70 nm is determined from statistical measurements over 200 nanospheres (**inset image of Figure 2.1a**) and the pores on the surface have a size distribution centered on 11 ± 1 nm. The porous structure and size are distinctly different from the dendritic ones.^[9] The different contrasts observed on the TEM image evidence that the mesopores are deeply embedded and interconnected in the nanospheres (**Figure 2.1b**). These mesoporous structures are further presented in high-angle annular dark-field scanning TEM (HAADF-STEM) image (**Figure 2.1c**). Considering the average pore diameter and wall thickness measured from the SEM analysis to be 11 and 9-10 nm, respectively, the average pore-to-pore distance is estimated to be roughly 20-21 nm. This is in good agreement with the low angle X-ray diffraction pattern displaying a sharp peak at 0.43° ($d=20.3$ nm) (**Figure 2.2a**), which is also a strong evidence of the high uniformity of the sample.

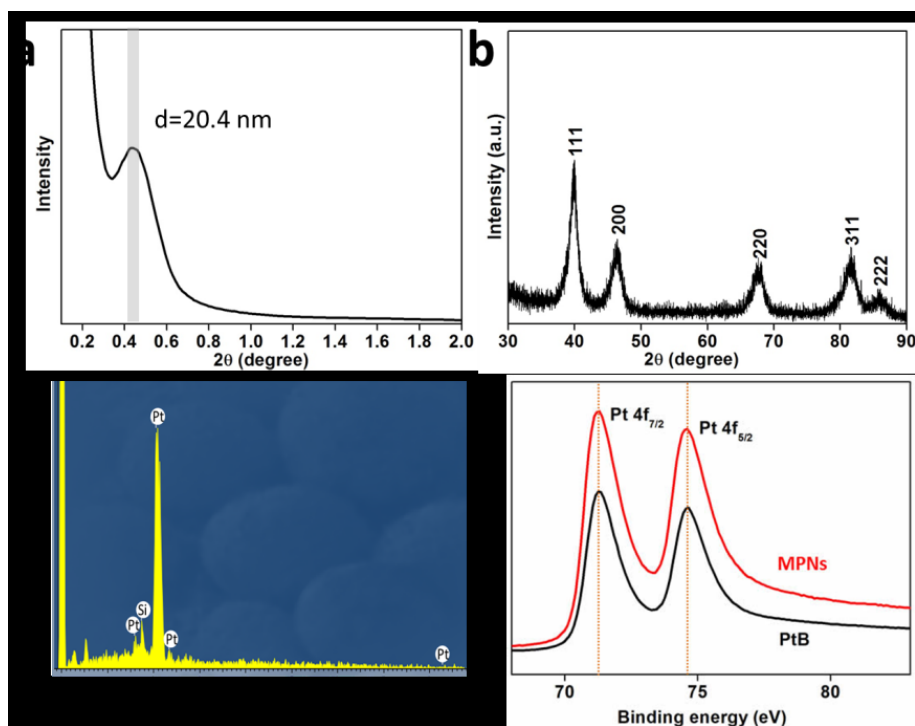


Figure 2 (a) Low-, and wide-angle XRD patterns of MPNs, (c) a representative EDX spectrum of MPNs. In the EDX spectrum, the additional signal originates from the Si substrate, and (d) Pt $4f$ XPS data of MPNs and Pt black (PtB).

The wide-angle XRD pattern (XRD) of the as-prepared MPNs can be assigned to a pure face-centered cubic (*fcc*) Pt structure (**Figure 2.2b**) and energy dispersive X-ray spectroscopy measurements further confirmed that the sample is free of other elemental impurities (**Figure 2.2c**). X-ray photoelectron spectroscopy (XPS) was then employed to analyze the valence state of the surface Pt in the MPNs. For comparison, commercially available Pt black (PtB) was characterized as well. It can be clearly noticed in **Figure 2.2d** that both samples show doublet peaks assignable to $\text{Pt}^0 4f_{7/2}$ and $\text{Pt}^0 4f_{5/2}$, respectively, indicating the existence of metallic state

Pt.^[12] Considering the resolution depth of Pt photoelectron spectra at the conditions (*i.e.*, 1.5 nm) of an inelastic-mean-free-path,^[13] the spectra are considered to be composed of the contribution from the top 2-3 surface atomic layers of Pt.

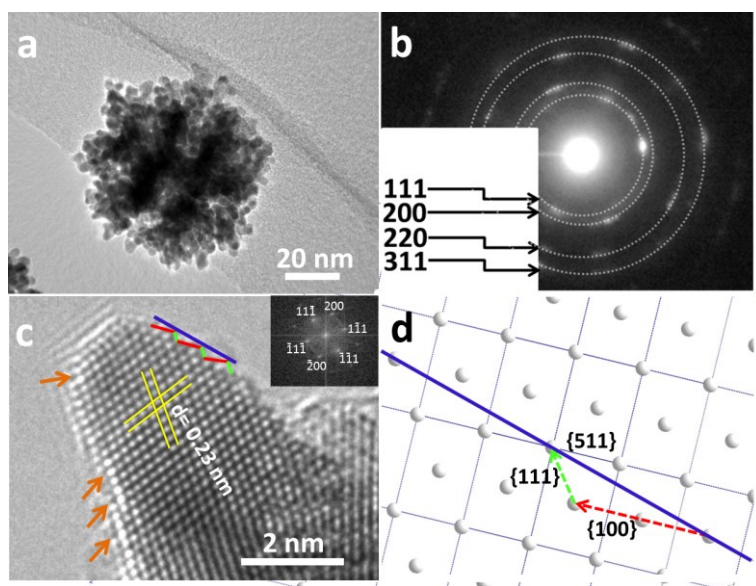


Figure 2.3 (a) Typical TEM image and (b) the corresponding selected area ED pattern of one single MPN. (c) HRTEM image focused on the edge of Pt pore walls projected along the $\langle 011 \rangle$ direction. (d) Schematic illustration for the exposed high-index facet. The inset image in panel (c) shows the corresponding FFT patterns of the HRTEM image.

In order to obtain more information on the surface atomic structure, high-resolution TEM (HRTEM) and TEM images of the MPNs were acquired. It can be observed that an entire nanosphere is typically composed of interconnected nanocrystals sizing from 6 to 8 nm (**Figure 2.3a**). The mesoporous structure can be clearly distinguished because of differences in the contrast. The selected-area electron diffraction (ED) pattern from **Figure 2.3b** along with the clear lattice fringes observed in the HRTEM image (**Figure 2.3c**) evidence the high degree of crystallization of the pore walls. Also, the lattice spacing of 0.23 nm is in good agreement with the *fcc* Pt $\{111\}$ crystal plane. The surface of the branched Pt nanocrystals is enclosed by $\{111\}$ and $\{100\}$ facets along with a large number of atomic steps, as indicated by the arrows in **Figure 2.3c**. Furthermore, some high-index facets (*e.g.*, $\{511\}$) were confirmed from the edge surface. A scheme shown in **Figure 2.3d** illustrates the positioning model for the high-index facet. The favorable molecule adsorption attributed to unsaturated atomic structures has been proved to be more active than the highly coordinated atomic surface.^[14]

To better understand the formation mechanism of the MPNs, the roles of the reagents were investigated in detail. It has previously been reported that nonionic surfactants, such as F127 and P123, can serve as

structure-directing agents in the preparation of mesoporous oxides and carbons.^[15] As shown in **Figure 2.4a**, in the absence of F127, only micrometer-sized Pt spheres with non-porous structure are obtained. When a small amount of F127 (2.0 mg) is added, mono-dispersed Pt nanoparticles with shallow pores start to appear (**Figure 2.4b**). Further increasing the amount of F127 (up to 10 mg) leads to the formation of concaved mesopores on the surface of the Pt nanoparticles (**Figure 2.4c**). With further increasing the amount of F127 (up to 30 mg), the desired mesoporous Pt nanospheres can be obtained (**Figure 2.4d**).

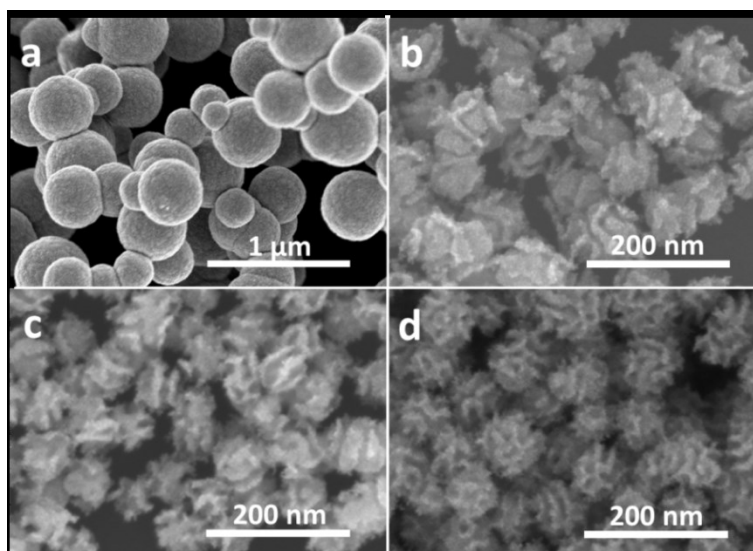


Figure 2.4 SEM images of the samples prepared under typical conditions with different amounts of F127 [(a) 0 mg, (b) 2.0 mg, (c) 10 mg, and (d) 30 mg, respectively].

The formation of the mesoporous particles is completely different from previous works, where porous or dendritic Pt nanoparticles with narrow interspaces less than 5 nm were obtained through fast reduction reactions.^[8a,9a] In this work, I believe that the slow deposition rate is responsible for the retention of the micelle arrangement at the greatest extent and thus, for the formation of well-defined mesoporous structures.^[16] Although the reduction kinetics can often be controlled by varying the reduction power of the reducing agent, here, we utilize another approach, *i.e.*, the ligand exchange of Pt precursor by adding bromide ions and oxygen to slow down the reduction reaction.

The mechanism of these two additives can be accounted for by the following ideas. The presence of bromide ions shifts the redox potential of the Pt ions toward a more negative potential through ligand exchange reactions to form $[\text{PtBr}_6]^{2-}$ with a redox potential is more negative (0.61 V vs. SHE) than that of $[\text{PtCl}_6]^{2-}$ (0.73 V vs. SHE), namely, the reduction of $[\text{PtBr}_6]^{2-}$ is slower. This ligand exchange reaction was confirmed by UV-vis measurements. As shown in **Figure 2.5a**, the absorption peak located at 260 nm in the $[\text{PtCl}_6]^{2-}$ solution corresponds to the absorption of $[\text{PtCl}_6]^{2-}$ complexes.^[17] After addition of KBr, the absorption peak at

260 nm disappears and two new characteristic features located at 310 and 365 nm can be observed, indicating that $[\text{PtCl}_6]^{2-}$ was successfully replaced by $[\text{PtBr}_6]^{2-}$ complexes.^[18] The presence of oxygen shifts the reduction potential toward a more positive potential.

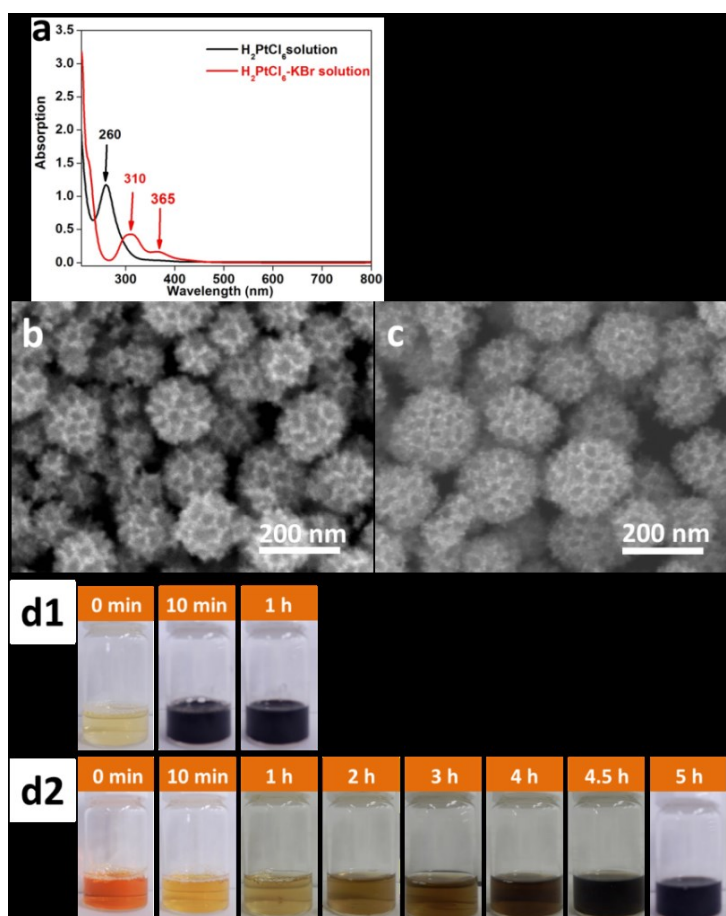


Figure 2.5 (a) UV-vis spectrum of (black plot) H_2PtCl_6 solution only and (red) H_2PtCl_6 solution after addition of KBr. SEM images of samples prepared (b) with oxygen but without KBr and (c) with KBr but without oxygen. Photographs of colloidal suspensions of (d1) H_2PtCl_6 solution, and (d2) H_2PtCl_6 -KBr solution taken at different reaction times at 70 °C.

The roles of Br^- and O_2 in the formation of the Pt nanospheres were carefully studied by a series of control experiments: samples were synthesized in the presence of oxygen but without bromide ions (**Figure 2.5b**), and in the presence of bromide ions but without oxygen (**Figure 2.5c**). In both cases, the reaction yields disconnected cavities on the surface of the Pt nanoparticles possessing a broad size distribution. The structures with interconnected mesopores can only be obtained when both Br^- and O_2 are simultaneously involved in the reaction (**Figure 2.1a**). The slow reaction favors a thermodynamic growth, which induces the exposure of $\{111\}$ facet. Also, the Br^- ions have been known to selectively adsorb on and preferably expose Pt $\{100\}$ facets.^[19] Therefore, in this study, the designed pore surfaces consisting of the interlaced Pt $\{111\}$ and $\{100\}$ facets (**Figure 2.3c**) is proved to enhance the oxygen reduction reaction activity, which is probably ascribed to

a synergetic effect between different facets.^[20] To the best of my knowledge, such mesoporous Pt nanospheres with designed pore surface were firstly reported. Thus, I believe that this slow metal growth is beneficial for the formation of uniformly sized mesopores and particles as it provides enough time for the surfactants to adhere to the metal seeds and effectively act as a template for the subsequent growth (**Figure 2.5d**).

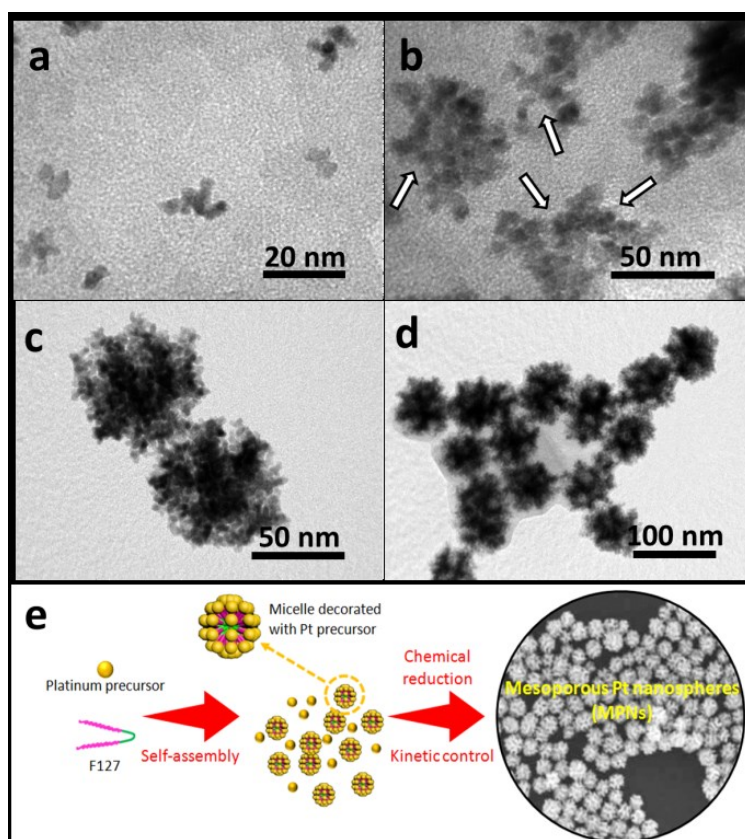


Figure 2.6 TEM images of Pt samples taken after different reaction periods: a) 3 h, b) 4 h, c) 6 h, and d) 12 h, respectively. e) Schematic illustration for the synthesis of MPNs.

The intermediate products at different reaction times were also investigated through TEM observation of the samples taken from the reaction flask after various periods of time (**Figure 2.6**). Within 3 h, almost no precipitate can be observed, indicating that the reduction rate is relatively slow. The little amount of particles collected formed small non-uniform aggregates (**Figure 2.6a**). With increasing the reaction time (4 h), the particle size increases by the continuous growth of fine particles (**Figure 2.6b**). It is noted that, at this stage, the concave or porous structure starts to be formed on the edges of the particles, as indicated by the arrows. After 6 h, the MPNs are formed (**Figure 2.6c**) and the morphology of the nanostructure remains stable even after longer reaction time (up to 12 h, **Figure 2.6d**). On the basis of these results, the mechanism responsible for the formation of MPNs can be described as follows. At the initial stage, F127 serves as protecting agent and to stabilize the primary Pt clusters through the interactions with the ethylene oxide (EO) chains of the

F127 micelles.^[21] As the reaction proceeds, the reduced Pt clusters with preferentially exposed of {100} facets from the solution continue to deposit on the spherical F127 micelles. Because of the extremely slow reduction rate caused by the ligand affection, there is enough time for F127 to effectively act as a template and to form an open mesoporous structure. The synthesis process of MPNs was schematically illustrated in **Figure 2.6e**.

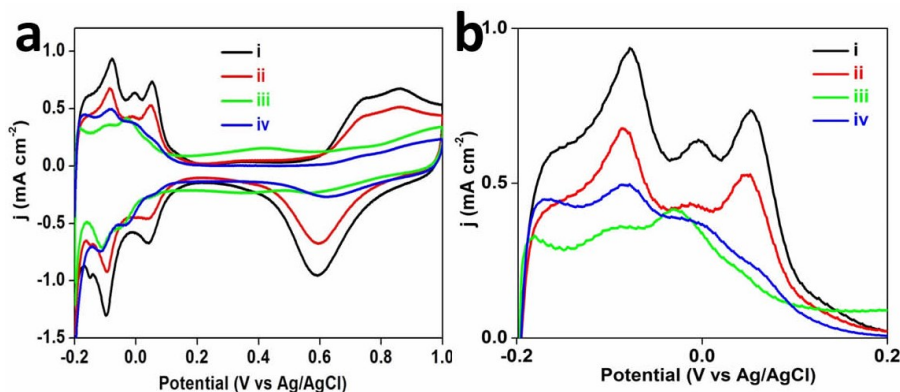


Figure 2.7 Cyclic voltammograms of (i) MPNs, (ii) shallow concave Pt nanoparticles, (iii) PtC-20%, and (iv) PtB catalysts recorded in 0.5 M H₂SO₄ solution at a scan rate of 50 mV s⁻¹. All the currents are normalized by electrode geometric surface area.

To investigate the nature of the Pt surface obtained through the slow reduction reactions in the presence of bromide ions, the surface crystallography of the MNPs was investigated by cyclic voltammetry and compared with those of dendritic Pt nanoparticles (DPNs) prepared in the presence of oxygen but without adding KBr (**Figure 2.5b**), and also with PtC-20% and PtB catalysts. The cyclic voltammograms (CVs) of MPNs and DPNs exhibit the typical characteristics of hydrogen and oxygen adsorption/desorption on polycrystalline Pt surface (**Figure 2.7**), while the CVs of the PtC-20% and PtB samples do not show any sharp peaks in the hydrogen region (*i.e.*, below 0.2 V vs. Ag/AgCl), which are similar to that of Pt{111} surface.^[22] MPNs and DPNs have a hydrogen desorption peak around -0.08 V vs. Ag/AgCl, which is assignable to {110} surfaces, and another sharp peak around 0.08 V, which can be assigned to a few atoms wide {100} surface.^[21] Interestingly, I found that only MPNs have an extra third peak between the peaks previously mentioned, which can be assigned to low coordination Pt sites.^[23,24] These clearly show that the nanostructured samples have more surface step defects than typical Pt nanoparticles.

Inspired by these attractive properties (*e.g.*, low-coordinated atomic surfaces), both the methanol oxidation reaction (MOR) and oxygen reduction reaction (ORR) were performed to evaluate the electrochemical performance of the MPNs. **Figure 2.8a** shows the typical CV curves of MOR catalyzed with the MPNs, DPNs,

PtC-20%, and PtB catalysts. The current densities were normalized by the Pt electrochemical surface area (ECSA) (MPNs ($25.1 \text{ m}^2 \text{ g}^{-1} \text{ Pt}$), DPNs ($17.1 \text{ m}^2 \text{ g}^{-1} \text{ Pt}$), commercial PtB ($14.3 \text{ m}^2 \text{ g}^{-1} \text{ Pt}$), and PtC-20% ($54 \text{ m}^2 \text{ g}^{-1} \text{ Pt}$)). The peak current density of the MPNs ($1.1 \text{ mA} \cdot \text{cm}^{-2}$) is much higher than that of the DPNs ($0.95 \text{ mA} \cdot \text{cm}^{-2}$), PtC-20% ($0.61 \text{ mA} \cdot \text{cm}^{-2}$), and PtB ($0.46 \text{ mA} \cdot \text{cm}^{-2}$). The reason for this superior activity arises from a large number of low-coordinated atoms present on the Pt surfaces, which facilitate the breakage of the C-H bonds during the decomposition of methanol.^[25] The chronoamperometric measurement at 0.6 V over 3000 s proved that the MPNs possess a better stability during the electrochemical measurement, in comparison to the other catalysts (**Figure 2.8b**).

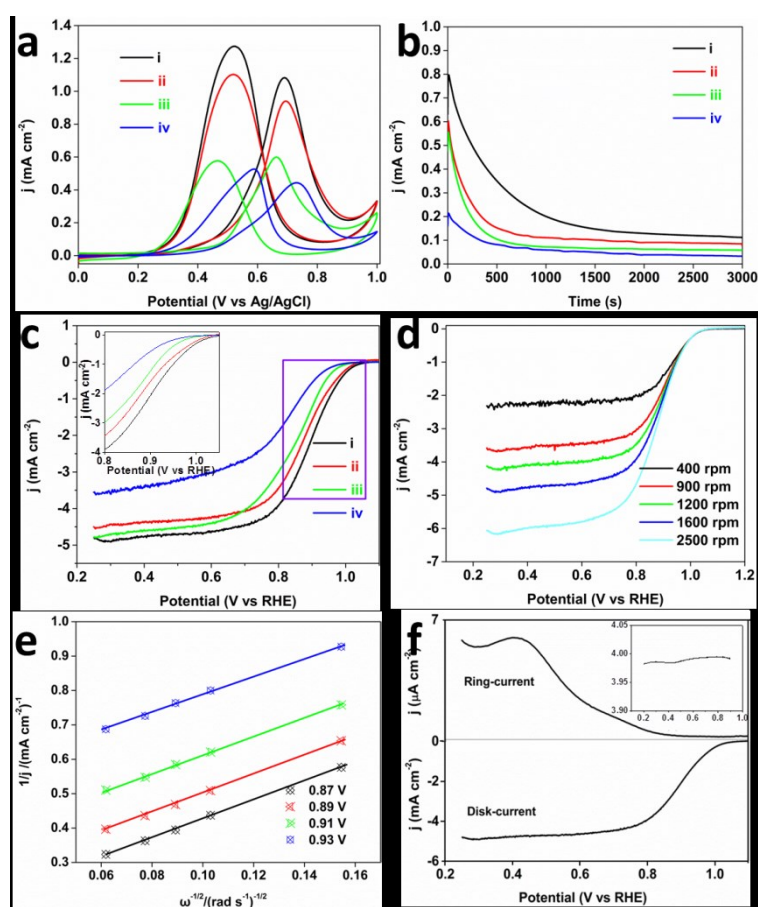


Figure 2.8 (a) Cyclic voltammograms of MOR recorded in $0.5 \text{ M H}_2\text{SO}_4 + 0.5 \text{ M CH}_3\text{OH}$ at a scan rate of $50 \text{ mV} \cdot \text{s}^{-1}$, (b) Chronoamperometric curves (recorded at 0.6 V) obtained in $0.5 \text{ M H}_2\text{SO}_4 + 0.5 \text{ M CH}_3\text{OH}$. (c) ORR polarization curves recorded in O_2 -saturated 0.1 M HClO_4 solution with a sweep rate of $10 \text{ mV} \cdot \text{s}^{-1}$ and a rotation rate of 1600 rpm, and d) ORR polarization curves of MPNs at different rotation rates, and e) corresponding Koutecky-Levich (K-L) plots of the MPNs at different potentials. f) The current collected on disk and ring electrodes catalyzed by MPNs. Inset shows the electron number transferred in ORR calculated by using the current collected on rotating ring-disk electrode. The K-L plots show the inverse current density (j^{-1}) as a function of the inverse of the square root of rotation speed ($\omega^{-1/2}$) at

various potentials. [(i) MPNs with interconnected mesopores, (ii) DPNs, (iii) PtC-20% catalyst, and (iv) PtB catalyst, respectively.] The inset image in panel (c) shows enlargement of the rectangle area. The currents in panel a) are normalized by the ECSA, whereas, the currents in panel c) are normalized by the electrode geometric surface area.

The ORR was further studied in O₂ saturated 0.1 M HClO₄. The MPNs show a more positive half-wave potential (0.88 V) than that of PtB (0.78 V), DPNs (0.86 V), and PtC-20% (0.84 V) (**Figure 2.8c**). The onset potential of the MPNs is positively shifted compared to the other samples. To further study the kinetics of the ORR, the polarization curves of the MPNs-modified rotation ring disk electrode (RRDE) were recorded at different rotation speeds. The limiting current density increases with increasing the rotation speed (**Figure 2.8d**). The corresponding Koutecky-Levich (K-L) plots at different potential values are plotted and the number of electrons transferred was calculated by the K-L equation,^[26] which is expressed by:

$$j^{-1} = j_K^{-1} + j_L^{-1} = j_K^{-1} + B^{-1} \omega^{-1/2} \quad (1)$$

$$B = 0.62nFC_0D_0^{2/3} \nu^{-1/6} \quad (2)$$

Where j is the measured current density; j_K and j_L are the kinetic- and diffusion-limited current densities; ω is the angular frequency of rotation; n represents the overall number of electrons transferred in oxygen reduction; F is the Faraday constant ($F=96485 \text{ C mol}^{-1}$); C_0 is the bulk concentration of O₂ in 0.1 M HClO₄ ($1.26 \times 10^{-6} \text{ mol cm}^{-3}$); D_0 is the diffusion coefficient of O₂ in 0.1 M HClO₄ solution ($1.93 \times 10^{-5} \text{ cm}^2 \text{ s}^{-1}$) ν is the kinematic viscosity of the electrolyte ($1.01 \times 10^{-2} \text{ cm}^2 \text{ s}^{-1}$). The number of electrons transferred (n) can be obtained from the slope of the K-L plots. **Figure 2.8e** shows four linear K-L plots at different potentials, suggesting the first-order reaction kinetics of oxygen reduction catalysed by the MPNs from 0.825 V to 0.925 V. The n value calculated from the equation: $n=4 \times I_d/(I_d + I_r/N)^{[27]}$ (where I_d is the disk current, I_r is the ring current and $N = 0.4$ is the current collection efficiency of Pt ring electrode), is in the ranging of 3.7-4.0, which is in good consistent with the number of electrons derived from the RRDE voltammograms (**Figure 2.8f**). All these results evidence that the ORR catalyzed by the MPNs follows a four-electron pathway.^[28]

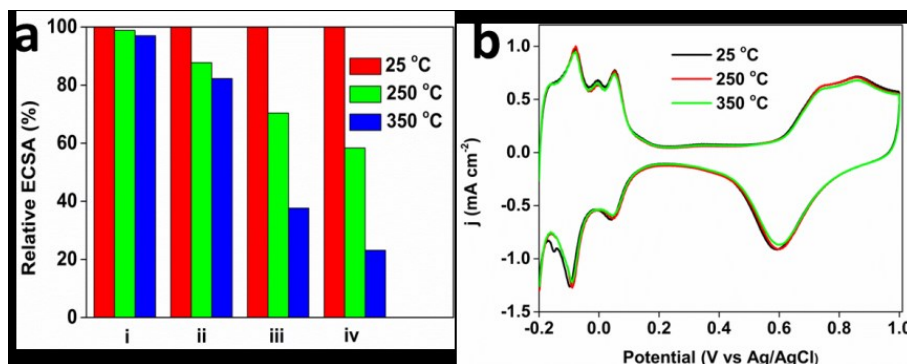


Figure 2.9 (a) ECSA retention after thermal treatment at various temperatures for 3 h, (b) Cyclic voltammograms of the MPNs before (black plot) and after thermal treatment at 250 °C (red plot), or 350 °C (green plot) for 3h, which are recorded in 0.5 M H₂SO₄ at a sweep rate of 50 mV s⁻¹. [(i) MPNs with interconnected mesopores, (ii) DPNs, (iii) PtC-20% catalyst, and (iv) PtB catalyst, respectively.] The inset image in panel (c) shows enlargement of the rectangle image area.

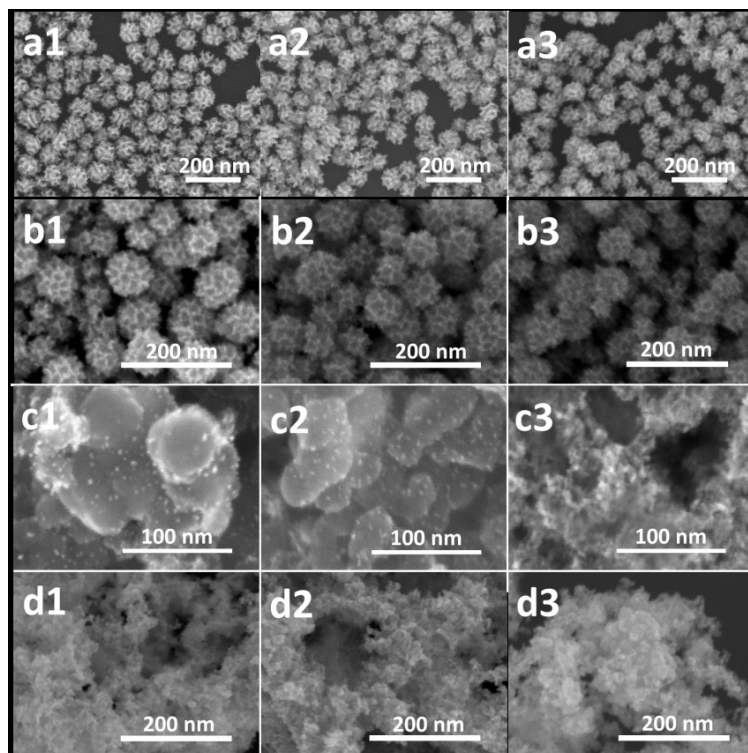


Figure 2.10 SEM image of (a) MPNs (b) shallow concave Pt nanoparticles, (c) 20%-PtC, and (d) PtB after thermal treatment at different temperatures [(a1, b1, c1,d1) 25 °C, (a2, b2, c2,d2) 250 °C, and (a3, b3, c3,d3) 350 °C, respectively].

It is well known that structural thermostability is a very important factor for practical catalysts because the performance highly depends on their ability to retain their shape and structure. In order to investigate the structural thermostability, the MPNs, DPNs, PtC-20%, and PtB were treated at 250 °C or 350 °C for 3 h. After calcination, the CV plots were recorded in 0.5 M H₂SO₄ at a scan rate of 50 mV · s⁻¹ and the Pt ECSA of each sample was calculated and compared. **Figure 2.9a** shows that 97% of initial ECSA of the MPNs can be retained even after the thermal treatment at 350 °C, which is much higher than for the DPNs (82%), PtC-20% (38%), or PtB (23%), showcasing the MPNs for their excellent thermostability. Because the well-defined mesoporous structure was less vulnerable to particle aggregation, the MPNs retain most of their ECSA after the treatment at 350 °C, in great contrast to the low thermal stabilities of the dendritic Pt nanoparticles caused by structural shrinkage.^[9] The serious decrease of ECSAs for the PtC-20% and PtB can be attributed to the

aggregation of the nanoparticles and the collapse of the carbon support at higher temperatures (**Figure 2.10c-d**). The morphologies of MPNs do not show any changes either (**Figure 2.10a**). Also, the CV curves are perfectly maintained even after thermal treatment at 250 °C and 350 °C (**Figure 2.9b**).

2.4. Conclusion

In summary, we have successfully synthesized mono-dispersed MPNs with interconnected mesopores by a one-pot method. Through systematic studies, we found that the kinetically controlled reduction reactions in the presence of F127 structure-directing agent are responsible for the formation of active interconnected mesopores in the Pt nanoparticles. Interestingly, the MPNs not only show an enhanced electrocatalytic performance but also exhibit a high structural thermostability, which make them a promising catalyst for practical applications. We strongly believe that this work will provide new insights towards the creation of novel metal-based materials.

References

- [1] (a) H. Wang, S. Ishihara, K. Ariga, Y. Yamauchi, *J. Am. Chem. Soc.*, 2012, **134**, 10819; (b) V. Malgras, Q. Ji, Y. Kamachi, T. Mori, F. K. Shieh, K. C. W. Wu, K. Ariga, Y. Yamauchi, *Bull. Chem. Soc. Jpn.*, 2015, **88**, 1171.
- [2] (a) Y. Wu, D. Wang, G. Zhou, R. Yu, C. Chen, Y. Li, *J. Am. Chem. Soc.*, 2014, **136**, 11594; (b) C. Chen, Y. Kang, Z. Huo, Z. Zhu, W. Huang, H. L. Xin, J. D. Snyder, D. Li, J. A. Herron, M. Mavrikakis, M. Chi, K. L. More, Y. Li, N. M. Markovic, G. A. Somorjai, P. Yang, V. R. Stamenkovic, *Science*, 2014, **343**, 1339; (c) B. Y. Xia, H. B. Wu, X. Wang, X. W. Lou, *Angew. Chem., Int. Ed.*, 2013, **52**, 12337.
- [3] (a) L. Wang, Y. Yamauchi, *J. Am. Chem. Soc.*, 2013, **135**, 16762; (b) B. Lim, M. Jiang, P. H. Camargo, E. C. Cho, J. Tao, X. Lu, Y. Zhu, Y. Xia, *Science*, 2009, **324**, 1302.
- [4] (a) X. Huang, Z. Zhao, J. Fan, Y. Tan, N. Zheng, *J. Am. Chem. Soc.*, 2011, **133**, 4718; (b) N. F. Yu, N. Tian, Z. Y. Zhou, L. Huang, J. Xiao, Y. H. Wen, S. G. Sun, *Angew. Chem., Int. Ed.*, 2014, **53**, 5097; (c) B. Y. Xia, H. B. Wu, Y. Yan, X. W. Lou, X. Wang, *J. Am. Chem. Soc.*, 2013, **135**, 9480; (d) C. Zhang, A. Yin, R. Jiang, L. Rong, L. Dong, T. Zhao, L. D. Sun, J. Wang, X. Chen and C. H. Yan, *ACS Nano*, 2013, **7**, 4561.
- [5] (a) P. K. Chen, N. C. Lai, C. H. Ho, Y. W. Hu, J. F. Lee, C. M. Yang, *Chem. Mater.*, 2013, **25**, 4269; (b) S. Chen, H. Su, Y. Wang, W. Wu and J. Zeng, *Angew. Chem. Int. Ed.*, 2015, **54**, 108.
- [6] Q. Li, P. Xu, B. Zhang, G. Wu, H. Zhao, E. Fu, H. L. Wang, *Nanoscale*, 2013, **5**, 7397.
- [7] (a) Y. Deng, J. Wei, Z. Sun, D. Zhao, *Chem. Soc. Rev.*, 2013, **42**, 4054; (b) H. K. Na, M. H. Kim, K. Park, S. R. Ryoo, K. E. Lee, H. Jeon, R. Ryoo, C. Hyeon, D. H. Min, *Small*, 2012, **8**, 1752; (c) J. Wei, H. Wang, Y. Deng, Z. Sun, L. Shi, B. Tu, M. Luqman, D. Zhao, *J. Am. Chem. Soc.*, 2011, **133**, 20369.
- [8] (a) G. S. Attard, J. M. Corker, C. G. Göltner, S. Henke, H. Templer, *Angew. Chem., Int. Ed. Engl.*, 1997, **36**, 1315; (b) H. Wang, H. Y. Jeong, M. Imura, L. Wang, L. Radhakrishnan, N. Fujita, T. Castle, O. Terasaki, Y. Yamauchi, *J. Am. Chem. Soc.*, 2011, **133**, 14526.
- [9] (a) L. Wang, Y. Yamauchi, *J. Am. Chem. Soc.*, 2009, **131**, 9152; (b) L. Wang, Y. Yamauchi, *Chem. –Eur. J.*, 2011, **17**, 8810.
- [10] J. Tang, J. Liu, C. Li, Y. Li, M. O. Tade, S. Dai, Y. Yamauchi, *Angew. Chem., Int. Ed.*, 2015, **54**, 588.
- [11] (a) X. Huang, S. Tang, J. Yang, Y. Tan, N. Zheng, *J. Am. Chem. Soc.*, 2011, **133**, 15946; (b) Y. Xiong, J. M.

MaLellan, J. Chen, Y. Yin, Z. Y. Li, Y. Xia, *J. Am. Chem. Soc.*, 2005, **127**, 17118; (c) Z. Zhang, Y. Yang, F. Nosheen, P. Wang, J. Zhang, J. Zhuang, X. Wang, *Small*, 2013, **9**, 3063; (d) A. X. Yin, X. Q. Min, Y. W. Zhang, C. H. Yan, *J. Am. Chem. Soc.*, 2011, **133**, 3816.

[12] K. Dücker, H. P. Bonzel, D. A. Wesner, *Surf. Sci.*, 1986, **166**, 141.

[13] S. Tanuma, C. J. Powell, D. R. Penn, *Surf. Interface Anal.*, 1991, **17**, 911.

[14] (a) N. Tian, Z. Y. Zhou, N. F. Yu, L. Y. Wang, S. G. Sun, *J. Am. Chem. Soc.*, 2010, **132**, 7580; (b) Z. Y. Zhou, Z. Huang, D. J. Chen, Q. Wang, N. Tian, S. G. Sun, *Angew. Chem. Int. Ed.*, 2010, **49**, 411.

[15] (a) T. Wang, X. Meng, P. Li, S. Ouyang, K. Chang, G. Liu, Z. Mei, J. H. Ye, *Nano Energy*, 2014, **9**, 50; (b) R. Liu, Y. Shi, Y. Wan, Y. Meng, F. Zhang, D. Gu, Z. Chen, B. Tu, D. Zhao, *J. Am. Chem. Soc.*, 2006, **128**, 11652; (c) S. Wang, Q. Zhao, H. Wei, J. Q. Wang, M. Chl, H. S. Cho, O. Terasaki, Y. Wan, *J. Am. Chem. Soc.*, 2013, **135**, 11849; (d) Y. Wan, H. Wang, Q. Zhao, M. Klingstedt, O. Terasaki, D. Zhao, *J. Am. Chem. Soc.*, 2009, **131**, 4541.

[16] (a) H. Atae-Esfahani, M. Imura, Y. Yamauchi, *Angew. Chem. Int. Ed.*, 2013, **52**, 13611; (b) X. Huang, Y. Li, Y. Chen, E. Zhou, Y. Xu, H. Zhou, X. Duan, Y. Huang, *Angew. Chem. Int. Ed.*, 2013, **52**, 2520.

[17] (a) Z. Tang, D. Geng, G. Lu, *J. Colloid Interface Sci.*, 2005, **287**, 159; (b) K. Hikosaka, J. Kim, M. Kajita, A. Kanayama, Y. Miyamoto, *Colloid Surf. B*, 2008, **66**, 195.

[18] (a) R. Dabestani, X. Wang, A. Bard, A. Campon, M. A. Fox, S. Webber, J. M. White, *J. Phys. Chem.*, 1986, **90**, 2729; (b) E. M. Glebov, V. F. Plyusnin, V. P. Grivin, A. B. Venediktov, S. V. Korenev, *Russ. Chem. B. Int. Ed.*, 2007, **56**, 2357.

[19] (a) T. Yu, D. Y. Kim, H. Zhang, Y. Xia, *Angew. Chem. Int. Ed.*, 2011, **50**, 2773; (b) Y. Xia, Y. Xiong, B. Lim, S. F. Skrabalak, *Angew. Chem. Int. Ed.*, 2009, **48**, 60; (c) C. K. Tsung, J. N. Kuhn, W. Huang, C. Aliaga, L. I. Hung, G. A. Somorjai, P. Yang, *J. Am. Chem. Soc.*, 2009, **131**, 5816; (d) M. Chen, B. Wu, J. Yang, N. Zheng, *Adv. Mater.*, 2012, **24**, 862.

[20] (a) V. Komanicky, A. Menzel, H. You, *J. Phys. Chem. B*, 2005, **109**, 23550; (b) L. Ma, C. Wang, B. Y. Xia, K. Mao, J. He, X. Wu, Y. Xiong, X. W. Lou, *Angew. Chem. Int. Ed.*, 2015, **54**, 5666.

[19] H. Wang, L. Wang, T. Sato, Y. Sakamoto, S. Tominaka, K. Miyasaka, N. Miyamoto, Y. Nemoto, O. Terasaki, Y. Yamauchi, *Chem. Mater.*, 2012, **24**, 1591.

[22] *Interfacial Electrochemistry*, ed. A. Wieckowski, 1999, ch. 14, pp. 231-248.

- [23] J. S. Gullón, P. Rodríguez, E. Herrero, A. Aldaz, J. M. Feliu, *Phys. Chem. Chem. Phys.*, 2008, **10**, 1359.
- [24] (a) R. Gómez, J. Clavilier, *J. Electroanal. Chem.*, 1993, **354**, 189; (b) C. Wang, H. Daimon, T. Onodera, T. Koda, S. Sun, *Angew. Chem. Int. Ed.*, 2008, **47**, 3588.
- [25] (a) N. Tian, Z. Y. Zhou, S. G. Sun, Y. Ding, Z. L. Wang, *Science*, 2007, **316**, 732; (b) C. Li, V. Malgras, A. Aldalbahi, Y. Yamauchi, *Chem.–Asian J.*, 2015, **10**, 316.
- [26] A. J. Bard and L. R. Faulkner, *Electrochemical Methods: Fundamentals and Applications*, John Wiley & Sons, New York, NY, 2nd edn, 2001.
- [27] O. Antonie, R. Durand, *J. Appl. Electrochem.*, 2000, **30**, 839.
- [28] (a) S. Guo, S. Sun, *J. Am. Chem. Soc.*, 2012, **134**, 2492; (b) L. Liu, E. Pippel, *Angew. Chem., Int. Ed.*, 2011, **50**, 2729; (c) L. Ruan, E. Zhu, Y. Chen, Z. Lin, X. Huang, X. Duan, Y. Huang, *Angew. Chem. Int. Ed.*, 2013, **52**, 12577.

Chapter 3. Tunable-Sized Polymeric Micelles and Their Assembly for Preparation of Large Mesoporous Pt Nanoparticles

3.1. Introduction

Micelle architectures provide a simple and versatile platform for synthesizing mesoporous structures in a wide variety of materials.^[1] Both pore size and the porous structure of the materials can be controlled by tuning the inter- and intra-molecular forces that drive the self-assembly of surfactants and block copolymers.^[2] Mesoporous materials with large pore sizes have inspired in a wide variety of applications because large pores facilitate fast and efficient transport of reactants.^[3] For example, Zhao et al. reported that three-dimensional (3D) ordered mesoporous silica with ultra-large accessible mesopores can be synthesized on high molecular weight (MW) block copolymer templates. They used solvent evaporation to make composite micelles composed of block copolymer and silica precursor to assemble the ordered mesostructure.^[4] Although these large-pore materials have been demonstrated, the compositions are still limited to carbon,^[5] silica,^[6] metal oxides^[7] and organosilicates.^[8] If these micelle templates could be applied to the preparation of noble metals, in particular, materials like platinum, these ultra-large accessible surfaces would be of great utility for electrocatalysis.

Mesoporous noble-metal materials (*e.g.*, Au, Pt, Pd) have most of the physical and chemical properties that make these metals good catalysts. Consequently, these structures exhibit enhanced catalytic properties for a range of reactions including small organic molecule oxidation, oxidation reduction reaction, and hydrogenation.^[9] Our previous work demonstrated that mesostructured noble-metals with a large-pore could be synthesized by using pore-directing agents such as the block polymer polystyrene-block-poly(ethylene oxide) (PS-*b*-PEO) via electrochemical deposition.^[10] However, this method required the metal species to be electrodeposited on conductive substrates, limiting this approach primarily to monolith films. Chemical reduction might provide a more flexible way to make metal nanoparticles in solution.^[11] To our knowledge, chemical reduction has never been used for the controlled synthesis of large-sized porous metallic nanoparticles with tunable pore sizes and particle sizes. Consequently, new synthetic strategies must be developed to enable the reduction of metals on block copolymer micelles, in order to create composite nanoparticles with large-size, open pores for high-performance electrocatalysts.

Here we report a simple micelle-based approach to make mesoporous Pt nanoparticles. By controlling the solvent composition, we are able to make nanoparticles with continuously tunable porous architectures and particle sizes. The Pt precursor is chemically reduced by ascorbic acid in the mixed solvents containing tetrahydrofuran (THF) and water. The concept of our approach is different from the traditional micelle

systems using dialysis and solvent evaporation,^[12] because the addition of water induces micellization of block copolymers. The solubility of the hydrophobic blocks depends on the tetrahydrofuran content, so micelle size can be tuned by varying the tetrahydrofuran content to create a fully tunable mesoporous Pt nanoparticle system. The as-prepared mesoporous Pt nanoparticles are referred to herein as Pt-x-(100-x), where x represents the percentage (v/v%) of THF in the precursor solutions. The electrochemical performance of the mesoporous structures was carefully examined and exhibited a great improvement in performance over conventional platinum catalysts, showing that the mesoporous design is a route to better catalytic activity.

3.2. Experimental Sections

3.2.1. Materials

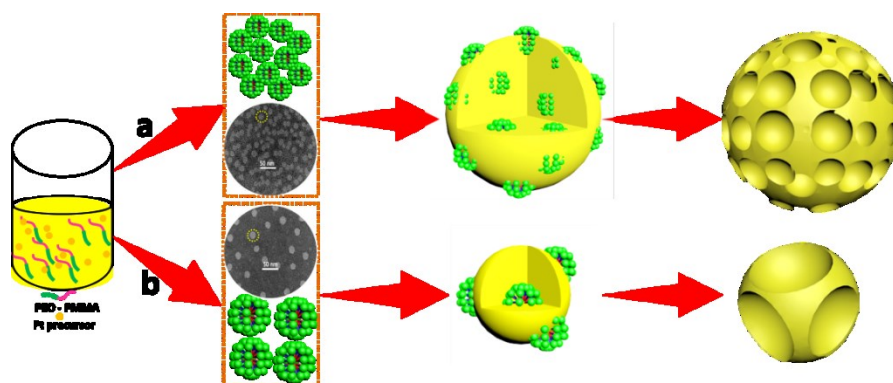
Block polymers poly(ethylene oxide)-*b*-poly(methyl methacrylate) (PEO₍₁₅₀₀₀₎-*b*-PMMA₍₉₀₀₀₎, PEO₍₁₀₅₀₀₎-*b*-PMMA₍₁₈₀₀₀₎, and PEO₍₁₀₅₀₀₎-*b*-PMMA₍₂₂₀₀₀₎) and polystyrene-*b*-poly(ethylene oxide) (PEO₍₇₅₀₀₎-*b*-PS₍₁₈₀₀₀₎) were purchased from Polymer Source. Tetrahydrofuran (THF), ascorbic acid (AA), K₂PtCl₄ and nitric acid (HNO₃) were obtained from Nacalai Tesque. The commercial Pt black and PtC-20% used for electrochemical measurement were obtained from Sigma-Aldrich. Nafion solution was purchased from Sigma-Aldrich. All chemicals were used directly without further purification.

3.2.2. Preparation of the Materials

Preparation of Large-pore Mesoporous Pt Nanoparticles

Formation process of mesoporous Pt nanoparticles is shown in **Scheme 1a**. 4 mg of poly(ethylene oxide)-*b*-poly(methyl methacrylate) (PEO₍₁₀₅₀₀₎-*b*-PMMA₍₁₈₀₀₀₎) was completely dissolved in 0.24 mL of THF. Then, deionized water, 0.5 mL of an aqueous solution of HNO₃ (0.1 M), 0.5 mL of an aqueous solution of K₂PtCl₄ (40 mM), and 1 mL of an aqueous solution AA (0.1 M) were added to the above THF/PEO₍₁₀₅₀₀₎-*b*-PMMA₍₁₈₀₀₀₎ solution, in sequence. A total volume of 3 mL was fixed to each synthesis, and the volume ratio of THF was varied in a wide range (e.g., 4%, 6%, 8%, 10%, 12%, and 14%) to control the solvent property. Due to the composition change in the precursor solutions, the obtained mesoporous Pt nanoparticles showed different structures. To make it clear, the as-prepared mesoporous Pt nanoparticles are abbreviated as mesoporous Pt-x-(100-x) nanoparticles, where x represents the volume ratio of THF in the precursor solution. The mixed solution was kept at room temperature until the solution color changed from yellow to black. Finally, the sample was collected by

centrifugation at 14,000 rpm for 20 min and the residual PEO₍₁₀₅₀₀₎-*b*-PMMA₍₁₈₀₀₀₎ was removed by five consecutive washing/centrifugation cycles with THF and water and used for characterization



Scheme 3.1 Formation process of (a) mesoporous Pt-8-92 at low THF content and (b) dimpled-like Pt-14-86 nanoparticles at high THF content.

3.2.3. Characterization

Field emission scanning electron microscope (SEM, HITACHI SU-8000) was used to observe morphology of Pt nanospheres with the accelerating voltage of 5 kV. Transmission electron microscopy (TEM, JEOL JEM-2100F) was operated to investigate the interior structure at 200 kV. The hydrodynamic diameter (D_h) and the zeta potential of the polymeric micelles were measured with an Otsuka ELSA particle analyzer. Smart lab X-ray diffraction (XRD: RIGAKU) was performed at a scanning rate of $0.5^\circ \cdot \text{min}^{-1}$ with a Cu $K\alpha$ radiation (40 kV, 30 mA). Small angle X-ray scattering (Rigaku NANO-Viewer) was used to evaluate the pore-to-pore distance with a Cu $K\alpha$ radiation (40 kV, 30 mA) and the camera length is 700 mm.

3.2.4. Electrochemical Test

To deposit the mesoporous Pt nanoparticles on Ketjen carbon black support, the reaction solution was taken immediately after the reaction completed and mixed with carbon black in 20 mL of mixed THF/ethanol (v/v = 2/1) solution. This mixture was sonicated for 1 h, and the supported sample was collected by centrifugation at 14,000 rpm for 20 min with THF and water and repeated four times. According to inductively coupled plasma atomic emission spectroscopy (ICP-AES), the average loading amounts of Pt on the carbon support were calculated to be 20 wt%. Before electrochemical measurement, the hybrid sample was collected and dried on glass substrates at room temperature. The samples were heated at 250°C in air for 1 hour to remove the block copolymer.

Electrochemical investigations were performed using a CHI 842B electrochemical analyzer (CHI Instrument, USA) to performed cyclic voltammograms (CVs), line-sweep voltammograms (LSVs) and

chronoamperometric curves (CA) of different types of Pt nanospheres and the commercial Pt black. The three-electrode cell consists of a reference electrode (Ag/AgCl electrode), a counter electrode (Pt wire) and a working electrode (glassy carbon electrode, GCE). All catalysts were dispersed in a mixture containing water, ethanol, and Nafion (0.5 wt.%) (v/v/v 4:1:0.1) to form a 5 mg mL^{-1} ink. $5 \text{ }\mu\text{L}$ of suspension was subsequently loaded on the GCE and dried at room temperature. Methanol electrooxidation measurements were carried out in $0.5 \text{ M H}_2\text{SO}_4$ containing 0.5 M methanol. ECSA was determined from the charge passed associated with the hydrogen desorption between -0.2 V to 0.2 V and a conversion value of $210 \text{ }\mu\text{C}\cdot\text{cm}^{-2}$ for the desorption of a hydrogen monolayer was used.

3.3. Results and Discussion

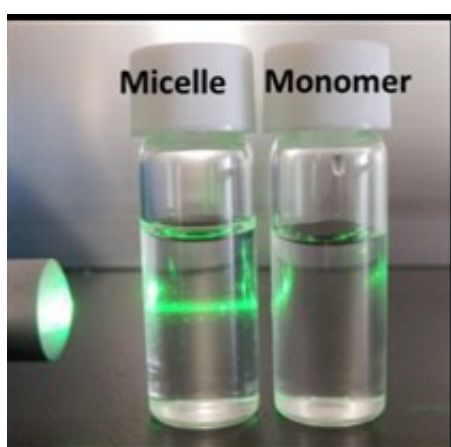


Figure 3.1 Photograph of the Tyndall effect shows the light scattering in the presence of micelles.

The hydrophilic and hydrophobic segments of the diblock polymer, PEO-*b*-PMMA, have similar solubility parameters in THF.^[13] Adding water causes the hydrophobic PMMA segments become less solvated, forming spherical micelles composed of the PMMA block as a core surrounded by a PEO shell, which is illustrated by the Tyndall effect (**Figure 3.1**). In aqueous solution, the $[\text{PtCl}_4]^{2-}$ ions are coordinated by water molecules to form Pt-water complexes.^[14] Previous report demonstrated that the coordinated complexes would be incorporated inside the ethylene oxide (EO) shells of the polymeric micelles by hydrogen bonding.^[15] During deposition of Pt, the PEO-*b*-PMMA micelles with metal-aqua complexes approach the seeds and directly act as a structural directing agent to form the mesoporous structure.

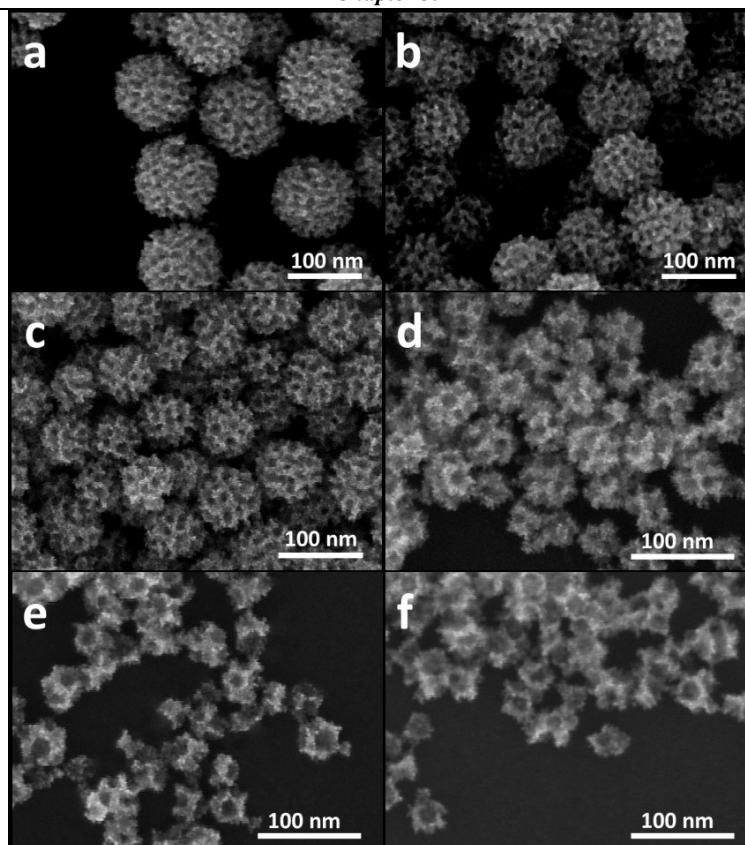


Figure 3.2 SEM images of (a) Pt-4-96, (b) Pt-6-94, (c) Pt-8-92, (d) Pt-10-90, (e) Pt-12-88, and (f) Pt-14-86 samples prepared from the mixed solvent with various volume ratios of THF:H₂O [(a) 4:96, (b) 6:94, (c) 8:92, (d) 10:90, (e) 12:88, and (f) 14:86, respectively].

The structural features of the mesoporous Pt nanoparticles were characterized by scanning electron microscope (SEM). **Figure 3.2** shows that both the porous structures and the particle sizes depend on the solvent compositions (herein, the volume ratio between THF and H₂O). The Pt-4-96, Pt-6-94, and Pt-8-92 samples prepared from THF:H₂O=4:96, 6:94, and 8:92 have a dense lattice of mesopores packed inside the spheres (**Figure 3.2a-c**). The porous structure gradually transform into dimpled mesopores by increasing the volume ratio of THF:H₂O to be 14:86 (**Figure 3.2e-f**). As the volume ratio of THF:H₂O is changed from 4:96, to 6:94, 8:92, 10:90, 12:88, and 14:86, we observed a corresponding decrease in particle size from (107±1) nm, to (86±1) nm, (62±1) nm, (46±1) nm, (37±1) nm, and (32±1) nm, while the pore sizes of the samples slightly increase from (8±0.5) nm, to (9±0.5) nm, (10±0.5) nm, (12±0.5) nm, (14±0.5) nm, and (14±0.5) nm, respectively (**Figure 3.3a-f**). These measurements were estimated from the SEM images. All the results demonstrate (see **Figure 3.3g**) that the solvent compositions play a key role in the variation of the pore sizes and the particle sizes, which ultimately determines the mesoporous structure of the nanoparticles.

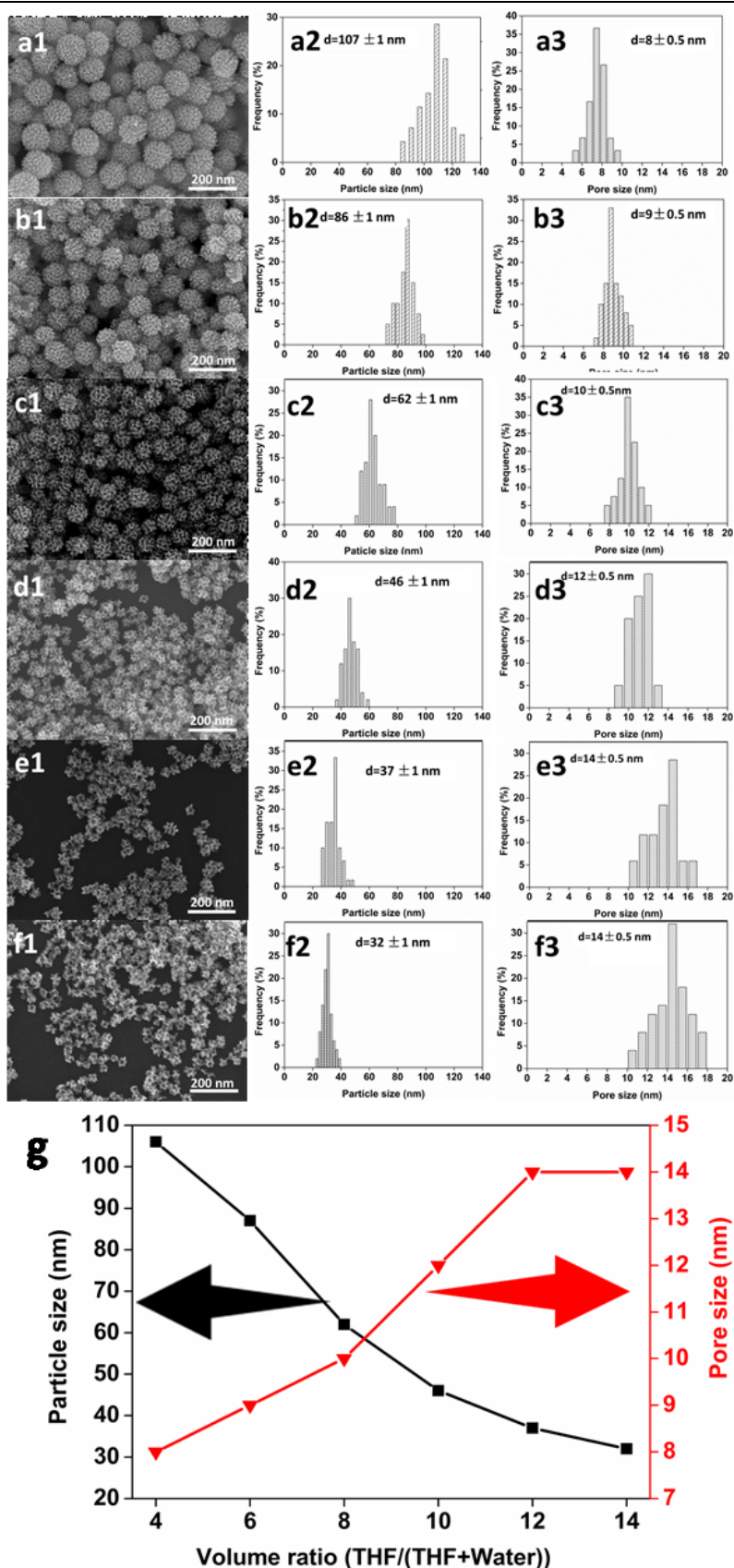


Figure 3.3 SEM images, particle size distribution and pore size distribution histograms of the mesoporous (a) Pt-4-96, (b) Pt-6-94, (c) Pt-8-92, (d) Pt-10-90, (e) Pt-12-88, and (f) Pt-14-86 nanoparticles. (g) The relationship between the parameters of particle and the solvent compositions.

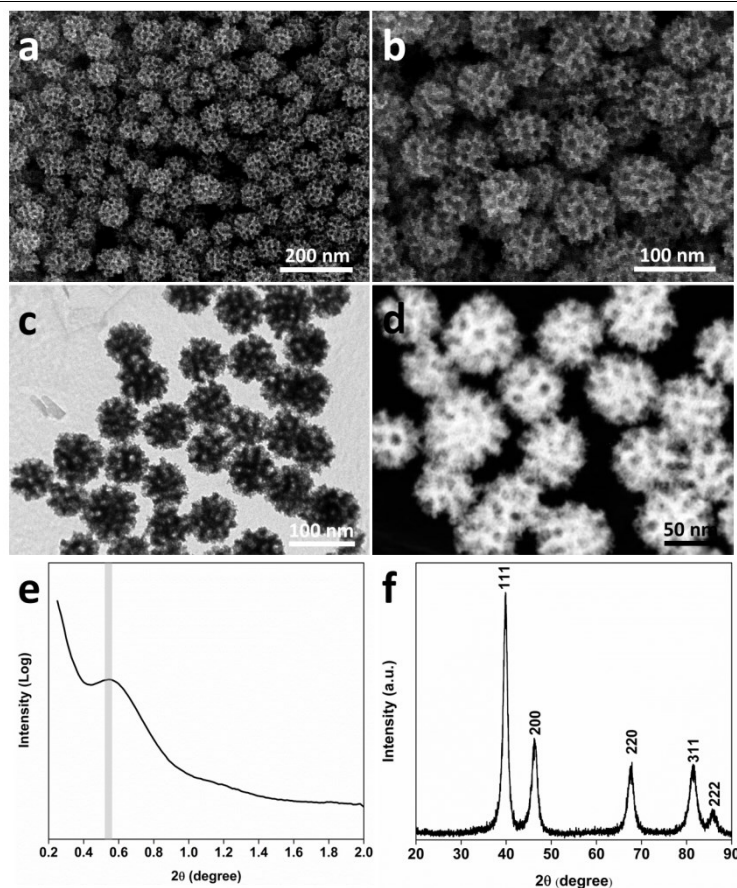


Figure 3.4 (a) Low- and (b) high-magnified SEM, (c) TEM, and (d) HAADF-STEM images of the mesoporous Pt-8-92 nanoparticles. (e) Low-, and (f) wide-angle XRD patterns of mesoporous Pt-8-92 nanoparticles prepared from the mixed solvent with a volume ratio of THF:H₂O=8:92.

Mesoporous Pt nanoparticles prepared from THF:H₂O=8:92 were investigated in detail with a combination of electron microscopy and X-ray characterization techniques. SEM and transmission electron microscopy (TEM) images of the particles prove that the densely packed spherical mesopores are distributed not only on their surfaces but also inside the nanoparticles (**Figure 3.4a-d**). Small angle X-ray scattering (SAXS) is a better way to determine the periodicity (*i.e.*, pore-to-pore distance) of the mesoporous structure in the entire ensemble of particles. The measurement shows a broad peak located at 0.55° ($d=16.0$ nm), which corresponds to the expected pore-to-pore distance of the mesoporous structure (**Figure 3.4e**). The wide-angle X-ray diffraction (XRD) pattern of the obtained sample displays five pure Pt peaks and can be assigned to 111, 200, 220, 311, and 222 diffraction peaks, respectively (**Figure 3.4f**). Examining the individual nanoparticles more closely with high resolution TEM (HRTEM) shows that the pore walls are composed of numerous, small interconnected nanoparticles (*ca.* 4-6 nm) (**Figure 3.5a**). Polycrystallinity was confirmed by the selected area electron diffraction (SAED) pattern (**Figure 3.5b**), which shows concentric rings composed of bright discrete diffraction spots that can be assigned to a face-centered cubic (*fcc*) Pt crystal for individual particles. The

HRTEM image taken from the edge of the particle had a lattice spacing of 0.23 nm, which corresponds to the *fcc* Pt {111} crystal plane (**Figure 3.5c-d**).

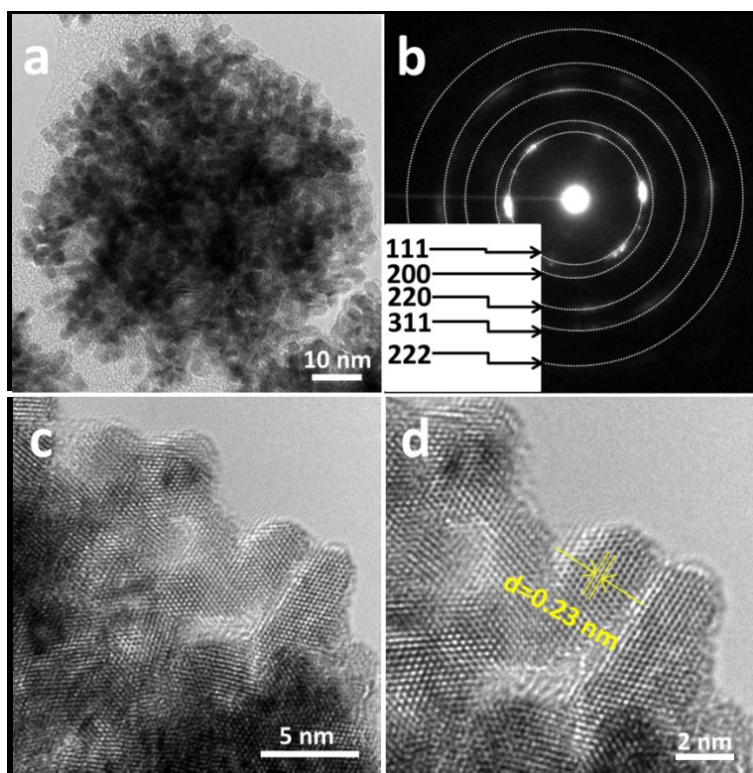


Figure 3.5 (a) Typical TEM images and (b) the corresponding SAED patterns of an individual Pt-8-92 nanoparticles. (c,d) HRTEM images focused on the edge of mesoporous Pt-8-92 nanoparticles.

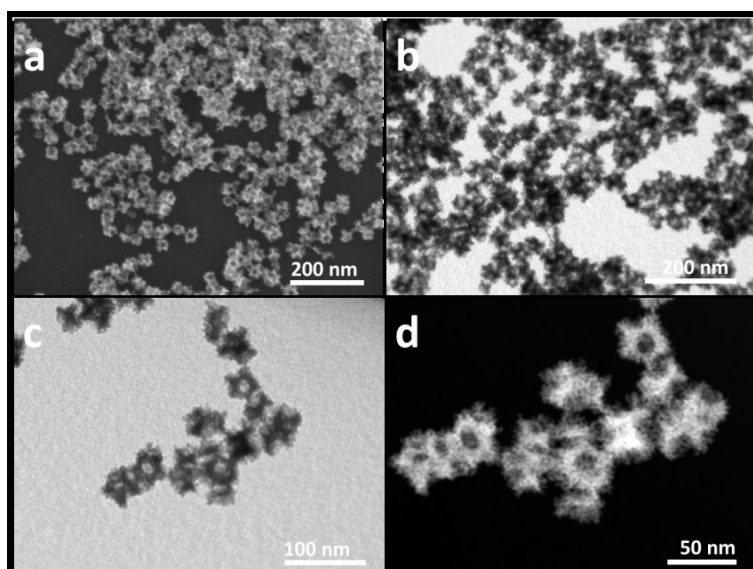


Figure 3.6 (a) SEM, (b,c) TEM and (d) the HAADF-STEM images of dimpled porous Pt-14-86 nanoparticles.

We examined the mesoporous Pt-14-86 nanoparticles synthesized at higher THF concentration to understand the influence of the solvent composition. The sample is highly dispersed, with a narrow particle size

distribution, and dimple-like pores (**Figure 3.6a**). Interestingly, the size of the nanoparticle is smaller, while the pores on the surface are larger and less numerous. Electron microscopy reveals that each nanoparticle possesses 1-2 central spherical pores, and several small branches surround its exterior (**Figure 3.6**). The particle sizes and shapes are directly related to the solvent composition.

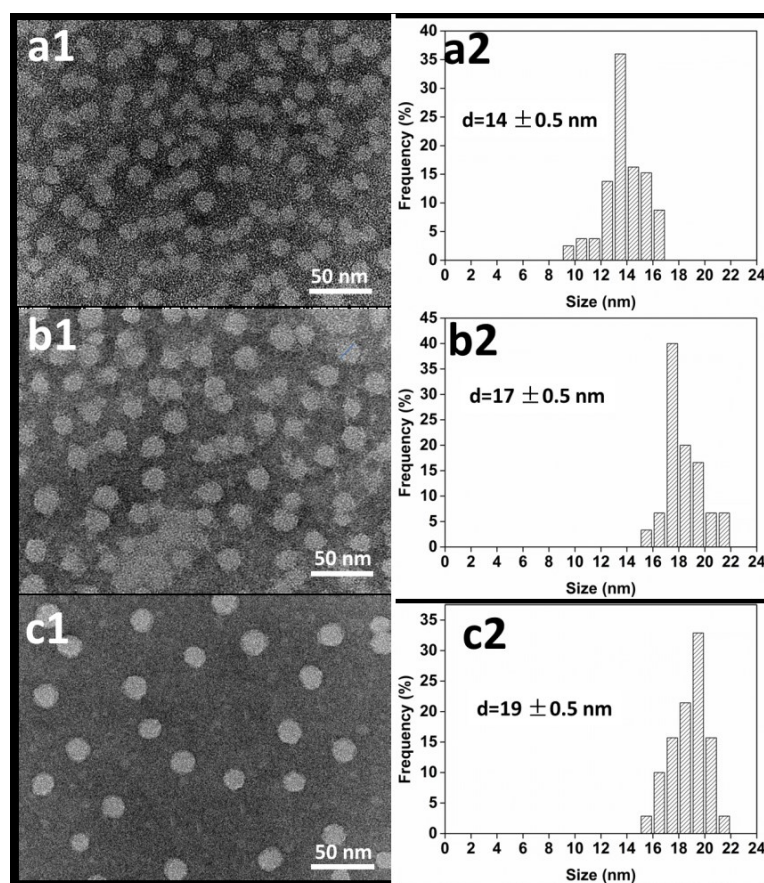


Figure 3.7 TEM images of polymeric micelles negatively stained by phosphotungstic acid dissolving PEO₁₀₅₀₀-*b*-PMMA₁₈₀₀₀ in various volume ratios of THF:H₂O: (a) 8:92, (b) 10:90, (c) 14:86. The corresponding histograms of the micelle size distributions are shown in the right column. **Note:** All the micelle solutions are prepared by fixing the weight concentration of PEO₁₀₅₀₀-*b*-PMMA₁₈₀₀₀.

In this study, solvent composition has a large impact on the final Pt structure, so we attempted to observe this effect directly in the polymeric micelles themselves. The polymeric micelles formed at various volume ratios of THF:H₂O were stained with 1.0 wt% phosphotungstic acid and studied with TEM. **Figure 3.7** shows that the spherical micelles formed in the mixed solvent of THF and H₂O. In the TEM micrograph, the bright spheres correspond to the PMMA micellar cores (lower electron density region) due to the negative staining by phosphotungstic acid.^[16] The micelle sizes increase from (14±0.5) nm to (17±0.5), and (19±0.5) nm as the volume ratio of THF:H₂O is increased from 8:92 to 10:90 to 14:86, respectively. This change in the micelle

sizes is probably due to the solubility change of hydrophobic PMMA block in the mixed solvents. Exactly as observed in our mesoporous Pt nanoparticles, the larger amount of THF causes the PMMA blocks to swell, leading to an expansion of the pore sizes in the Pt nanoparticles.

It must be considered that THF in the PEO-*b*-PMMA solution maybe affects the number of the free unimer and the micelle in solution. At low THF the fraction of micelle is increased, because the block polymer unimer (*e.g.*, PEO-*b*-PMMA) tend to form the micelle in high volume ratio of water/THF.^[4,17] This high micelle concentration facilitates the ready assembly of large number of micelles, resulting in large-sized spherical particles. On the other hand, at higher THF content, swollen micelles are formed, and their micelle concentration is decreased, which favors the formation of smaller-sized Pt nanoparticles with enlarged pores. Our results are consistent with a previous study on mesoporous silica, in which a high THF concentration promoted the formation of hollow structure bu isolated micelle, whereas a low THF concentration resulted in the formation of mesoporous structure derived from a large number of well-packed micelles.^[4] When the THF concentration was increased even more (THF/H₂O 16:84), hemi-spherical Pt nanoparticles with a few enlarged pores on the surface were observed (**Figure 3.8**). To our knowledge, tuning the particle sizes, the pore sizes, and the number of pores on the surface by simply changing the solvent compositions have not been reported previously. We believe this concept provides a new way to construct the internal structure of metallic nanoparticles. To investigate the growth of Pt particles in the solution phase, we observed the intermediate prouducts at different raction times by TEM (**Figure 3.9**). The Pt precursor was first reduced to tiny nanocrystals, which were likely stabilized by the EO chains of the micelles. As the reaction proceeded, the tiny crystals grew larger and began to coat on the spherical PEO-*b*-PMMA micelles. After 100 min, the mesoporous structures start to form.

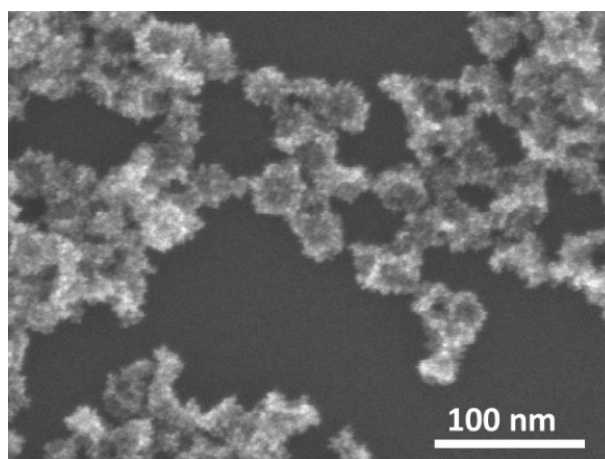


Figure 3.8 SEM images of the Pt-16-84 nanoparticles prepared from the mixed solvent with volume ratio of THF:H₂O=16:84.

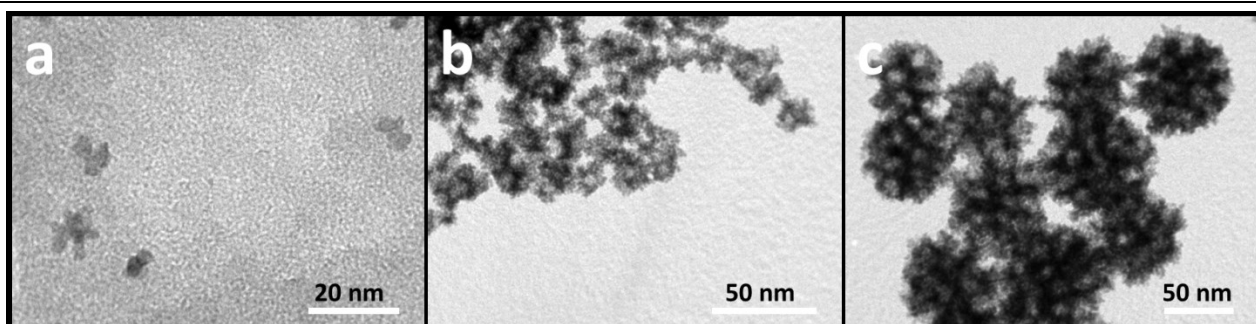


Figure 3.9 TEM images of Pt samples taken after different reaction time intervals: a) 60 min, b) 100 min, and d) 120 min. The volume ratio of THF:H₂O is fixed at 8:92

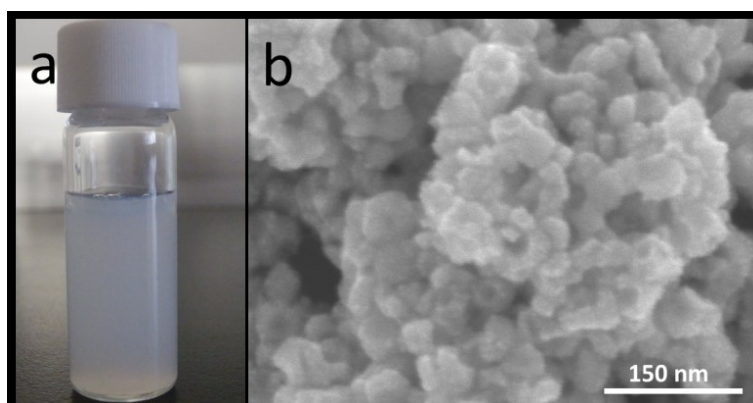


Figure 3.10 (a) Photograph of the PEO₍₇₅₀₀₎-*b*-PS₍₁₈₀₀₀₎ solution by using a mixed solvent with volume ratio of THF:H₂O=8:92. (b) SEM image of sample prepared by using the PEO₍₇₅₀₀₎-*b*-PS₍₁₈₀₀₀₎ as pore-directing agent

In the present synthesis, the use of hydrophobic PMMA block in the diblock polymer PEO-*b*-PMMA is critical for the formation of mesoporous Pt nanoparticles. When the PEO₍₁₀₅₀₀₎-*b*-PMMA₍₁₈₀₀₀₎ was replaced with a block polymer with rigid hydrophobic block (for example, PEO₍₇₅₀₀₎-*b*-PS₍₁₈₀₀₀₎) without changing other conditions, a turbid solution instead of transparent solution was obtained (**Figure 3.10a**). Even when I succeeded in obtaining transparent solution of PEO₍₇₅₀₀₎-*b*-PS₍₁₈₀₀₀₎ and Pt precursor by addition of a large amount of THF, only particle aggregates are obtained (**Figure 3.10b**), which is different from our previous electrochemical deposition system.^[10] We conclude that the PMMA blocks in the PEO-*b*-PMMA is more “soft” and “weakly” in hydrophobicity than the PS block in the PEO-*b*-PS. Furthermore, the porous structures can be facilely tuned by changing the molecular weights of PMMA block due to its pore directing effect. The pore sizes of mesoporous Pt nanoparticles can be well enlarged from (10±0.5) nm to (15±0.5) nm by changing the block copolymer from PEO₍₁₀₅₀₀₎-*b*-PMMA₍₁₈₀₀₀₎ to PEO₍₁₀₅₀₀₎-*b*-PMMA₍₂₂₀₀₀₎ (**Figure 3.11b-c**). On the contrary, (5±0.5) nm dendritic-like pores are realized by replacing PEO₍₁₀₅₀₀₎-*b*-PMMA₍₁₈₀₀₀₎ with PEO₍₁₅₀₀₀₎-*b*-PMMA₍₉₀₀₀₎ (**Figure 3.11a**).

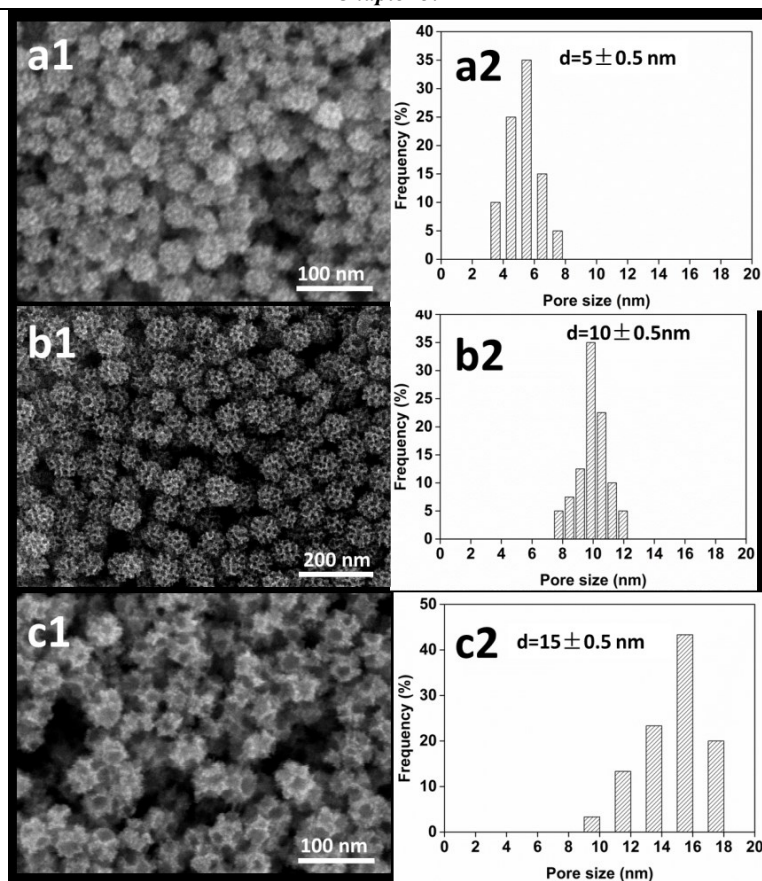


Figure 3.11 SEM images and the corresponding histograms of pore size distributions of the mesoporous Pt nanoparticles prepared by changing the molecular weight of polymers: (a) PEO₁₅₀₀₀-*b*-PMMA₉₀₀₀ (dominate pore size: 5 ± 0.5 nm), (b) PEO₁₀₅₀₀-*b*-PMMA₁₈₀₀₀ (10 ± 0.5), and (c) PEO₁₀₅₀₀-*b*-PMMA₂₂₀₀₀ (15 ± 0.5 nm). **Note:** The solvent composition is fixed at volume raion of THF:H₂O=8:92.

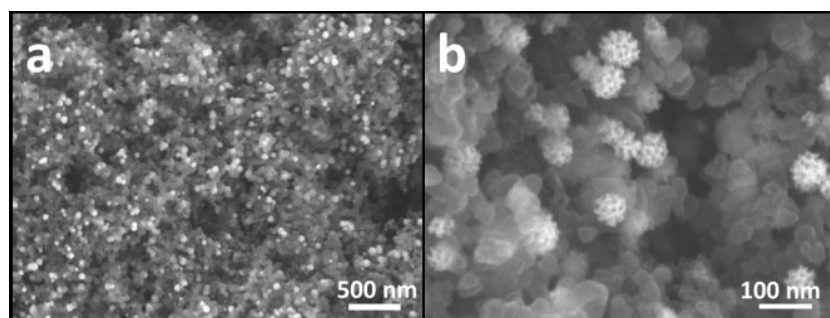


Figure 3.12 SEM images of the mesoporous Pt nanoparticles loaded on the carbon support after annealed at 250 °C under air atmosphere.

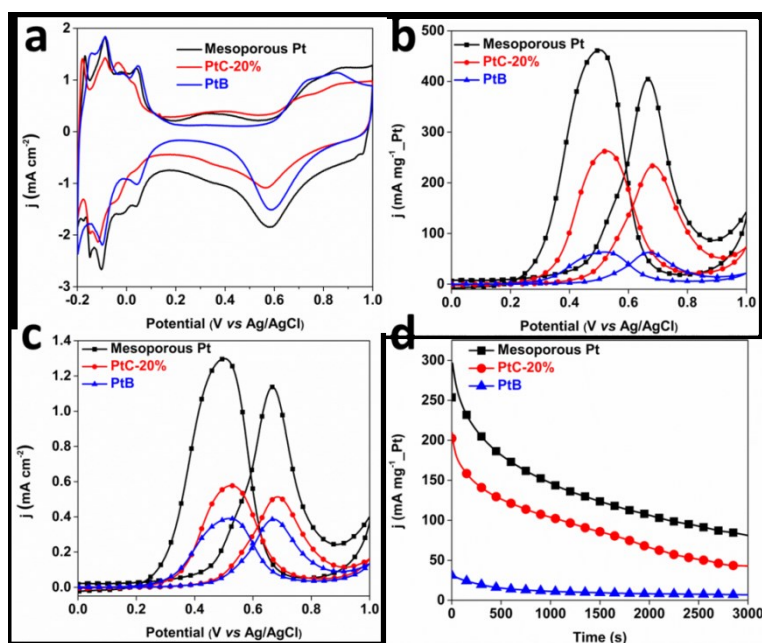


Figure 3.13 (a) Cyclic voltammograms of samples recorded in 0.5 M H_2SO_4 solution at a scan rate of 50 mV s^{-1} . (b,c) Cyclic voltammograms, (d) chronoamperometric curves (recorded at 0.6 V) for methanol oxidation reactions catalyzed by mesoporous Pt-8-92 nanoparticles, commercial PtB catalyst, and PtC-20% catalyst in 0.5 M $\text{H}_2\text{SO}_4 + 0.5 \text{ M CH}_3\text{OH}$.

Electrocatalytic activity depends on both particle size and the porous structure of Pt nanoparticles. We examined the activity of the mesoporous Pt nanoparticles for the methanol oxidation reaction (MOR). For comparison with the performance of commercially available catalysts (Pt black is abbreviated as PtB while 20wt% Pt supported on carbon is abbreviated as PtC-20%), all the mesoporous Pt nanoparticles were deposited on a carbon support (Ketjen black, abbreviated as KB) with a mass loading amount of 20% by sonicating the mixture of mesoporous Pt nanoparticles and KB in ethanol and water solution. This procedure was followed by washing with ethanol and water for several times. Finally, the samples were calcinated in air at $250 \text{ }^\circ\text{C}$ to completely remove the block copolymer and other contamination, leaving the mesoporous Pt structure remaining (**Figure 3.12**). The electrochemical surface area (ECSA) of all the samples was measured by cyclic voltammetry (CV) in a 0.5 M H_2SO_4 solution (**Figure 3.13a**). PtB and PtC-20% were characterized under the same conditions as the mesoporous Pt nanoparticles to generate a clear comparison. Clear features of hydrogen and oxygen adsorption/desorption on mesoporous Pt catalyst are indications of the cleanliness of the catalyst surface. The ECSA was calculated by integrating the charge passed in the hydrogen adsorption/desorption regions, assuming a value of $210 \mu\text{C}\cdot\text{cm}^{-2}$ for the adsorption of a hydrogen monolayer.^[18] The ECSA values was $32 \text{ m}^2 \text{ g}^{-1} \text{ Pt}$ for mesoporous Pt-8-92 while the ECSA was $15 \text{ m}^2 \text{ g}^{-1} \text{ Pt}$ and $55 \text{ m}^2 \text{ g}^{-1} \text{ Pt}$ for PtB and PtC-20% catalysts, respectively. The ECSA of mesoporous Pt nanoparticles is

lower than that of the commercial PtC-20% (*ca.* 4 nm), probably due to the tiny nanoparticles being connected in the mesoporous structure.

The typical CV curves for MOR catalyzed by the three catalysts in 0.5 M H₂SO₄ containing 0.5 M methanol solution at a scan rate of 50 mV s⁻¹ are shown in **Figure 3.13b-c**. The characteristic methanol oxidation peaks were identified in the forward and backward scans.^[19] The mass activity of the mesoporous Pt-8-92 nanoparticles (405 mA·mg⁻¹_Pt) in the forward sweep outperformed the commercial PtC-20% (235 mA·mg⁻¹_Pt) and PtB (68 mA·mg⁻¹_Pt) catalysts, suggesting the superior utilization efficiency of the Pt in the mesoporous Pt nanoparticles. Even when the activities were normalized by ECSA, the mesoporous Pt nanoparticles still exhibited the best catalytic activity toward MOR (1.29 mA cm⁻²), which is much higher than that of PtC-20% (0.5 mA cm⁻²) and PtB (0.4 mA cm⁻²) catalysts. Additionally, the mesoporous Pt nanoparticles exhibited a negatively shifted onset potential toward MOR, indicating that oxidation of methanol was easier to trigger on its surface.^[20] Such improved catalytic activity of the mesoporous Pt-8-92 nanoparticles can be ascribed to highly crystallinity and the 3D accessible mesoporous structure.^[21] Compared to previously reported Pt-based catalysts (**Table 3.1**), our prepared mesoporous Pt-8-92 nanoparticles exhibited higher current densities in mass activity.

Table 3.1 Comparison of the activity of mesoporous Pt nanoparticles with previous reported Pt-based catalysts.

Sample name	Condition	Scan rate (mV s ⁻¹)	Mass activity (mA mg ⁻¹ _Pt)	Ref.
Mesoporous Pt nanoparticles	0.5 M H ₂ SO ₄ + 0.5 M CH ₃ OH	50	403	Present work
Porous Pt nanoparticles	0.5 M H ₂ SO ₄ + 0.5 M CH ₃ OH	50	203	<i>Angew. Chem. Int. Ed.</i> , 2015, 54 , 11073-11077.
Porous Pt nanorods	0.5 M H ₂ SO ₄ + 0.5 M CH ₃ OH	50	209	<i>Angew. Chem. Int. Ed.</i> , 2013, 52 , 8050-8053.
Hollow dendritic Pt nanocube	0.5 M H ₂ SO ₄ + 0.5 M CH ₃ OH	50	242	<i>Chem. Commun.</i> , 2014, 50 , 15337-15340.
Hollow Pt nanospheres	0.5 M H ₂ SO ₄ + 1 M CH ₃ OH	50	ca. 220	<i>J. Mater. Chem. A</i> , 2014, 2 , 13738-13743.
Ultrathin Pt nanowire	0.5 M H ₂ SO ₄ + 1 M CH ₃ OH	50	581	<i>Angew. Chem. Int. Ed.</i> , 2013, 52 , 12577-12581.
Dendritic Au@Pt nanoparticle	0.5 M H ₂ SO ₄ + 0.5 M CH ₃ OH	50	120	<i>Chem. Mater.</i> , 2010, 22 , 6310-6318.
Pd@Pt nanoparticles	0.1 M HClO ₄ + 0.5 M CH ₃ OH	50	ca.350	<i>Chem. Eur. J.</i> , 2014, 20 , 7901-7905.

Nanoflower Pt ₃ Co	0.1 M HClO ₄ + 1.0 M CH ₃ OH	50	385.1	<i>J. Power Sources</i> , 2014, 268 , 744-751.
Pt ₁ Ni ₁ nanowork	0.5 M H ₂ SO ₄ + 1.0 M CH ₃ OH	50	136	<i>Nanoscale</i> , 2014, 6 , 4635-4641.
TeCuPt nanowires	0.5 M H ₂ SO ₄ + 1.0 M CH ₃ OH	20	245	<i>J. Mater. Chem. A</i> , 2015, 3 , 5850-5858.
Octahedra PtAg alloy	0.5 M H ₂ SO ₄ + 1.0 M CH ₃ OH	50	ca. 350	<i>Nanoscale</i> , 2014, 6 , 12310-12314.
Dendritic Au@Pd@Pt nanoparticles	0.5 M H ₂ SO ₄ + 1 M CH ₃ OH	50	430	<i>Chem. Mater.</i> , 2011, 23 , 2457-2465.
Pt ₃ V/C	0.1 M HClO ₄ + 1 M CH ₃ OH	20	480	<i>J. Am. Chem. Soc.</i> , 2014, 136 , 10206-10209.
Hollow Pd@Pt nanoparticles	0.5 M H ₂ SO ₄ + 1.0 M CH ₃ OH	50	500	<i>J. Power Sources</i> , 2015, 274 , 604-610.
Hollow Pt-on-Pd nanodendrites	0.5 M H ₂ SO ₄ + 1 M CH ₃ OH	50	580	<i>J. Am. Chem. Soc.</i> , 2013, 135 , 16762-16765.
PtPdTe nanowire	0.5 M H ₂ SO ₄ + 1 M CH ₃ OH	50	595	<i>Angew. Chem. Int. Ed.</i> , 2013, 52 , 7472-7476.
Dendritic Au@Pt nanoparticle	0.1 M H ₂ SO ₄ + 2 M CH ₃ OH	100	426	<i>Chem. Mater.</i> , 2014, 26 , 6928-6940.

The dependence of catalytic activity on pore size and nanoparticle size was further studied by comparing the performances of the mesoporous Pt nanoparticles (**Table 3.2**). We found that the catalytic activity of samples depends on the ECSAs, which vary depending on both nanoparticle sizes and the pore sizes. In the case of larger particles, the inner parts of Pt surface are not accessible, and the ECSAs are lower, decreasing catalytic mass-activity. With decreasing the particle sizes (to 62 nm), the catalytic activity gradually increased up to 405 mA·mg⁻¹ Pt, owing to the enhanced ECSAs. But decreasing the particle sizes any further results in a smaller ECSA, because the pore sizes are increased while the number of pores on the surface is decreased. We concluded that larger mesopores or less numbers of them, results in a smaller ESCA and ultimately leads to a loss in mass-activity.

Table 3.2 The activity of the mesoporous Pt nanoparticles prepared by using different solvent composition.

Solvent composition		Particle Size (nm)	Pore Size (nm)	ECSA (m ² g ⁻¹)	Mass activity (mA g ⁻¹)	Specific activity (mA cm ⁻²)
THF (vol%)	Water (vol%)					
4	96	107±1	8±0.5	19	240	1.25
6	94	86±1	9±0.5	28	345	1.22

8	92	62±1	10±0.5	32	405	1.29
10	90	46±1	12±0.5	26	320	1.23
12	88	37±1	14±0.5	25	300	1.21
14	86	32±1	14±0.5	25	300	1.21

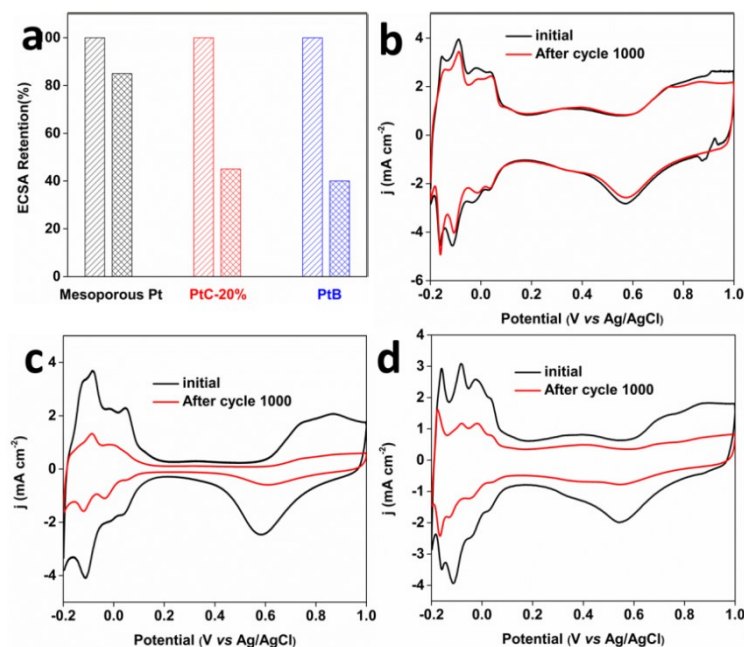


Figure 3.14 (a) Comparison of ECSA retention of mesoporous Pt nanoparticles, commercial PtB catalyst, and PtC-20% catalyst after cycling treatments in a potential range of -0.2 V to 1.0 V at a scan rate of $100 \text{ mV} \cdot \text{s}^{-1}$. Comparison of the electrochemical durability of (b) mesoporous Pt nanoparticles, (c) PtB, and (d) PtC-20% catalysts. The cycling measurements were carried out in 0.5 M H_2SO_4 solution with a sweep rate of 0.1 V s^{-1} at a potential range of -0.2 V to 1.0 V. All the currents are normalized by electrode geometric surface area.

The chronoamperometric data recorded at 0.6 V for 3000 s show the mesoporous Pt nanoparticles possessed a slower current decay and a higher current density than that of PtC-20% and PtB catalysts (**Figure 3.13d**). The structural stability of our mesoporous Pt nanoparticle can be well supported by the ECSA retention after cycling treatment. The mesoporous Pt nanoparticles lost only 15% of the initial Pt ECSA, while the commercial PtC-20% and PtB lost 55% and 60% of their initial ECSA (**Figure 3.14**), respectively. We believe the higher stability of the mesoporous structure is because it is less vulnerable to aggregation (**Figure 3.15**).^[22]

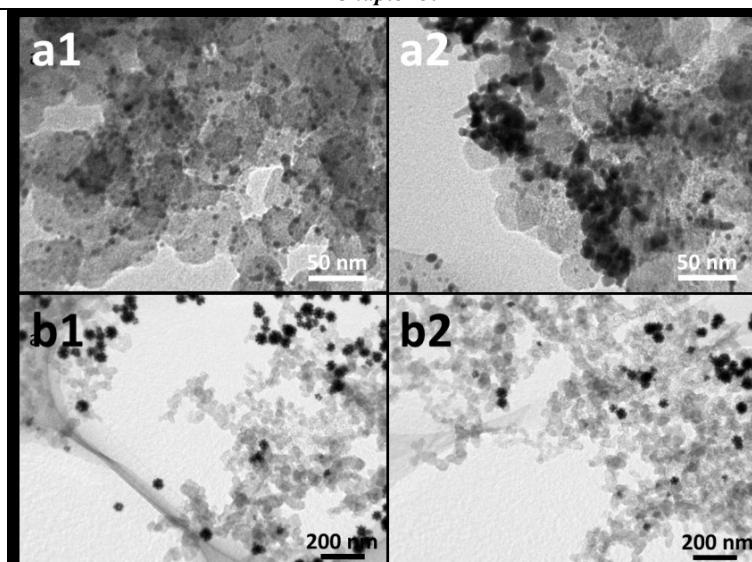


Figure 3.15 The SEM images of (a) the commercial PtC-20% and (b) mesoporous PtC. (a1,b1) before (a2,b2) after the durability tests, carried out in 0.5 M H₂SO₄ solution with a sweep rate of 0.1 V s⁻¹ at room temperature.

3.4. Conclusion

In summary, we have demonstrated a novel polymeric micelle approach for the preparation of Pt nanoparticles with continuously tunable mesoporous structures. The essence of this approach is that the solvent properties successfully stimulate the variations in the polymeric micelles by selectively changing the solvents and the block copolymers. Continuously tunable porous structures are significantly important for the future design of the porous materials with superior catalytic activities.

References

- [1] (a) Y. Sakamoto, M. Kaneda, O. Terasaki, D. Zhao, J. M. Kim, G. Stucky, H. J. Shin, R. Ryoo, *Nature*, 2000, **408**, 449; (b) Y. Fang, Y. Lv, J. Tang, H. Wu, D. Jia, D. Feng, B. Kong, Y. Wang, A. A. Elzatahry, D. Al-Dahyan, Q. Zhang, G. Zheng, D. Zhao, *Angew. Chem. Int. Ed.*, 2015, **54**, 8425; (c) S. Wang, Q. Zhao, H. Wei, J. Q. Wang, M. Cho, H. S. Cho, O. Terasaki, Y. Wan, *J. Am. Chem. Soc.*, 2013, **135**, 11849; (d) B. Kong, J. Tang, Y. Zhang, T. Jiang, X. Gong, C. Peng, J. Wei, J. Yang, Y. Wang, X. Wang, G. Zheng, C. Selomulya, D. Zhao, *Nature Chem.*, 2016, **8**, 171; (e) T. Suteewong, H. Sai, R. Cohen, S. Wang, M. Bradbury, B. Baird, S. M. Gruner, U. Wiesner, *J. Am. Chem. Soc.*, 2011, **133**, 172.
- [2] (a) K. C. Kao, C. H. Lin, T. Y. Chen, Y. H. Liu, C. Y. Mou, *J. Am. Chem. Soc.*, 2015, **137**, 3779; (b) C. Li, B. Jiang, N. Miyamoto, J. H. Kim, V. Malgras, Y. Yamauchi, *J. Am. Chem. Soc.*, 2015, **137**, 11558; (c) Q. Yue, J. Li, W. Luo, Y. Zhang, A. A. Elzatahry, X. Wang, C. Wang, W. Li, X. Cheng, A. Alghamdi, A. M. Abdullah, Y. Deng, D. Zhao, *J. Am. Chem. Soc.*, 2015, **137**, 11558; (d) L. Han, K. Miyasaka, O. Terasaki, S. Che, *J. Am. Chem. Soc.*, 2011, **133**, 11524.
- [3] (a) Y. Deng, J. Wei, Z. Sun, D. Zhao, *Chem. Soc. Rev.*, 2013, **42**, 4054; (b) Y. Wang, T. Brezesinski, M. Antonietti, B. Smarsly, *ACS Nano*, 2009, **3**, 1373.
- [4] J. Wei, H. Wang, Y. Deng, Z. Sun, L. Shi, B. Tu, M. Luqman, D. Zhao, *J. Am. Chem. Soc.*, 2011, **133**, 20369.
- [5] (a) J. Zhang, Y. Deng, J. Wei, Z. Sun, D. Gu, H. Bongard, C. Liu, H. Wu, B. Tu, F. Schüth, D. Zhao, *Chem. Mater.*, 2009, **21**, 3996-4005; (b) J. Shim, J. Lee, Y. Ye, J. Hwang, S. K. Kim, T. H. Lim, U. Wiesner, J. Lee, *ACS Nano*, 2012, **6**, 6870-6881.
- [6] D. Niu, Z. Liu, Y. Li, X. Luo, J. Zhang, J. Gong, J. Shi, *Adv. Mater.*, 2014, **26**, 4947.
- [7] (a) Y. Li, W. Luo, N. Qin, J. Dong, J. Wei, W. Li, S. Feng, J. Chen, J. Xu, A. A. Elzatahry, M. H. Es-Saheb, Y. Deng, D. Zhao, *Angew. Chem. Int. Ed.*, 2014, **53**, 9035; (b) E. Ortel, A. Fischer, L. Chuenchom, J. Polte, F. Emmerling, B. Smarsly, R. Kraehnert, *Small*, 2012, **8**, 298.
- [8] R. M. Grudzien, J. P. Blitz, S. Pikus, M. Jaronie, *J. Colloid Interface Sci.*, 2009, **333**, 354.
- [9] (a) X. Huang, Y. Li, Y. Chen, E. Zhou, Y. Xu, H. Zhou, X. Duan, Y. Huang, *Angew. Chem. Int. Ed.*, 2013, **52**, 2520; (b) L. Wang, Y. Yamauchi, *J. Am. Chem. Soc.*, 2009, **131**, 9152-9153; (c) S. Chen, H. Su, Y. Wang, W. Wu, J. Zeng, *Angew. Chem. Int. Ed.*, 2015, **54**, 108; (d) J. Ge, D. He, L. Bai, R. You, H. Lu, C. Tan, Y. B. Kang, B. Xiao, Y. Wu, Z. Deng, W. Huang, H. Zhang, X. Hong, Y. Li, *J. Am. Chem. Soc.*, 2015, **137**, 14566; (e) L. Zhao, C. Xu, H. Su, J. Liang, S. Lin, L. Gu, X. Wang, M. Chen, N. Zheng, *Adv. Sci.*, 2015, **2**, 1500100.

- [10] (a) A. Takai, Y. Yamauchi, K. Kuroda, *J. Am. Chem. Soc.*, 2010, **132**, 208; (b) C. Li, Ö. Dag, T. D. Dao, T. Nagao, Y. Sakamoto, T. Kimura, O. Terasaki, Y. Yamauchi, *Nat. Commun.*, 2015, **6**, 6608.
- [11] (a) B. Y. Xia, H. B. Wu, N. Li, Y. Yan, X. W. Lou, X. Wang, *Angew. Chem. Int. Ed.*, 2015, **54**, 3797; (b) L. Bu, J. Ding, S. Guo, X. Zhang, D. Su, X. Zhu, J. Yao, J. Guo, G. Lu, X. Huang, *Adv. Mater.*, 2015, **27**, 7204; (c) H. Lv, Z. Xi, Z. Chen, S. Guo, Y. Yu, W. Zhu, Q. Li, X. Zhang, M. Pan, G. Lu, S. Mu, S. Sun, *J. Am. Chem. Soc.*, 2015, **137**, 5859; (d) J. Mao, Y. Liu, Z. Chen, D. Wang, Y. Li, *Chem. Commun.*, 2014, **50**, 4588; (e) H. H. Li, S. Y. Ma, Q. Q. Fu, X. J. Liu, L. Wu, S. H. Yu, *J. Am. Chem. Soc.*, 2015, **137**, 7862; (f) B. Jiang, C. Li, V. Malgras, Y. Bando, Y. Yamauchi, *Chem. Commun.*, 2016, **52**, 1186.
- [12] (a) I. Bannat, K. Wessels, T. Oekermann, J. Rathousky, D. Bahnemann, M. Wark, *Chem. Mater.*, 2009, **21**, 1645; (b) Y. Li, B. P. Bastakoti, V. Malgras, C. Li, J. Tang, J. H. Kim, Yusuke Yamauchi, *Angew. Chem. Int. Ed.*, 2015, **54**, 11073.
- [13] (a) K. Edelmann, M. Janich, E. Hoinkis, W. Pyckhout-Hintzen, S. Höring. Macromo, *Chem. Phys.*, 2001, **202**, 1638; (b) A. H. Yuwono, Y. Zhang, J. Wang, X. H. Zhang, H. Fan, W. Ji, *Chem. Mater.*, 2006, **18**, 5876.
- [14] (a) Ö. Çelik, Ö. Dag, *Angew. Chem. Int. Ed.*, 2001, **40**, 3799-3803; (b) Y. Yamauchi, A. Tonegawa, M. Komatsu, H. Wang, L. Wang, Y. Nemoto, N. Suzuki, K. Kuroda, *J. Am. Chem. Soc.*, 2012, **134**, 5100-5109; (c) C. Albayrak, G. Gülten, Ö. Dag, *Langmuir* 2007, **23**, 855-860.
- [15] (a) H. Wang, L. Wang, T. Sato, Y. Sakamoto, S. Tominaka, K. Miyasaka, N. Miyamoto, Y. Nemoto, O. Terasaki, Y. Yamauchi, *Chem. Mater.* 2012, **24**, 1591; (b) A. F. Demirörs, B. E. Eser, Ö. Dag, *Langmuir* 2005, **21**, 4156; (c) C. Albayrak, A. M. Soylu, Ö. Dag, *Langmuir*, 2008, **24**, 10592.
- [16] (a) Y. He, Z. Li, P. Simone, T. P. Lodge, *J. Am. Chem. Soc.*, 2006, **128**, 2745; (b) M. R. Libera, R. F. Egerton, *Polym. Rev.*, 2010, **50**, 321; (c) J. P. Patterson, M. P. Robin, C. Chassenieux, O. Colombani, R. K. O'Reilly, *Chem. Soc. Rev.*, 2014, **43**, 2412.
- [17] (a) Elizabeth G. Kelley, Thomas P. Smart, Andrew J. Jackson, Millicent O. Sullivan, Thomas H. Epps, III, *Soft Matter.*, 2011, **7**, 7094; (b) A. H. Yuwono, Y. Zhang, J. Wang, X. H. Zhang, H. Fan, W. Ji, *Chem. Mater.*, 2006, **18**, 5876.
- [18] (a) B. Lim, M. Jiang, P. H. C. Camargo, E. C. Cho, J. Tao, X. Lu., Y. Zhu, Y. Xia, *Science*, 2009, **324**, 1302; (b) B. Y. Xia, H. B. Wu, Y. Yan, X. W. Lou, X. Wang, *J. Am. Chem. Soc.*, 2013, **135**, 9480; (c) H. W. Liang, X. A. Cao, F. Zhou, C. H. Cui, W. J. Zhang, S. H. Yu, *Adv. Mater.*, 2011, **23**, 1467; (d) L. Dai, S. Mo, Q. Qin, X. Zhao, N. Zheng, *Small*, 2016, **12**, 1572;

- [19] (a) M. Sogaard, M. Odgaard, E. M. Skou, *Solid State Ionics*, 2001, **145**, 31; (b) B Jiang, C Li, V Malgras, Y Yamauchi, *J. Mater. Chem. A*, 2015, **3**, 18053; (c) J. Ding, X. Zhu, L. Bu, J. Yao, J. Guo, S. Guo, X. Huang, *Chem. Commun.*, 2015, **51**, 9722; (d) M. Wang, X. Wang, J. Li, L. Liu, *J. Mater. Chem. A*, 2013, **1**, 8127.
- [20] (a) K. Zhang, W. Yang, C. Ma, Y. Wang, C. Sun, Y. Chen, P. Duchesne, J. Zhou, J. Wang, Y. Hu, M. N. Banis, P. Zhang, F. Li, J. Li, L. Chen, *NPG Asia Materials*, 2015, **7**, 153; (b) G. Zhang, C. Huang, R. Qin, Z. Shao, D. An, W. Zhang, Y. Wang, *J. Mater. Chem. A*, 2015, **3**, 5204.
- [21] (a) E. A. Franceschini, G. A. Planes, F. J. Williams, G. J. A. A. Soler-Illia, H. R. Corti, *J. Power Sources*, 2011, **196**, 1723; (b) B. Jiang, C. Li, M. Imura, J. Tang, Y. Yamauchi, *Adv. Sci.*, 2015, **2**, 1500112; (c) Q. Shi, Y. Song, C. Zhu, H. Yang, D. Du, Y. Lin, *ACS Appl. Mater. Interfaces*, 2015, **7**, 24288; (d) E. A. Franceschini, M. M. Bruno, F. J. Williams, F. A. Viva, H. R. Corti, *ACS Appl. Mater. Interfaces*, 2013, **5**, 10437.
- [22] (a) J. Kibsgaard, Y. Gorlin, Z. Chen, T. F. Jaramillo, *J. Am. Chem. Soc.*, 2012, **134**, 7758; (b) C. Zhu, D. Du, A. Eychmüller, Y. Lin, *Chem. Rev.*, 2015, **115**, 8896; (c) B. Jiang, C. Li, V. Malgras, M. Imura, S. Tominaka, Y. Yamauchi, *Chem. Sci.*, 2016, **7**, 1575.

Chapter 4. Surfactant-Directed Synthesis of Bimetallic Mesoporous Pt-based Electrocatalysts

4.1. Bimetallic Mesoporous PtPd Spheres through Surfactant-Directed Synthesis

4.1.1. Introduction

Noble metal nanostructures have received much attention due to their broad applications in hydrogenation reactions, coupling reactions, fuel cells, and localized surface plasma resonances, *etc.*^[1] Thanks to previously extensive efforts, noble metal catalysts have made significant progress in the applications of fuel cells for solving the problem of energy crisis. To enhance electrochemical catalytic performance in fuel cells, most of the previous studies not only focused on the composition but also concentrated on the nanostructure of catalysts. In particular, Pt-based multi-metallic architectures such as dendritic core-shell Au@Pt nanoparticle,^[2] polyhedral PtCu₃ alloy,^[3] hollow Pt-Pd nanocage,^[4] hollow Pt-Ni nanosphere,^[5] PtPdTe nanowires,^[6] and Pt-on-Pd_{0.85}Bi_{0.15} nanowires^[7] have represented as emerging classes of nanomaterials, showing excellent performances compared with irregular Pt nanoparticles as well as monometallic Pt.

Among various Pt-based metallic nanostructures, the preparation of mesoporous Pt-based nanostructure is considered as one of effective strategies to improve the electrochemical activity owing to their high surface areas, abundant active sites and accessible pores. In this study, my target is to synthesize Pt-based ‘multi-metallic’ mesoporous spheres to enhance the electrochemical activity towards methanol oxidation reaction (MOR) and reduce the usage of Pt at the same time. Soft- and hard-templating methods have been proposed so far to synthesize mesoporous metals.^[8] Solution phase synthesis is also recognized as an environmentally friendly approach and easily extended to large-scale production.^[9] However, it should be noted that most of previously reported mesoporous metal materials are based on monometallic Pt nanostructures.^[10] In most cases, the mesoporous metals possess randomly arranged and small-sized pores, which seriously inhibits effective circulation of reactant/product species within the pores.

Therefore, to explore a facile and reliable strategy for preparation of multimetallic mesoporous spheres with ultra-large mesopores is of great importance for both fundamental research and practical applications. Here, I have successfully synthesized bimetallic PdPt spheres with ultra-large mesopores by surfactant-directing method. Mesoporous bimetallic PdPt spheres exhibited superior electrochemical activity compared to commercial Pt black (PtB) and dendritic Pt spheres (with small-sized pores).

4.1.2. Experimental Sections

4.1.2.1. Materials

All chemicals and solvents were used as received without further purification. H_2PtCl_6 , K_2PtCl_4 , Na_2PdCl_4 , NaBH_4 , ascorbic acid (AA), cetyltrimethylammonium bromide (CTAB), and methanol were purchased from Nacalai Tesque, Inc. (Kyoto, Japan). Pluronic F127 and nonionic surfactant Brij58 were obtained from Sigma-Aldrich. Commercial PB (HiSPEC®1000) was supplied by Johnson Matthey Company. All solutions were prepared with deionized water treated with a Millipore water purification system (Millipore Corp.).

4.1.2.2. Preparation of Mesoporous Bimetallic PdPt Spheres

In a typical synthesis of mesoporous bimetallic PdPt spheres, 0.6 mL of Na_2PdCl_4 solution (20.0 mM), 1.2 mL of K_2PtCl_4 solution (20.0 mM), 1.8 mL of H_2PtCl_6 solution (20.0 mM), 60.0 μL of HCl solution (6.0 M), and 60.0 mg of Pluronic F127 were mixed. After F127 was completely dissolved, 3.0 mL of ascorbic acid (AA) solution (0.1 M) was added to the above solution, giving the final Na_2PdCl_4 , K_2PtCl_4 , H_2PtCl_6 precursor amounts of 0.012, 0.024, and 0.036 mmol, respectively. In the typical condition, the relative mole ratio of Pt/Pd species was 5.00. Then, the mixed solution was continuously sonicated in a water bath for 4 hours at 40 °C. Finally, the sample was collected by centrifugation at 14,000 rpm for 20 min and the residual Pluronic F127 was removed by three consecutive washing/centrifugation cycles with ethanol and water.

4.1.2.3. Characterization

Scanning electron microscope (SEM) observation was carried out using a Hitachi SU-8000 microscope operated at 5.00 kV. Transmission electron microscope (TEM) and high-angle annular dark-field scanning TEM (HAADF-STEM) observations were carried out using a JEOL JEM-2100F operated at 200 kV equipped with an energy-dispersive spectrometer. The samples for TEM study were prepared by depositing a drop of the diluted colloidal suspension on a carbon-coated copper grid. A wide-angle powder X-ray diffraction (XRD) pattern was recorded with a Rigaku Rint 2500 diffractometer with monochromated Cu $K\alpha$ radiation. Low-angle XRD patterns were recorded by using a NANO VIEWER (Rigaku, Japan).

4.1.2.4. Electrochemical Test

Both CV and chronoamperometric experiments were performed using a CHI 842B electrochemical analyzer (CHI Instruments, USA). A conventional three-electrode cell was used, including an Ag/AgCl (containing saturated KCl) electrode as a reference electrode, a platinum wire as a counter electrode, and a modified glassy carbon electrode (GCE) as a working electrode. The modified GCE was coated with as-produced samples (5.0 μg) and dried at room temperature. Then, 5.0 μL of Nafion (0.05 wt %) was coated on the surface of the

modified GCE and dried before electrochemical experiments. Prior to electrochemical experiments, the GCEs modified with the samples were activated electrochemically by cycling the electrode potential between -0.2 V and +1.5 V (vs. Ag/AgCl) in 0.5 M H₂SO₄ until CVs that were characteristic for a clean Pt electrode were obtained.

4.1.3. Results and Discussion

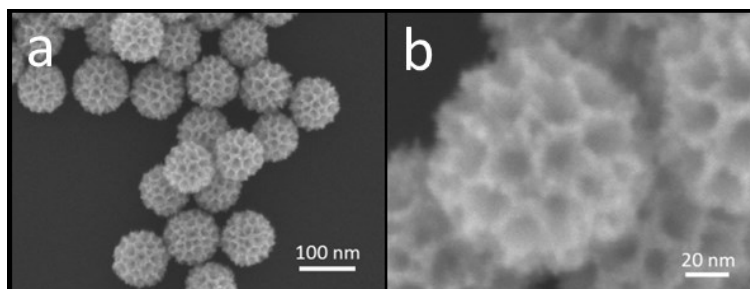


Figure 4.1.1 (a) Low- and (b) high-magnified SEM images of the typical mesoporous bimetallic PdPt spheres obtained at typical conditions.

Scanning electron microscope (SEM) was employed to characterize the morphology of as-prepared sample under the typical condition (**Figure 4.1.1a**). It clearly reveals that all the particles are fairly uniform in size and shape. Any by-products, such as non-porous particles, non-spherical shape, or bulks were not observed. Highly magnified SEM image (**Figure 4.1.1b**) shows that well-defined mesoporous structures are observed over the entire area of the particle surface. The average mesopore size is estimated to be 18.5 ± 0.5 nm with the wall thickness of 8.0 ± 0.5 nm. The mesopores observed on the particle surface are deeply concaved into the center of the spherical particles.

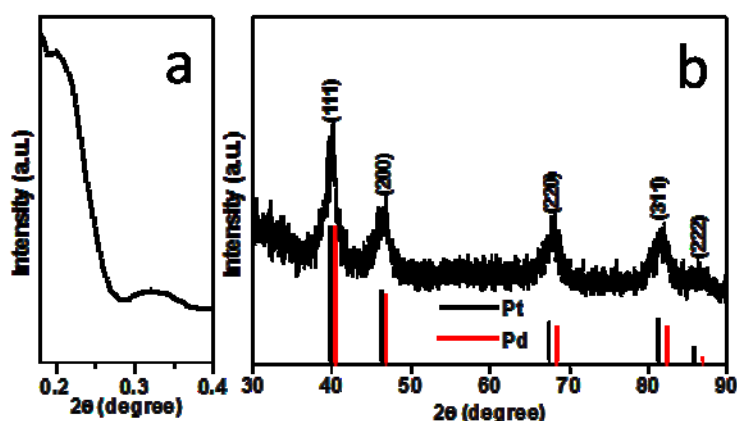


Figure 4.1.2 (a) Low-angle and (b) wide-angle XRD patterns of the mesoporous bimetallic PdPt spheres prepared under typical conditions.

To confirm the mesostructural periodicity, the typical sample was characterized by low-angle X-ray diffraction measurement (**Figure 4.1.2a**). One clear broad peak centered at $2\theta = 0.33^\circ$ ($d = 26.8$ nm) supports the formation of periodic mesoporous structure. As seen in SEM images (**Figure 4.1.2b**), the mesopores are closely assembled each other in random manner, although the mesopore size is quite uniform. In this case, the d -spacing ($d = 26.8$ nm) means the pore-to-pore distance (*i.e.*, equal to sum of the wall thickness and the mesopore size), which is in agreement with the SEM data (**Figure. 1b**).

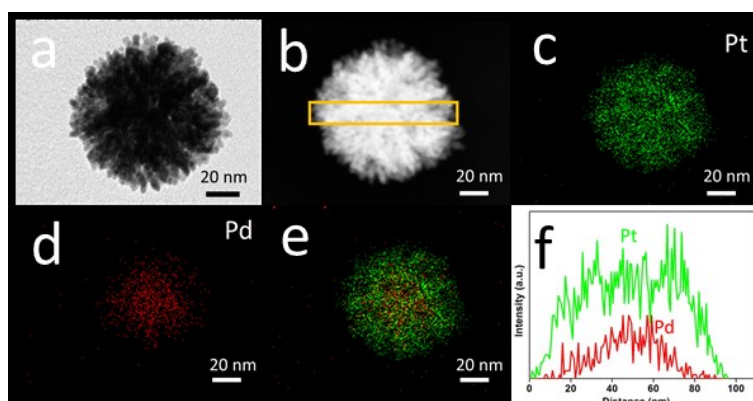


Figure 4.1.3 (a) TEM image, (b) HAADF-STEM image, (c-e) elemental mapping images and (f) compositional line profiles of the mesoporous bimetallic PdPt spheres prepared under typical conditions.

For better understanding the distribution of Pd and Pt in the nanoparticles, elemental mapping was investigated for individual sphere (**Figure 4.1.3**). From **Figure 4.1.3c-e**, both Pt and Pd are uniformly distributed. The elemental mapping reveals that most of Pd content is concentrated in the particle center, whereas Pt is placed on the entire sphere. The line-scanning profiles (**Figure 4.1.3f**) of one sphere more clearly reveal the elemental composition of bimetallic materials, consisting of the higher Pd content at the center, which is in agreement with the elemental mapping results. The wide-angle XRD peaks (**Figure 4.1.2b**) are assigned to (111), (200), (220), and (311) diffraction peaks of face-centered-cubic (fcc) crystal structure. However, it is very difficult to resolve Pt and Pd crystals in the wide-angle XRD patterns because of the fact that the lattice mismatch ratio is only 0.77 % for Pt/Pd.^[11]

Furthermore, the molar ratio of Pt/Pd was confirmed to be 2.66 by the inductively coupled plasma (ICP), which agreed with result obtained by energy-dispersive X-ray spectroscopy (EDS). This value is smaller compared to the starting composition with Pt/Pd of 5.00. All the Pd species dissolved in the precursor solution are reduced to form the cores, while the dissolved Pt species are not completely reduced (*i.e.*, un-deposited Pt species are still remained in the solution after the reaction). In the present system, Pd species

are more easily and preferentially reduced, although the standard reduction potential for Pt complexes ($[\text{PtCl}_4]^{2-}/\text{Pt}$: +0.76 V vs. SHE and $[\text{PtCl}_6]^{2-}/[\text{PtCl}_4]^{2-}$: +0.68 V vs. SHE) is higher than that for ($[\text{PdCl}_4]^{2-}/\text{Pd}$: +0.59 V vs. SHE). Similar anomalous behavior has been reported for the co-deposition of Pd and Pt.^[12] Sometimes, the reduction of metal species cannot be interpreted simply according to their standard reduction potentials in the presence of multiple metal precursors and organic additives (e.g., surfactant molecules) due to their complicated reduction kinetics and coordination effect.^[13]

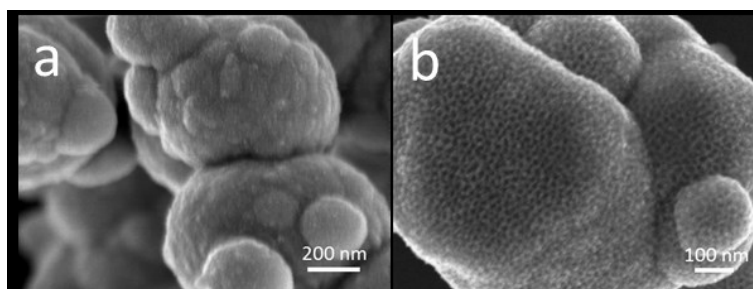


Figure 4.1.4 SEM images of samples prepared (a) without F127 and (b) with 5.0 mg F127.

As demonstrated above, mesoporous bimetallic PdPt spheres can be synthesized by a simple way in aqueous solution. More control experiments were carried out for understanding the formation mechanism. In general, F127 is well known as one of typical block copolymers and has been utilized as a pore-directing agent for mesoporous oxide and carbon materials.^[14] Some reports have also demonstrated that F127 can be used as a protecting for preventing the particle aggregations.^[15] As shown in **Figure 4.1.4a**, nonporous bulk aggregations were formed in absence of F127. When 5 mg of F127 was used, heavily aggregated porous structure was obtained (**Figure 4.1.4b**), because insufficient F127 cannot inhibit particle aggregation effectively, resulting in formation of irregularly-shaped large particles. Further increasing the amount of F127 (60 mg, which is under the typical conditions) resulted in the highly dispersed spheres with mesoporous structure. Thus, it is obvious that the F127 served as the pore-directing agent as well as protecting agent for preventing the particle aggregations and/or suppressing the random growth of the mesoporous metals.^[16]

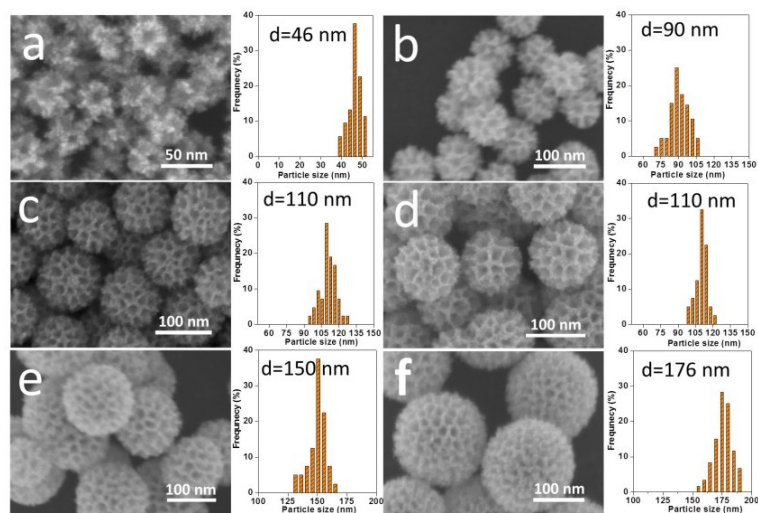


Figure 4.1.5 SEM images and particle sizes distributions of the samples prepared by varying the molar ratios of $\text{H}_2\text{PtCl}_6/\text{K}_2\text{PtCl}_4$: a) 0:100 b) 10:90 c) 20:80 d) 40:60 e) 90:10 (f) 100:0.

Interestingly, I found that the particle sizes were easily tuned by varying the molar ratios of $\text{H}_2\text{PtCl}_6/\text{K}_2\text{PtCl}_4$. **Figure 4.1.5** shows the SEM images and the corresponding particle size distribution histograms of the samples prepared by changing the molar ratios of $\text{H}_2\text{PtCl}_6/\text{K}_2\text{PtCl}_4$. When K_2PtCl_4 was used as the only Pt precursor (*i.e.*, $\text{H}_2\text{PtCl}_6/\text{K}_2\text{PtCl}_4=0:100$), the average particle size was around 46 nm (**Figure 4.1.5a**), which is less than half of size of the sample prepared under the typical condition. When a small amount of H_2PtCl_6 was fed together with K_2PtCl_4 (*i.e.*, $\text{H}_2\text{PtCl}_6/\text{K}_2\text{PtCl}_4=10:90$), the average particle size became 90 nm (**Figure 4.1.5b**). When I increased the molar ratio of $\text{H}_2\text{PtCl}_6/\text{K}_2\text{PtCl}_4$ from 20:80 to 40:60, the average particle size was further increased to 110 nm and well-defined mesoporous architectures were developed on the particle surface (**Figure 4.1.5c-d**). It is noted that further increasing the molar ratio of $\text{H}_2\text{PtCl}_6/\text{K}_2\text{PtCl}_4$ to 90:10 or 100:0, the reaction cannot take place at 40 °C. Therefore, I increased the temperature to 45 °C, resulting in the formation of mesoporous bimetallic PdPt spheres with the average size of 150 nm and 176 nm, respectively (**Figure 4.1.5e-f**). Even though the molar ratios of $\text{H}_2\text{PtCl}_6/\text{K}_2\text{PtCl}_4$ were varied, the obtained mesopores sizes were almost constant, which is also an evidence for the formation of surfactant-directed mesopores.

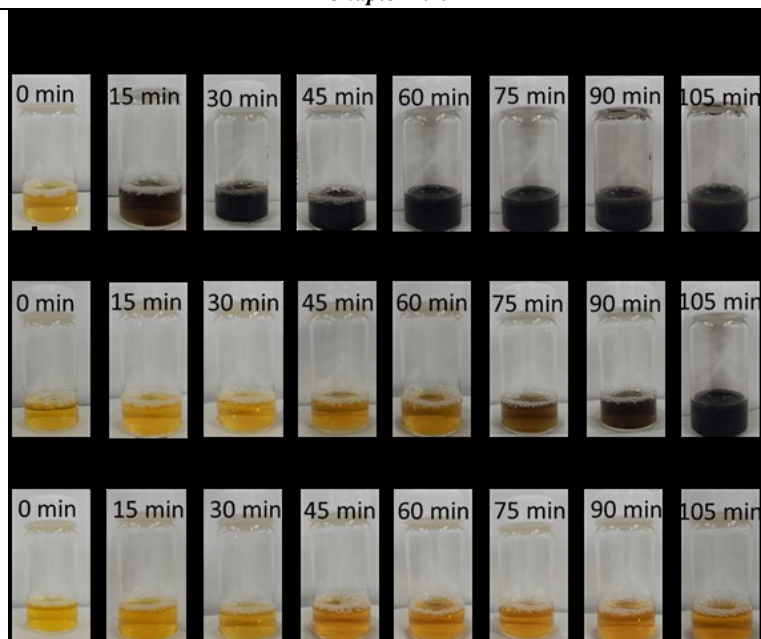


Figure 4.1.6 Photographs of colloidal suspensions taken at different reaction times at 40 °C ((a) $\text{H}_2\text{PtCl}_6/\text{K}_2\text{PtCl}_4=0:100$, (b) $\text{H}_2\text{PtCl}_6/\text{K}_2\text{PtCl}_4=60:40$ and (c) $\text{H}_2\text{PtCl}_6/\text{K}_2\text{PtCl}_4=100:0$, respectively).

To further discuss the above particle size control, the reduction rates were visibly monitored (**Figure 4.1.6**), in which changing the reaction solutions to black means the metal deposition. When the K_2PtCl_4 was used as precursor, the colour of reaction solution was changed from initial yellow to black in 30 min. While we used both K_2PtCl_4 and H_2PtCl_6 as precursors, the solution colour gradually changed from yellow to black till 75 min. When only the H_2PtCl_6 as used as precursor, the solution colour did not change from yellow to black at 40 °C. From above results, I proposed that the addition of H_2PtCl_6 slowed the reduction rate of the metal specie. Considering reduction behaviours of two Pt complexes ($[\text{PtCl}_4]^{2-}/\text{Pt}$: +0.76 V vs. SHE and $[\text{PtCl}_6]^{2-}/[\text{PtCl}_4]^{2-}$: +0.68 V vs. SHE), it is understandable that $[\text{PtCl}_6]^{2-}$ ions have a lower tendency toward reduction than $[\text{PtCl}_4]^{2-}$ ions. Therefore, by replacing K_2PtCl_4 with H_2PtCl_6 , the deposition rate greatly delays. In general, a balance between nucleation and crystal growth determines the final size of the particles in the products. In the present system, the dissolved Pt and Pd species are reacted with ascorbic acid (AA) at initial stage. Then, the nuclei are generated and grew further by interaction of the dissolved metal species with AA to form the final products. The slow reduction rate plays a key role in achieving the Pt growth on the Pd nucleus. Therefore, with a decrease in the reduction rate of metal species by addition of H_2PtCl_6 , the number of nuclei formed at the early stage is thought to be decreased. These nuclei serve as seeds and undergo further crystal growth to afford the final products with larger particle size.

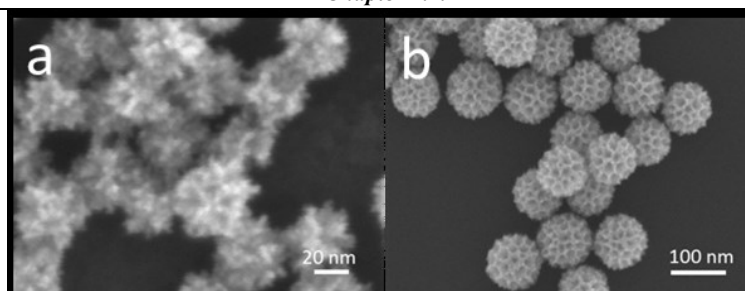


Figure 4.1.7 SEM images of samples prepared (a) without HCl and (b) with HCl.

Ascorbic acid is used as a reducing agent, and is oxidized according to the following equilibrium equation: $C_6H_8O_6 \leftrightarrow C_6H_6O_6 + 2H^+ + 2e^-$. Thus, in principle the reduction capacity of AA can be decreased by precise control of pH. Hydrochloric acid (HCl) can decrease of reduction capacity of AA for retarding reduction of metal precursors, which favours for ordered mesoporous spheres. In the present reaction system, I used the optimized amount of HCl to control the crystal growth rate. **Figure 4.1.7** shows that the morphology of the obtained particles prepared both in the presence and absence of HCl.

Overall, the controls of F127 concentration and compositional ratios of H_2PtCl_6 and K_2PtCl_4 as Pt precursors, and the use of HCl are responsible for mono-dispersed mesoporous PdPt spheres with uniform particle sizes. Even when the total amounts of Pt and Pd precursors are increased two times higher than the typical condition (*i.e.*, the compositional ratios of Pt and Pd precursors are constant.), the pore sizes and the particle sizes are not changed, indicating the present method has a great potential to large-scale production for industrial applications.

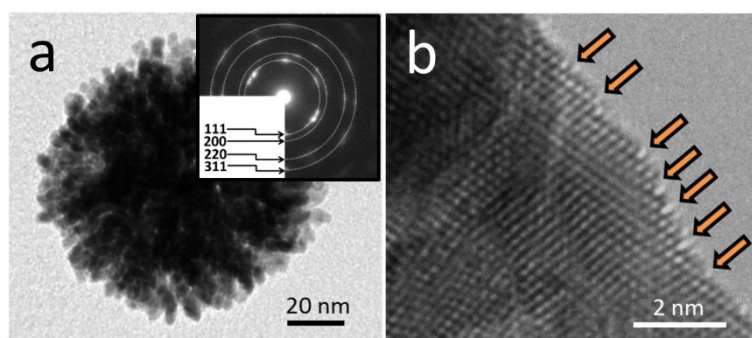


Figure 4.1.8 (a) TEM and (b) HRTEM images of the typical mesoporous bimetallic PdPt spheres. The kink and step sites are indicated by arrows. The SAED patterns obtained from an individual sphere are shown in an inset image in panel (a).

Many previous studies have proved that high crystallized Pt, especially the Pt surface with kink and step sites, exhibit high activity in the electrocatalysis. Therefore, the crystallinity of mesoporous bimetallic PdPt

spheres was studied by high-resolution transmission electron microscope (TEM). The TEM image of an individual mesoporous bimetallic PdPt sphere reveals the mesoporous structure inside the particle, judging from the significantly different contrast (**Figure 4.1.8**). Unlike mesoporous silica and carbon,^[17] the electron beam cannot pass through the metallic sample. Therefore, it is hard to clearly visualize the mesoporous structure over the entire area. As seen in **Figure 4.1.8a**, the mesopore walls are built by a large quantity of connected nanoparticles. Interestingly, the lattice fringes corresponding to the Pt crystal are coherently extended across over several particles, indicating that the mesopore walls have a good crystallinity. A grain size of ca. 7.4 nm was calculated from the (111) diffraction peak based on the Scherrer equation,^[18] indicating that each mesoporous bimetallic PdPt sphere consisted of a multitude of grain particles. Selected-area electron diffraction (SAED) patterns of an individual sphere (inset of **Figure 4.1.8a**) showed polycrystalline reflections indexed to (111), (200), (220), and (311) of the *fcc* crystal, which suggested that the nanosphere was constructed by randomly aggregated small grain particles rather than oriented growth. Some atomic edge and kink sites caused by unsaturated Pt coordination atoms can be observed on the atomic Pt surface, which is highly valuable for high electrocatalytic performance (**Figure 4.1.8b**).^[19]

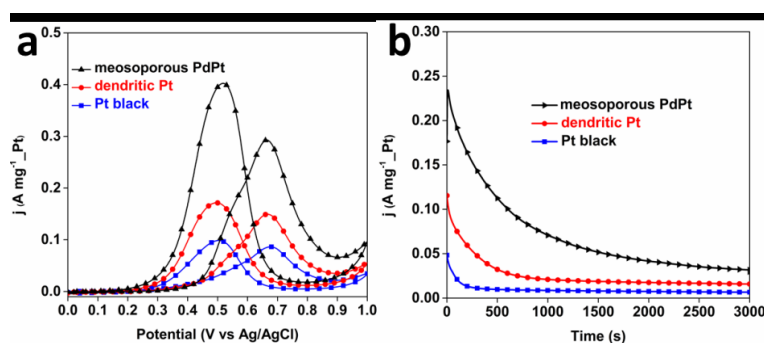


Figure 4.1.9 (a) Cyclic voltammograms and (b) Chronoamperometric curves (recorded at 0.6 V) for MOR catalyzed by different catalysts in 0.5 M H_2SO_4 containing 0.5 M methanol.

The electrochemically active surface area (ECSA) of as-prepared samples can be estimated by measuring the total charge passed during the hydrogen adsorption-desorption. The specific ECSAs of the mesoporous bimetallic PdPt spheres, dendritic Pt nanoparticles^[20] and PtB are 29.9, 19.9, and 13.5 $\text{m}^2 \text{g}^{-1}$, respectively. To evaluate the electrocatalytic activity of the samples, methanol oxidation reaction (MOR) was selected as a probe reaction. The cyclic voltammetric (CV) measurement was carried out in 0.5 M H_2SO_4 containing 0.5 M methanol to investigate the activities of mesoporous bimetallic PdPt spheres. The CV curves (**Figure 4.1.9a**) showed the typical features of methanol oxidation on Pt surface. Mesoporous bimetallic PdPt spheres (0.298 $\text{A} \cdot \text{mg}^{-1}$ Pt) exhibited better catalytic performance than those of dendritic Pt spheres (with small-sized and

disordered mesopores) ($0.152 \text{ A}\cdot\text{mg}^{-1}\text{Pt}$), and commercial PtB ($0.087 \text{ A}\cdot\text{mg}^{-1}\text{Pt}$). As well known, pure Pd element is little effective toward MOR in acidic electrolyte. As mentioned above, because of highly miscible of the Pd and Pt atoms, the pseudo Pt-Pd alloy structure should be formed at the internal surface of mesoporous PdPt spheres, which is favourable for reducing the electronic binding energy in Pt and improving catalytic activity.^[21] As a result, the mesoporous bimetallic PdPt spheres exhibited a higher activity compared to dendritic Pt and PtB catalysts. Even when the activity was normalized by ECSAs, mesoporous PdPt ($0.997 \text{ mA cm}^{-2}\text{Pt}$) samples still exhibited higher activity than that of dendritic Pt ($0.764 \text{ mA cm}^{-2}\text{Pt}$) nanoparticles and PtB ($0.643 \text{ mA cm}^{-2}\text{Pt}$). A probable reason for the superior activity is a large amount of kink and step sites created on the mesoporous surfaces (**Figure 4.1.9b**). This benefits to breaking C-H bonds in methanol decomposition, thereby an improved catalytic performance was observed in MOR.^[22]

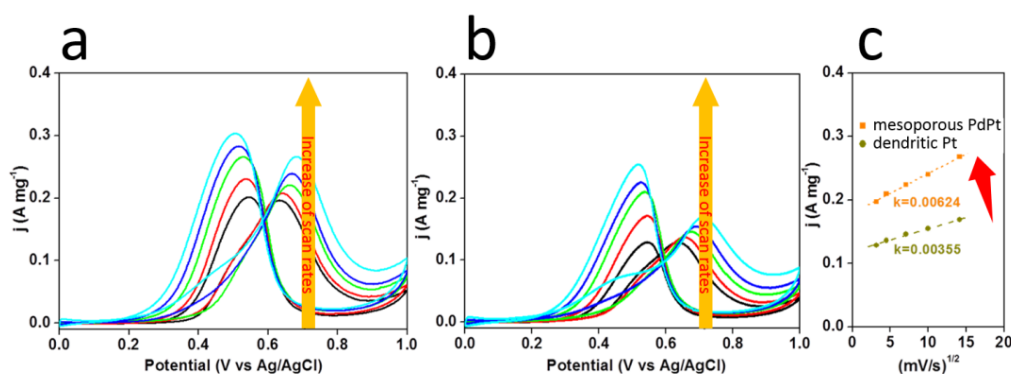


Figure 4.1.10. Cyclic voltammograms of (a) mesoporous PdPt spheres (with large-sized pores) and (b) dendritic Pt catalyst (with small-sized pores) at scan rate of 10, 20, 50, 100, 200 mV s^{-1} . (c) the relationship of forward oxidation peak current density vs. scan rate for the mesoporous PdPt sphere and dendritic Pt catalyst.

Another important reason for improving the electrochemical activity is that the ultra-large mesoporous structure can accelerate the transport for reactants and products. As shown in **Figure 4.1.10** in proportion to the scan rate, the forward oxidation peak current densities of mesoporous PdPt spheres and dendritic Pt spheres are increased linearly with the square root of the scan rate, suggesting that the oxidation of methanol at electrodes is a diffusion-controlled process. The slope of mesoporous PdPt spheres is significantly larger than that of dendritic Pt spheres, revealing that the diffusion efficiency of methanol molecules inside large-sized pores is higher than that inside small-sized and dendritic pores.^[23] As an effective catalyst, the stability is a very important factor for MOR. Thus, the stability of catalysts were also investigated by chronoamperometric measurement at 0.6 V for 3000 s in 0.5 M H_2SO_4 containing 0.5 M CH_3OH . It is obvious that our mesoporous catalysts possess excellent stability during the electrochemical measurement, in comparison to dendritic Pt

spheres and commercial PtB catalyst (**Figure 4.1.9b**) in a long period of 3000 s.

4.1.4. Conclusion

In summary, we have successfully developed a facile synthetic method for preparation of multimetallic mesoporous spheres with ultra-large mesopores. In the synthesis, the concentration of F127, and reduction kinetics of metal species are critical to formation of uniform ultra-large mesoporous structure. Because of the high surface area, large-sized mesopores, the mesoporous spheres exhibit enhanced electrochemical activity for MOR. This present approach, based on a green and environment-friendly process in dilute surfactant solution, could be extended to the synthesis of other metal and alloy system with ultra-large mesopores for high-performance catalysts and also will be used as a promising approach for large-scale industrial production.

References

- [1] (a) S. Wang, Q. Zhao, H. Wei, J. Q. Wang, M. Cho, H. S. Cho, O. Terasaki, Y. Wan, *J. Am. Chem. Soc.*, 2013, **135**, 11849; (b) J. Ma, L. Xu, L. Xu, H. Wang, S. Xu, H. X. Li, S. Xie, H. Li, *ACS Catal.*, 2013, **3**, 985; (c) C. Fang, Y. H. Lee, L. Shao, R. Jiang, J. Wang, Q. H. Xu, *ACS Nano*, 2013, **7**, 9354; (d) C. Koenigsmann, E. Sutter, T. A. Chiesa, R. R. Adzic, S. S. Wong, *Nano Lett.*, 2012, **12**, 2013; (e) P. C. Angelomé, H. H. Mezerji, B. Goris, I. P. Santos, J. Pérez-Juste, S. Bals, L. M. Liz-Marzán, *Chem. Mater.*, 2012, **24**, 1393.
- [2] H. Ataee-Esfahani, L. Wang, Y. Nemoto, Y. Yamauchi, *Chem. Mater.*, 2010, **22**, 6310.
- [3] Y. Jia, Y. Jiang, J. Zhang, L. Zhang, Q. Chen, Z. Xie, L. Zheng, *J. Am. Chem. Soc.*, 2014, **136**, 3748.
- [4] L. Wang, Y. Yamauchi, *J. Am. Chem. Soc.*, 2013, **135**, 16762.
- [5] H. Li, H. Lin, Y. Hu, H. Li, P. Li, X. Zhou, *J. Mater. Chem.* **2011**, *21*, 18447.
- [6] H. H. Li, S. Zhao, M. Gong, C. H. Cui, D. He, H. W. Liang, L. Wu, S. H. Yu, *Angew. Chem. Int. Ed.*, 2013, **52**, 7472.
- [7] H. Liao, Y. Hou, *Chem. Mater.*, 2013, **25**, 457.
- [8] (a) H. J. Shin, R. Ryoo, Z. Liu, O. Terasaki, *J. Am. Chem. Soc.*, 2001, **123**, 1246; (b) G. S. Attard, P. N. Bartlett, N. R. B. Coleman, J. M. Elliott, J. R. Owen, J. H. Wang, *Science* 1997, **278**, 838; (c) G. S. Attard, C. G. Goltner, J. M. Corker, S. Henke, R. H. Templer, *Angew. Chem. Int. Ed.* 1997, **36**, 1315.
- [9] (a) L. Wang, Y. Yamauchi, *Chem. Mater.*, 2009, **21**, 3562; (b) L. Wang, Y. Yamauchi, *J. Am. Chem. Soc.*, 2009, **131**, 9152; (c) H. Ataee-Esfahani, M. Imura, Y. Yamauchi, *Angew. Chem. Int. Ed.*, 2013, **52**, 13611.
- [10] (a) C. Li, T. Sato, Y. Yamauchi, *Angew. Chem. Int. Ed.* 2013, **52**, 8050; (b) S. M. Alia, G. Zhang, D. Kisailus, D. Li, S. Gu, K. Jensen, Y. Yan, *Adv. Funct. Mater.*, 2010, **20**, 3742; (c) Q. Li, P. Xu, B. Zhang, G. Wu, H. Zhao, E. Fu, H. L. Wang, *Nanoscale*, 2013, **5**, 7397; (d) S. Yang, X. Luo, *Nanoscale*, 2014, **6**, 4438.
- [11] B. Lim, M. J. Jiang, P. H. C. Camargo, E. C. Cho, J. Tao, X. M. Lu, Y. M. Zhu, Y. N. Xia, *Science*, 2009, **324**, 1302.
- [12] (a) Y. Kim, Y. Noh, E. J. Lim, S. Lee, S. M. Choi, W. B. Kim, *J. Mater. Chem. A*, 2014, **2**, 6976; (b) Z. Peng, H. Yang, *J. Am. Chem. Soc.*, 2009, **131**, 7542; (c) C. Xu, Q. Hao, H. Duan, *J. Mater. Chem. A*, **2014**, *2*, 8875; d) L. Sun, Z. Zhang, B. Xu, X. Wang, *Chem. Asian J.*, 2013, **8**, 1523.
- [13] (a) Y. Park, Y. W. Lee, S. W. Kang, S. W. Han, *Nanoscale*, 2014, **6**, 9798; (b) S. W. Kang, Y. W. Lee, Y. Park, B. S. Choi, J. W. Hong, K. H. Park, S. W. Han, *ACS Nano*, 2013, **7**, 7945.
- [14] (a) T. Wang, X. Meng, P. Li, S. Ouyang, K. Chang, G. Liu, Z. Mei, J. Ye, *Nano Energy*, 2014, **9**, 50; (b) T. W. Kim, R. Ryoo, M. Kruk, K. P. Gierszal, M. Jaroniec, S. Kamiya, O. Terasaki, *J. Phys. Chem. B*, 2004, **108**, 11480.
- [15] (a) Y. Wan, D. Zhao, *Chem. Rev.*, 2007, **107**, 2821; (b) C. Yang, H. Sui, X. Li, J. Han, X. Luo, H. Zhang, H. Sun, H. Sun, Y. Zhou, B. Yang, *CrystEngComm*, 2013, **15**, 3490; (c) H. Ataee-Esfahani, J. Liu, M. Hu, N. Miyamoto, S.

- Tominaka, K. C. W. Wu, Y. Yamauchi, *Small*, 2013, **9**, 1047.
- [16] (a) Ö. Çelik, Ö. Dag, *Angew. Chem. Int. Ed.* 2001, **40**, 3799; (b) K. Suzuki, K. Ikari, H. Imai, *J. Am. Chem. Soc.* **2003**, **126**, 462; (c) C. Li, T. Sato, Y. Yamauchi, *Chem. Commun.*, 2014, **50**, 11753.
- [17] (a) Y. Wan, H. Wang, Q. Zhao, M. Klingstedt, O. Terasaki, D. Zhao, *J. Am. Chem. Soc.*, 2009, **131**, 4541; (b) Y. Ma, L. Han, K. Miyasaka, P. Oleynikov, S. Che, O. Terasaki, *Chem. Mater.*, 2013, **25**, 2184; (c) T. Y. Yang, J. Liu, R. F. Zhou, Z. G. Chen, H. Y. Xu, S. Z. Qiao, M. J. Monteiro, *J. Mater. Chem. A*, 2014, **2**, 18139; (d) S. B. Hartono, T. P. Phuoc, M. Yu, Z. Jia, M. J. Monteiro, S. Z. Qiao, C. Z. Yu, *J. Mater. Chem. B*, 2014, **2**, 718.
- [18] S. V. Bagul, S. D. Chavhan, R. Sharma, *J. Phys. Chem. Solids.*, 2007, **68**, 1623.
- [19] (a) X. Huang, Z. Zhao, J. Fan, Y. Tan, N. Zheng, *J. Am. Chem. Soc.*, 2011, **133**, 4718; (b) H. Wang, L. Wang, T. Sato, Y. Sakamoto, S. Tominaka, K. Miyasaka, N. Miyamoto, Y. Nemoto, O. Terasaki, Y. Yamauchi, *Chem. Mater.*, 2012, **24**, 1591.
- [20] C. Li, M. Imura, Y. Yamauchi, *Phys. Chem. Chem. Phys.*, 2014, **16**, 8787.
- [21] M. Yamauchi, H. Kobayashi, H. Kitagawa, *ChemPhysChem*, 2009, **10**, 2566.
- [22] (a) B. Y. Xia, H. B. Wu, X. Wang, X. W. Lou, *Angew. Chem. Int. Ed.*, 2013, **52**, 12337; (b) T. Yu, D. Y. Kim, H. Zhang, Y. Xia, *Angew. Chem. Int. Ed.*, 2011, **50**, 2773; (c) H. Zhang, M. Jin, Y. Xia, *Angew. Chem. Int. Ed.*, 2012, **51**, 7656. d) G. A. Somorjai, D. W. Blakely, *Nature*, 1975, **258**, 580.
- [23] (a) L. Tang, Y. Wang, Y. Li, H. Feng, J. Lu, J. Li, *Adv. Funct. Mater.*, 2009, **19**, 2782; (b) L. Dong, R. R. S. Gari, Z. Li, M. M. Craig, S. Hou, *Carbon*, 2010, **48**, 781; (c) D. Wen, A.-K. Herrmann, L. Borchardt, F. Simon, W. Liu, S. Kaskel, A. Eychmüller, *J. Am. Chem. Soc.*, 2014, **136**, 2727; (d) E. A. Franceschini, M. M. Bruno, F. J. Williams, F. A. Viva, H. R. Corti, *ACS Appl Mater & Inter.*, 2013, **5**, 10437.

4.2. Morphosynthesis of Nanoporous Pseudo Pd@Pt Bimetallic Particles with Controlled Electrocatalytic Activity

4.2.1. Introduction

Fuel cells technology is being developed as a clean and efficient energy alternative to fossil fuels.^[1] Up to now, platinum (Pt) is one of the most effective electrocatalysts to facilitate the oxidation reaction of various fuel molecules (*e.g.* methanol,^[2] ethanol,^[3] and formic acid^[4]) as well as the reduction reaction of oxygen.^[5] However, some significant challenges associated with the use of pure Pt, including the high cost, the slow kinetics of cathode reaction, and self-poisoning by intermediates, still hinder the commercialization of fuel cell technology. Therefore, it is urgent to design better Pt-based electrocatalysts and improve their overall catalytic performance by solving these issues. Pioneering works revealed that the activity of Pt can be enhanced by atomic level control of the composition, morphology, and surface structure.^[6] Additionally, by combining Pt with less expensive metals, it is possible to reduce the Pt content while increasing its intrinsic activity *via* the modification of the electronic structure of Pt surface atoms.^[7] Along this direction, significant effort has been made for the synthesis of bimetallic Pt-based nanocrystals (*e.g.*, PtPd,^[8] PtCo,^[9] PtNi,^[10] PtAu,^[11] and PtCu^[12]).

Especially, the core-shell metallic nanostructures with a large spectrum of compositions represent an emerging class of catalysts, because their properties can be effectively adjusted by manipulation of compositions and/or nanostructural features.^[13] Among metallic core-shell structures, Pd@Pt bimetallic nanostructures have attracted increasing interest because Pd has unique advantages compared with other metals, including relatively low cost, good resistance to CO poisoning and low lattice mismatch with Pt (only 0.77%).^[14] Several synthetic methods have been developed to synthesize bimetallic Pt-Pd colloids, such as seed-mediated method,^[15] solvothermal method,^[16] galvanic replacement,^[17] and co-reduction method.^[18] Nevertheless, these methods often require multiple steps and take specialized synthetic techniques, that make them challenging scale up. Although a few papers describing a one-step method to synthesize Pd@Pt nanocrystals has been reported, most of previously reported Pd@Pt nanostructures have nonporous shells, which limit the function of the core-shell structures. Considering the unique structures of porous nanocrystals (*e.g.*, high surface area, three-dimensional molecular accessibility, and the large number of edge atoms), nanoporous Pd@Pt bimetallic particles are expected to further enhance electrocatalytic performance and improve the Pt utilization efficiency.

In this work, I describe a facile and one-step method for preparation of nanoporous pseudo Pd@Pt bimetallic particles. The morphologies of Pd@Pt particles with diverse compositions and particle sizes can be varied

from the spheres to cubes by changing the molar ratios of Pd/Pt species. By optimizing the compositions of Pd_x@Pt_{100-x} particles (x means the molar percentage of Pd, confirmed by inductively coupled plasma mass spectroscopy (ICP-MS) analysis), I found that the Pd₂₇@Pt₇₃ particles exhibit the best catalytic activity toward methanol oxidation reaction (490 mA mg⁻¹ Pt). The previous study has demonstrated that the core-shell Pd@Pt nanoparticle can be achieved by co-reduction of Pd and Pt precursors, but this route lacks systematic controls over shapes, sizes, and compositions.^[19] Here I demonstrate the ligand effect to manipulate the reduction rate and the selective adsorption of certain facets by using bromide ions for preparing shape-, size- and composition-controlled nanoporous core-shell Pd@Pt particles. I believe that this method provides a general approach for the shape- and composition-controlled synthesis of nanoporous core-shell Pt-based particles.

4.2.2. Experimental Sections

4.2.2.1. Materials

All chemicals and solvents were used as received without further purification. H₂PtCl₆, Na₂PdCl₄ ascorbic acid (AA), H₂SO₄, and methanol were purchased from Nacalai Tesque, Inc. (Kyoto, Japan). Commercial Pt black, PtC-20%, Pluronic F127 and potassium bromide (KBr) were obtained from Sigma-Aldrich. All solutions were prepared with deionized water treated with a Millipore water purification system (Millipore Corp.).

4.2.2.2. Preparation of Nanoporous Pd@Pt Nanospheres

In a typical synthesis, 0.6 mL of Na₂PdCl₄ (20.0 mM) and 1.8 mL of H₂PtCl₆ (20.0 mM) solution were added to 5.0 mL of deionized water that contained 100 mg Pluronic F127 and 300 mg KBr. Then, 4.0 mL ascorbic acid (0.1 M) was added to this solution. After that, the mixed solution was kept in an oil bath for 4 h at 70 °C. During the reaction time, the solution color gradually changed from brown into black. After cooling to room temperature, the product was washed with a mixture of water and ethanol by centrifuging at 14,000 rpm for 20 min. The washing step was repeated for 6 times. The samples were kept in ethanol for further use and were dried prior to electrochemical characterization at room temperature. Different compositions of Pd@Pt were obtained using the same process but with the different molar ratios of Pd/Pt in precursor, as shown in **Table 4.2.1**.

4.2.2.3. Characterization

Scanning electron microscopy (SEM) imaging was carried out using a Hitachi SU-8000 microscope operated at 5 kV. Transmission electron microscopy (TEM) and high-angle annular dark-field scanning TEM (HAADF-STEM) observations were performed using a JEOL JEM-2100F operated at 200 kV equipped with an energy-dispersive spectrometry analyzer. The samples for TEM characterizations were prepared by depositing a drop of the diluted colloidal suspension on a grid. Wide-angle powder X-ray diffraction (XRD) spectra were acquired with a Rigaku Rint 2500 diffractometer with monochromated Cu KR radiation. Low-angle XRD spectra were obtained by using a NANO VIEWER (Rigaku, Japan) equipped with a Micro Max-007 HF high-intensity micro-focus rotating anode X-ray generator. X-ray photoelectronic spectroscopy (XPS) spectra were obtained at room temperature by using a JPS-9010TR (JEOL) instrument with an Mg K α X-ray source. All the binding energies were calibrated via referencing to C 1 s binding energy (284.6eV).

4.2.2.4. Electrochemical Test

Cyclic voltammograms (CV) and chronoamperometric (CA) experiments were performed using a CHI 842B electrochemical analyzer (CHI Instruments, USA). A conventional three-electrode cell was used, including an Ag/AgCl (saturated KCl) reference electrode, a platinum wire as a counter electrode, and a modified glassy carbon electrode (GCE, 3 mm in diameter) as a working electrode. The modified GCE was coated with the sample (5.0 μ g) and dried at room temperature. Then, 5.0 μ L of Nafion (0.05 wt %) was coated on the surface of the modified GCE and dried before electrochemical experiments. Prior to the electrochemical measurements, the GCE modified with the as-prepared sample was electrochemically activated by a potential cycling between -0.2 V and +1.5 V (vs. Ag/AgCl) in 0.5 M H₂SO₄ until the obtained CVs became characteristic of a clean Pt electrode. Methanol electro-oxidation measurements were performed in a solution of 0.5 M H₂SO₄ containing 0.5 M methanol at a scan rate of 50 mV s⁻¹. The chronoamperometric measurement was carried out at a constant potential of 0.6 V for 3000 s.

4.2.3. Results and Discussion

Table 4.2.1 The molar ratios of the precursors and products and their parameters.

Samples	Molar ratio of Pd/Pt in the precursors	Molar ratio of Pd/Pt in the products	Average pore-to-pore distance (nm)	Average particle sizes (nm)

Pd ₂₁ @Pt ₇₉	17/83	21/79	16.4	82
Pd ₂₇ @Pt ₇₃	25/75	27/73	16.4	79
Pd ₃₈ @Pt ₆₂	33/67	38/62	16.4	70
Pd ₅₅ @Pt ₄₅	50/50	55/45	18.8	65

The morphology of nanoporous Pd@Pt particles was characterized by scanning electron microscope (SEM). The low-magnification SEM images (**Figure 4.2.1a1-d1**) show highly dispersed Pd@Pt particles with a narrow particle size distribution. The high-magnification SEM images (**Figure 4.2.1a2-d2**) clearly reveal that all the obtained samples are highly porous and the observed nanopores are uniformly distributed over entire of the external surface. The periodicity of the nanoporous architectures was further studied by low-angle X-ray diffraction (XRD). As shown in **Figure 4.2.2a**, one sharp peak was clearly observed for all the samples, indicating the periodicity of the nanoporous structures. The pore-to-pore distances calculated from the peak centers show similar values, although a very small deviation of *ca.* 2 nm is seen in **Table 4.2.1**.

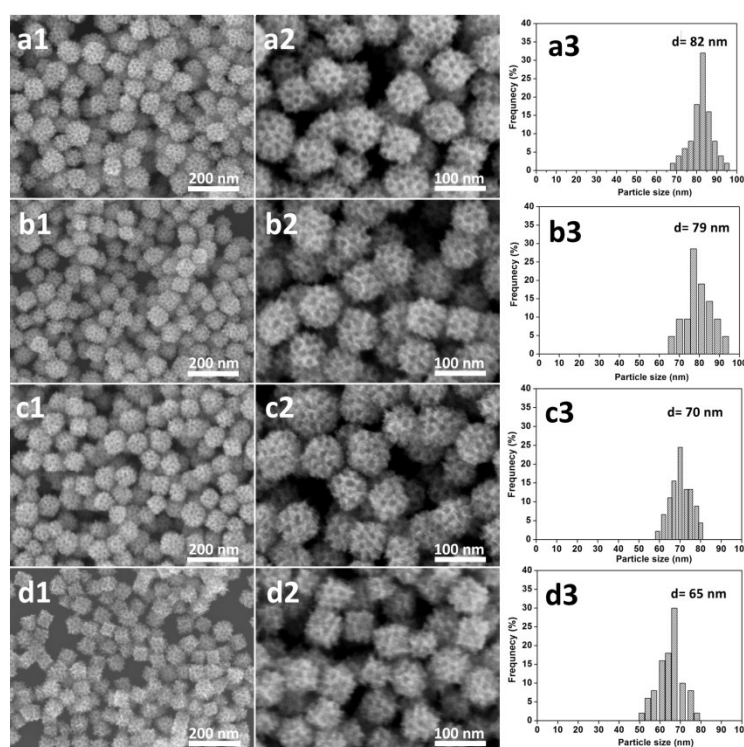


Figure 4.2.1 Low- and high-magnification SEM images and the particle size distributions of nanoporous of the a) Pd₂₁@Pt₇₉, b) Pd₂₇@Pt₇₃, c) Pd₃₈@Pt₆₂, and d) Pd₅₅@Pt₄₅ particles.

The SEM images of the samples also show that the morphologies of the Pd@Pt particles are dependent on the precursor compositions. Specifically, when the reactions were carried out with a low concentration of Pd precursor (e.g., molar ratio of Pd/Pt=17/83, 25/75, or 33/67), shape of the sample was dominant in the spheres (**Figure 4.2.1a1-c1**). As the Pd/Pt ratio increased to Pd/Pt=50/50, nanoporous particles with cubic shapes were obtained (**Figure 4.2.1d1**). Interestingly, the average particle sizes of as-prepared samples decreased from 82 nm to 79 nm, 70 nm, and 65 nm with increasing the Pd molar ratio in the feeding solutions (**Figure 4.2.1a3-d3**), as summarized in **Table 4.2.1**. As discussed later, the reduction of Pd species are more easily and preferentially performed over that of Pt species and then the Pd nuclei served as seeds for the subsequent deposition of Pt. Increasing the amount of Pd species should definitely increase the number of nuclei at the beginning of the reaction, which would result in the smaller particles.^[20]

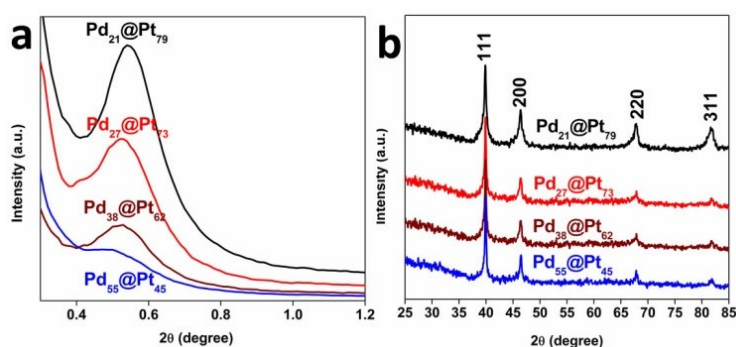


Figure 4.2.2 (a) Low-angle and b) wide-angle XRD patterns of nanoporous Pd₂₁@Pt₇₉, Pd₂₇@Pt₇₃, Pd₃₈@Pt₆₂, and Pd₅₅@Pt₄₅ particles prepared by changing the molar ratio of the Pd/Pt precursors.

The exact compositions of the samples were confirmed by ICP-MS, and the exact compositions in the precursor solutions and the final products were listed in **Table 4.2.1**. The crystalline structure of these nanoporous Pd@Pt samples was examined by wide-angle X-ray diffraction (XRD) (**Figure 4.2.2b**). Four representative diffraction peaks were observed in the XRD patterns, corresponding to the (111), (200), (220), and (311) planes of a face centered cubic (*fcc*) structure. However, it is very difficult to resolve Pt and Pd crystals in the wide-angle XRD patterns owing to the similarity of crystalline structures between Pt and Pd.^[14a]

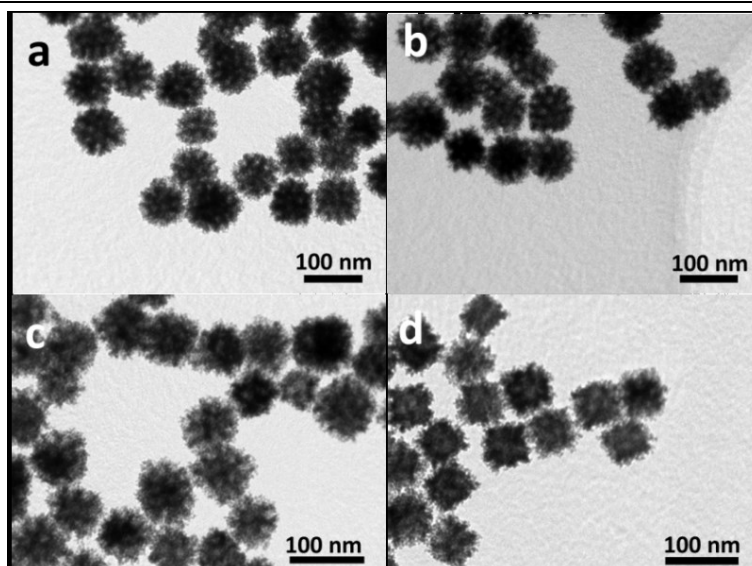


Figure 4.2.3 TEM images of the nanoporous (a) Pd₂₁@Pt₇₉, (b) Pd₂₇@Pt₇₃, (c) Pd₃₈@Pt₆₂, and (d) Pd₅₅@Pt₄₅ particles.

The morphologies and nanoporous structures of the Pd@Pt particles were studied by transmission electron microscopy (TEM). **Figure 4.2.3** reveals that the obtained products are highly dispersed and they possess complete nanoporous structure, which is favorable for improving the active surface area. The Pd₅₅@Pt₄₅ sample possesses a large Pd core and less porosity compared with the Pd₂₁@Pt₇₉, Pd₂₇@Pt₇₃ and Pd₃₈@Pt₆₂ samples, which is probably due to the preferred formation of Pd nanocube cores in the presence of the bromide species, as discussed later.

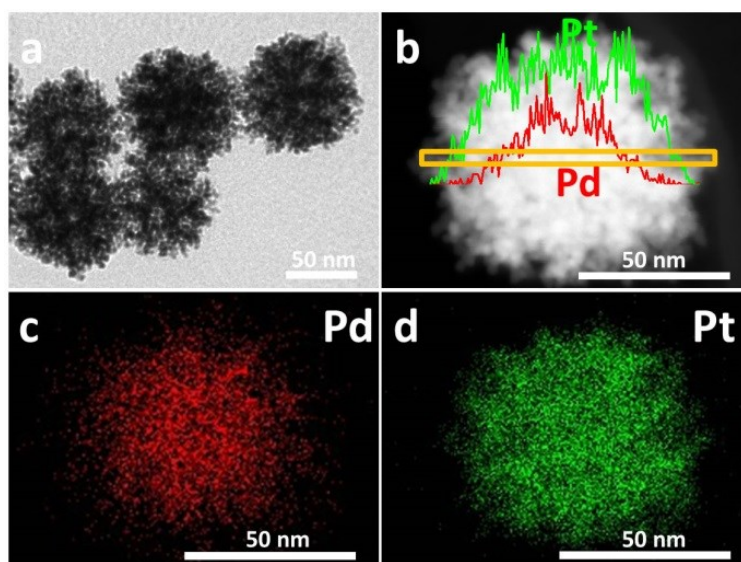


Figure 4.2.4 (a) TEM, (b) HAADF-STEM, and (c-d) elemental mapping images of the nanoporous Pd₂₇@Pt₇₃ particles. Inset image in the panel (b) shows the cross-sectional compositional line profile of one nanoporous Pd₂₇@Pt₇₃ particle.

Figure 4.2.4a shows that the Pd₂₇@Pt₇₃ particle is composed of a large number of tiny interconnected particles.

In order to understand the distribution of Pd and Pt in the particle and confirm the core-shell structure, elemental mapping of the Pd₂₇@Pt₇₃ particles was investigated. As shown in **Figure 4.2.4c-d**, the elemental mapping images reveal that the Pd is concentrated at the center of particle and the Pt is uniformly distributed in the whole particle, indicating that the Pd species are preferentially reduced and used up early while the Pt species are reduced throughout the entire reaction. The line-scanning profiles (inset of **Figure 4.2.4b**) clearly reveal the distribution of both Pd and Pt elements across an individual particle, consisting of the higher Pd content at the center, which is in agreement with the elemental mapping results.

In addition, the element mapping of other obtained Pd₂₁@Pt₇₉, Pd₃₈@Pt₆₂, and Pd₅₅@Pt₄₅ particles were also investigated, showcasing the content of the Pd core gradually increases by increasing the molar ratios of Pd/Pt precursors (**Figure 4.2.5**). These results show that Pt and Pd regions are not completely separated in the particle, which is different from complete core-shell structured materials prepared by seed-growth method.^[21] Therefore, the obtained sample in this study is defined as pseudo core-shell structures.

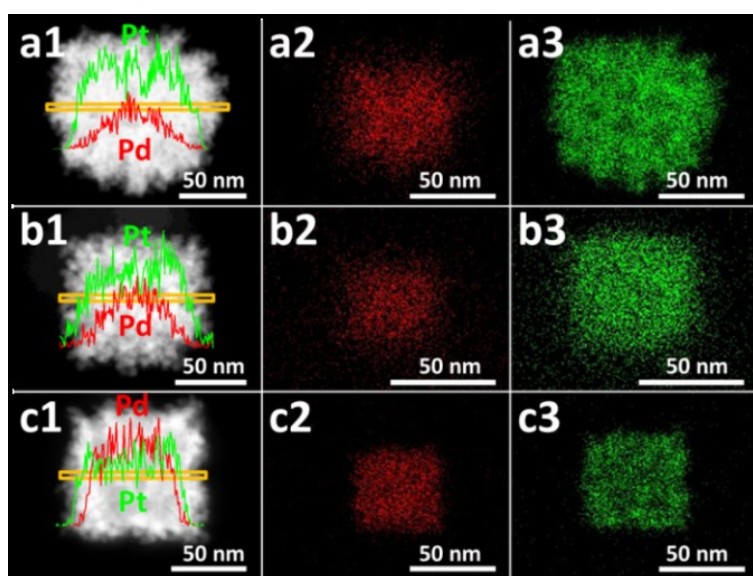


Figure 4.2.5 HAADF-STEM, and elemental mapping images of the nanoporous (a) Pd₂₁@Pt₇₉, (b) Pd₃₈@Pt₆₂, and (c) Pd₅₅@Pt₄₅ particles. Inset images in the panel (a1, b1, c1) show the corresponding cross-sectional compositional line profile.

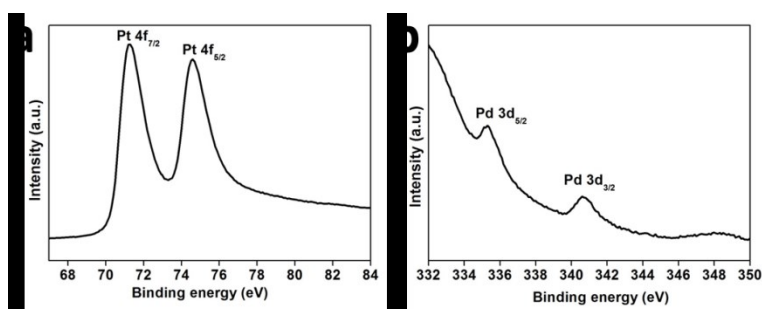


Figure 4.2.6 High resolution XPS spectra of nanoporous Pd₂₇@Pt₇₃ particles on (a) Pt 4*f* and (b) Pd 3*d*.

The surface element composition and electronic state of Pt and Pd in the samples were measured by X-ray photoelectron spectroscopy (XPS). The surface Pd/Pt molar ratio of the nanoporous Pd₂₇@Pt₇₃ particles calculated from the XPS spectra is 4/96. This value shows a remarkable contradiction with that determined by ICP measurement, indicating that the surface of the Pd₂₇@Pt₇₃ sample is rich in Pt, which agreed with elemental mapping data (**Figure 4.2.4**). The doublet peaks with binding energy of 71.2 eV and 74.6 eV are assigned to the Pt⁰ 4*f*_{7/2} and Pt⁰ 4*f*_{5/2}, respectively (**Figure 4.2.6a**). The binding energy of Pd 3*d*_{3/2} and Pd 3*d*_{1/2} located at 335.3 eV and 340.6 eV can be ascribed to metallic Pd⁰ (**Figure 4.2.6b**).

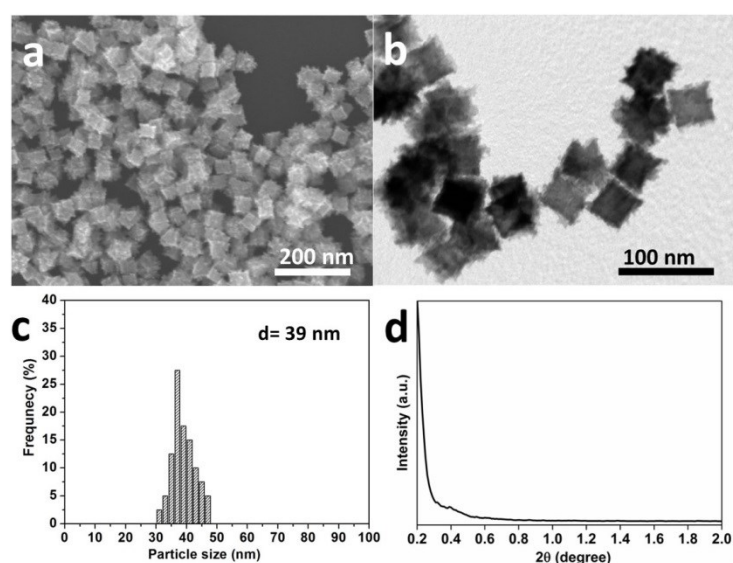


Figure 4.2.7 (a) SEM image, (b) TEM image, (c) histogram of particle size distribution, and (d) low-angle pattern of Pd₇₃@Pt₂₇ particles prepared at a molar ratio of Pd/Pt=67/33. Inset image in the panel (b) shows SAED pattern of the individual particle.

In order to understand the formation mechanism of nanoporous Pd@Pt particles, more control experiments were carried out. In this study, I found that the molar ratios of Pd/Pt precursor, and the use of surfactant F127 and bromide ions are responsible for formation of nanoporous Pd@Pt structures. In the absence of F127, non-porous products were heavily aggregated, suggesting that F127 serves as the pore-directing agent as well as protecting agent for preventing the particle aggregations.^[22] As mentioned above, the morphologies of the Pd@Pt particles with nanoporous structure can be tuned from sphere to cube by adjusting the molar ratios of Pd/Pt precursors (**Table 4.2.1**), but the pore sizes almost keep constant. However, Pd₇₃@Pt₂₇ cubes (with the average particle size of 39 nm) without any porous structures could be only obtained when a high molar ratio of Pd/Pt (*e.g.*, 67/33) is used in the feeding solution (**Figure 4.2.7**). On the other hand, when the reaction is

performed in the absence of Pd, nanoporous Pt particles are generated, which is in agreement with our previously reported results.^[23] Based on the above experimental observation, I conclude that only when the molar ratio between the Pd and Pt species reach a certain value, well-defined nanoporous Pd@Pt particles can be formed. Previous studies have demonstrated that nonionic surfactants (*e.g.* F127, Brij58) are very effective agents for synthesis of nanoporous Pt structures with uniformly sized pores, but they are not useful for nanoporous Pd structures, probably due to a weak interaction between the surfactants and the Pd species.^[24] Only cationic surfactants, such as cetyltrimethylammoniumchloride (CTAC), have been utilized to obtain nanoporous Pd structures, owing to a strong affinity between the cationic $[C_{16}TA]^+$ surfactants and the anionic $[PdCl_4]^{2-}$ species.^[25] In this study, it is also found that the formation of nanoporous Pd@Pt particles (consisting of Pd dense core and nanoporous Pt shell) is attributed to the stronger interaction between the F127 and the Pt species compared to that of the F127 and the Pd species.

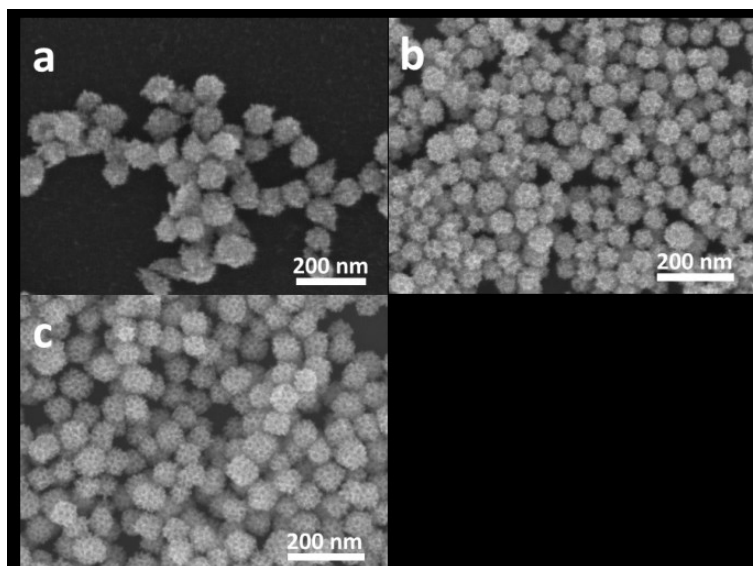


Figure 4.2.8 SEM images of Pd₂₇@Pt₇₃ particles prepared by different amount of KBr ((a) 0 mg, (b) 100 mg, and (c) 300 mg).

Various studies have demonstrated that kinetic control is critical for shape-controlled synthesis of noble-metal nanocrystals in solution phase.^[26] In this study, KBr is used to manipulate the reduction kinetics of Pd²⁺ and Pt⁴⁺ species and assist in obtaining the nanoporous Pd@Pt structure. It has been reported that $[PtCl_6]^{2-}$ and $[PdCl_4]^{2-}$ complexes can be replaced into $[PtBr_6]^{2-}$ and $[PdBr_4]^{2-}$ because Br⁻ ions have stronger coordination with Pt⁴⁺ and Pd²⁺ than Cl⁻ ions.^[27] Considering reduction potential ($[PtBr_6]^{2-}/[PtBr_4]^{2-}$: +0.61 V vs. SHE, $[PtCl_6]^{2-}/[PtCl_4]^{2-}$: +0.73 V vs. SHE, $[PdBr_4]^{2-}/Pd$: +0.49 V vs. SHE, and $[PdCl_4]^{2-}/Pd$: +0.62 V vs. SHE), it is easy to understand that the reduction rate can be greatly delayed by addition of bromide ions. Slow reaction

rate benefits for formation of nanoporous structure because it provides enough time for surfactant micelles to adhere to the metal seeds and effectively act as a template.^[19,28] As shown in **Figure 4.2.8a**, in the absence of KBr, only dendritic Pd@Pt particles were obtained owing to the fast-nucleation and fast-growth process.^[29] When a small amount of KBr (100 mg) is added, Pd@Pt particles with concave surface are obtained (**Figure 4.2.8b**). Further increasing the amount of KBr (300 mg) yields well-defined nanoporous surface of Pd@Pt particles (**Figure 4.2.8c**). Previous studies have demonstrated that bromide species can serve as a shape-directing agent by selective adsorption of the metal (100) crystal faces, inducing the formation of nanocube structure.^[30] Therefore, the cube-shaped Pd@Pt particles are obtained in the presence of high molar ratio of the Pd/Pt (*e.g.*, Pd/Pt=50/50). On the basis of these results, KBr is thought to work as reduction inhibitor as well as shape-directing agent to manipulate the nucleation, the growth rate, and the ultimate shape, and nanoporous structure.

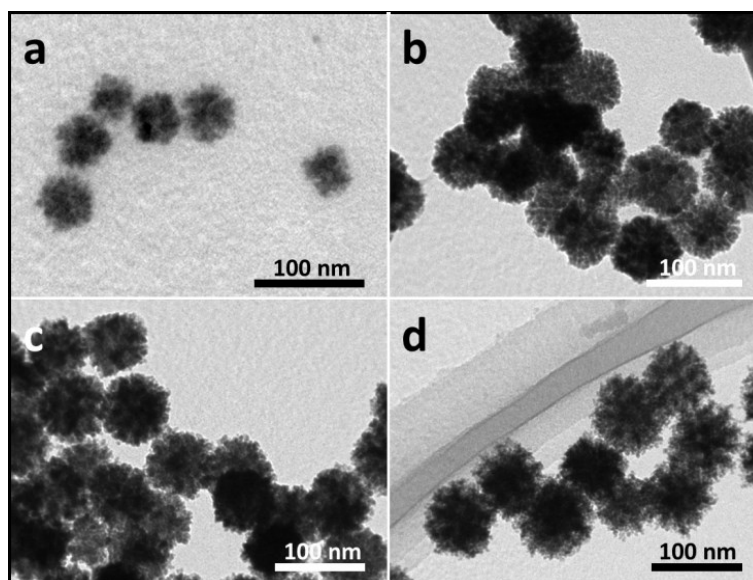


Figure 4.2.9 TEM images of Pd₂₇@Pt₇₃ samples taken at different reaction times (a) 0.5 h (b) 1.5 h (c) 2 h (d) 4 h.

To elucidate the morphological evolution of the Pd@Pt particles, the intermediates of Pd@Pt (prepared from the precursor with the molar ratio of Pd/Pt=25/75) were taken at different reaction time and then were characterized by TEM. Almost no precipitate can be observed when the reaction time is within 0.5 h. The Pd@Pt particles with average particle size of 40 nm are formed after a reaction time of 0.5 h, as shown in **Figure 4.2.9a**. Upon increasing the reaction time (1.5 h, and 2 h), the nanoporous structure becomes clearer and the particle gradually grow up to 60 nm and 70 nm, respectively (**Figure 4.2.9b-c**). Further extending the reaction time to 4 h, no significant change is observed for Pd@Pt particles in terms of sizes and shapes (**Figure 4.2.9d**). The compositions of intermediates at the different growth stages were also estimated by

energy-dispersive X-ray spectroscopy (EDX) analysis. The Pd/Pt atomic ratio of Pd@Pt intermediates is close 70/30 at initial stage (0.5 h). As the reaction proceeded 1.5 h and 2 h, the Pd/Pt atomic ratio of Pd@Pt intermediate changed from 55/46 then to 45/65. When reaction is extended to 4 h, the Pd/Pt atomic ratio in Pd@Pt particles is estimated to be round 26/73. From these results, at initial stage, the preformed Pd seeds can serve as *in-situ* nuclei for the subsequent heterogeneous deposition of Pt.^[31] As the reaction proceeds, the Pd species are used up and the Pt species continue homogeneous growth of Pt on the particles.

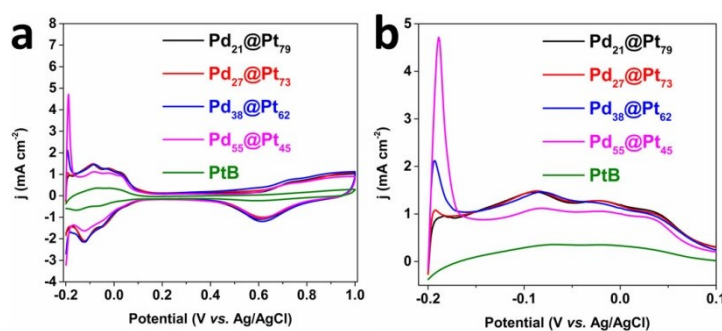


Figure 4.2.10 (a,b) CV curves of the nanoporous Pd₂₁@Pt₇₉, Pd₂₇@Pt₇₃, Pd₃₈@Pt₆₂, and Pd₅₅@Pt₄₅ particles and PtB catalyst recorded in 0.5 M H₂SO₄ solution at a scan rate of 50 mV s⁻¹. (b) Enlarged CV curves in the potential range of -0.2 to 0.1 V.

The obtained Pd@Pt particles with different molar ratios of Pd/Pt were further characterized by surface-sensitive electrochemical measurements.^[32] The Pd@Pt particles were investigated in 0.5 M H₂SO₄ solution by cyclic voltammetry, as shown in **Figure 4.2.10**. The nanoporous Pd₃₈@Pt₆₂ and Pd₅₅@Pt₄₅ samples not only exhibit typical adsorption peak of hydrogen on surface of pure Pt but also show a remarkable adsorption peak of hydrogen on the surface of pure Pd at around -0.18 V. However, this adsorption peak of hydrogen at around -0.18 V on Pd₂₇@Pt₇₃ sample significantly decreased. Such peak completely disappeared on the Pd₂₁@Pt₇₉ sample, suggesting that the core Pd was blocked by the Pt shell. Generally, it is not proper for calculating the electrochemically active surface area (ECSA) of Pd-containing Pt electrocatalysts by measuring the total charge passed in the hydrogen region, because hydrogen atoms are absorbed in the bulk Pd lattice by the dissolution adsorption mechanism.^[33] But, some literature has demonstrated that the ECSAs of Pd-containing electrocatalysts can be calculated by integrating the charges associated with the hydrogen region.^[34] In this case, the Pd cores in the Pd₂₁@Pt₇₉ and Pd₂₇@Pt₇₃ samples are almost completely covered by Pt. Therefore, the ECSAs of the Pd₂₁@Pt₇₉, Pd₂₇@Pt₇₃, and Pt black (PtB) samples are roughly calculated by integrating the charges associated with the hydrogen region. The ECSAs of Pd₂₁@Pt₇₉, Pd₂₇@Pt₇₃, and PtB are

38.2 m² g⁻¹, 38.4 m² g⁻¹, and 10.2 m² g⁻¹, respectively.

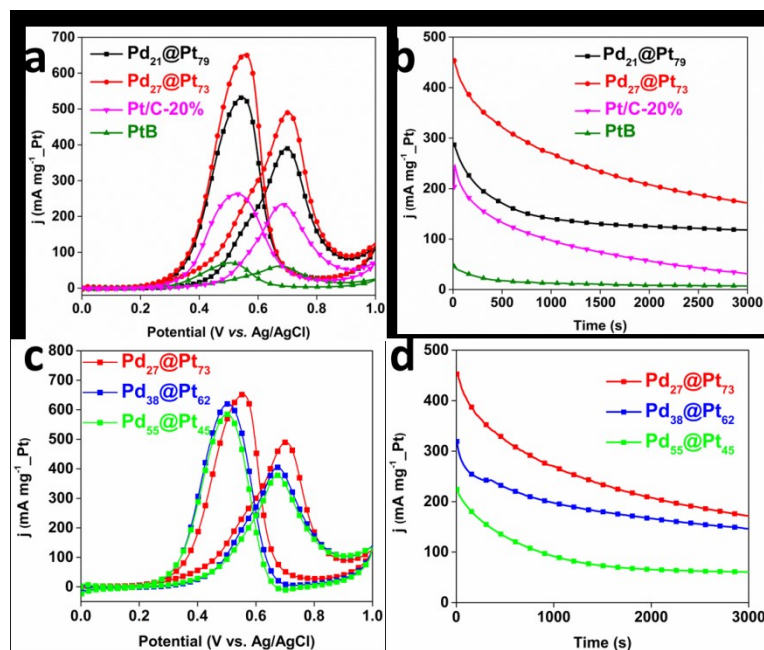


Figure 4.2.11 (a) CV curves of MOR catalyzed by the nanoporous Pd₂₁@Pt₇₉, Pd₂₇@Pt₇₃, Pt/C-20% and PtB catalysts, recorded in 0.5 M H₂SO₄+0.5 M CH₃OH at a scan rate of 50 mV·s⁻¹. (b) Chronoamperometric curves (recorded at 0.6 V) obtained in 0.5 M H₂SO₄ +0.5 M CH₃OH catalyzed by the nanoporous Pd₂₁@Pt₇₉, Pd₂₇@Pt₇₃, Pt/C-20%, and PtB catalysts. (c) CV curves of the nanoporous Pd₂₇@Pt₇₃, Pd₃₈@Pt₆₂, Pd₅₅@Pt₄₅ particles obtained in 0.5 M H₂SO₄+0.5 M CH₃OH at a scan rate of 50 mV·s⁻¹. (d) chronoamperometric curves (recorded at 0.6 V) of the nanoporous Pd₂₇@Pt₇₃, Pd₃₈@Pt₆₂, Pd₅₅@Pt₄₅ particles obtained in 0.5 M H₂SO₄+0.5 M CH₃OH.

To evaluate the performance of Pd@Pt particles, the electrocatalytic activity towards methanol oxidation reaction (MOR) was investigated. **Figure 4.2.11a** shows the typical cyclic voltammograms (CVs) of methanol oxidation in 0.5 M H₂SO₄ containing 0.5 M methanol solution at a scan rate of 50 mV s⁻¹ on nanoporous Pd@Pt particles with different compositions, and PtB catalyst and Pt/C-20%. All the current densities were normalized by Pt mass (mass activity). All of the nanoporous Pd@Pt samples possess a much higher electrochemical activity than that of PtB, and Pt/C-20% (**Figure 4.2.11a,c**). As is well known, pure Pd scarcely exhibits electrocatalytic performance toward MOR in acidic electrolyte. Therefore, I ascribe the enhanced activity of the nanoporous Pd@Pt particles to the porous structure together with electronic effect by the Pd core.^[32c,35] Many literatures have reported that the ligand effects and strain effects producing in the boundary between the core Pd and Pt shell can decrease the Pt-Pt distance, which improves the electrocatalytic performance.^[17b,36] The nanoporous Pd₂₇@Pt₇₃ nanoparticles also exhibit a negatively shifted onset potential, compared to that of commercial PtB, and Pt/C-20% catalysts, indicating that the MOR can be more easily

triggered on the nanoporous Pd₂₇@Pt₇₃ nanoparticles (**Figure 4.2.11a,c**). The peak current densities of nanoporous Pd₂₁@Pt₇₉, Pd₂₇@Pt₇₃, Pd₃₈@Pt₆₂, and Pd₅₅@Pt₄₅ particles are 390, 490, 418, and 380 mA mg⁻¹ Pt, respectively, indicating that the electrocatalytic activity of the nanoporous Pd@Pt particles is composition-dependent. Nanoporous Pd₂₇@Pt₇₃ particles exhibited the best electrocatalytic activity for MOR. The obtained maximum electrocatalytic activity of nanoporous Pd₂₇@Pt₇₃ particles (490 mA mg⁻¹ Pt) is about 7 and 2.1 times as large as that of the PtB catalyst (70 mA mg⁻¹ Pt) and Pt/C-20% (230 mA mg⁻¹ Pt). Even when the electrocatalytic activity was normalized by the metal mass (Pt+Pd), the nanoporous Pd₂₇@Pt₇₃ (408 mA mg⁻¹ (Pt+Pd)) still exhibited higher activity than that of commercial PtB (70 mA mg⁻¹ Pt) and Pt/C-20% (230 mA mg⁻¹ Pt) catalysts. Compared to previously reported Pt-based catalysts (**Table 4.2.2**), the as-prepared Pd₂₇@Pt₇₃ nanostructures exhibit higher current densities in mass activity, suggesting that the nanoporous Pd@Pt nanoparticles have potential for use in fuel cells. I also examined the stability of the nanoporous Pd@Pt particles in comparison to PtB and Pt/C-20%. **Figure 4.2.11b** and **Figure 4.2.11d** show that the nanoporous Pd₂₇@Pt₇₃ particles exhibited a slower current decay and the higher oxidation current and thus are more durable than that of PtB and Pt/C-20%. The probable reason is that the nanoporous structures in the Pd@Pt particles are less vulnerable to aggregation and dissolution than PtB and Pt/C-20% catalyst.

Table 4.2.2. Comparison of the activity of nanoporous Pd₂₇@Pt₇₃ particles with previous reported Pt-based catalysts.

Sample names	Electrolytes	Scan rate (mV s ⁻¹)	Mass activity (mA mg ⁻¹ Pt)	Reference
Nanoporous Pd ₂₇ @Pt ₇₃ particles	0.5 M H ₂ SO ₄ +0.5 M CH ₃ OH	50	490	Present work
Dendritic Au@Pt nanoparticles	0.5 M H ₂ SO ₄ +0.5 M CH ₃ OH	50	120	<i>Chem. Mater.</i> , 2010, 22 , 6310
Ag@Pt nanoparticles	0.5 M H ₂ SO ₄ +0.5 M CH ₃ OH	50	150	<i>Phys. Chem. Chem. Phys.</i> , 2013, 15 , 3490
Pd@Pt nanoparticles	0.5 M H ₂ SO ₄ +0.5 M CH ₃ OH	50	376	<i>J. Phys. Chem. C</i> , 2010, 114 , 11861
Pd@Pt nanoparticles	0.1 M HClO ₄ +0.5 M CH ₃ OH	50	ca. 350	<i>Chem. Eur. J.</i> , 2014, 20 , 7901
Nanoflower Pt ₃ Co	0.1 M HClO ₄ +1.0 M CH ₃ OH	50	385.1	<i>J. Power Sources</i> , 2014, 268 , 744
PdPt alloy nanoparticles/Graphite	0.5 M H ₂ SO ₄ +1.0 M CH ₃ OH	20	460.2	<i>J. Mater. Chem. A</i> , 2015, 3 , 5204
Octahedra PtAg alloy	0.5 M H ₂ SO ₄ +1.0 M CH ₃ OH	50	ca. 350	<i>Nanoscale</i> , 2014, 6 , 12310

Hollow Pd@Pt nanoparticles	0.5 M H ₂ SO ₄ +1.0 M CH ₃ OH	50	500	<i>J. Power Sources</i> , 2015, 274 , 604
TeCuPt nanowires	0.5 M H ₂ SO ₄ +1.0 M CH ₃ OH	20	245	<i>J. Mater. Chem. A</i> , 2015, 3 , 5850
Pt ₁ Ni ₁ chain-like nanohybrids	0.5 M H ₂ SO ₄ +1.0 M CH ₃ OH	50	136	<i>Nanoscale</i> , 2014, 6 , 4635
Hollow Pd@Pt nanoparticles	0.5 M H ₂ SO ₄ +1.0 M CH ₃ OH	50	580	<i>J. Am. Chem. Soc.</i> , 2013, 135 , 16762
Au@Pd@Pt nanoparticles	0.5 M H ₂ SO ₄ +1.0 M CH ₃ OH	50	430	<i>Chem. Mater.</i> , 2011, 23 , 2457

4.2.4. Conclusion

We have successfully prepared nanoporous Pd@Pt particles with controlled compositions, particle sizes, and morphologies by a facile one-step method. The Pd/Pt feeding ratios are found to be critical for the formation of nanoporous Pd@Pt particles with different shapes. The as-prepared nanoporous Pd@Pt particles demonstrated composition-dependent electrocatalytic activity toward MOR. Among all the samples, nanoporous Pd₂₇@Pt₇₃ particles exhibit the best catalytic performance toward MOR with mass activity up to 490 mA mg⁻¹ Pt, which is 7 times and 2.1 times higher than that of commercial Pt/C catalyst (70 mA mg⁻¹ Pt) and Pt/C-20% (230 mA mg⁻¹ Pt), respectively. We believe that this facile synthetic approach can be scaled up easily and should be highly valuable for routinely producing new multimetallic core-shell structure with controlled shapes, compositions, sizes and shell thicknesses.

References

- [1] (a) S. H. Joo, S. J. Choi, I. Oh, J. Kwak, Z. Liu, O. Terasaki, R. Ryoo, *Nature*, 2001, **412**, 169; (b) H. A. Gasteiger, S. S. Kocha, B. Sompalli, F. T. Wagner, *Appl. Catal. B Environ.*, 2005, **56**, 9; (c) Y. Qi, T. Bian, S. I. Choi, Y. Jiang, C. Jin, M. Fu, H. Zhang, D. Yang, *Chem. Commun.*, 2014, **50**, 560; (d) X. Huang, S. Tang, H. Zhang, Z. Zhou, N. Zheng, *J. Am. Chem. Soc.*, 2009, **131**, 13916; (e) C. Li, Y. Yamauchi, *Chem. Eur. J.*, 2014, **20**, 729; (f) B. Y. Xia, H. B. Wu, X. Wang, X. W. Lou, *Angew. Chem. Int. Ed.*, 2013, **52**, 12337.
- [2] (a) H. Ataee-Esfahani, J. Liu, M. Hu, N. Miyamoto, S. Tominaka, K. W. Wu, Y. Yamauchi, *Small*, 2013, **9**, 1047; (b) D. Xu, Z. Liu, H. Yang, Q. Liu, J. Zhang, J. Fang, S. Zou, K. Sun, *Angew. Chem. Int. Ed.*, 2009, **48**, 4217; (c) X. Liu, C. H. Cui, M. Gong, H. H. Li, Y. Xue, F. J. Fan, S. H. Yu, *Chem. Commun.*, 2013, **49**, 8704.
- [3] (a) F. Saleem, Z. Zhang, B. Xu, X. Xu, P. He, X. Wang, *J. Am. Chem. Soc.*, 2013, **135**, 18304; (b) X. Huang, Z. Zhao, J. Fan, Y. Tan, N. Zheng, *J. Am. Chem. Soc.*, 2011, **133**, 4718; (c) C. Zhu, S. Guo, S. Dong, *Adv. Mater.*, 2012, **24**, 2326.
- [4] (a) Y. Jia, Y. Jiang, J. Zhang, L. Zhang, Q. Chen, Z. Xie, L. Zheng, *J. Am. Chem. Soc.*, 2014, **136**, 3748; (b) N. Tian, Z. Y. Zhou, S. G. Sun, Y. Ding, Z. L. Wang, *Science*, 2007, **316**, 732; (c) P. Zhang, X. Dai, X. Zhang, Z. Chen, Y. Yang, H. Sun, X. Wang, H. Wang, M. Wang, H. Su, D. Li, H. Li, Y. Qi, *Chem. Mater.*, 2015, **27**, 6402; (d) C. Xu, Q. Hao, H. Duan, *J. Mater. Chem. A*, 2014, **2**, 8875.
- [5] (a) L. Ma, C. Wang, B. Y. Xia, K. Mao, J. He, X. Wu, Y. Xiong, X. W. Lou, *Angew. Chem. Int. Ed.*, 2015, **54**, 5666; (b) X. Huang, E. Zhu, Y. Chen, Y. Li, C. Y. Chiu, Y. Xu, Z. Lin, X. Duan, Y. Huang, *Adv. Mater.*, 2013, **25**, 2974; (c) X. Zhao, S. Chen, Z. Fang, J. Ding, W. Sang, Y. Wang, J. Zhao, Z. Peng, J. Zeng, *J. Am. Chem. Soc.*, 2015, **137**, 2804; (d) L. Zhang, M. Wei, S. Wang, Z. Li, L. X. Ding, H. Wang, *Chem. Sci.*, 2015, **6**, 3211.
- [6] (a) D. Y. Wang, H. L. Chou, C. C. Cheng, Y. H. Wu, C. M. Tsai, H. Y. Lin, Y. L. Wang, B. J. Hwang, C. C. Chen, *Nano Energy*, 2015, **11**, 631; (b) Q. Gao, Y. M. Ju, D. An, M. R. Gao, J. W. Liu, C. H. Cui, S. H. Yu, *ChemSusChem*, 2013, **6**, 1878; (c) C. Li, T. Sato, Y. Yamauchi, *Angew. Chem. Int. Ed.*, 2013, **52**, 8050; (d) H. H. Li, C. H. Cui, S. Zhao, H. B. Yao, M. R. Gao, F. J. Fan, S. H. Yu, *Adv. Energy Mater.*, 2012, **2**, 1182.
- [7] (a) Y. Wu, D. Wang, G. Zhou, R. Yu, C. Chen, Y. Li, *J. Am. Chem. Soc.*, 2014, **136**, 11595; (b) S. S. Li, J. J. Lv, L. N. Teng, A. J. Wang, J. R. Chen, J. J. Feng, *ACS Appl. Mater. Interface*, 2014, **6**, 10549; (c) H. Li, H. Lin, Y. Hu, H. Li, P. Li, X. Zhou, *J. Mater. Chem.*, 2011, **21**, 18447.
- [8] L. Wang, Y. Nemoto, Y. Yamauchi, *J. Am. Chem. Soc.*, 2011, **133**, 9674.
- [9] B. P. Vinayan, R. Nagar, N. Rajalakshmi, S. Ramaprabhu, *Adv. Funct. Mater.*, 2012, **22**, 3519.
- [10] (a) C. Cui, L. Gan, H. H. Li, S. H. Yu, M. Hegen, P. Strasser, *Nano Lett.*, 2012, **12**, 5885; (b) J. Wu, A. Gross, H. Yang, *Nano Lett.*, 2011, **11**, 798.

- [11] H. Atae-Esfahani, L. Wang, Y. Nemoto, Y. Yamauchi, *Chem. Mater.*, 2010, **22**, 6310.
- [12] (a) M. Wang, W. Zhang, J. Wang, A. Minett, V. Lo, H. Liu, J. Chen, *J. Mater. Chem. A*, 2013, **1**, 2391; (b) Z. Zhang, Y. Yang, F. Nasheen, P. Wang, J. Zhang, J. Zhuang, X. Wang, *Small*, 2013, **9**, 3063.
- [13] (a) S. Zhou, K. McIlwrath, G. Jackson, B. Eichhorn, *J. Am. Chem. Soc.*, 2006, **128**, 1780; (b) V. Mazumder, M. Chi, K. L. More, S. Sun, *Angew. Chem. Int. Ed.*, 2010, **49**, 9368.
- [14] (a) B. Lim, M. J. Jiang, P. C. Camargo, E. C. Cho, J. Tao, X. Lu, Y. Zhu, Y. Xia, *Science*, 2009, **324**, 1302; (b) Y. Lim, S. K. Kim, S. C. Lee, J. Choi, K. S. Nahm, S. J. Yoo, P. Kim, *Nanoscale*, 2014, **6**, 4038; (c) S. S. Li, J. N. Zheng, X. Ma, Y. Y. Hu, A. J. Wang, J. R. Chen, J. J. Feng, *Nanoscale*, 2014, **6**, 5708; (d) H. Lee, S. E. Habas, G. A. Somorjai, P. Yang, *J. Am. Chem. Soc.*, 2008, **130**, 5406.
- [15] (a) R. Zhao, Y. Liu, C. Liu, G. Xu, Y. Chen, Y. Tang, T. Lu, *J. Mater. Chem. A*, 2014, **2**, 20855; (b) S. Xie, S. I. Choi, N. Lu, L. T. Roling, J. A. Herron, L. Zhang, J. Park, J. Wang, M. J. Kim, Z. Xie, M. Mavrikakis, Y. Xia, *Nano Lett.*, 2014, **14**, 3570.
- [16] R. Choi, S. I. Choi, C. H. Choi, K. M. Nam, S. I. Woo, J. T. Park, S. W. Han, *Chem. Eur. J.*, 2013, **19**, 8190.
- [17] (a) H. Zhang, M. Jin, J. Wang, W. Li, P. C. Camargo, M. J. Kim, D. Yang, Z. Xie, Y. Xia, *J. Am. Chem. Soc.*, 2011, **133**, 6078; (b) H. H. Li, S. Y. Ma, Q. Q. Fu, X. J. Liu, L. Wu, S. H. Yu, *J. Am. Chem. Soc.*, 2015, **137**, 7862.
- [18] Y. Kim, Y. W. Lee, M. Kim, S. W. Han, *Chem. Eur. J.*, 2014, **20**, 7901.
- [19] H. Atae-Esfahani, M. Imura, Y. Yamauchi, *Angew. Chem. Int. Ed.*, 2013, **52**, 13611.
- [20] (a) C. K. Tsung, J. N. Kuhn, W. Huang, C. Aliaga, L. I. Hung, G. A. Somorjai, P. Yang, *J. Am. Chem. Soc.*, 2009, **131**, 5816; (b) R. Long, S. Zhou, B. J. Wiley, Y. Xiong, *Chem. Soc. Rev.*, 2014, **43**, 6288.
- [21] (a) X. Sun, D. Li, Y. Ding, W. Zhu, S. Guo, Z. L. Wang, S. Sun, *J. Am. Chem. Soc.*, 2014, **136**, 5745-5749; (b) S. E. Habas, H. Lee, V. Radmilovic, G. A. Somorjai, P. Yang, *Nat. Mater.*, 2007, **6**, 692.
- [22] (a) Y. Wan, D. Zhao, *Chem. Rev.*, 2007, **107**, 2821; (b) C. Yang, H. Sui, X. Li, J. Han, X. Luo, H. Zhang, H. Sun, H. Sun, Y. Zhou, B. Yang, *CrystEngComm*, 2013, **15**, 3490.
- [23] B. Jiang, C. Li, V. Malgras, M. Imura, S. Tominaka, Y. Yamauchi, *Chem. Sci.*, 2016, **7**, 1575.
- [24] (a) L. Wang, Y. Yamauchi, *J. Am. Chem. Soc.*, 2011, **132**, 13636; (b) H. Wang, L. Wang, T. Sato, Y. Sakamoto, S. Tominaka, K. Miyasaka, N. Miyamoto, Y. Nemoto, O. Teasaki, Y. Yamauchi, *Chem. Mater.*, 2012, **24**, 1591.
- [25] (a) C. Li, B. Jiang, N. Miyamoto, J. H. Kim, V. Malgras, Y. Yamauchi, *J. Am. Chem. Soc.*, 2015, **137**, 11558; (b) K. Qi, Q. Wang, W. Zheng, W. Zhang, X. Cui, *Nanoscale*, 2014, **6**, 15090.
- [26] (a) Y. Sun, Y. Xia, *Science*, 2002, **298**, 2176; (b) N. R. Jana, L. Gearheart, C. J. Murphy, *J. Phys. Chem. B*, 2011, **105**, 4065.

- [27] (a) A. X. Yin, X. Q. Min, Y. W. Zhang, C. H. Yan, *J. Am. Chem. Soc.*, 2011, **133**, 3816; (b) M. Jin, H. Zhang, Z. Xie, Y. Xia, *Angew. Chem. Int. Ed.*, 2011, **50**, 7850.
- [28] B. Jiang, C. Li, M. Imura, J. Tang, Y. Yamauchi, *Adv. Sci.*, 2015, **2**, 1500112.
- [29] L. Wang, Y. Yamauchi, *J. Am. Chem. Soc.*, 2009, **131**, 9152.
- [30] (a) H. Lee, S. E. Habas, S. Kweskin, D. Butcher, G. A. Somorjai, P. Yang, *Angew. Chem. Int. Ed.*, 2006, **45**, 7824; (b) T. Yu, D. Y. Kim, H. Zhang, Y. Xia, *Angew. Chem. Int. Ed.* 2011, **50**, 2773.
- [31] B. Liu, M. Jiang, T. Yu, P. H. C. Camargo, Y. Xia, *Nano Res.*, 2010, **3**, 69.
- [32] (a) V. R. Stamenkovic, B. Fowler, B. S. Mun, G. Wang, P. N. Ross, C. A. Lucas, N. M. Markovic, *Science*, 2007, **315**, 493-497; (b) H. Zhang, Y. Yin, Y. Hu, C. Li, P. Wu, S. Wei, C. Cai, *J. Phys. Chem. C*, 2010, **114**, 11861.
- [33] J. Y. Wang, Y. Y. Kang, H. Yang, W. B. Cai, *J. Phys. Chem. C*, 2009, **113**, 8366.
- [34] (a) C. Li, T. Sato, Y. Yamauchi, *Chem. Commun.*, 2014, **50**, 11753; (b) S. W. Kang, Y. W. Lee, Y. Park, B. S. Choi, J. W. Hong, K. H. Park, S. W. Han, *ACS Nano*, 2013, **7**, 7945; (c) S. Lai, C. Fu, Y. Chen, X. Yu, X. Lai, C. Ye, J. Hu, *J. Power Sources*, 2015, **274**, 604.
- [35] (a) C. Li, B. Jiang, M. Imura, V. Malgras, Y. Yamauchi, *Chem. Commun.*, 2014, **50**, 15337; (b) J. Kibsgaard, Y. Gorlin, Z. Chen, T. F. Jaramillo, *J. Am. Chem. Soc.*, 2012, **124**, 7758; (c) B. Jiang, C. Li, V. Malgras, Y. Yamauchi, *J. Mater. Chem. A*, 2015, **3**, 18053.
- [36] (a) X. Wang, M. Vara, M. Luo, H. Huang, A. Ruditskiy, J. Park, S. Bao, J. Liu, J. Howe, M. Chi, Z. Xie, Y. Xia, *J. Am. Chem. Soc.*, 2015, **137**, 15036; (b) S. Xie, S. I. Choi, N. Lu, L. T. Roling, J. A. Herron, L. Zhang, J. Park, J. Wang, M. J. Kim, Z. Xie, M. Mavrikakis, Y. Xia, *Nano Lett.* 2014, **14**, 3570.

Chapter 5. Trimetallic Mesoporous Spheres through Surfactant-Directed Synthesis

5.1. Mesoporous Trimetallic PtPdRu Spheres as Superior Electrocatalysts

5.1.1. Introduction

Direct methanol fuel cells (DMFCs) are considered to be a promising energy-conversion device owing to its high energy conversion efficiency, low pollutant emissions, relative ease of storage and transportation, and high energy density.^[1] Platinum (Pt) materials are presently the most commonly used catalysts because they meet all the requirements for DMFCs, such as high efficiency, durability, and capability of scale-up. As is well known, heterogeneous catalytic reactions can occur only when the reactants are adsorbed onto a catalyst surface.^[2] Thus, creating Pt nanostructures with a more highly accessible surface area has been a reliable method to dramatically improve catalytic activity.^[3]

Generally, when the particle size of the catalyst gradually decreases, the number of functional atoms or active sites on particle surfaces increases. For example, small-sized Pt nanoparticles (<5 nm), supported on the substrates (*e.g.* activated carbon, mesoporous carbon, graphene, carbon nanotube), have become widely as commercial catalysts.^[4] However, the catalytic activity of such small-sized Pt nanoparticles can decline because of particle aggregation in part due to their high surface energies.^[5] By virtue of their topology, mesoporous architectures enable the creation of high surface area frameworks with material connectivity that limits aggregation, improving stability without sacrificing catalytic activity.

Multicomponent catalysts with diverse compositions can effectively enhance the catalytic activity because there is a close relationship between the composition and the performance.^[6] Along this direction, great efforts have been made to develop morphology- and composition-controlled Pt-based nanostructures with a wide range of compositions, including Au@Pt,^[7] PtNi,^[8] PtPd,^[9] PtCo,^[10] PtCu^[11]. The rationale being that the electrocatalytic activity and stability of Pt can be improved by downshifting the d-band center via alloying with different 3d transition metals. For example, PtRu nanosponges with controlled surface compositions exhibit enhanced Pt mass activity toward methanol oxidation reaction, which is about 2.6 times higher than that of commercial Pt/C catalyst owing to an enhanced CO tolerance on PtRu alloys.^[12]

Despite the significant progress in the synthesis of Pt-based catalysts, there have been few reports of trimetallic Pt-based nanostructures with mesoporous architectures. This is partly due to the difficulty of controlling the reduction kinetics of metals with different redox potentials, and complexation effects with the surfactant during the nucleation and growth phase.^[13] Therefore, it is essential to develop a general and simple method for the preparation of mesoporous trimetallic Pt-based catalysts to further optimize the electrocatalytic performance.

Here, I report a simple one-pot method that produces trimetallic PtPdRu spheres with uniform nanoporous structure on the surface by a wet chemical reduction approach. The trimetallic nanoporous PtPdRu spheres exhibited an enhanced catalytic activity toward methanol oxidation reaction compared with commercial Pt black. Our approach, which is consistent with the requirements of green chemistry without the need for any seeds, and organic solvent, is widely applicable to other multimetallic metals and has realistic potential for large-scale production.

To prepare mesoporous trimetallic spheres, Pluronic F127 (0.004 mmol) was ultrasonically dissolved in the precursor solution containing RuCl_3 (0.02 mmol), Na_2PdCl_4 (0.006 mmol), and K_2PtCl_4 (0.03 mmol), and hydrochloric acid (0.0036 mmol). After addition of ascorbic acid (AA) reducing agent, the mixture was mixed for several hours. The final product was collected and washed by several consecutive washing/centrifugation cycles using ethanol and water. The detailed experimental procedure is given in the experimental section.

5.1.2. Experimental Sections

5.1.2.1. Materials

All chemicals and solvents were used as received without further purification. K_2PtCl_4 , Na_2PdCl_4 , RuCl_3 , ascorbic acid (AA), cetyltrimethylammonium bromide (CTAB), and methanol were purchased from Nacalai Tesque, Inc. (Kyoto, Japan). Pluronic F127 and nonionic surfactant Brij58 were obtained from Sigma-Aldrich. Commercial PB (HiSPEC®1000) was supplied by Johnson Matthey Company. All solutions were prepared with deionized water treated with a Millipore water purification system (Millipore Corp.).

5.1.2.2. Preparation of Mesoporous Trimetallic PtPdRu Spheres

To synthesize trimetallic nanoporous PtPdRu nanospheres, 0.3 mL Na_2PdCl_4 (20.0 mM in water), 1.5 mL K_2PtCl_6 (20.0 mM in water), 1.0 mL RuCl_3 (20 mM in water), 60 μL HCl solution (6.0 M in water) and 50.4 mg Pluronic F127 were mixed together. After completely dissolving F127 under sonication, an aqueous solution of 2.0 mL ascorbic acid (0.1 M) was added to the aforementioned solution. Then, the mixed solution was kept for several hours. The residual Pluronic F127 was removed by several consecutive washing/centrifugation cycles with ethanol and water. Finally, the sample was collected by centrifuging at 14000 rpm for 20 min. The as-prepared sample was stored in ethanol until the time of use and then dried at room temperature.

5.1.2.3. Characterization

Scanning electron microscope (SEM) observation was carried out using a Hitachi SU-8000 microscope operated at 5.00 kV. Transmission electron microscope (TEM) and high-angle annular dark-field scanning TEM (HAADF-STEM) observations were carried out using a JEOL JEM-2100F operated at 200 kV equipped with an energy-dispersive spectrometer. The samples for TEM study were prepared by depositing a drop of the diluted colloidal suspension on a carbon-coated copper grid. A wide-angle powder X-ray diffraction (XRD) pattern was recorded with a Rigaku Rint 2500 diffractometer with monochromated Cu K α radiation. Low-angle XRD patterns were recorded by using a NANO VIEWER (Rigaku, Japan).

5.1.2.4. Electrochemical Test

Both CV and chronoamperometric experiments were performed using a CHI 842B electrochemical analyzer (CHI Instruments, USA). A conventional three-electrode cell was used, including an Ag/AgCl (containing saturated KCl) electrode as a reference electrode, a platinum wire as a counter electrode, and a modified glassy carbon electrode (GCE) as a working electrode. The modified GCE was coated with as-produced samples (5.0 μg) and dried at room temperature. Then, 5.0 μL of Nafion (0.05 wt %) was coated on the surface of the modified GCE and dried before electrochemical experiments. Prior to electrochemical experiments, the GCEs modified with the samples were activated electrochemically by cycling the electrode potential between -0.2 V and +1.5 V (*vs.* Ag/AgCl) in 0.5 M H₂SO₄ until CVs that were characteristic for a clean Pt electrode were obtained.

5.1.3. Results and Discussion

The morphology and the mesoporous structure of the resulting product were characterized by electron microscopy (**Figure 5.1.1**). The low-magnification scanning electron microscope (SEM) image reveals that the as-prepared product consists of uniform spheres without any byproducts (*e.g.*, irregular shaped particles, nonporous bulk) (**Figure 5.1.1a-b**). The obtained spheres had an average diameter of *ca.* 100 nm (**Figure 5.1.1c**). Interestingly, uniformly porous cavities (*ca.* 10 \pm 0.5 nm) were distributed over entire external surface of the particles (**Figure 5.1.1b**), which is favorable for improving the active surface area and the mass transport of guest molecules. Transmission electron microscope (TEM) images show that the product has an overall well-defined spherical shape with holey surfaces (**Figure 5.1.1d**). High-resolution TEM (HRTEM) image (**Figure 5.1.1e**) taken from the edge part of spheres reveals that they are composed of a large number of tiny interconnected nanocrystals. The lattice spacing distance of the sample is 0.20 nm, which is in good

agreement with a face-centered cubic (*fcc*) (200) crystal plane. The concentric rings in selected-area electron diffraction (ED) (**Figure 5.1.1f**) patterns taken from one particle indicate it is the polycrystalline.

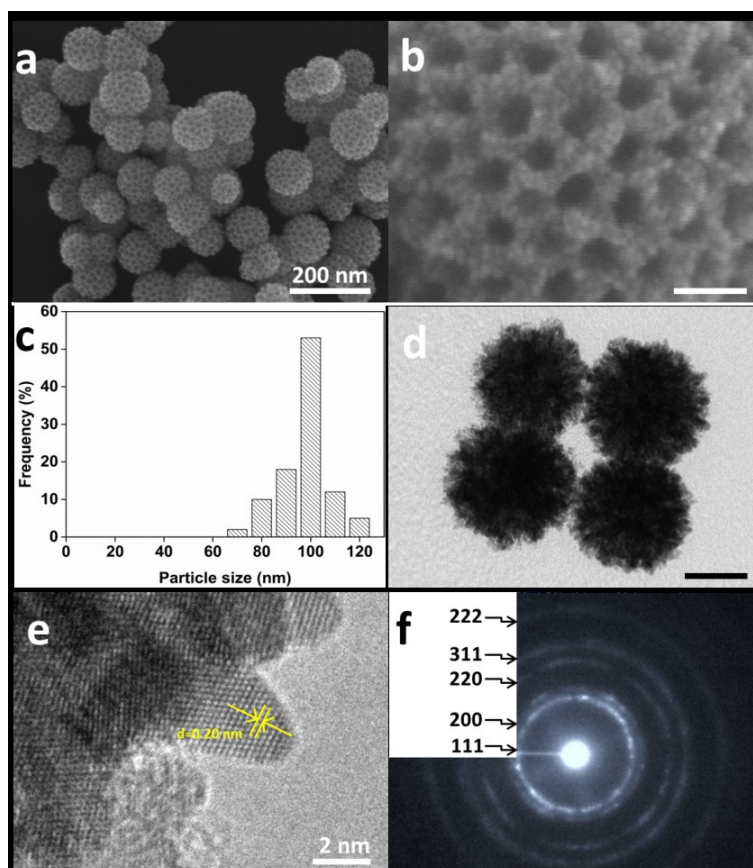


Figure 5.1.1 (a) Low magnification SEM image, (b) high magnification SEM image, (c) particle size distribution histogram, (d) TEM image, (e) high resolution TEM image, and (f) electron diffraction patterns of trimetallic mesoporous PtPdRu spheres.

Electron microscopy provides a direct evidence of the formation of the mesoporous structure, but it is local information. To get better information on the ensemble of the mesoporous sample, the product was further characterized by low-angle X-ray diffraction (XRD). A diffraction peak in the low-angle region at 0.43° was clearly observed, corresponding to the periodicity (*i.e.*, pore-to-pore distance) of 20.5 nm (**Figure 5.1.2a**). The BET surface area of the sample was measured to be *ca.* $28 \text{ m}^2 \text{ g}^{-1}$. The crystalline structure of the trimetallic mesoporous sphere was determined by wide-angle XRD (**Figure 5.1.2b**). The XRD patterns show five peaks, corresponding to (111), (200), (220), (311), and (222) diffraction peaks of a face-centered cubic (*fcc*) crystal structure. The diffraction peaks are broad, indicating the product is made of the tiny nanocrystals. The average grain size is *ca.* 4 nm calculated from the (111) diffraction peak based on the Scherrer equation,^[14] which is in agreement with TEM observation (**Figure 5.1.2d**). Owing to a very high lattice match between Pt and Pd

(99.23%), the peaks of the Pd and Pt elements in the XRD pattern are overlapped. However, compared with standard diffraction patterns of Pt, the diffraction peaks of product are slightly shifted to higher angles. In order to clearly confirm this peak shift, careful XRD measurement was carried out in the 2θ range of 80° to 85° at very slow scanning rate ($0.01^\circ \cdot \text{min}^{-1}$). As shown in the inset of **Figure 5.1.2b**, the (311) peak of trimetallic mesoporous PtPdRu is clearly shifted in the higher angle range, indicating the incorporation of smaller sized Ru atoms into the Pt and Pd crystals.^[15] The electronic states of Pt, Pd, and Ru in mesoporous PtPdRu spheres were measured by X-ray photoelectron spectroscopy (XPS). The doublet peak located at 71.4 eV and 74.4 eV can be assigned to the Pt^0 4f_{7/2} and Pt^0 4f_{5/2}. The binding energy of Pd 3d_{5/2} and Pd 3d_{3/2} located at 335.3 eV and 340.6 eV are ascribed to metallic Pd⁰. The metallic Ru⁰ d_{3/2} is located at 284.4 eV. The result clearly revealed that the Pt, Pd, and Ru elements are successfully reduced into metallic state.

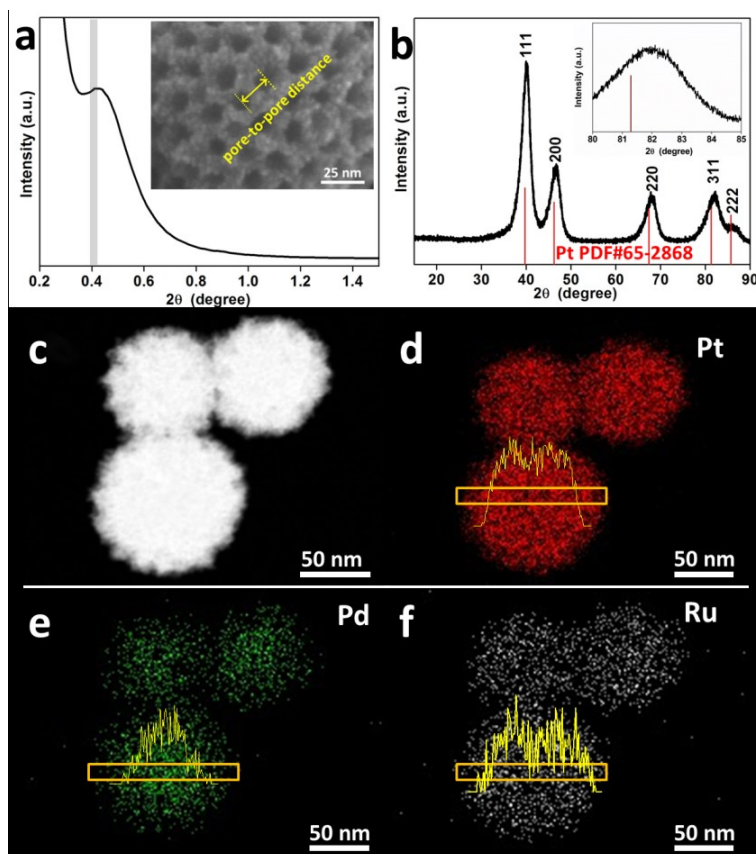


Figure 5.1.2 (a) Low-angle XRD, (b) wide angle XRD patterns of trimetallic nanoporous PtPdRu sphere, (c) high-angle annular dark-field scanning TEM (HAADF-STEM), and (d-f) elemental mapping images of the trimetallic nanoporous PtPdRu spheres. Inset image in the panel (b) shows the slow scanning XRD profile at $2\theta = 80\text{--}85^\circ$. Inset image in the panel (d-f) shows the cross-sectional compositional line profiles of Pt, Pd, Ru elements, respectively, in individual sphere.

The atomic ratios of Pt:Pd:Ru was measured to be 84:8:8 by the inductively coupled plasma atomic emission spectrometry data (ICP-AES). In order to understand the distribution of Pt, Pd and Ru in the spheres, elemental mapping was employed. **Figure 5.1.2d-f** shows that the Pd, Pt, and Ru are evenly distributed on the entire of the sphere, although the Pd is slightly concentrated at the interior of the particle. The line-scanning profiles (inset of **Figure 5.1.2d-f**) clearly reveal the distribution of Pt, Pd and Ru elements across an individual particle, consisting with the higher Pt content and lower content Pd and Ru, which is in agreement with the ICP data. Previous studies reveal that the reduction of multiple metal species cannot be interpreted simply in terms of their standard reduction potentials in the presence of organic additives (*e.g.*, surfactant molecules) due to their complicated reduction kinetics and complexation effect.^[16] In the present system, although the standard reduction potential of Pd complexes ($[\text{PdCl}_4]^{2-}/\text{Pd}$: +0.59 V vs. SHE) is lower than that of Pt complexes ($[\text{PtCl}_4]^{2-}/\text{Pt}$: +0.76 V vs. SHE) and higher than that of Ru complexes (Ru^{3+}/Ru : +0.39 V vs. SHE), the Pd species are more easily and preferentially reduced and Pd element slightly concentrated at the interior of sphere as shown in elemental mapping image.

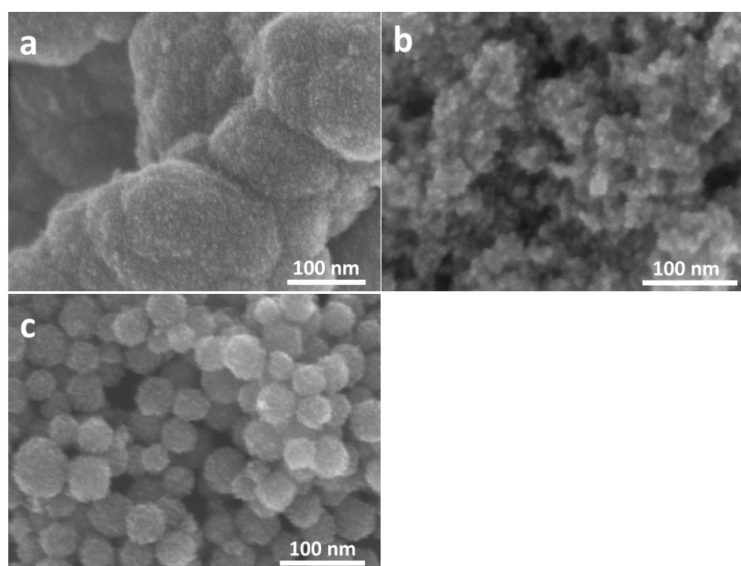


Figure 5.1.3 SEM images of the samples prepared at different conditions: (a) in the absence of F127, (b) by replacing AA with NaBH_4 , (c) in the absence of HCl.

Hydrochloric acid, ascorbic acid, and surfactant (F127) were necessary for the synthesis of mesoporous trimetallic PtPdRu spheres in this method. When no surfactant was used, non-porous aggregates are obtained, revealing that the surfactants not only serves as pore directing agent, but also play a key role for preventing the particle aggregations (**Figure 5.1.3a**).^[17] When the concentration of surfactant F127 is above critical micelle concentration (CMC), it self-assembles into spherical micelles composed of a PEO shell and a PPO core that

serves as a pore-directing agent to form the mesoporous structure. During deposition of the metals, the metal precursors are incorporated in the PEO shell region of the micelles by the hydrogen bonding.^[18] The spherical-like shapes are constructed through the close packing of hybrid of micelles and deposited metals. Recent works have shown that the morphology and structure of metallic materials are strongly dependent on reducing agents and reduction rates.^[19] Therefore, I selected a mild reducing agent to give a slow reduction rate. When ascorbic acid was replaced with stronger reducing agents (*e.g.*, NaBH₄), the reduction rate increased significantly and yielded only small nanoparticles owing to uncontrollable metal deposition (**Figure 5.1.3b**). Additionally, when the reaction is carried out in the absence of HCl, non-porous spheres are obtained (**Figure 5.1.3c**). In this study, HCl can decrease the reduction capacity of ascorbic acid and further manipulate reduction kinetics, according to the following equilibrium equation: $C_6H_8O_6 \leftrightarrow C_6H_6O_6 + 2H^+ + 2e^-$. Generally, slow reaction rate can provide enough time for metal seeds to approach and adsorb on the surface of the micelles template.^[20] During the further growth of metals, the micelles can effectively act as a template for the formation of mesoporous structure.

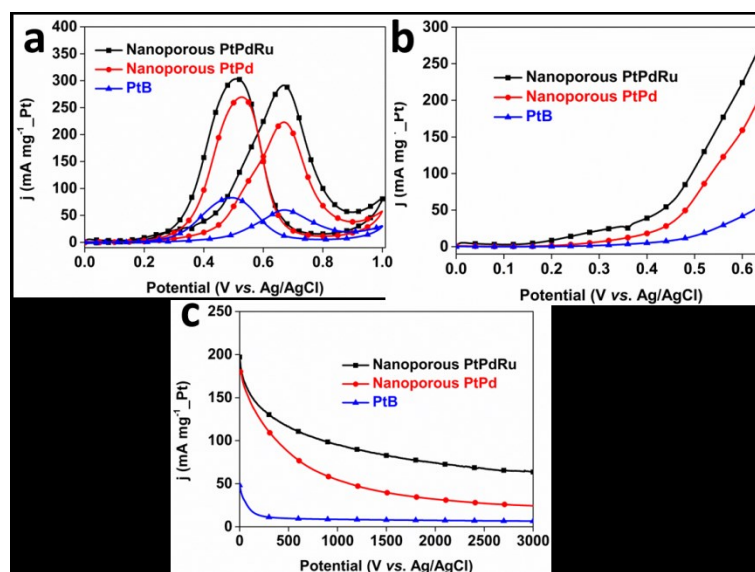


Figure 5.1.4 (a) Cyclic voltammograms (CVs), (b) chronoamperometric curves (recorded at 0.6 V) for methanol oxidation reactions catalyzed by mesoporous trimetallic PtPdRu catalyst (black plots), mesoporous binary nanoporous PtPd catalyst (red plots), and PtB catalyst (blue plots).

The as-prepared mesoporous trimetallic PtPdRu spheres are expected to have enhanced catalytic performance compared with those of the bimetallic PtPd and Pt black (PtB) catalysts. The current densities were normalized by the Pt mass activity. **Figure 5.1.4a** shows the cyclic voltammograms (CVs) of methanol oxidation reaction catalyzed by the three different catalysts. The characteristic methanol oxidation peaks were

identified in the forward and backward sweeps in 0.5 M H₂SO₄ containing 0.5 M methanol solution at a scan rate of 50 mV s⁻¹. It was evident that the mesoporous trimetallic PtPdRu sample shows a higher electrochemical activity than bimetallic PtPd and PtB catalysts. The current density of mesoporous trimetallic PtPdRu spheres was 294 mA mg⁻¹ Pt, which was about ~1.3, and 4.9 times higher than bimetallic PtPd (225 mA mg⁻¹ Pt), and PtB (60 mA mg⁻¹ Pt) catalysts, respectively (**Figure 5.1.4a**). Furthermore, the mesoporous trimetallic PtPdRu spheres exhibit a negatively shifted onset potential for electrochemical oxidation of methanol compared to those of bimetallic PtPd, and PtB catalysts, indicating the mesoporous trimetallic PtPdRu catalyst is capable to trigger the methanol oxidation efficiently (**Figure 5.1.4b**). In general, the ratio of the forward peak current density and the backward peak current density (I_f/I_b) can be used to monitor the tolerance of the catalysts for CO-poisoning.^[21] The I_f/I_b values are 0.97, 0.80, and 0.72 for the trimetallic nanoporous PtPdRu, bimetallic PtPd catalyst and PtB catalyst, respectively. It is known that the incorporation of Ru and/or Pd into the Pt catalyst improves the tolerance for CO poisoning.^[22] The tolerance to CO poisoning of nanoporous PtPdRu can be partially attributed to neighboring Ru atoms, which can provide oxygen-containing species for reaction intermediates to complete the oxidation^[23] and the Pd atom, which increases Pt d-band vacancies and modify the electronic structure.^[24] Chronoamperometry, which is a useful method for evaluating of electrocatalyst stability in fuel cells, was employed to investigate the stability of different catalysts. **Figure 5.1.4c** reveals that the mesoporous trimetallic PtPdRu spheres exhibit slower current decay and keep higher catalytic current owing to the mesoporous structure is less vulnerable to aggregation.

5.1.4. Conclusion

In summary, we have synthesized mesoporous trimetallic PtPdRu spheres *via* a facile and green method without the need for any organic solvent, pre-formed seeds or high temperatures. The presence of HCl, F127 and ascorbic acid was essential for the formation of the mesoporous trimetallic PtPdRu materials. These mesoporous trimetallic PtPdRu spheres show enhanced electrochemical activities toward methanol oxidation reaction compared with bimetallic PtPd catalysts and PtB catalyst. This simple synthetic procedure should offer a general approach to design other trimetallic nanoporous Pt-based catalysts with the appropriate precursor solution to make other promising catalysts for fuel cells and other catalytic reactions.

References

- [1] (a) N. S. Porter, H. Wu, Z. Quan, and J. Fang, *Acc. Chem. Res.*, 2013, **46**, 1867; (b) L. Wang, Y. Yamauchi, *J. Am. Chem. Soc.*, 2013, **135**, 16762; (c) H. Huang, X. Wang, *J. Mater. Chem. A*, 2014, **2**, 6266; (d) C. H. Cui, S. H. Yu, *Acc. Chem. Res.*, 2013, **46**, 1427; (e) X. Zhao, J. Zhang, L. Wang, H. X. Li, Z. Liu, W. Chen, *ACS Appl. Mater. Interface*, 2015, **7**, 26333
- [2] (a) Q. Zhang, I. Lee, J. Ge, F. Zaera, Y. Yin, *Adv. Funct. Mater.*, 2010, **20**, 2201; (b) G. Ertl, H. Knözinger, J. Weitkamp (eds), *Handbook of heterogeneous catalysis*, VCH: Weinheim, 1997.
- [3] (a) C. Zhu, D. Du, A. Eychmüller, Y. Lin, *Chem. Rev.*, 2015, **115**, 8896; (b) L. Wang, Y. Nemoto, Y. Yamauchi, *J. Am. Chem. Soc.*, 2011, **133**, 9674; (c) Y. Song, R. M. Garcia, R. M. Dorin, H. Wang, Y. Qiu, E. N. Coker, W. A. Steen, J. E. Miller, J. A. Shelnutt, *Nano Lett.* 2007, **7**, 3650; (d) H. H. Li, S. Zhao, M. Gong, C. H. Cui, D. He, H. W. Liang, L. Wu, S. H. Yu, *Angew. Chem. Int. Ed.*, 2013, **52**, 7472.
- [4] (a) C. Zhai, M. Zhu, D. Bin, F. Ren, C. Wang, P. Yang, Y. Du, *J. Power. Sources*, 2015, **275**, 483; (b) X. Huang, Z. Zeng, S. Bao, M. Wang, X. Qi, Z. Fan, H. Zhang, *Nat. Commun.*, 2013, **4**, 1444; (c) S. H. Patil, B. Anothumakkool, S. D. Sathaye, K. R. Patil, *Phys. Chem. Chem. Phys.*, 2015, **17**, 26101; (d) Y. Lim, S. K. Kim, S. C. Lee, J. Choi, K. S. Nahm, S. J. Yoo, P. Kim, *Nanoscale*, 2014, **6**, 4038; (e) Y. J. Wang, N. Zhao, B. Fang, H. Li, X. T. Bi, H. Wang, *Chem. Rev.*, 2015, **115**, 3433.
- [5] (a) R. J. White, R. Luque, V. L. Budarin, J. H. Clark, D. *Chem. Soc. Rev.*, 2009, **38**, 481; (b) D. Astruc, F. Lu, J. R. Aranzas, *Angew. Chem. Int. Ed.*, 2005, **44**, 7852; (c) X. Chen, G. Wu, J. Chen, X. Chen, Z. Xie, X. Wang, *J. Am. Chem. Soc.*, 2011, **133**, 3693-3695; (d) L. Cademartiri, G. A. Ozin, *Adv. Mater.*, 2009, **21**, 1013.
- [6] (a) Y. Zhou, D. Wang, Y. Li, *Chem. Commun.*, 2014, **50**, 6141; (b) B. Jiang, C. Li, V. Malgras, Y. Yamauchi, *J. Mater. Chem. A*, 2015, **3**, 18053; (c) L. Bu, J. Ding, S. Guo, X. Zhang, D. Su, X. Zhu, J. Yao, J. Guo, G. Lu, X. Huang, *Adv. Mater.*, 2015, **27**, 7204; (d) H. Lv, Z. Xi, Z. Chen, S. Guo, Y. Yu, W. Zhu, Q. Li, X. Zhang, M. Pan, G. Lu, S. Mu, S. Sun, *J. Am. Chem. Soc.*, 2015, **137**, 5859; (e) B. Jiang, C. Li, V. Malgras, Y. Bando, Y. Yamauchi, *Chem. Commun.*, 2016, **52**, 1186.
- [7] (a) H. Atae-Esfahani, L. Wang, Y. Nemoto, Y. Yamauchi, *Chem. Mater.*, 2010, **22**, 6310; (b) I. Banerjee, V. Kumaran, V. Santhanam, *J. Phys. Chem. C*, 2015, **119**, 5982.
- [8] (a) X. Huang, E. Zhu, Y. Chen, Y. Li, C. Y. Chiu, Y. Xu, Z. Lin, X. Duan, Y. Huang, *Adv. Mater.*, 2013, **25**, 2974; (b) J. Zhang, H. Yang, J. Fang, S. Zou, *Nano Letter.*, 2010, **10**, 638.
- [9] (a) S. S. Li, J. N. Zheng, X. Ma, Y. Y. Hu, A. J. Wang, J. R. Chen, J. J. Feng, *Nanoscale*, 2014, **6**, 5708; (b) Y. T. Liang, S. P. Lin, C. W. Liu, S. R. Chung, T. Y. Chen, J. H. Wang, K. W. Wang, *Chem. Commun.*, 2015, **51**, 6605; (c) H. S. Chen,

- Y. T. Liang, T. Y. Chen, Y. C. Tseng, C. W. Liu, S. R. Chung, C. T. Hsieh, C. E. Lee, K. W. Wang, *Chem. Commun.*, 2014, **50**, 11165.
- [10] (a) C. Li, M. Imura, Y. Yamauchi, *Chem. Eur. J.*, 2014, **20**, 3277; (b) C. Wang, C. Lin, L. Zhang, Z. Quan, K. Sun, B. Zhao, F. Wang, N. Porter, Y. Wang, J. Fang, *Chem. Eur. J.*, 2014, **20**, 1753.
- [11] (a) X. Sun, K. Jiang, N. Zhang, S. Guo, X. Huang, *ACS Nano*, 2015, **9**, 7634; (b) F. Saleem, Z. Zhang, B. Xu, X. Xu, P. He, X. Wang, *J. Am. Chem. Soc.*, 2013, **135**, 18304; (c) Y. Qi, T. Bian, S. I. Choi, Y. Jiang, C. Jin, M. Fu, H. Zhang, D. Yang, *Chem. Commun.*, 2014, **50**, 560.
- [12] M. Xiao, L. Feng, J. Zhu, C. Liu, W. Xing, *Nanoscale*, 2015, **7**, 9467.
- [13] (a) V. Malgras, H. Atae-Esfahani, H. Wang, B. Jiang, C. Li, K. W. Wu, J. H. Kim, Y. Yamauchi, *Adv. Mater.*, 2016, **28**, 993; (b) C. Li, B. Jiang, N. Miyamoto, J. H. Kim, V. Malgras, Y. Yamauchi, *J. Am. Chem. Soc.*, 2015, **137**, 11558.
- [14] (a) C. Bock, C. Paquet, M. Couillard, G. A. Botton, B. R. MacDougall, *J. Am. Chem. Soc.*, 2004, **126**, 8028; (b) B. D. Cullity, *Elements of X-ray Diffraction*; Addison-Wesley Publishing Co., Inc.: Reading, MA, 1956; p 150.
- [15] (a) Y. Wang, G. Wang, G. Li, B. Huang, J. Pan, Q. Liu, J. Han, L. Xiao, J. Lu, L. Zhuang, *Energy Environ. Sci.*, 2015, **8**, 177; (b) L. Ma, H. He, A. Hsu, R. Chen, *J. Power Sources*, 2013, **241**, 696.
- [16] (a) Y. Park, Y. W. Lee, S. W. Kang, S. W. Han, *Nanoscale*, 2014, **6**, 9798; (b) S. W. Kang, Y. W. Lee, Y. Park, B. S. Choi, J. W. Hong, K. H. Park, S. W. Han, *ACS Nano*, 2013, **7**, 7945.
- [17] (a) Y. Fang, D. Gu, Y. Zou, Z. Wu, F. Li, R. Che, Y. Deng, B. Tu, D. Zhao, *Angew. Chem. Int. Ed.*, 2010, **49**, 7987; (b) K. Suzuki, K. Ikari, H. Imai, *J. Am. Chem. Soc.*, 2003, **126**, 462; (c) L. Wang, Y. Yamauchi, *J. Am. Chem. Soc.*, 2009, **131**, 9152; (d) S. Wang, Q. Zhao, H. Wei, J. Q. Wang, M. Cho, H. S. Cho, O. Terasaki, Y. Wan, *J. Am. Chem. Soc.*, 2013, **135**, 11849.
- [18] (a) Ö. Çelik, Ö. Dag, *Angew. Chem. Int. Ed.*, 2001, **40**, 3799; (b) H. Wang, S. Ishihara, K. Ariga, Y. Yamauchi, *J. Am. Chem. Soc.*, 2012, **134**, 10819; (c) C. Li, T. Sato, Y. Yamauchi, *Angew. Chem. Int. Ed.*, 2013, **52**, 8050.
- [19] (a) L. Shi, A. Wang, T. Zhang, B. Zhang, D. Su, H. Li, Y. Song, *J. Phys. Chem. C*, 2013, **117**, 12526; (b) L. Wang, C. Hu, Y. Nemoto, Y. Tateyama, Y. Yamauchi, *Cryst. Growth Des.*, 2010, **10**, 3454.
- [20] (a) H. Atae-Esfahani, M. Imura, Y. Yamauchi, *Angew. Chem. Int. Ed.*, 2013, **52**, 13611; (b) X. Huang, Y. Li, Y. Chen, E. Zhou, Y. Xu, H. Zhou, X. Duan, Y. Huang, *Angew. Chem. Int. Ed.*, 2013, **52**, 2520; (c) B. Jiang, C. Li, V. Malgras, M. Imura, S. Taminaka, Y. Yamauchi, *Chem. Sci.*, 2016, **7**, 1575.
- [21] (a) C. Xu, L. Wang, R. Wang, K. Wang, Y. Zhang, F. Tian, Y. Ding, *Adv. Mater.*, 2009, **21**, 2165; (b) L. Kuai, B. Geng, S. Wang, Y. Sang, *Chem. Eur. J.*, 2012, **18**, 9423; (c) C. Li, Y. Yamauchi, *Phys. Chem. Chem. Phys.*, 2013, **15**, 3490.

- [22] (a) Z. Liu, J. Y. Lee, W. Chen, M. Han, L. M. Gan, *Langmuir*, 2004, **20**, 181; (b) T. J. Schmidt, H. A. Gasteiger, R. J. Behm, *Electrochem. Commun.*, 1999, **1**, 1; (c) P. K. Babu, H. S. Kim, E. Oldfield, A. Wieckowski, *J. Phys. Chem. B*, 2003, **107**, 7595; (d) J. Y. Lee, D. H. Kwak, Y. W. Lee, S. Lee, K. W. Park, *Phys. Chem. Chem. Phys.*, 2015, **17**, 8642.
- [23] (a) H. A. Gasteiger, N. Marković, P. N. Ross, Jr., E. J. Cairns, *J. Phys. Chem.*, 1994, **98**, 617; b) X. Teng, S. Maksimuk, S. Frommer, H. Yang, *Chem. Mater.*, 2007, **19**, 36; (c) C. Lu, C. Rice, R. I. Masel, P. K. Babu, P. Waszczuk, H. S. Kim, E. Oldfield, A. Wieckowski, *J. Phys. Chem. B*, 2002, **106**, 9581.
- [24] (a) X. Chen, Z. Cai, X. Chen, M. Oyama, *J. Mater. Chem. A*, 2014, **2**, 315; (b) H. H. Li, C. H. Cui, S. Zhao, H. B. Yao, M. R. Gao, F. J. Fan, S. H. Yu, *Adv. Energy Mater.* 2012, **2**, 1182.

5.2. Synthesis of Ternary PtPdCu Spheres with Three-Dimensional Nanoporous Architectures toward Superior Electrocatalysts

5.2.1. Introduction

Platinum (Pt) catalysts have attracted considerable attention because they are effective catalysts for both anodic oxidation (e.g., methanol, hydrogen) and cathodic reduction (oxygen) in fuel cells.^[1] However, the commercialization of fuel cells has been seriously obstructed by the slow kinetics of cathodic reactions, the poor stability, and the high cost of non-replaceable Pt.^[2] Considerable efforts have been made to develop Pt-based catalysts with high performance while using a minimal amount of Pt.^[3] One of the promising strategies is to introduce nonprecious metals into Pt catalyst to form multicomponent Pt-based composites, such as random/intermetallic alloys or core-shell structures, owing to the modification of the electronic structure and the rearrangement of surface atoms.^[4] Recently, many studies have revealed that Pt-based ternary catalysts with tuneable compositions have enhanced electrocatalytic activity toward fuel cells compared to their unitary or binary counterparts. For instance, Qu et al. reported a two-step synthesis of ternary Pt/PdCu nanoboxes by the hydrothermal method at relative high temperature. The catalytic activity of ternary Pt/PdCu nanoboxes toward ethanol oxidation was 6 times enhanced in comparison with that of the PdCu catalysts. The probable reason is the synergetic effect between the individual components in the ternary system.^[4a] Recently, ultrathin one-dimensional ternary PtPdTe nanowires synthesized by using Te wires as template exhibited an enhanced Pt mass activity toward methanol oxidation reaction, which is 2.4 times higher than that of binary PtTe catalyst.^[5] Similar results have been observed with other ternary catalysts such as FePtAu, PtNiFe, PtAuRu, and so on.^[6] Thus, developing novel Pt-based ternary catalysts is currently one of the most effective strategies to enhance the usage efficiencies.

On the other hand, it has been well-established that the performances of catalysts can be affected depending on their morphologies, sizes, compositions, and porous structures. Among these nanostructures, three-dimensional (3D) nanoporous structures are proved to be effective constructions to achieve a high catalytic performance.^[7] This 3D nanoporous structure consists of interconnected metallic nanoparticles embedded in the pore walls, offering large surface areas, abundant active sites, and facilitate the diffusion of reactant/product species. In addition, self-standing nanoporous structures are less vulnerable to aggregation and dissolution than nanoparticles during the catalytic progress. For instance, dendritic platinum nanostructures favor high catalytic performance and utilization efficiency owing to their high surface areas and lower densities.^[1c] Liu *et al.* reported a strategy for the synthesis of PtRh alloy with a 3D nanoporous structure which have a better catalytic activity and durability than Pt black.^[4b] Despite great advances in 3D

nanoporous structure, however, only a few facile methods for creating ternary metal catalysts with 3D nanoporous structures have been reported so far because of the difficulties encountered in kinetic control of nucleation/growth in the multiple metal precursors and the limitation in formation of concave metallic porous structures.^[8] Therefore, the development of a facile and effective route for large-scale preparation of Pt-based ternary catalyst with 3D porous nanostructure is still an urgent matter to be addressed.

In the present work, I report a facile strategy for synthesizing ternary PtPdCu spheres with a 3D nanoporous structure by aqueous one-pot method. Unlike high temperature-based and organic solvent-based approaches, our strategy is consistent with the requirements of green chemistry as only water is used as solvent. More importantly, I combine the respective advantages of ternary hetero-structure and 3D nanoporous structure to maximize the catalytic performance. Compared with binary nanoporous PtPd catalyst, dendritic Pt catalyst and Pt black catalyst, the ternary nanoporous PtPdCu catalyst exhibited 1.7, 2.8 and 4.9 times higher electrochemical activity, respectively.

5.2.2. Experimental Sections

5.2.2.1. Materials

All chemicals and solvents were used as received without further purification. H_2PtCl_6 , Na_2PdCl_4 , CuCl_2 , ascorbic acid (AA), hydrochloric acid, sulfuric acid and methanol were purchased from Nacalai Tesque, Inc. (Kyoto, Japan). Pluronic F127 and nonionic surfactant Brij58 were obtained from Sigma-Aldrich. Commercial PB (HiSPEC®1000) was supplied by Johnson Matthey Company. All solutions were prepared with deionized water treated with a Millipore water purification system (Millipore Corp.).

5.2.2.2. Preparation of Materials

Preparation of ternary nanoporous PtPdCu spheres

In a typical synthesis of ternary nanoporous PtPdCu spheres, 1.5 mL Na_2PdCl_4 (20.0 mM), 1.5 mL H_2PtCl_6 (20.0 mM), 1.5 mL CuCl_2 (20 mM), 0.2 mL HCl solution (6.0 M) and 50.0 mg Pluronic F127 were mixed. After dissolving F127 under sonication, 2.0 mL ascorbic acid (0.1 M) was added to the aforementioned solution, giving a 0.03 mmol of Na_2PdCl_4 , H_2PtCl_6 and CuCl_2 in an equimolar ratio. Then, the mixed solution was kept in an oil bath for 4 h at 95 °C. The residual Pluronic F127 was removed by several consecutive washing/centrifugation cycles with ethanol and water. Finally, the sample was collected by centrifuging at

14000 rpm for 20 min. The as-prepared sample was stored in ethanol until the time of use and then dried at room temperature.

Preparation of bimetallic nanoporous PtPd spheres

The synthesis of nanoporous PtPd spheres was similar to the synthesis of nanoporous PtPdCu spheres except without addition of CuCl_2 . 1.5 mL Na_2PdCl_4 (20.0 mM), 1.5 mL H_2PtCl_6 (20.0 mM), 0.1 mL HCl solution (6.0 M) and 50.0 mg Pluronic F127 were mixed. After dissolving F127 under sonication, an aqueous solution of 2.0 mL ascorbic acid (0.1 M) was added to the aforementioned solution. Then, the mixed solution was kept in an oil bath for 4 h at 95 °C. The residual Pluronic F127 was removed by several consecutive washing/centrifugation cycles with ethanol and water. Finally, the sample was collected by centrifuging at 14000 rpm for 20 min. The as-prepared sample was stored in ethanol until the time of use and then dried at room temperature.

Preparation of dendritic Pt nanoparticles

The dendritic Pt nanoparticles were prepared by a wet chemical reduction process reported previously.^[9] Firstly, an aqueous solution consisting of nonionic Brij58 surfactant was prepared under stirring. Then, K_2PtCl_4 and ascorbic acid (AA) were added to the surfactant Brij58 solutions, making the final concentration of K_2PtCl_4 and AA to be 5 mM and 12.5 mM, respectively. The final concentration of Brij58 in solution was 0.5 wt%. Then, the reaction solution was incubated without any external treatment for 12 h at room temperature. Finally, the sample was collected by centrifugation at 14000 rpm for 20 min and the residual Brij58 was removed by several consecutive washing/centrifugation cycles with ethanol and water. The as-prepared sample was stored in ethanol and then dried at room temperature.

5.2.2.3. Characterization

Scanning electron microscope (SEM) observation was carried out using a Hitachi SU-8000 microscope operated at 5.00 kV. Transmission electron microscope (TEM) and high-angle annular dark-field scanning TEM (HAADF-STEM) observations were carried out using a JEOL JEM-2100F operated at 200 kV equipped with an energy-dispersive spectrometer. The samples for TEM study were prepared by depositing a drop of the diluted colloidal suspension on a carbon-coated copper grid. A wide-angle powder X-ray diffraction (XRD) pattern was recorded with a Rigaku Rint 2500 diffractometer with monochromated $\text{Cu K}\alpha$ radiation. Low-angle XRD patterns were recorded by using a NANO VIEWER (Rigaku, Japan).

5.2.2.4. Electrochemical Test

Both CV and chronoamperometric experiments were performed using a CHI 842B electrochemical analyzer (CHI Instruments, USA). A conventional three-electrode cell was used, including an Ag/AgCl (containing saturated KCl) electrode as a reference electrode, a platinum wire as a counter electrode, and a modified glassy carbon electrode (GCE) as a working electrode. The modified GCE was coated with as-produced samples (5.0 μg) and dried at room temperature. Then, 5.0 μL of Nafion (0.05 wt %) was coated on the surface of the modified GCE and dried before electrochemical experiments. Prior to electrochemical experiments, the GCEs modified with the samples were activated electrochemically by cycling the electrode potential between -0.2 V and +1.5 V (*vs.* Ag/AgCl) in 0.5 M H_2SO_4 until CVs that were characteristic for a clean Pt electrode were obtained.

5.2.3. Results and Discussion

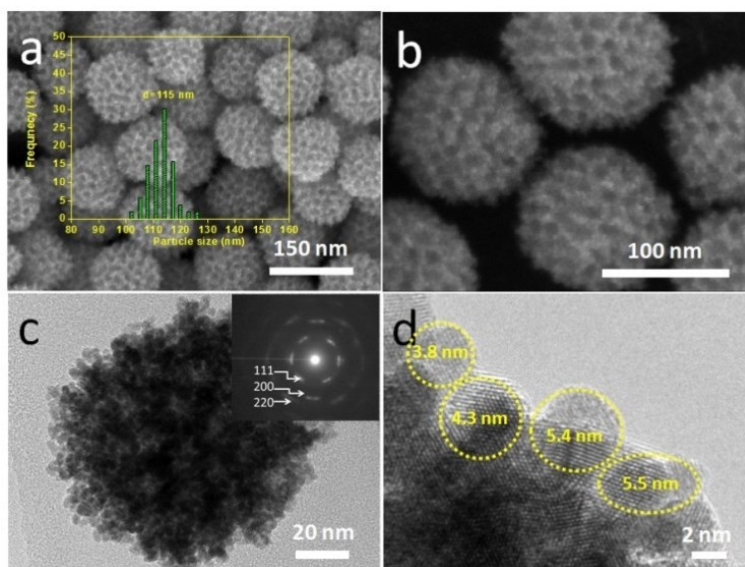


Figure 5.2.1 (a) Low magnification SEM image and particle size distribution, (b) high magnification SEM image, (c) TEM image, (d) HRTEM image of typical nanoporous PtPdCu spheres. The inset in panel (c) is the SAED pattern obtained from the single PtPdCu sphere.

The nanoporous structure of the obtained samples was firstly studied by scanning electron microscope (SEM). Well dispersed nanoporous spheres with uniform size and a diameter of 115 ± 15 nm can be observed over the entire area (**Figure 5.2.1a**). The highly magnified SEM image (**Figure 5.2.1b**) shows that well-defined nanopores are uniformly distributed over the particle surface. The structure of the samples is further investigated by TEM. Figure 1c-d reveals that the pore walls are composed of a multitude of interconnected small nanoparticles with an average size of 5 nm. Even at the particle center, sponge-like nanoporous

structures are formed. It also be seen from diffraction spots with arcs in the selected-area electron diffraction (SAED) that the sample is highly polycrystalline (**Figure 5.2.1c inset**).

SEM and TEM observations are powerful tools for determining the nanoporous structures, even though these data remain “local”. In order to get the average information from the entire sample, the PtPdCu spheres are characterized by low-angle X-ray diffraction (XRD) patterns. A broad peak in the low-angle region ($d = 17.5$ nm) was observed, corresponding to the periodicity (i.e., pore-to-pore distance) of the nanoporous structure in the obtained sample (**Figure 5.2.2a**). The nitrogen isotherm of the ternary nanoporous PtPdCu spheres gave a large surface area of $63.5 \text{ m}^2 \text{ g}^{-1}$. This value is comparable or higher than those of most reported dendritic Pt catalysts and other Pt-based catalysts.^[8b-d]

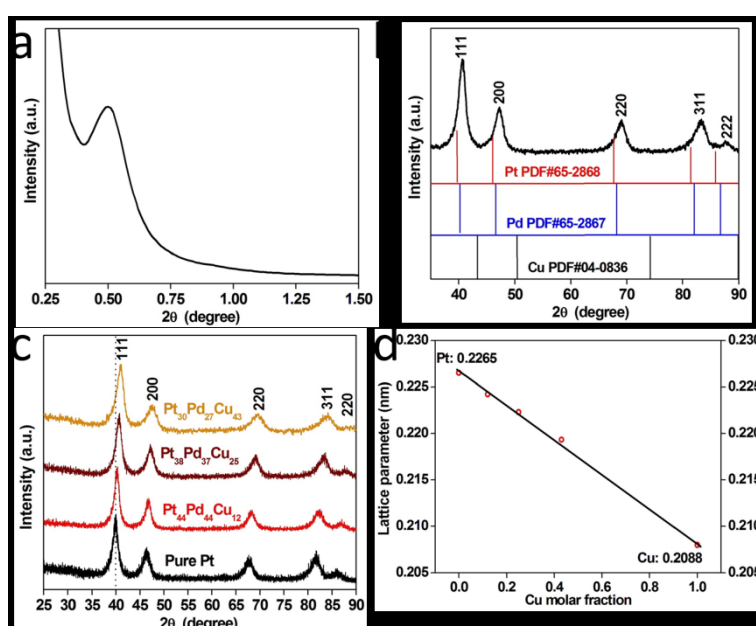


Figure 5.2.2 (a) Low-angle and (b) wide-angle XRD patterns of the typical nanoporous PtPdCu spheres, (c) wide-angle XRD patterns of the pure Pt, and ternary nanoporous PtPdCu spheres with different molar ratios of Cu, (d) the relationship of the (111) diffraction angles vs. different molar ratios of Cu in ternary nanoporous PtPdCu.

The wide-angle XRD patterns (**Figure 5.2.2b**) of the typical sample is characteristic of a metallic face-centered cubic (fcc) structure. No other diffraction peaks of monocomponent Cu, Pt, or Pd were observed, indicating the probable formation of single-phase alloys. Compared with the standard diffraction patterns of Pd and Pt, all the diffraction peaks of PtPdCu are slightly shifted to higher angles, suggesting the substitution of the smaller Cu metal atoms.^[10] The average grain size can be calculated from the (200) diffraction peak based on the Scherrer equation,^[11] returning a diameter of approximately 6.0 nm, supporting the averaged nanoparticle size observed in **Figure 5.2.1c-d**. The Pt:Pd:Cu atomic ratio in the sphere measured by inductively coupled plasma mass spectrometry (ICP-MS) is *ca.* 38:37:25. The quasi-equimolarity of Pt and Pd suggests Pt and Pd precursors were completely reduced. On the other hand, the Cu species have not

completely reacted, which may be ascribed to the Cu^{2+} species having a lower reduction potential (Cu^{2+}/Cu : +0.34 V vs. Standard Hydrogen Electrode, SHE) than that of Pt and Pd species ($[\text{PdCl}_4]^{2-}/\text{Pd}$: +0.62 V vs. SHE, $[\text{PtCl}_6]^{2-}/[\text{PtCl}_4]^{2-}$: +0.73 V vs. SHE, and $[\text{PtCl}_4]^{2-}/\text{Pt}$: +0.76 V vs. SHE).^[12] The Cu content in the samples can be increased, by increasing the amount of Cu precursor in the synthesis. As a result, the XRD peaks shift linearly towards higher angles with increasing the amount of amount of Cu precursor (Figure 5.2.2c). According to Vegard's law, the diffraction peak of the metal alloy with the molar composition should locate between the peaks of pure metals^[13] and a linear relation should exist between the crystal lattice parameter of an alloy and the content of the constituent elements (Figure 5.2.2c).^[14] Therefore, I can confirm that the as-prepared ternary PtPdCu spheres display an alloy phase. In addition, the ternary PtPdCu spheres with a uniform porous structure could be well retained even after modifying the Cu content from 5.4% to 23.8% (Figure 5.2.3).

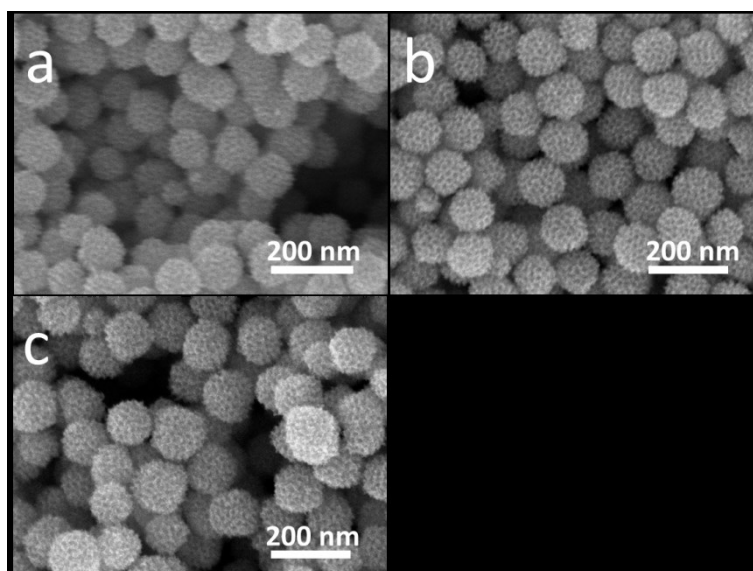


Figure 5.2.3 SEM images of the ternary nanoporous PtPdCu spheres with different amount of Cu: (a) nanoporous $\text{Pt}_{44}\text{Pd}_{44}\text{Cu}_{12}$ spheres, (b) nanoporous $\text{Pt}_{38}\text{Pd}_{37}\text{Cu}_{25}$ spheres, and (c) nanoporous $\text{Pt}_{30}\text{Pd}_{27}\text{Cu}_{43}$ spheres.

The electronic states of Pd, Pt, and Cu in the nanoporous PtPdCu spheres were investigated by X-ray photoelectron spectroscopy (XPS). As shown in Figure 5.2.4a, the Pt^0 4f doublet located at 71.1 eV and 74.5 eV can be observed. Figure 5.2.4b shows that the binding energy of Cu 2p_{3/2} and Cu 2p_{1/2} located at 932.1 eV and 951.8 eV can be ascribed to metallic Cu^0 . It has been generally known that Cu is easily oxidized in air, but the Cu atoms in the alloy state are stable. The binding energies at 335.2 eV and 340.5 eV are assigned to the Pd 3d_{5/2} and Pd 3d_{3/2} (Figure 5.2.4c). The Pt 4f binding energy in ternary nanoporous PtPdCu spheres negatively shift (around 0.2 eV) compared to that in the commercial Pt black, indicating that Pt atoms would accept a partial charge transferred (Figure 5.2.4d).^[15] This change in the electronic state of Pt further confirms the formation of an alloy phase. The peaks of these elements indicate that metallic state of Pt, Pd and Cu exist

in the sample.

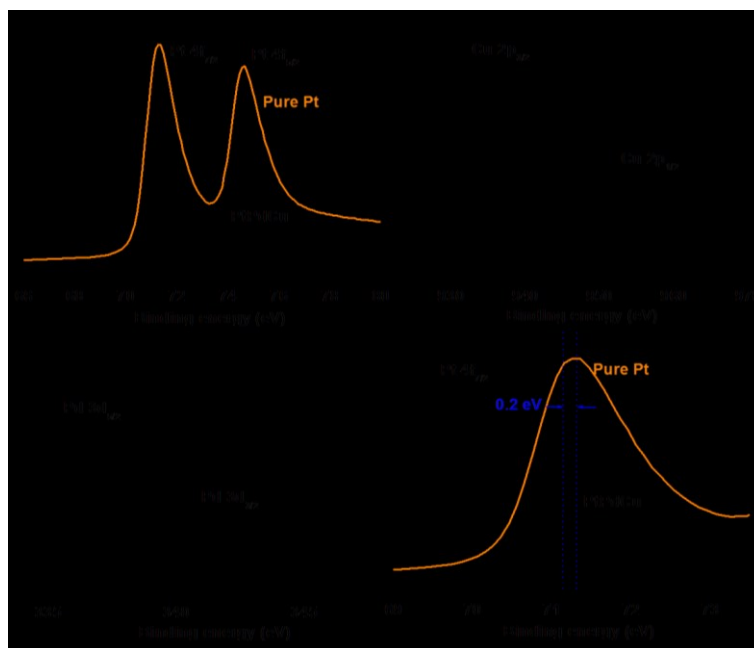


Figure 5.2.4 High resolution XPS spectra of the typical nanoporous PtPdCu spheres ((a) Pt $4f$, (b) Cu $2p$, (c) Pd $3d$, and (d) Comparison of the XPS spectra of the Pt $4f_{7/2}$ for both PtPdCu spheres and pure Pt).

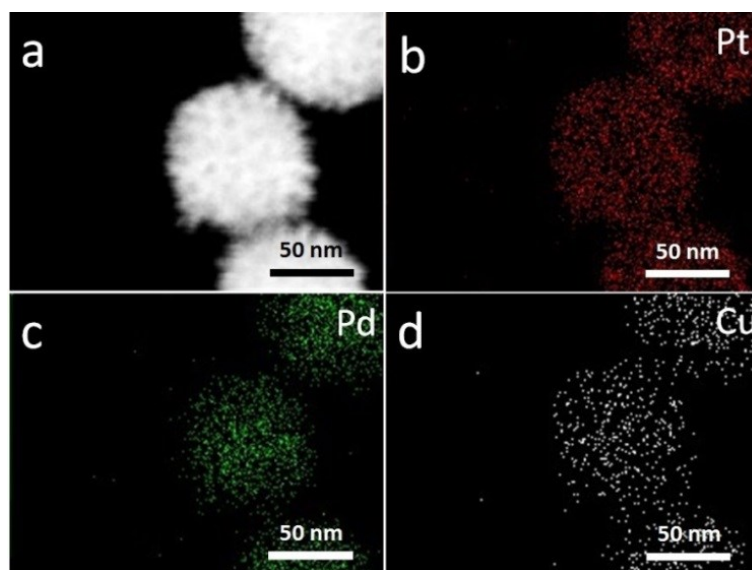


Figure 5.2.5 (a) High-angle annular dark-field scanning TEM (HAADF-STEM) showing the nanoporous structure, and (b-d) elemental mapping images of the typical nanoporous PtPdCu spheres.

Considering the standard reduction potentials of each precursor, it is expected that a Pt/Pd rich core is preferentially formed, followed by the growth of a Cu-rich shell in the ternary PtPdCu spheres. In the present system, however, Pd, Pt, and Cu are uniformly distributed, as shown in the elemental mapping images (**Figure 5.2.5**). It was observed that the reduction of the Cu precursor only occurs when a second or third

metal precursor was mixed with the Cu precursor (e.g., Pd/Cu, Pt/Cu, or Pd/Pt/Cu) (**Figure 5.2.6**). These results indicate that the reduction of Cu precursor only takes place with the trigger of the preformed noble metal nanocrystal seeds. At the initial stage, the noble metal nuclei are reduced and serve as seeds to induce the formation of Cu atoms on the surface of noble metal nuclei.^[16] Afterwards, the Cu atoms mixed with the noble metal atoms through interdiffusion processes.^[16b,17]

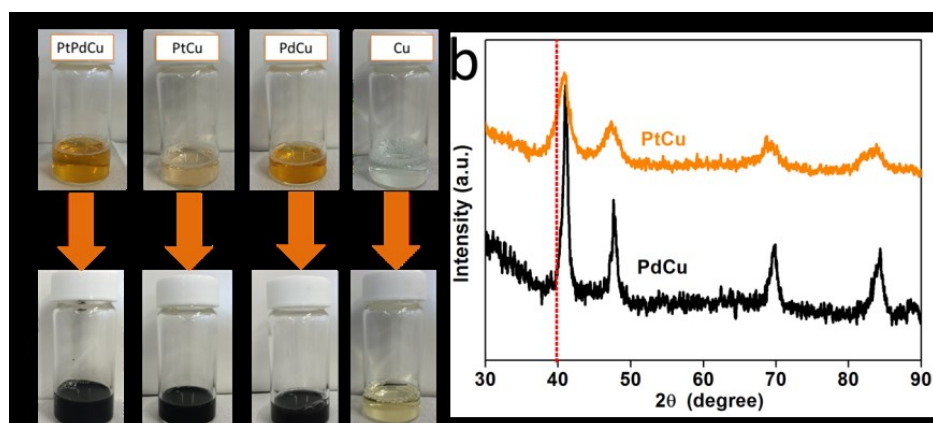


Figure 5.2.6 (a) Photographs of different precursors before and after reduction reaction, (b) XRD patterns of binary PtCu, and binary PdCu nanostructure obtained in (a).

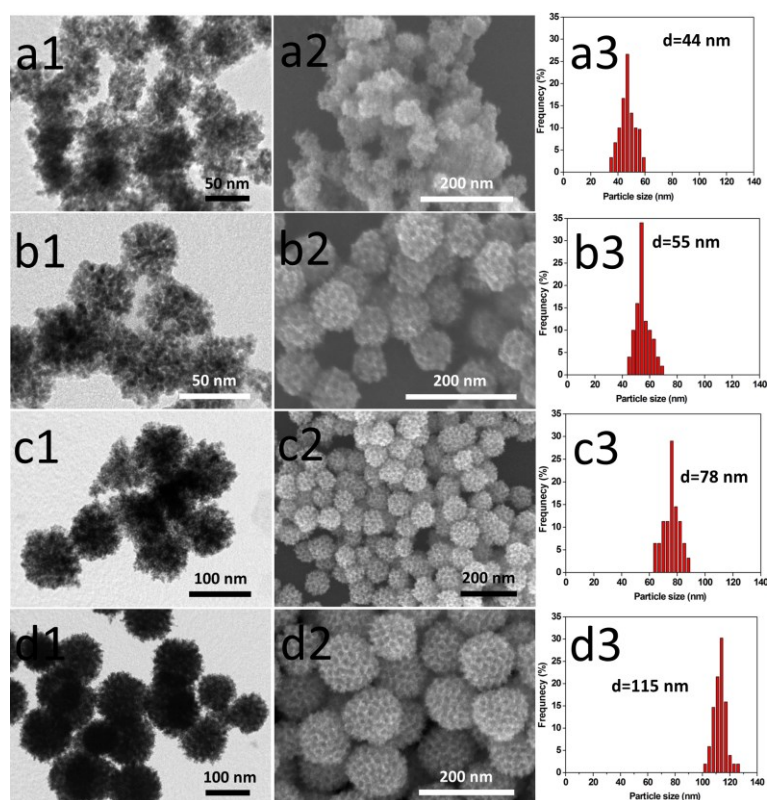


Figure 5.2.7 TEM, SEM images and particle sizes distributions of the samples taken at different reaction times: (a) 3

min, (b) 30 min, (c) 60 min and (d) 90 min.

We further studied the time-dependent morphological change by SEM and TEM. In **Figure 5.2.7a**, the TEM image shows that at the beginning of the reaction (3 min), small-sized particles (around 44 nm). At this time, the nanoporous structure is not well developed on the particle surface. With increasing the reaction time, the diameter of the particles expands up to ~55 nm (**Figure 5.2.7b**) (30 min) then to ~78 nm (**Figure 5.2.7c**) (60 min). During the particle growth, the nanoporous structure becomes prominent as the particle size increases. When the reaction time is further extended to 90 min, the size of nanoparticles reaches around 115 nm (**Figure 5.2.7d**). It has been recognized that F127 can be served as both stabilizing agent and pore-shaping agent during the synthesis of nanoporous oxide, nanoporous carbon, and nanoporous metals.^[18] Without the addition of F127, only non-porous aggregates were obtained. When a smaller amount of F127 (3 mg) was used, similar nanoporous structure was observed, but some particles were significantly aggregated. Thus, the insufficient amount of F127 cannot inhibit particle aggregation effectively. When the amount of F127 was increased up to 50 mg, the desired ternary PtPdCu spheres were found without any by-products. In the solution, the dissolved metal species are coordinated by water molecules to form metal-aqua complexes. The coordinated water molecules usually interact with ethylene oxide (EO) groups of the F127 micelles, as demonstrated in our previous studies.^[1a,8a] Therefore, the metal-aqua complexes dissolving in the solution are incorporated in the PEO shell region of the micelles. The F127 micelles can directly act as a structural directing agent. The above results reveal that the F127 play an important role in formation of both the spherical shape and the nanoporous structure.

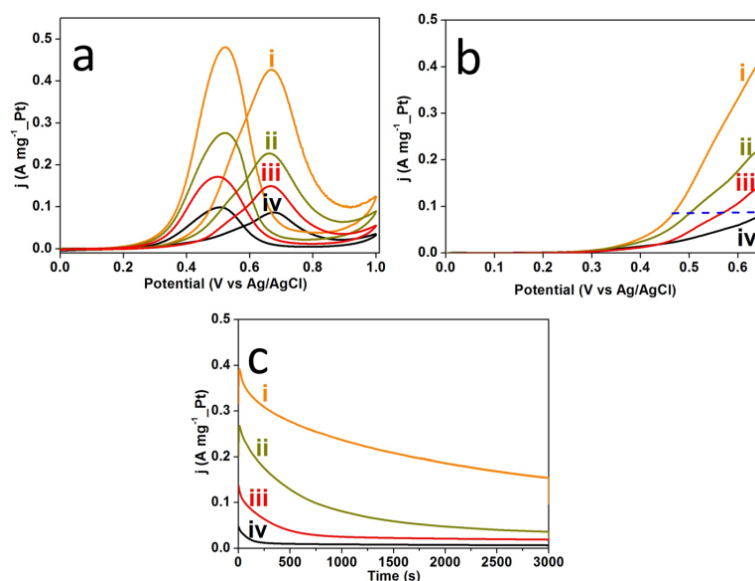


Figure 5.2.8 (a) cyclic voltammograms, (b) linear-sweep voltammograms, and (c) chronoamperometric curves

(recorded at 0.6 V) for methanol oxidation reactions catalyzed by (i) nanoporous PtPdCu catalyst, (ii) binary nanoporous PtPd catalyst, (iii) dendritic Pt catalyst and (iv) Pt black catalyst.

To evaluate the performance of the ternary nanoporous PtPdCu spheres, the electrochemical catalytic activity toward methanol oxidation reaction was investigated. Nanoporous PtPd spheres, dendritic Pt nanoparticles, and Pt black were used for comparison. **Figure 5.2.8a** shows the typical cyclic voltammograms (CVs) of methanol oxidation in 0.5 M H₂SO₄ containing 0.5 M methanol solution at a scan rate of 50 mV s⁻¹ on ternary nanoporous PtPdCu catalyst, binary nanoporous PtPd catalyst, dendritic Pt catalyst and Pt black catalyst. All the current densities were normalized by the Pt mass (mass activity). All the catalysts exhibited typical features of methanol oxidation performance on the Pt surface. The as-prepared nanoporous ternary PtPdCu catalyst exhibit superior electrochemical activity as its current densities is 0.43 A mg⁻¹_Pt, which is about 1.7, 2.8 and 4.9 times than that of binary nanoporous PtPd (0.252 A mg⁻¹_Pt), dendritic Pt nanoparticles (0.153 A mg⁻¹_Pt), and Pt (0.087 A mg⁻¹_Pt) black catalysts, respectively. This result highly supports the assumption that ternary compositions in all-metal catalysts have higher catalytic activity than unitary or binary counterparts due to the synergetic function of individual components. Furthermore, our as-prepared ternary nanoporous PtPdCu spheres exhibited a negatively-shifted onset potential for electrochemical oxidation of methanol compared to that of binary nanoporous PtPd, and Pt black catalysts, indicating that the methanol oxidation reactions were facilitated (**Figure 5.2.8b**).

The origin of the enhancement in MOR for ternary nanoporous PtPdCu spheres with three-dimensional nanoporous architectures can be explained by composition and porous structure effects. Firstly, in the PtPdCu alloy system, the electronic structure modification (lowering d-band shift) of Pt surface by alloying with heteroatoms (*e.g.*, Cu or Pd), as demonstrated in the XPS analysis, can promote the catalytic activity,^[10,19] which has been commonly observed in Pt-based alloys.^[20] Second, the enhanced activity may be attributed to the nanoporous structure with high surface area to facilitate the diffusion of reactant/product species.^[21]

Compared to previously reported Pt-based catalysts (**Table 5.2.1**), our prepared ternary nanoporous PtPdCu catalyst exhibits higher current densities, showing the potential of this material for practical electrocatalytic applications in methanol oxidation reaction. **Figure 5.2.8c** clearly reveals that both the ternary nanoporous PtPdCu catalyst and binary PtPd have a higher durability toward methanol oxidation compared with nanoparticles because the nanoporous structure provides a superior stability by preventing aggregation.

Table 5.2.1 Comparison of the activity of ternary nanoporous PtPdCu spheres with previous reported Pt-based

catalysts

Sample names	Electrolytes	Scan rate (mV s ⁻¹)	Mass activity (A mg ⁻¹ _Pt)	Reference
Nanoporous PtPdCu nanoparticles	0.5 M H ₂ SO ₄ +0.5 M CH ₃ OH	50	0.43	Present work
Dendritic Au@Pt nanoparticles	0.5 M H ₂ SO ₄ +0.5 M CH ₃ OH	50	0.12	[22]
Core-shell Ag@Pt nanoparticles	0.5 M H ₂ SO ₄ +0.5 M CH ₃ OH	50	0.15	[23]
Nanodendrites PtCu	0.5 M H ₂ SO ₄ +1 M CH ₃ OH	50	0.34	[17a]
Core-shell Pd@Pt	0.1 M HClO ₄ +0.5 M CH ₃ OH	50	0.35	[24]
Hollow Pt-Ru	0.5 M H ₂ SO ₄ +0.5 M CH ₃ OH	50	0.38	[3b]
Nanoflower Pt ₃ Co	0.1 M HClO ₄ +1.0 M CH ₃ OH	50	0.39	[25]
Concave PtPdCu	0.1 M HClO ₄ +1.0 M CH ₃ OH	50	0.16	[19c]

5.2.4. Conclusion

In summary, we have demonstrated a facile aqueous-phase method for the fabrication of ternary PtPdCu spheres with 3D nanoporous structure. F127 plays a critical role in formation of the porous structure and in giving a spherical morphology. The electrocatalytic activity of this catalyst toward methanol oxidation was also evaluated in comparison with binary nanoporous PtPd and Pt black catalysts. Due to the porous effect, the ternary nanoporous PtPdCu catalyst has a superior activity than the corresponding binary nanoporous PtPd, dendritic Pt nanoparticles and Pt black catalysts. In addition, this facile and simple synthetic procedure can be extended to the fabrication of many other ternary metal catalysts by selecting appropriate precursor solutions, which will lead to favorable compositions.

References

- [1] (a) C. Li, T. Sato, Y. Yamauchi, *Angew. Chem. Int. Ed.*, 2013, **52**, 8050; (b) Q. Li, P. Xu, B. Zhang, G. Wu, H. Zhao, E. Fu, H. L. Wang, *Nanoscale*, 2013, **5**, 7397; (c) L. Wang, Y. Yamauchi, *Chem. Mater.* 2009, **21**, 3562-3569; (d) X. Huang, Z. Zhao, J. Fan, Y. Tan, N. Zheng, *J. Am. Chem. Soc.*, 2011, **133**, 4718; (e) T. Yu, D. Y. Kim, H. Zhang, Y. Xia, *Angew. Chem. Int. Ed.*, 2011, **50**, 2773.
- [2] (a) B. Lim, M. Jiang, P. H. Camargo, E. C. Cho, J. Tao, X. Lu, Y. Zhu, Y. Xia, *Science*, 2009, **324**, 1302; (b) C. Chen, Y. Kang, Z. Huo, Z. Zhu, W. Huang, H. L. Xin, J. D. Snyder, D. Li, J. A. Herron, M. Mavrikakis, M. Chi, K. L. More, Y. Li, N. M. Markovic, G. A. Somorjai, P. Yang, V. R. Stamenkovic, *Science*, 2014, **343**, 1339.
- [3] (a) Y. C. Tseng, H. S. Chen, C. W. Liu, T. H. Yeh, K. W. Wang, *J. Mater. Chem. A*, 2014, **2**, 4270; (b) H. A. Esfahani, J. Liu, M. Hu, N. Miyamoto, S. Tominaka, K. C. W. Wu, Y. Yamauchi, *Small*, 2013, **9**, 1047; (c) C. Li, M. Imura, Y. Yamauchi, *Chem. Eur. J.* 2014, **20**, 3277; (d) C. Hu, X. Zhai, Y. Zhao, K. Bian, J. Zhang, L. Qu, H. Zhang, H. Luo, *Nanoscale*, 2014, **6**, 2768; (e) X. Niu, M. Lan, H. Zhao, C. Chen, *Chem. Eur. J.*, 2013, **19**, 9534.
- [4] (a) C. Hu, H. Cheng, Y. Zhao, Y. Hu, Y. Liu, L. Dai, L. Qu, *Adv. Mater.*, 2012, **24**, 5493; (b) Y. Zhang, M. Janyasupab, C. W. Liu, X. Li, J. Xu, C. C. Liu, *Adv. Funct. Mater.*, 2012, **22**, 3570; (c) F. Taufany, C. J. Pan, J. Rick, H. L. Chou, M. C. Tsai, B. J. Hwang, D. G. Liu, J. F. Lee, M. T. Tang, Y. C. Lee, C. I. Chen, *ACS Nano*, 2011, **5**, 9370.
- [5] H. H. Li, S. Zhao, M. Gong, C. H. Cui, D. He, H. W. Liang, L. Wu, S. H. Yu, *Angew. Chem. Int. Ed.*, 2013, **52**, 7472.
- [6] (a) S. Guo, S. Zhang, X. Sun, S. Sun, *J. Am. Chem. Soc.*, 2011, **133**, 15354; (b) J. Luo, L. Y. Wang, D. Mott, P. N. Njoki, N. Kariuki, C. J. Zhong, T. He, *J. Mater. Chem.*, 2006, **16**, 1665; (c) F. Ren, C. Wang, C. Zhai, F. Jiang, R. Yue, Y. Du, P. Yang, J. Xu, *J. Mater. Chem. A*, 2013, **1**, 7255.
- [7] (a) Y. X. Zhang, H. C. Zeng, *J. Phys. Chem. C*, 2007, **111**, 6970; (b) H. Li, Y. J. Li, L. L. Sun, X. L. Zhao, *Electrochim. Acta*, 2013, **108**, 74; (c) S. J. Guo, S. J. Dong, E. K. Wang, *ACS Nano*, 2010, **4**, 547.
- [8] (a) H. A. Esfahani, M. Imura, Y. Yamauchi, *Angew. Chem. Int. Ed.*, 2013, **52**, 13611; (b) L. Wang, Y. Yamauchi, *Chem. Eur. J.* 2011, **17**, 8810; (c) L. Wang, Y. Yamauchi, *J. Am. Chem. Soc.*, 2013, **135**, 16762; (d) Y. J. Song, R. M. Garcia, R. M. Dorin, H. R. Wang, Y. Qiu, E. N. Coker, W. A. Steen, J. E. Miller, J. A. Shelnut, *Nano Lett.*, 2007, **7**, 3650; (e) X. W. Teng, X. Y. Wang, S. Maksimuk, H. Yang, *Small*, 2006, **2**, 249.
- [9] C. Li, M. Imura, Y. Yamauchi, *Phys. Chem. Chem. Phys.*, 2014, **16**, 8787.
- [10] H. H. Li, C. H. Cui, S. Zhao, H.-B. Yao, M. R. Gao, F. J. Fan, S. H. Yu, *Adv. Energy Mater.*, 2012, **2**, 1182.
- [11] S. V. Bagul, S. D. Chavhan, R. Sharma, *J. Phys. Chem. Solids*, 2007, **68**, 1623.
- [12] (a) C. Li, Y. Yamauchi, *Chem. Eur. J.*, 2014, **20**, 729; (b) D. Xu, S. Bliznakov, Z. Liu, J. Fang, N. Dimitrov, *Angew. Chem. Int. Ed.*, 2010, **49**, 1282.

- [13] (a) D. Sun, G. Zhang, X. Jiang, J. Huang, X. Jing, Y. Zheng, J. He, Q. Li, *J. Mater. Chem. A*, 2014, **2**, 1767-1773; (b) W. Li, X. Zhao, T. Cochell, A. Manthiram, *Appl. Catal. B: Environ.*, 2013, **129**, 426; (c) C. Wang, B. Peng, H. N. Xie, H. X. Zhang, F. F. Shi, W. B. Cai, *J. Phys. Chem. C*, 2009, **113**, 13841; (d) Y. Jiang, Y. Jia, J. Zhang, L. Zhang, H. Huang, Z. Xie, L. Zheng, *Chem. Eur. J.*, 2013, **19**, 3119.
- [14] (a) X. H. Zhong, Y. Y. Feng, W. Knoll, M. Y. Han, *J. Am. Chem. Soc.*, 2003, **125**, 13559; (b) D. Xu, Z. Liu, H. Yang, Q. Liu, J. Zhang, J. Fang, S. Zou, K. Sun, *Angew. Chem. Int. Ed.*, 2009, **48**, 4217.
- [15] (a) X. Yu, D. Wang, Q. Peng, Y. Li, *Chem. Eur. J.*, 2013, **19**, 233; (b) G. Wang, B. Huang, L. Xiao, Z. Ren, H. Chen, D. Wang, H. D. Abruña, J. Lu, L. Zhuang, *J. Am. Chem. Soc.*, 2014, **136**, 9643.
- [16] (a) D. Wang, Y. Li, *J. Am. Chem. Soc.*, 2010, **132**, 6280; (b) D. Wang, Y. Li, *Adv. Mater.*, 2011, **23**, 1044.
- [17] (a) M. Gong, G. Fu, Y. Chen, Y. Tang, T. Lu, *ACS Appl. Mater. Inter.*, 2014, **6**, 7301; (b) W. Chen, R. Yu, L. Li, A. Wang, Q. Peng, Y. Li, *Angew. Chem. Int. Ed.*, 2010, **49**, 2917; (c) K. Lee, S. W. Kang, S. U. Lee, K. H. Park, Y. W. Lee, S. W. Han, *ACS Appl. Mater. Inter.*, 2012, **4**, 4208.
- [18] (a) X. Wang, C. Liang, S. Dai, *Langmuir*, 2008, **24**, 7500; (b) L. Wang, Y. Yamauchi, *J. Am. Chem. Soc.*, 2009, **131**, 9152; (c) J. Wei, D. Zhou, Z. Sun, Y. Deng, Y. Xia, D. Zhao, *Adv. Funct. Mater.*, 2013, **23**, 2322; (d) R. Liu, Y. Shi, Y. Wan, Y. Meng, F. Zhang, D. Gu, Z. Chen, B. Tu, D. Zhao, *J. Am. Chem. Soc.*, 2006, **128**, 11652.
- [19] (a) S. Zhang, S. Guo, H. Zhu, D. Su, S. Sun, *J. Am. Chem. Soc.*, 2012, **134**, 5060; (b) X. Huang, Y. Chen, E. Zhu, Y. Xu, X. Duan, Y. Huang, *J. Mater. Chem. A*, 2013, **1**, 14449; (c) A. X. Yin, X. Q. Min, W. Zhu, W. C. Liu, Y. W. Zhang, C. H. Yan, *Chem. Eur. J.*, 2012, **18**, 777; (d) Y. Qi, T. Bian, S. I. Choi, Y. Jiang, C. Jin, M. Fu, H. Zhang, D. Yang, *Chem. Commun.*, 2014, **50**, 560.
- [20] (a) Y. Tong, H. S. Kim, P. K. Babu, P. Waszczuk, A. Wueckowski, E. Oldfield, *J. Am. Chem. Soc.*, 2002, **124**, 468, (b) C. Zhang, S. Y. Hwang, A. Trout, Z. Peng, *J. Am. Chem. Soc.*, 2014, **136**, 7805; (c) S. I. Choi, S. Xie, M. Shao, J. H. Odell, N. Lu, H. C. Peng, L. Protsailo, S. Guerrero, J. Park, X. Xia, J. Wang, M. J. Kim, Y. Xia, *Nano Lett.*, 2013, **13**, 3420.
- [21] (a) M. Wang, W. Zhang, J. Wang, A. Minett, V. Lo, H. Liu, J. Chen, *J. Mater. Chem. A*, 2013, **1**, 2391; (b) L. X. Ding, A. L. Wang, G. R. Li, Z. Q. Liu, W. X. Zhao, C. Y. Su, Y. X. Tong, *J. Am. Chem. Soc.*, 2012, **134**, 5730; (c) C. Li, B. Jiang, M. Imura, V. Malgras, Y. Yamauchi, *Chem. Commun.*, 2014, **50**, 15337.
- [22] H. A. Esfahani, L. Wang, Y. Nemoto, Y. Yamauchi, *Chem. Mater.*, 2010, **22**, 6310.
- [23] C. Li, Y. Yamauchi, *Phys. Chem. Chem. Phys.*, 2013, **15**, 3490.
- [24] Y. Kim, Y. W. Lee, M. Kim, S. W. Han, *Chem. Eur. J.*, 2014, **20**, 7901-.
- [25] J. N. Zheng, L. L. He, C. Chen, A. J. Wang, K. F. Ma, J. J. Feng, *J. Power Sources*, 2014, **268**, 744.

Chapter 6. Synthesis of Pt-free Metallic Electrocatalysts for Electrochemical Application

6.1. Surfactant-Directed Synthesis of Mesoporous Pd Films with Perpendicular Mesochannels as Efficient Electrocatalysts

6.1.1. Introduction

‘Surfactant assembly’ provides a general way for preparing ordered mesoporous materials.^[1] Many mesoporous materials with different mesostructures and morphologies have been obtained by optimizing the synthetic conditions, even a same surfactant can result in different mesopore arrangements by changing the concentration. Among various morphologies, mesoporous films have sparked many keen interests in a wide range of potential applications (*e.g.*, catalysis, energy storage, photonic therapy) due to their high accessible active surface, superior structural stability and unique functions.^[2] In general, the surfactant micelles tend to orient parallel to the substrate in order to reduce the surface energy at the interface, resulting in mesochannels inevitably oriented parallel to the substrate and making the internal mesopores inaccessible. Considering practical applications, a precise control over the mesopore orientation is a critical issue to overcome in order to fully exploit the internal pores. Perpendicularly oriented mesochannels in films are an ideal structure which allows the diffusion of reagents from the exterior region to the inner parts, thus favoring the high utilization efficiency brought by the mesopores.^[3] Although several strategies employing high magnetic field,^[4] electro-assisted self-assembly,^[5] air flow,^[6] confined effect,^[7] and optimal evaporation-induced self-assembly (EISA)^[8] have been previously employed for achieving vertically oriented mesochannels, the compositions in pore walls have been mostly limited to silica, carbons, organosilica, titania, and alumina. To the best of our knowledge, there have been no reports on metal films with perpendicular mesochannels.

Mesoporous metal films possess a high surface area and their fairly stable metallic frameworks provide a large number of catalytically active sites, thereby exhibiting fascinating catalytic properties.^[9] Palladium (Pd) has been well known as an exceptional catalyst for a rich variety of applications, including oxidation of fuels, carbon-carbon coupling reactions and hydrogen storage/detections.^[10] Therefore, mesoporous Pd films with perpendicular mesochannels can bring out many superior electrochemical applications which cannot be achieved by other previously reported mesoporous films.^[4-8] Although several approaches using lyotropic liquid crystals, surfactant micelles, hard-templates have been utilized for the preparation of mesoporous metals,^[11] mesoporous metal films with perpendicular mesochannels have never been achieved.

Herein, I report a sophisticated amperometric approach which reduces the Pd species decorated on the surface of the micelles leading to the formation of continuous Pd films with vertically aligned mesochannels. The resulting mesoporous Pd films distinctly fully exploit the ultra-high surface area ensued from the mesoporous architecture and clearly exhibit linearly increasing electro-catalytic activities with increasing the film

thickness. In this work, a solution containing cationic surfactant, cetylmethylammonium chloride ($C_{16}TAC$), and Na_2PdCl_4 was firstly prepared and used as electrolyte. Then, a conductive Au substrate was employed as a working electrode for the electrodeposition of Pd at a constant potential for 600 s under optimized conditions. After completely removing the surfactants, Pd films with perpendicular mesochannels were obtained.

6.1.2. Experimental Sections

6.1.2.1. Materials

Sodium tetrachloropalladate (Na_2PdCl_4), 0.5 M sulfuric acid, and formic acid were purchased from Nacalai. Co. Cetylmethylammonium chloride solution (25 wt% in water) was purchased from Sigma-Aldrich. All the chemicals were used without further purification.

6.1.2.2. Preparation of Mesoporous Pd Films with Perpendicular Channels

The electrochemical fabrication of mesoporous Pd films was performed by using a CHI 842B electrochemical analyzer (CH Instrument, U.S.) with a standard three-electrode cell system, including an Ag/AgCl (saturated KCl) electrode as the reference electrode, a platinum wire as the counter electrode, and gold-coated silicon (Au-Si) substrate as the working electrode. The Au-Si substrate was set in an aqueous solution (9.0 mL) containing 0.5 mL of cetylmethylammonium chloride solution and 0.5 mL of 40 mM sodium tetrachloropalladate (Na_2PdCl_4) in a water bath pre-heated at 50 °C. Due to the strong interaction between $[C_{16}TA]^+$ and $[PdCl_4]^{2-}$, the precipitate was formed when the Pd precursor was added to the surfactant solution. With the increase of bath temperature (over 50 °C), the mixture becomes transparent. Therefore, here 50 °C was selected in the present work. A constant potential of 0.0 V vs. Ag/AgCl was then used for electrodepositing the mesoporous Pd films with perpendicular channels. The obtained films were then soaked in ethanol for 24 h to thoroughly remove the surfactants, and then dried with nitrogen gas for further characterizations. The electrochemical surface area (ECSA) of the films was calculated according to the method proposed by Woods.^[*J. Electroanal. Chem.* 1971, 31, 29] At a potential of about 1.50 V vs. RHE, a Pd oxide monolayer would form on the Pd surface. With the assumption of $424 \mu C \cdot cm^{-2}$ for the reduction of the Pd oxide, the ECSA of Pd can be calculated. The geometric area of the mesoporous Pd electrode used in this experiment was $0.3 cm^2$. The nonporous Pd films were also prepared following the same procedure, but without adding CTAC.

6.1.2.3. Characterization

Scanning electron microscopy (SEM) images were obtained using a Hitachi HR-SEM SU8000 microscope at an accelerating voltage of 5 kV. Transmission electron microscopy (TEM) and high-resolution TEM (HRTEM) images were taken using a JEOL JEM-2100F microscope at an accelerating voltage of 200 kV. Small angle X-ray scattering (SAXS) profiles were recorded by a Rigaku NANO-Viewer (Cu $K\alpha$ radiation) with a camera length of 700 mm operated

at 40 kV and 30 mA. Wide-angle film X-ray diffraction (XRD) profiles were recorded with a Rigaku SmartLab 3kW-BU diffractometer with monochromated Cu K α radiation.

6.1.2.4. Electrochemical Test

Cyclic voltammograms (CVs) were performed with a CHI 842B electrochemical analyzer (CH Instrument, USA). A conventional three-electrode cell was used, including an Ag/AgCl electrode as a reference electrode, a platinum wire as a counter electrode, and the Pd films (mesoporous Pd, nonporous Pd or Pd black) as a working electrode. In the case of the commercially available Pd black (PdB) catalyst, a glassy carbon electrode (GCE) was used as the working electrode. Prior to the surface coating, the GCE was polished with 1.0 and 0.05 μm alumina powder, rinsed with deionized water and dried under a nitrogen gas flow. 5.0 μg of the PdB suspension was then coated on the surface of the GCE. After drying in atmospheric condition, a Nafion solution (5.0 μL , 0.5 wt%) was subsequently coated on the surface and dried at room temperature before further electrochemical measurements. All potential values were referenced to an Ag/AgCl (saturated KCl) electrode. The formic acid oxidation reaction investigations were carried out in 0.5 M H₂SO₄ solution containing 0.5 M formic acid.

6.1.3. Results and Discussion

The top surface and cross-section of the obtained films were studied by scanning electron microscope (SEM) and transmission electron microscopy (TEM). From the top-view, uniformly sized mesopores are distinctly distributed over the entire area of the film without any defects, cracks, or bumps (**Figure 6.1.1a-b**). The size of the mesopores is homogeneously distributed with a predominant pore size of 2.1 ± 0.2 nm separated by pore walls of 3.3 ± 0.2 nm. Various mesoporous materials have been synthesized using cetyltrimethylammonium chloride/bromide (C₁₆TAC/C₁₆TAB) with the same hydrocarbon chain length as the pore directing agents. The cross-sectional TEM image and the high-angle annular dark-field scanning TEM (HAADF-STEM) image show that cylindrical channels are distributed perpendicular to the substrate (**Figure 6.1.1c-e**). In the high-resolution TEM image, it can be observed that the framework is highly crystallized without any amorphous domains, although the lattice fringes can be slightly distorted at certain locations (**Figure 6.1.1d**). The clear lattice fringes with a constant d spacing of 0.225 nm can be ascribed to the (111) lattice planes of *fcc* Pd crystals. A uniform thickness of 24 nm was distinctly grown on the Au surface (**Figure 6.1.1c**).

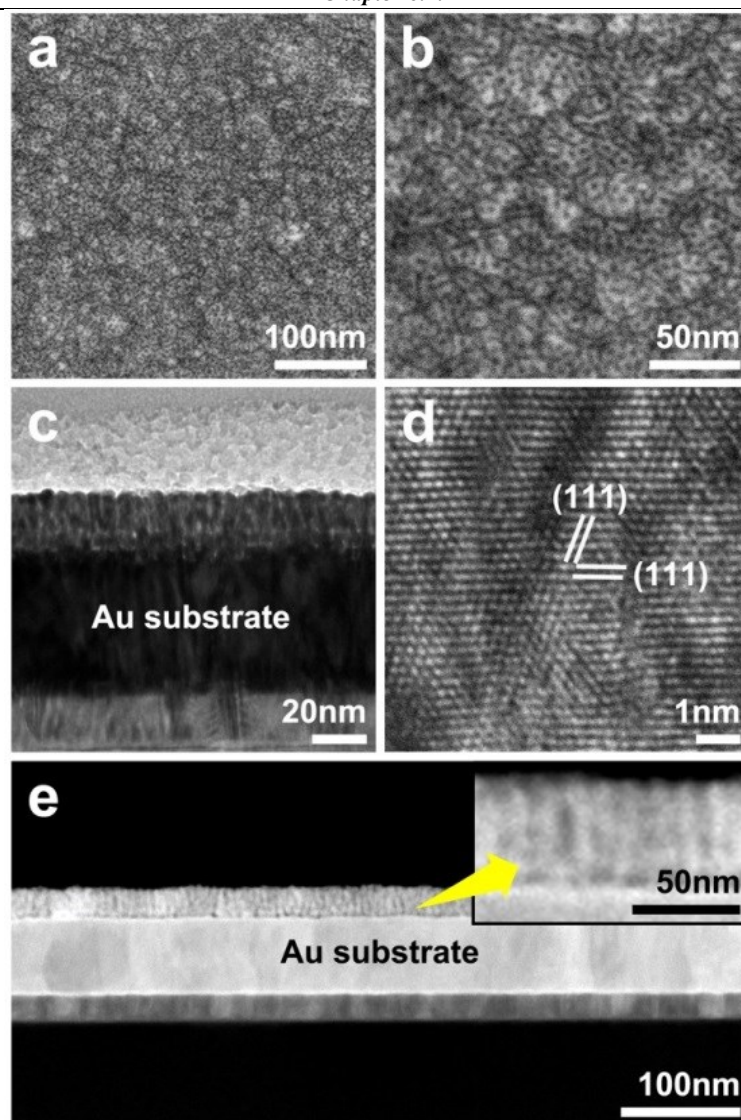


Figure 6.1.1 (a, b) SEM images of the top-surface of the obtained Pd films. (c, d, e) Cross-sectional TEM images of the obtained Pd films [(c) Bright-field TEM image, (d) high resolution TEM image, and (e) HAADF-STEM image].

2D grazing-incidence small-angle X-ray scattering (GI-SAXS) was employed to further confirm the orientation of mesochannels (**Figure 6.1.2**). The two intense spots correspond to the in-plane periodicity of the obtained films (**Figure 6.1.2a**). The absence of out-of-plane periodicity can rule out any possibility of other three-dimensional (3D) mesostructures.^[12] The intensity profile collected in the in-plane direction plotted against q value (**Figure 6.1.2c**) reveals a peak centered at $q=1.17 \text{ nm}^{-1}$ corresponding to a pore-to-pore d -spacing of 5.4 nm. Considering the wall thickness ($\sim 3.3 \text{ nm}$) and the pore size ($\sim 2.1 \text{ nm}$), the GI-SAXS data are in good agreement with the SEM results. The crystalline structure of Pd was examined by wide-angle X-ray diffraction (XRD). The XRD patterns obtained from the electro-deposited films only gave two diffraction peaks assigned to the (111) and (222) diffraction planes of face-centered cubic (fcc) Pd (JCPDS No.

87-643) (**Figure 6.1.2d**), indicating that the Pd crystals have a preferential orientation according to the (111) plane parallel to the substrate on the seed layer (Au). The Pd crystal growth along the [111] direction is consistent with TEM result (**Figure 6.1.2d**).

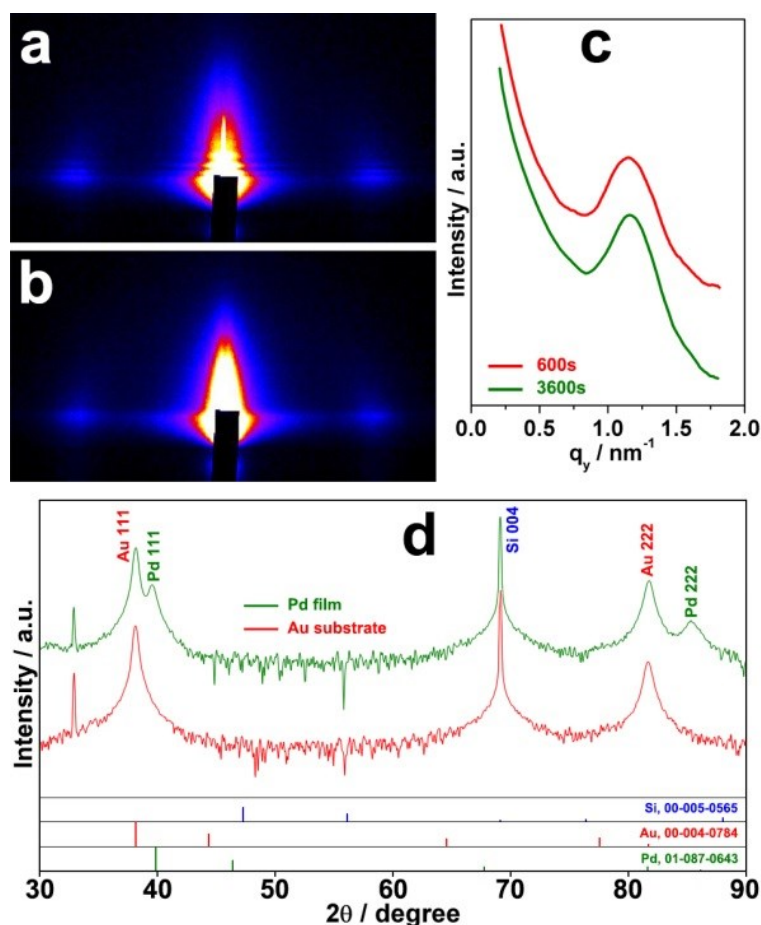


Figure 6.1.2 (a, b) 2D GI-SAXS patterns of the obtained Pd films with perpendicular mesochannels after different deposition times of (a) 600 s and (b) 3600 s. (c) Intensity profile collected in the in-plane direction against q value. (d) Wide-angle XRD patterns of bare Au substrate and the obtained Pd film with perpendicular mesochannels prepared for a deposition time of 600 s.

Conceptually different from the evaporation-induced self-assembly (EISA) method which is generally utilized for preparing mesoporous films,^[13] the electrodeposition approach used in this work allows an easy control over the film thickness by changing the deposition time. From cross-sectional images study, the film thickness was determined to increase linearly with the deposition time, with an average growth rate of 0.076 nm s^{-1} (**Figure 6.1.3**). The 2D GI-SAXS spots are unaffected by increasing the deposition time (**Figure 6.1.2b-c**), suggesting that any film thicknesses can be obtained by choosing a suitable deposition time without any interfering with the perpendicularly aligned mesoporous structures. No difference in the vertically aligned

mesochannels is noticed even when the deposition time increases up to 7200 nm (*i.e.*, The film thickness increases up to 540 nm) (**Figure 6.1.4**).

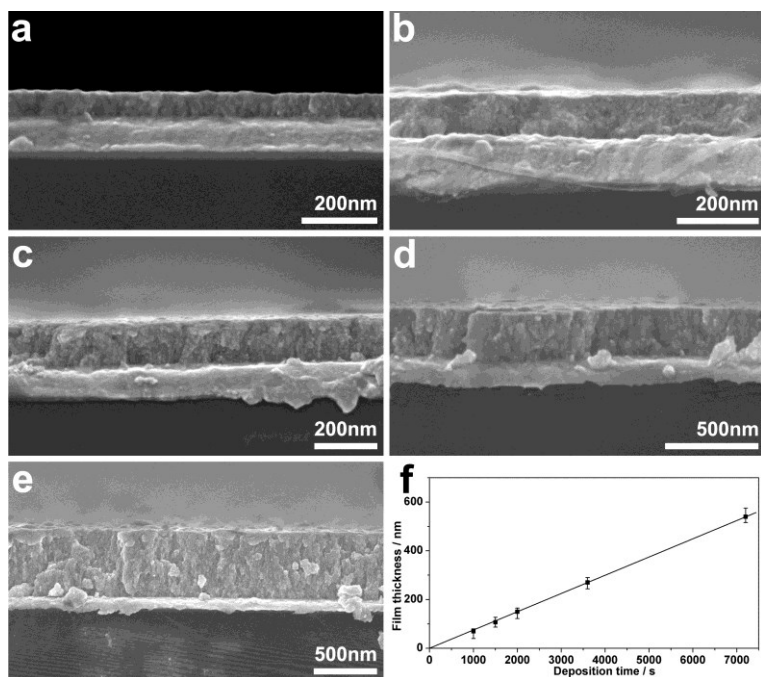


Figure 6.1.3 (a-e) Cross-sectional SEM images of the obtained films with various deposition times. [(a) 1000 s, (b) 1500 s, (c) 2000 s, (d) 3600 s, and (e) 7200 s]. (f) Relationship between the film thickness and the deposition time.

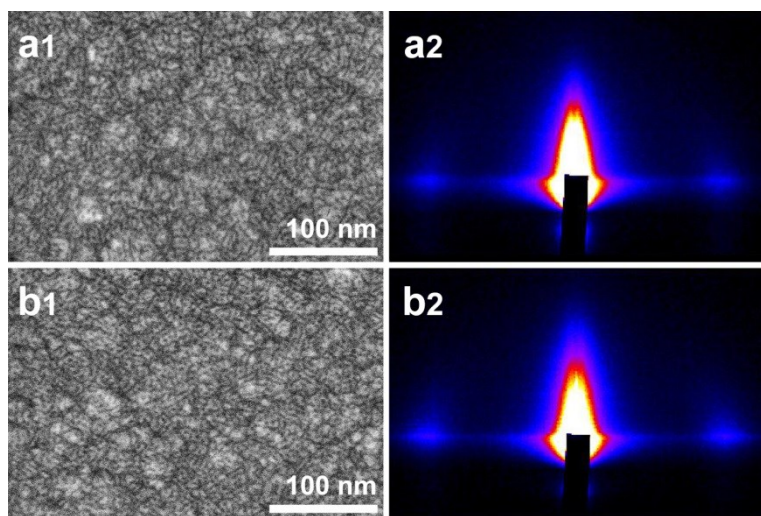


Figure 6.1.4 (a1, b1) Top surface SEM images and (a2, b2) 2D GI-SAXS patterns of the as-prepared Pd films with various thicknesses [(a) 270 nm and (b) 540 nm]. The deposition times are 3600 sec and 7200 sec, respectively.

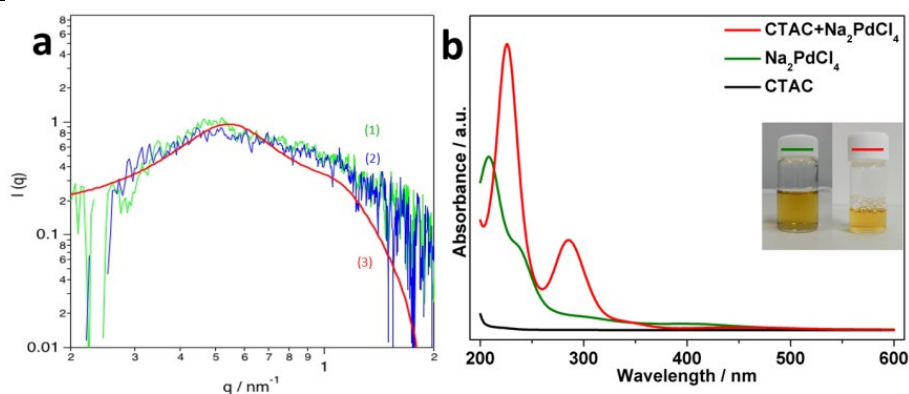


Figure 6.1.5 (a) SAXS patterns of (1) C_{16}TAC solution and (2) $\text{C}_{16}\text{TAC} + \text{Na}_2\text{PdCl}_4$ mixture. The line (3) is the theoretical curve calculated based on the form factor of mono-disperse hard sphere with the radius of 2.2 nm and the structure factor for dispersed spheres. The structure factor is based on Ornstein-Zernike and Percus-Yevick approximations^[2] and is calculated with the parameters of hard-sphere interaction distance ($R_{hs} = 5.9 \text{ nm}$) and the micellar volume fraction ($f = 0.24$). (b) UV-vis spectra of various solutions (Na_2PdCl_4 solution, C_{16}TAC solution, $\text{C}_{16}\text{TAC} + \text{Na}_2\text{PdCl}_4$ mixture). The photographs of Na_2PdCl_4 solution before and after mixing with C_{16}TAC are shown in the inset.

The surfactant assembly, which is usually concentration-dependent, is critical to determine the final mesoporous structure. As the surfactant concentration increases, the surfactant assembly changes from free surfactants to spherical and cylindrical micelles.^[14] In our system, the concentration of C_{16}TAC is 43 mM, which is higher than its critical micelle concentration (CMC, 16 mM), suggesting the formation of spherical micelles in the electrolyte (**Figure 6.1.5a**). It has been known that the strongly charged anionic inorganic species interacting with the cationic surfactants.^[15] The interactions between the C_{16}TAC micelles and the Pd precursors in the electrolyte were studied by UV-vis absorption (**Figure 6.1.5b**). The $[\text{PdCl}_4]^{2-}$ species exhibit two absorption maxima at 210 and 235 nm.^[16a] After being mixed with C_{16}TAC micelle solution, a significant change is observed with the newly formed absorption bands at 226 nm and 285 nm, which are attributed to the interactions between the anionic $[\text{PdCl}_4]^{2-}$ species and the cationic $[\text{C}_{16}\text{TA}]^+$ surfactants.^[16b] From the small-angle X-ray scattering (SAXS) measurement of the electrolyte after the addition of $[\text{PdCl}_4]^{2-}$ species, it is found that the spherical micelles are still retained (**Figure 6.1.5a**). It is probably that the spherical micelles decorated with $[\text{PdCl}_4]^{2-}$ species approach the working electrode when an exterior potential is applied. The Pd species are reduced initially on the working electrode surface. Due to its reduction, each $[\text{PdCl}_4]^{2-}$ releases four chloride ions, which then probably binds to the surfactants more strongly and induce the spherical-to-rod transition. The formed rod-like micelles can be well oriented perpendicular on its surface due to its stronger affinity with the hydrophobic core than the hydrophilic shell of the micelles, although cylinder micelles and

lamellar phases generally have a strong tendency to align parallel to the substrate surfaces due to their lower energy.^[17] The subsequent Pd deposition and re-assembly of surfactant molecules lead to a continuous growth along the longitudinal direction of the cylindrical micelles perpendicularly orientated on the substrate (**Figure 6.1.6**).

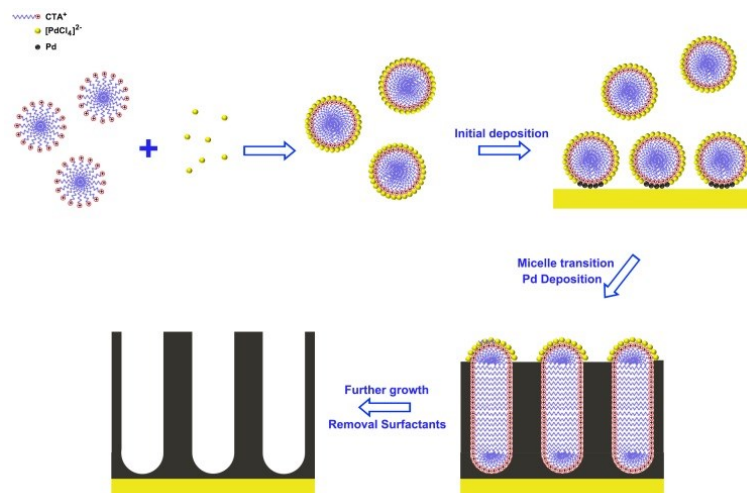


Figure 6.1.6 Scheme illustrating the formation of mesoporous Pd films with perpendicular mesochannels obtained from dynamic transition of spherical micelle assemblies.

The retention of the ordered mesophases formed by the surfactant assembly is critical for designing the pore walls. In the case of metals, their crystallized walls are formed simultaneously with the reduction of metal species, unlike post-treated crystallized/graphitized pore walls. In the present system, the crystal growth can be controlled by tuning the reduction conditions. Especially, electrochemical reduction is useful for strict controls of the growth speed and the crystallinity of the deposited metals. Various constant potentials in the range of -0.5 V and 0.3 V (*vs.* Ag/AgCl) were employed for the electrodeposition of Pd films. The mesoporous structures in the obtained films were studied by SEM and 2D GI-SAXS (**Figure 6.1.7**). During the formation of mesoporous metals, the reduced metal atoms are primarily formed at the hydrophilic region of the micelles where they agglomerate and coalesce until a thick wall is obtained, giving the structure enough mechanical stability. A slow reduction reaction generally allows the surfactant templates to be distorted so large crystals can grow.^[18a] When a high potential is applied (*e.g.*, 0.2 V, and 0.3 V (*vs.* Ag/AgCl) in the present work), the reduction of the Pd precursors becomes slower and the mesoporous structures cannot be achieved (**Figure 6.1.7**). Therefore, an appropriate reduction rate is necessary for the preparation of mesoporous metals. Well-ordered mesoporous structures can be obtained when a potential in the range of 0.1 V and -0.1 V (*vs.* Ag/AgCl) is applied, as evidenced by the top-surface SEM images and the 2D GI-SAXS profiles (**Figure**

6.1.7). When the reduction rate is further increased, the initially formed Pd crystals are larger and end up exceeding the size of the hydrophilic volume of the micelles, destroying the ordering of the micelle assembly (Figure 6.1.7).^[18b] Through the above results, a moderate potential (*i.e.*, -0.1 V, 0 V, and 0.1 V (*vs.* Ag/AgCl)) is essential to control the Pd reduction rate without interfering with the micelle assembly.

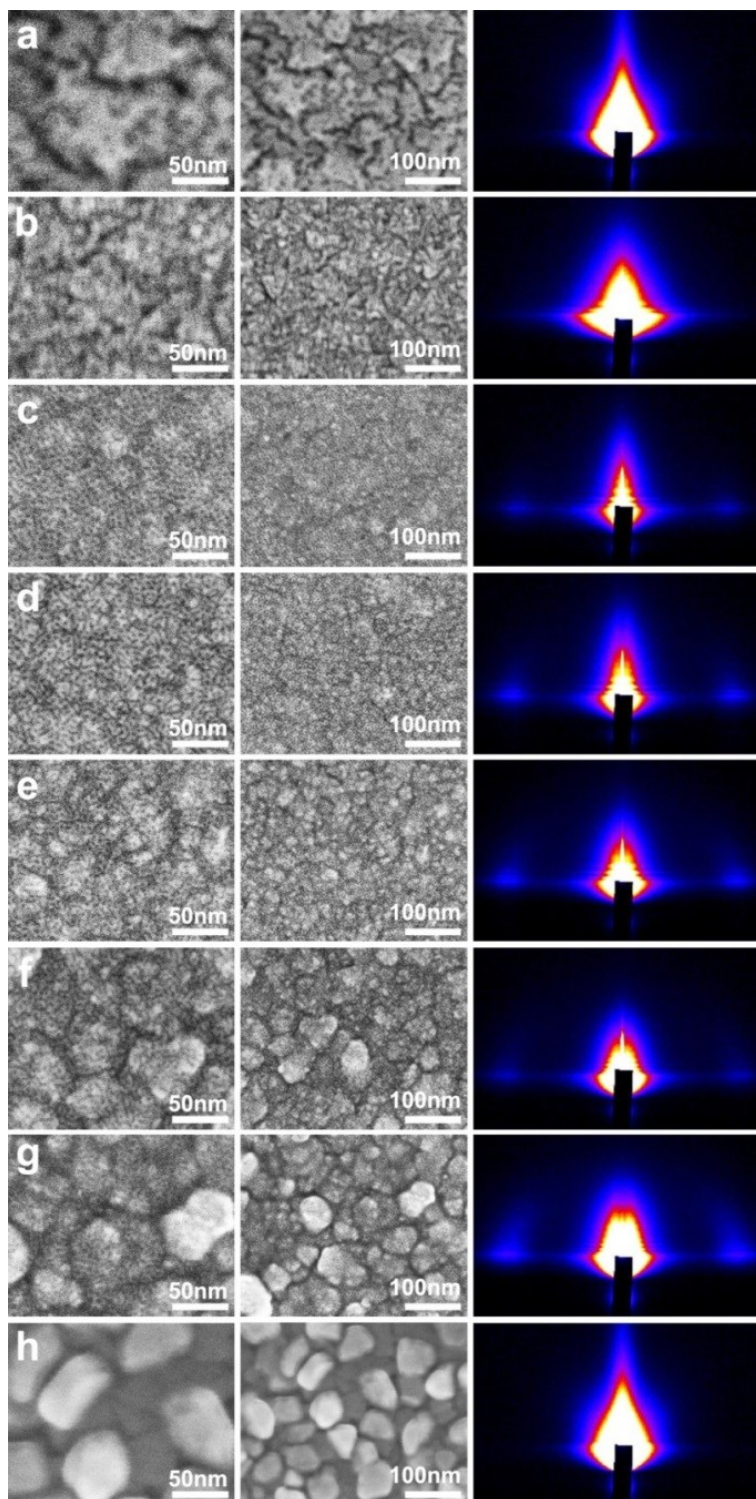


Figure 6.1.7 SEM and 2D GI-SAXS patterns of the mesoporous Pd films under various potentials [(a) 0.3 V (*vs.* Ag/AgCl), (b) 0.2 V (*vs.* Ag/AgCl), (c) 0.1 V (*vs.* Ag/AgCl), (d) 0.0 V (*vs.* Ag/AgCl), (e) -0.1 V (*vs.* Ag/AgCl), (f) -0.2 V

(vs. Ag/AgCl), (g) -0.3 V (vs. Ag/AgCl), and (h) -0.5 V (vs. Ag/AgCl), respectively.].

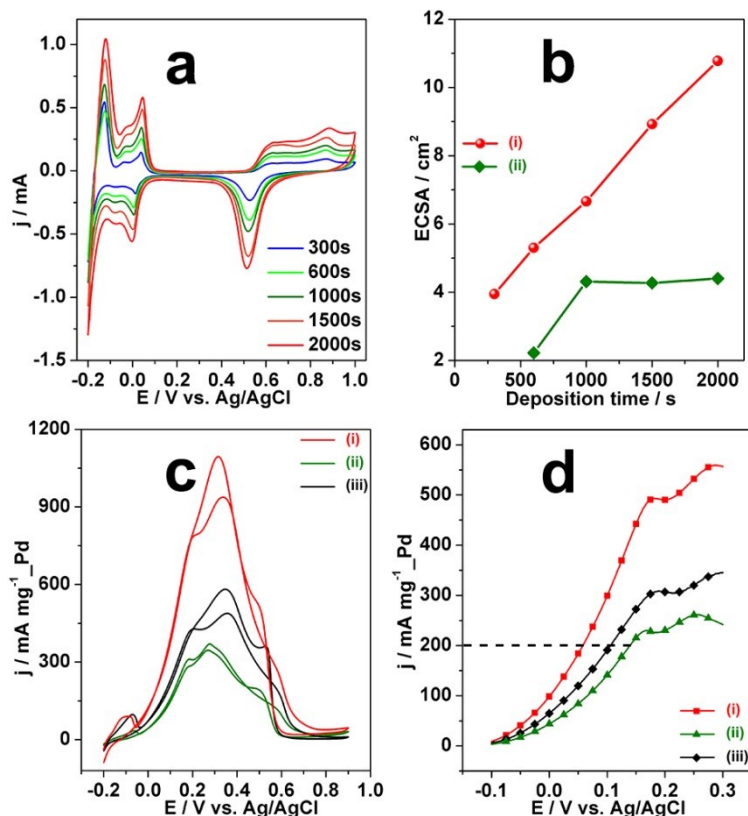


Figure 6.1.8 (a) CVs in 0.5 M H₂SO₄ of the obtained Pd films with perpendicular mesochannels with various film thicknesses (The deposition times are 300 s, 600 s, 1000 s, 1500 s, 2000 s, respectively). (b) Relationship between the ECSAs and the deposition times. The mesoporous Pd film (i) is compared to a nonporous Pd film (ii). (c) CV curves and (d) potential dependent steady-state current density for formic acid oxidation catalyzed by a Pd film with perpendicular mesochannels (i), a nonporous Pd film (ii), and a commercially available PdB catalyst (iii). The formic acid oxidation reaction is performed in 0.5 M H₂SO₄ containing 0.5 M HCOOH.

Motivated by the fact that the perpendicularly aligned mesochannels have naturally a superior mass transportation than other architectures, electrochemical measurements were carried out. Here, cyclic voltammograms (CVs) in a 0.5 M H₂SO₄ solution were firstly performed on the obtained Pd films with various thicknesses. A noticeable current increase in the hydrogen and oxygen adsorption/desorption regions was observed (**Figure 6.1.8a**). The electrochemical surface area (ECSA) was calculated by using the method proposed by Woods (see Supplementary Information for details). The ECSA was determined to increase linearly with the film thickness (*i.e.*, deposition time), unlike nonporous Pd films prepared without surfactants (**Figure 6.1.8b**). The volume-normalized ECSA of Pd film with perpendicular mesochannels is calculated to be 737 m²·cm⁻³, which is much higher than that of the mesoporous Pt films prepared from lyotropic liquid

crystals (at most $460 \text{ m}^2 \cdot \text{cm}^{-3}$).^[19] Thus, it is found that the perpendicularly oriented mesochannels are able to make the whole inner porous structure accessible.

To gain deeper insights regarding the electrocatalytic properties of the Pd films with perpendicular mesochannels, formic acid oxidation reaction was selected as a model reaction. The mesoporous Pd film was evaluated and compared to a nonporous Pd film and a commercially available Pd black (PdB) catalyst. The typical CV curves for HCOOH oxidation catalyzed by different catalysts are shown in **Figure 6.1.8c**. It can be clearly observed that the Pd film with perpendicular mesochannels shows a higher current density of $934.6 \text{ mA mg}^{-1} \text{ Pd}$, which is around 2.7 and 1.9 times higher than those of the nonporous Pd film ($343.0 \text{ mA mg}^{-1} \text{ Pd}$) and the PdB ($485.8 \text{ mA mg}^{-1} \text{ Pd}$), respectively. In addition, the steady-state current densities obtained on the three different catalysts are also compared (**Figure 6.1.8d**). At a given oxidation current density, as indicated by dashed line in **Figure 6.1.8d**, the corresponding potential on the mesoporous Pd film is much lower than that on the nonporous Pd film and the PdB. The potential on the mesoporous Pd film is negatively shifted by $\sim 80 \text{ mV}$ and $\sim 50 \text{ mV}$, compared with the nonporous Pd film and PdB catalyst, respectively. Thus, the mesoporous Pd film with perpendicular mesochannels exhibits a strongly enhanced catalytic activity (*i.e.*, enhanced Pd utilization efficiency). This is probably attributed to a higher active surface caused by the accessible mesochannels perpendicularly aligned to the substrate.

6.1.4. Conclusion

In this work, we demonstrated a novel approach for the successful preparation of Pd films with perpendicular mesochannels. The pore size is uniform and straight mesochannels are evenly distributed in the entire area of the obtained films regardless the substrate sizes. A highly enhanced electrocatalytic performance toward formic acid oxidation was observed. The present approach is not only highly reliable and effective for creating vertically aligned mesoporous electrocatalysts, but also paves the way for other metals and alloys towards achieving a superior catalytic activity.

References

- [1] (a) Y. Sakamoto, M. Kaneda, O. Terasaki, D. Zhao, J. M. Kim, G. Stucky, H. J. Shin, R. Ryoo, *Nature*, 2000, **408**, 449. (b) T. Suteewong, H. Sai, R. Cohen, S. Wang, M. Bradbury, B. Baird, S. M. Gruner, U. Wiesner, *J. Am. Chem. Soc.*, 2011, **133**, 172. (c) E. L. Crepaldi, G. J. A. A. Soler-Illia, D. Grosso, F. Cagnol, F. Ribot, C. Sanchez, *J. Am. Chem. Soc.*, 2003, **125**, 9770. (d) D. Zhao, J. Feng, Q. Huo, N. Melosh, G. H. Fredrickson, B. F. Chmelka, G. D. Stucky, *Science*, 1998, **279**, 548. (e) L. Han, K. Miyasaka, O. Terasaki, S. Che, *J. Am. Chem. Soc.*, 2011, **133**, 11524.
- [2] K. C. Wu, W. X. Jiang, Y. Yamauchi, *J. Mater. Chem.*, 2011, **21**, 8934.
- [3] (a) X. Feng, Z. Liu, M. Hsieh, M. Chen, P. Liu, C. Chen, N. Zheng, *ACS Nano*, 2012, **6**, 4434; (b) M. Lin, C. Huang, M. Lo, C. Mou, *J. Phys. Chem. C*, 2008, **112**, 867; (c) Z. Teng, G. Zheng, Y. Dou, W. Li, C. Mou, X. Zhang, A. M. Asiri, D. Zhao, *Angew. Chem. Int. Ed.*, 2012, **51**, 2173. (d) B. C. Chen, H. P. Lin, M. C. Chao, C. Y. Mou, C. Tang, *Y. Adv. Mater.*, 2004, **16**, 1657.
- [4] (a) S. H. Tolbert, A. Firouzi, G. D. Stucky, B. F. Chmelka, *Science*, 1997, **278**, 264. (b) Y. Yamauchi, M. Sawada, M. Komatsu, A. Sugiyama, T. Osaka, N. Hirota, Y. Sakka, K. Kuroda, *Chem. Asian J.*, 2007, **2**, 1505. (c) Y. Yamauchi, M. Sawada, T. Noma, H. Ito, S. Furumi, Y. Sakka, K. Kuroda, *J. Mater. Chem.*, 2005, **15**, 1137.
- [5] (a) A. Walcarius, E. Sibottier, M. Etienne, J. Ghanbaja, *Nat. Mater.*, 2007, **6**, 602. (b) Y. Guillemin, M. Etienne, E. Aubert, A. Walcarius, *J. Mater. Chem.*, 2010, **20**, 6799. (c) J. Cheng, S. J. Rathi, P. Stradins, G. L. Frey, R. T. Collins, S. K. R. Williams, *RSC Adv.*, 2014, **4**, 7627.
- [6] F. Shan, X. Lu, Q. Zhang, J. Wu, Y. Wan, F. Bian, Q. Lu, Z. Fei, P. J. Dyson, *J. Am. Chem. Soc.*, 2012, **134**, 20238.
- [7] (a) Q. Lu, F. Gao, S. Komarneni, T. E. Mallouk, *J. Am. Chem. Soc.*, 2004, **126**, 8650. (b) Y. Yamauchi, T. Nagaura, S. Inoue, *Chem. Asian J.*, 2009, **4**, 1059.
- [8] C. Ma, L. Han, Z. Jiang, Z. Huang, J. Feng, Y. Yao, S. Che, *Chem. Mater.*, 2011, **23**, 3583.
- [9] (a) T. Fujita, P. Guan, K. McKenna, X. Lang, A. Hirata, L. Zhang, T. Tokunaga, S. Arai, Y. Yamamoto, N. Tanaka, Y. Ishikawa, N. Asao, Y. Yamamoto, J. Erlebacher, M. Chen, *Nat. Mater.*, 2012, **11**, 775; (b) S. C. Warren, L. C. Messina, L. S. Slaughter, M. Kamperman, Q. Zhou, S. M. Gruner, F. J. DiSalvo, U. Wiesner, *Science*, 2008, **320**, 1748. (c) K. S. Choi, E. W. McFarland, G. D. Stucky, *Adv. Mater.*, 2003, **15**, 2018.
- [10] (a) H. Zhang, M. Jin, Y. Xiong, B. Lim, Y. Xia, *Acc. Chem. Res.*, 2013, **46**, 1783; (b) H. Lee, S. E. Habas, G. A. Somorjai, P. Yang, *J. Am. Chem. Soc.*, 2008, **130**, 5406. (c) L. X. Yin, J. Liebscher, *Chem Rev.*, 2007, **107**, 133. (d) G. Li, H. Kobayashi, S. Dekura, R. Ikeda, Y. Kubota, K. Kato, M. Takata, T. Yamamoto, S. Matsumura, H. Kitagawa, *J. Am. Chem. Soc.*, 2014, **136**, 10222.
- [11] (a) G. S. Attard, Bartlett, P. N. N. R. B. Coleman, J. M. Elliott, J. R. Owen, J. H. Wang, *Science*, 1997, **278**, 838. (b)

- H. Wang, H. Y. Jeong, M. Imura, L. Wang,; L. Radhakrishnan, N. Fujita, T. Castle, O. Terasaki, Y. Yamauchi, *J. Am. Chem. Soc.*, 2011, **133**, 14526.
- [12] H. Miyata, T. Suzuki, A. Fukuoka, T. Sawada, M. Watanabe, T. Noma, K. Takada, T. Mukaide, K. Kuroda, *Nat. Mater.*, 2004, **3**, 651.
- [13] (a) G. J. A. A. Soler-Illia, P. C. Angelomé, M. C. Fuertes, D. Grosso, C. Boissiere, *Nanoscale*, 2012, **4**, 2549; (b) T. Brezesinski, J. Wang, J. Polleux, B. Dunn, S. H. Tolbert, *J. Am. Chem. Soc.*, 2009, **131**, 1802.
- [14] A. Stein, S. G. Rudisill, N. D. Petkovich, *Chem. Mater.*, 2014, **26**, 259.
- [15] (a) Q. Huo, D. I. Margolese, U. Ciesla, D. G. Demuth, P. Feng, T. E. Gier, P. Sieger, A. Firouzi, B. F. Chamelka, F. Schüth, G. D. Stucky, *Chem. Mater.*, 1994, **6**, 1176. (b) A. Monnier, F. Schüth, Q. Huo, D. Kumar, D. Margolese, R. S. Maxwell, G. D. Stucky, M. Krishnamurty, P. Petroff, A. Firouzi, M. Janicke, B. F. Chmelka, *Science*, 1993, **261**, 1299.
- [16] (a) G. Berhault, M. Bausach, L. Bisson, L. Becerra, C. Thomazeau, D. Uzio, *J. Phys. Chem. C*, 2007, **111**, 5915.
- [17] K. C. Kao, C. H. Lin, T. Y. Chen, Y. H. Liu, C. Y. Mou, *J. Am. Chem. Soc.*, 2015, **137**, 3779.
- [18] (a) G. S. Attard, C. G. Göltner, J. M. Corker, S. Henke, R. H. Templer, *Angew. Chem. Int. Ed. Engl.*, 1997, **36**, 1315; (b) C. Li, Ö. Dag, T. D. Dao, T. Nagao, Y. Sakamoto, T. Kimura, O. Terasaki, Y. Yamauchi, *Nat. Commun.*, 2015, **6**, Article number: 6608.
- [19] (a) J. M. Elliott, G. S. Attard, P. N. Bartlett, N. R. B. Coleman, D. A. S. Merckel, J. R. Owen, *Chem. Mater.*, 1999, **11**, 3602; (b) Y.; Yamauchi, A. Tonegawa, M. Komatsu, H. Wang, L. Wang, Y. Nemoto, N. Suzuki, K. Kuroda, *J. Am. Chem. Soc.*, 2012, **134**, 5100. (c) A. Takai,; Y. Yamauchi,; K. Kuroda, *J. Am. Chem. Soc.*, **2010**, 132, 208.

6.2. Three-Dimensional Hyperbranched PdCu Nanostructures with High Electrocatalytic Activity

6.2.1. Introduction

In the past decades, fuel cells have been considered as promising devices for energy conversion owing to their high efficiency, low operation temperatures, and low pollutant emissions.^[1] Presently, platinum (Pt) nanomaterials are still the most efficient electrocatalysts for both anodic and cathodic reactions. The commercialization of fuel cells has been obstructed by the high cost of Pt and the limited reserves in nature. Recent advances demonstrated that porous/dendritic Pt crystals,^[2] core-shell nanoparticles with monolayer Pt shell,^[3] and alloys with other transition metals^[4] can effectively decrease the usage of Pt while still maintaining the possibility to enhance the performance. However, these approaches only reduce the usage of Pt, and do not fully solve the problem of Pt requirements.^[5] Therefore, the development of less expensive and more abundant Pt-free electrocatalysts with improved catalytic activity and durability is still an urgent matter to address.

Palladium (Pd) and Pd-based catalysts represent promising substitutes to Pt for catalyzing the oxidation of small fuel molecules due to their relatively low cost and abundance. Especially, Pd has exhibited a superior activity in catalyzing the formic acid oxidation (FAO) through a direct oxidation process (a direct dehydrogenation pathway) without poisonous intermediates (carbon monoxide), which is distinctly different from Pt-based catalysts.^[6] However, it should be mentioned that the Pd atoms on the surface easily dissolve and migrate during reactions taking place in acid solution, resulting in the aggregation of the nanoparticles and in the loss of surface area and activity.^[7] Recent experimental results indicated that three-dimensional (3D) constructions composed of one-dimensional (1D) metallic nanostructures (*e.g.* nanorods, nanowires, and nanodendrites/branches) can be considered as effective candidates to improve the activity and stability of fuel cells.^[8] Such kind of assembly not only retains^[8] the inherent anisotropic 1D morphology, which suffers less from dissolution and Ostwald ripening/aggregation,^[9] but also has many unique structural characteristics such as the porosity, the permeability, and interconnected open-pore structures, which can enhance the catalytic activity and stability.^[10] For instance, Xia *et al.* reported that the interconnected 3D Pt nanowire assemblies exhibited a significant enhanced electrocatalytic activity and durability for methanol oxidation reaction compared with a commercial Pt/C catalyst because of their unique architecture.^[11] Besides the structure, embedding non-precious-metal atoms into Pd lattice to form the Pd-based alloy catalysts is another effective strategy to enhance the activity and stability owing to the modulation of the electronic configuration.^[12] The

synthesis of mono-dispersed PdCo and PdCu nanoparticles with a controlled composition was reported by Ho et al. The latter exhibits an enhanced Pd mass activity toward FAO, which is about 2 times higher than that of Pd catalyst, owing to the effect of Cu on the electronic landscape of the PdCu alloy structure.^[13]

Despite the significant progress in the synthesis of bimetallic Pd-based alloy, produce branched Pd-based alloy with 3D structures remains a challenge as the face-centered-cubic (*fcc*) Pd structure has no intrinsic driving force towards the growth of anisotropic structure in a solution phase.^[14] 3D branched PdCu nanostructures are less vulnerable to aggregation and dissolution and can decrease the Pd consumption and increase the utilization of Pd. Thus, it is essential to develop bimetallic Pd-based catalyst with 3D architectures composed of 1D metallic nanostructure to maximize their performance and increase their catalytic stability.

Herein, I demonstrate a facile one-step method for the preparation of three-dimensional alloyed PdCu nanostructures composed of 1D branches. The impact of the reagents on the formation of such 3D PdCu nanostructure is investigated in detail. The results indicate that the slow reduction kinetics retarded by the presence of hydrochloric acid (HCl) and the bromide ions (Br^-) adsorbing selectively on certain facets of the PdCu seeds during the reduction a progress, are key factors for the successful formation of 3D branched PdCu nanostructures. More importantly, because of the unique structural advantage and the incorporation of Cu atoms, the as-prepared 3D branched PdCu nanostructures show enhanced catalytic activity compared with the commercial Pd black (PdB) and 10 wt% Pd on carbon (PdC-10%).

In a typical synthesis of 3D branched PdCu nanostructures, 1.5 mL Na_2PdCl_4 solution (20.0 mM), 1.5 mL CuCl_2 solution (20.0 mM), 0.1 mL HCl solution (6.0 M), 80 mg KBr and 50.0 mg Pluronic F127 were mixed and dissolved in the deionized water under sonication. An aqueous solution of 2.0 ml ascorbic acid (0.1 M) was added to the solution which was then kept in an oil bath for 30 min at 90 °C. The residual Pluronic F127 was removed by several consecutive washing/centrifugation cycles with ethanol and water. Finally, the sample was collected by centrifuging at 14000 rpm for 20 min. The as-prepared sample was stored in ethanol until the time of use and then dried at room temperature.

6.2.2. Experimental Sections

6.2.2.1. Materials

All chemicals and solvents were used as received without further purification. Na_2PdCl_4 , CuCl_2 , ascorbic acid (AA), hydrochloric acid, sulfuric acid and methanol were purchased from Nacalai Tesque, Inc. (Kyoto, Japan).

Pluronic F127, HCl and NaBr were obtained from Sigma-Aldrich. Commercial PB (HiSPEC®1000) was supplied by Johnson Matthey Company. All solutions were prepared with deionized water treated with a Millipore water purification system (Millipore Corp.).

6.2.2.2. Preparation of the Branched PdCu Nanostructures

In a typical synthesis of 3D branched PdCu nanostructures, 1.5 ml Na_2PdCl_4 solution (20.0 mM), 1.5 ml CuCl_2 solution (20.0 mM), 0.1 ml HCl solution (6.0 M), 80 mg KBr and 50.0 mg Pluronic F127 were mixed and dissolved under sonication. An aqueous solution of 2.0 ml ascorbic acid (0.1 M) was added to the solution which was then kept in an oil bath for 30 min at 90 °C. The residual Pluronic F127 was removed by several consecutive washing/centrifugation cycles with ethanol and water. Finally, the sample was collected by centrifuging at 14000 rpm for 20 min. The as-prepared sample was stored in ethanol until the time of use and then dried at room temperature.

6.2.2.3. Characterization

The scanning electron microscope images (SEM) were obtained with a Hitachi SU-8000 microscope operated at 5 kV. The transmission electron microscopy (TEM) and high-angle annular dark-field scanning TEM (HAADF-STEM) characterizations were carried out using a JEOL JEM-2100F operated at 200 kV equipped with an energy-dispersive spectrometry analyzer. The samples for TEM and HRTEM characterizations were prepared by depositing a drop of the diluted colloidal suspension on a grid. Wide-angle powder X-ray diffraction (XRD) spectrum was acquired with a Rigaku Rint 2500 diffractometer with monochromated Cu K radiation. Low-angle XRD profiles were obtained by using a NANO VIEWER (Rigaku, Japan) equipped with a Micro Max-007 HF high-intensity micro-focus rotating anode X-ray generator. X-ray photoelectronic spectroscopy (XPS) spectra was carried out at room temperature by using a JPS-9010TR (JEOL) instrument with an Mg $K\alpha$ X-ray source. All the binding energies were calibrated via referencing to C 1s binding energy (284.6 eV).

6.2.2.4. Electrochemical Test

Cyclic voltammograms (CV) and chronoamperometric (CA) experiments were performed using a CHI 842B electrochemical analyzer (CHI Instruments, USA). A conventional three-electrode cell was used, including an Ag/AgCl (saturated KCl) reference electrode, a platinum wire as a counter electrode, and a modified glassy carbon electrode (GCE) as a working electrode. The modified GCE was coated with the as-prepared samples

(5.0 μg) and dried at room temperature. Then, 5.0 μL of Nafion (0.05 wt%) was coated on the surface of the modified GCE and dried before the electrochemical measurements. Prior to electrochemical measurements, the GCE modified with the as-prepared sample was activated electrochemically by cycling the electrode potential between -0.2 V and +1.2 V (vs Ag/AgCl) in 0.5 M HClO_4 . Formic acid electro-oxidation measurements were performed in a solution of 0.5 M HClO_4 containing 0.5 M formic acid at a scan rate of 50 mV s^{-1} . Mass current densities were normalized by the loaded Pd amount, which was determined by inductively coupled plasma mass spectroscopy (ICP-MS).

6.2.3. Results and Discussion

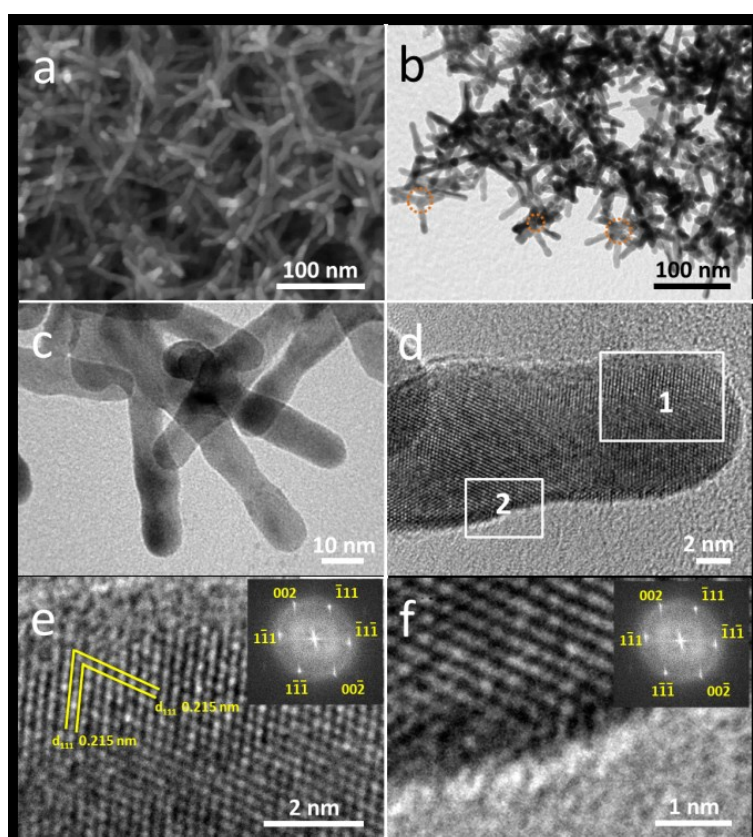


Figure 6.2.1 (a) Representative SEM and (b, c) TEM images of the 3D branched PdCu nanostructures, d) HRTEM image of a single-crystal PdCu branch, e, f) Magnified HRTEM images of the edge surface derived from the rectangle areas marked in (d), respectively. The corresponding FFT patterns were shown as inset in panel (e, f).

The morphology of the obtained products is examined by scanning electron microscope (SEM) and transmission electron microscopy (TEM). As shown in **Figure 6.2.1a**, the as-prepared products display highly branched 3D multipods. The TEM images reveal that each PdCu nanostructure consists of 3-7 branches (**Figure 6.2.1b,c**). The width and length of the branches are in the range of 8-11 nm and 20-50 nm, respectively.

The branches originating from a same center extend in different directions to form a 3D structure, as marked in **Figure 6.2.1b**. The detailed structural features of the branches were characterized by high-resolution TEM (HRTEM), as shown in **Figure 6.2.1d**. The lattice spacing of the 3D branched PdCu nanostructures (**Figure 6.2.1e**) was measured to be around 0.215 nm, which is between the {111} lattice spacing of pure Pd (0.223 nm) and Cu (0.208 nm), indicating the successful incorporation of Cu atoms into the Pd lattice. The continuous fringes running through the branches suggest that they are monocrystalline. Fast Fourier transform (FFT) patterns of the atomic lattice fringes were identical, as displayed in the insets of **Figure 6.2.1e** and **f**, further supporting the monocrystalline nature of the branched PdCu nanostructures.

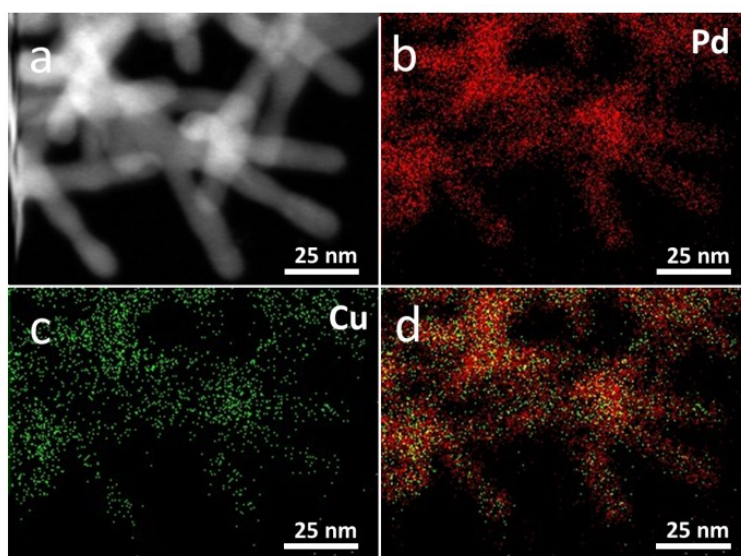


Figure 6.2.2 (a) HAADF-STEM and (b-d) elemental mapping images of the 3D branched PdCu nanostructures.

The elemental mapping images (**Figure 6.2.2a-d**) confirm that the Pd and Cu are uniformly distributed throughout the branch, which suggests the formation of a homogeneous PdCu alloy structure. In addition, the energy dispersive X-ray spectroscopy (EDS) also returns a Pd:Cu atomic ratio of 80:20, although an equal feeding molar ratio was utilized, in accordance to the inductively coupled plasma atomic emission spectrometry data (ICP-AES), indicating that the reduction of the Cu species was incomplete. The possible reason is that the Cu^{2+} species ($\text{Cu}^{2+}/\text{Cu}=0.34$ V vs. Standard Hydrogen Electrode, SHE) have a lower reduction potential than that of $[\text{PdCl}_4]^{2-}$ species ($[\text{PdCl}_4]^{2-}/\text{Pd}: +0.62$ V vs. SHE).^[15]

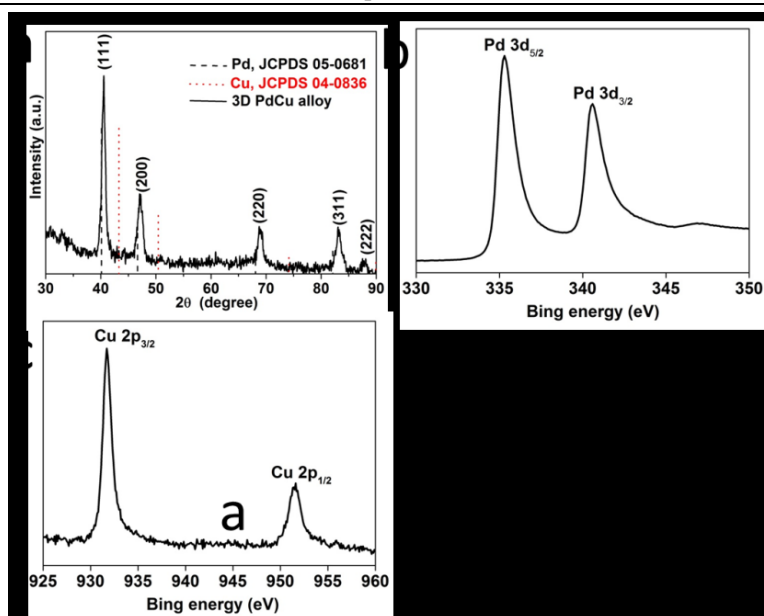


Figure 6.2.3 (a) Wide-angle XRD pattern of the 3D branched PdCu nanostructures, high resolution XPS spectra for (b) Pd 3d, (c) Cu 2p of the 3D branched PdCu nanostructures.

The crystalline structure of the typical 3D branched PdCu nanostructures was examined by wide-angle X-ray diffraction (XRD). As shown in **Figure 6.2.3a**, the diffraction peaks of the PdCu sample at 40.5 °, 47.1 °, 68.9 °, 83.2 °, 87.8 ° can be clearly assigned to the (111), (200), (220), (311), and (222) diffraction planes, respectively. No other diffraction peaks were observed, indicating the formation of a single-phase PdCu alloy. When compared to standard diffraction patterns of Pd, all the diffraction peaks of the 3D branched PdCu nanostructures are shifted to higher angles, suggesting the partial substitution of large Pd atoms by smaller Cu atoms.^[16] The composition of the 3D branched PdCu nanostructures prepared in standard conditions was confirmed by ICP-AES, from which the Cu content in the sample was measured to be 14 wt%. The electronic structure was analyzed by X-ray photoelectron spectroscopy (XPS). **Figure 6.2.3b** shows the XPS spectra centered on the Pd 3d region. The two peaks located at 335.3 and 340.6 eV can be assigned to the metallic Pd 3d_{5/2} and Pd 3d_{3/2}, whereas the peaks at 931.7 and 951.6 eV can be ascribed to the metallic Cu 2p_{3/2} and Cu 2p_{1/2} (**Figure 6.2.3c**). The slight shifts in the binding energies of the 3D PdCu alloy compared to pure Pd (Pd 3d_{5/2}: 335.0 eV) and Cu (Cu 2p_{3/2}: 932.6 eV) suggest the presence of electronic interactions between Pd and Cu.^[17]

Various control experiments were set in order to assess the role of the reagents during the synthesis. As shown in **Figure 6.2.4a**, in the case where no KBr was used (in the presence of HCl, 0.6 mmol), irregular PdCu nanoparticles were produced. By increasing the amount of KBr up to 10 mg, branched PdCu nanostructures

start to appear (**Figure 6.2.4b**). The desired 3D branched PdCu nanostructures could only be obtained after using more than 80 mg KBr (**Figure 6.2.4c**). An excess amount of KBr (150 mg) caused the branched structure to overgrow, leading to the formation of PdCu nanostructures with much longer branches (**Figure 6.2.4d**). The results suggest that the Br^- ions have a significant influence on the PdCu nanoarchitecture. It is well established that the Br^- ions preferentially adsorb on the (100) facets of *fcc* metals (e.g., palladium and palladium alloy), which prevents growth along the $\langle 100 \rangle$ direction and is responsible for directing the formation of the nanowire construction.^[18] In addition, when KBr is replaced by KCl or KI (in an equivalent molar ratio), irregular PdCu aggregates are obtained (**Figure 6.2.4e-f**). Consequently, only the use of Br^- ions as structure-directing agent can lead to the formation of branched PdCu nanostructures. The possible reason is that the binding strengths of halide ions to the Pd surface increase in the order of $\text{Cl}^- < \text{Br}^- < \text{I}^-$. As a result, weak chemisorption (Cl^-) or strong chemisorption (I^-) on the Pd surface are not favorable to the formation of branched structure.^[18c,19]

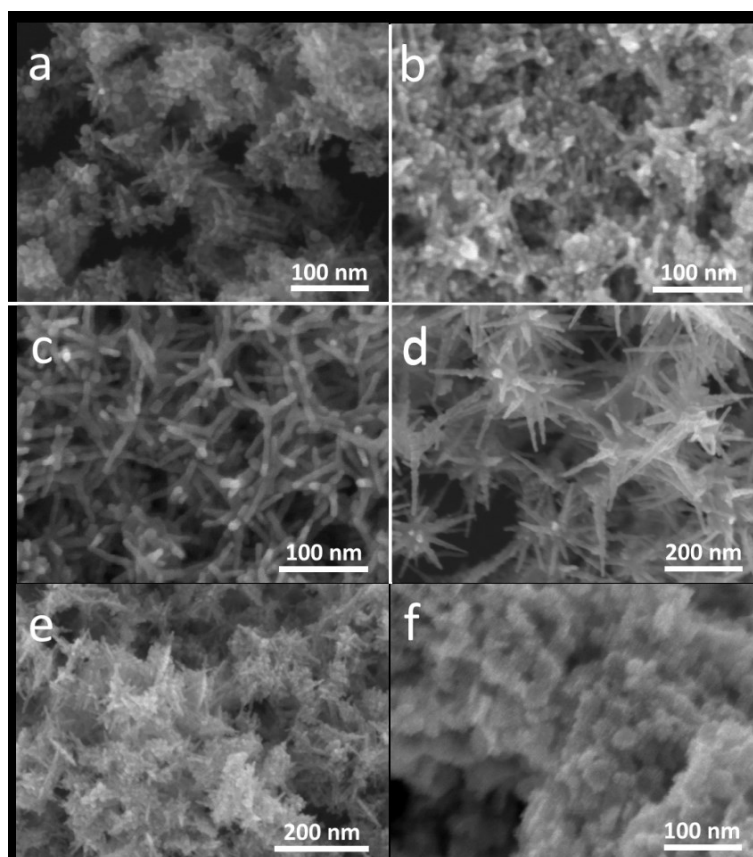


Figure 6.2.4 SEM images of the samples prepared with different amounts of KBr: (a) 0 mg, (b) 10 mg (c) 80 mg, and (d) 150 mg. and SEM images of the samples prepared by replacing KBr with (e) KCl and (f) KI.

The effect of HCl on the morphology of the PdCu nanostructures was also investigated. When the reaction was

carried out in the absence of HCl, but in presence of 80 mg KBr, only irregular PdCu nanoparticles were obtained, owing to the fast reduction kinetics (**Figure 6.2.5a**). When 0.3 or 0.6 mmol HCl is added to the reaction system, the precursor is reduced at a much lower reduction rate, as HCl tends to decrease the reduction capacity of ascorbic acid. In such case, the branched PdCu nanostructures can be obtained (**Figure 6.2.5b,c**). Further increasing the amount of HCl (up to 1.2 mmol) yielded sea-urchin PdCu nanostructures with increased branch length (**Figure 6.2.5d**). The increased branch length can be attributed to the decrease the number of seeds in the solution due to the slow reduction rate at initial stage. In addition, when HCl was replaced by equal amount of other strong acids (*e.g.*, HNO₃ or H₂SO₄), the 3D branched nanostructure could be well retained, indicating that the slow reduction kinetics induced by the presence of H⁺, instead of the anions (*e.g.*, Cl⁻, NO₃⁻, SO₄²⁻), takes the central role in the formation of 3D branched nanostructures (**Figure 6.2.5e,f**).

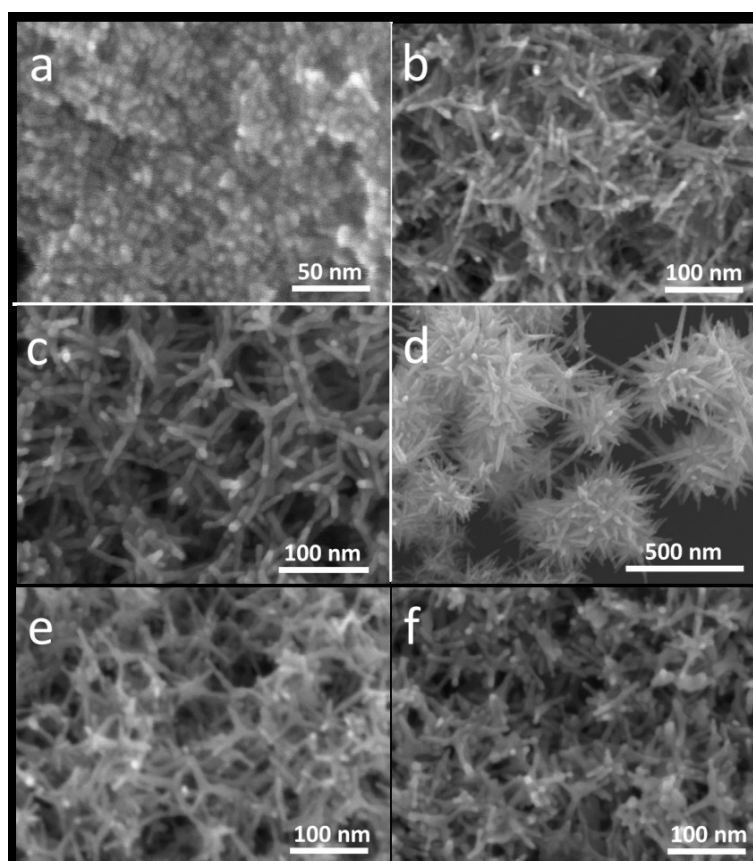


Figure 6.2.5 SEM images of the samples prepared with different amounts of HCl: a) 0 mmol, b) 0.3 mmol c) 0.6 mmol, and d) 1.2 mmol and SEM images of the samples prepared by replacing HCl with (e) HNO₃ and (f) H₂SO₄.

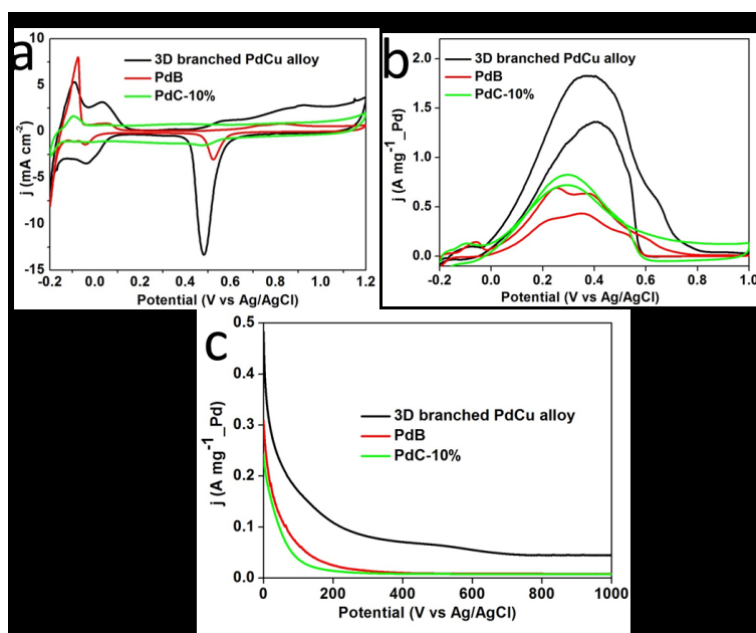


Figure 6.2.6 Cyclic voltammograms of the 3D branched PdCu nanostructures, commercial PdB and PdC-10% samples in a) a 0.5 M HClO₄ solution and b) a mixture of 0.5 M HClO₄ and 0.5 M HCOOH at a scanning rate of 50 mV s⁻¹. c) Chronoamperometric curves for formic acid oxidation. The currents in panel a) are normalized by the electrode geometric surface area.

While Pd-based nanostructures are known to be efficient electrocatalysts for oxidizing organic fuel molecules, alloying them with 3d transition metals can greatly enhance their catalytic activity and stability. Herein, I selected the electrocatalytic oxidation of formic acid as a probe reaction to characterize the activity of the 3D branched PdCu nanostructures in acidic media. For comparison, commercial PdB and PdC-10% were selected as references under the same conditions. The cyclic voltammograms were recorded in a 0.5 M HClO₄ aqueous solution at a scanning rate of 50 mV s⁻¹ (**Figure 6.2.6a**). The clear features of hydrogen desorption/adsorption (from 0.1 to -0.2 V) is an indication of the cleanliness of the catalytic surface. It is well known that the hydrogen atoms are essentially absorbed in the bulk Pd lattice by “dissolution adsorption mechanism”.^[20] The sharp peaks below 0 V is related to this dissolution adsorption process. The electrochemically active surface area (ECSA) of the Pd-based electrocatalysts cannot be precisely calculated by measuring the total charge passed in the “hydrogen region”. Thus, I calculated the ECSA of the samples by integrating the charges associated with the PdO peak. The ECSA of the 3D branched PdCu nanostructures, commercial PdB and PdC-10% are 76.9 m² g⁻¹, 15.7 m² g⁻¹, and 37.3 m² g⁻¹, respectively. The results suggest that the 3D branched PdCu nanostructures provide a much larger surface area and more catalytic active sites than other Pd-based catalysts, as shown in **Table 6.2.1**. **Figure 6.2.6b** shows the catalytic activity of the 3D branched PdCu

nanostructures, commercial PdB and PdC-10% catalyst toward FAO in a 0.5 M HClO₄ aqueous solution containing 0.5 M HCOOH. The current density was normalized by the Pd mass activities. The measured current density on the 3D branched PdCu nanostructures (1.84 A mg⁻¹_Pd) is about 2.7 and 2.2 times more than that of commercial PdB (0.69 A mg⁻¹_Pd) and PdC-10% catalyst (0.84 A mg⁻¹_Pd), respectively. The enhanced catalytic activity of the branched PdCu nanostructures is attributed to the large surface area, which is provided by the assembly of 3D constructions and the synergistically enhanced electronic properties resulting from the alloy.^[21] Compared to previously reported Pd-based catalysts (**Table 6.2.1**), our prepared 3D branched PdCu nanostructures also exhibit a higher current density, showing the potential of this material for practical electrocatalytic applications such as formic acid oxidation. As an effective catalyst, the stability is a very important factor for fuel cells. Thus, the stability of catalysts was also investigated by chronoamperometric measurement for 1000 s in a 0.5 M HClO₄ containing 0.5 M HCOOH. **Figure 6.2.6c** clearly reveals that the branched PdCu nanostructures exhibited a slower current decay and a higher catalytic current intensity compared to the commercially available electrocatalysts. The high stability of the as-prepared 3D branched PdCu catalyst mainly originates from the one-dimensional structures, which suffers less from dissolution and aggregation.

Table 6.2.1. Comparison of the surface area and the activity of 3D branched PdCu nanostructure with previous reported Pd-based catalysts.

Sample name	Surface area (m ² g ⁻¹)	Condition	Scan rate (mV s ⁻¹)	Mass activity (A mg ⁻¹ _Pd)	Reference
3D branched PdCu alloy	76.9	0.5 M HClO ₄ + 0.5 M HCOOH	50	1.84	Present work
Mesoporous Pd film	--	0.5 M H ₂ SO ₄ + 0.5 M HCOOH	50	0.93	<i>J. Am. Chem. Soc.</i> , 2015, 137 , 11558
Pd/Graphite Oxide	41.8	0.5 M H ₂ SO ₄ + 0.5 M HCOOH	50	0.90	<i>J. Power Sources</i> , 2015, 280 , 491
Single crystalline Pd tripods	20	0.5 M H ₂ SO ₄ + 0.5 M HCOOH	50	0.49	<i>Chem. Commun.</i> , 2015, 51 ,

		0.5 M HCOOH			7195
Branched Pd tertrapods	--	0.5 M H ₂ SO ₄ + 0.5 M HCOOH	50	0.37	<i>Nanoscale</i> , 2014, 6 , 2776.
Pd-P nanoparticle networks	18.9	0.5 M H ₂ SO ₄ + 0.5 M HCOOH	50	0.61	<i>Chem. Commun.</i> , 2014, 50 ,13451.
Nanobranched porous Pd-Sn	18.6	0.5 M H ₂ SO ₄ + 0.5 M HCOOH	50	0.98	<i>J. Power Sources</i> , 2015, 280 , 141.
Nanowire PdNi/Graphite Oxide	98.2	0.5 M H ₂ SO ₄ + 0.5 M HCOOH	50	0.94	<i>J. Mater. Chem. A</i> , 2015, 3 , 14001
PdCo nanoassemblies	--	0.5 M H ₂ SO ₄ + 0.5 M HCOOH	50	0.28	<i>Appl. Catal. B</i> , 2013, 138 , 229.
Mono-dispersed PdCu nanoparticle	--	0.1 M H ₂ SO ₄ + 0.5 M HCOOH	50	0.35	<i>Chem. Asian J.</i> , 2011 , 6, 1515.

6.2.4. Conclusion

In summary, we successfully synthesized 3D branched PdCu nanostructures by a facile one-pot method. The simultaneous presence of HCl and KBr reagents is essential for the formation of 3D PdCu nanostructure. The as-prepared 3D branched PdCu nanostructures display an enhanced electrocatalytic activity and long-term stability toward the FAO compared to PdB or PdC-10%, which is mainly attributed to the unique structural features and the synergistic benefit from alloying Pd with Cu.

References

- [1] (a) Q. Gao, Y. M. Ju, D. An, M. R. Gao, C. H. Cui, J. W. Liu, H. P. Cong, S. H. Yu, *ChemSusChem*, 2013, **6**, 1878; (b) K. Qi, Q. Wang, W. Zheng, W. Zhang, X. Cui, *Nanoscale*, 2014, **6**, 15090.
- [2] (a) H. Wang, S. Ishihara, K. Ariga, Y. Yamauchi, *J. Am. Chem. Soc.*, 2012, **134**, 10819; (b) T. Yu, D. Y. Kim, H. Zhang, Y. Xia, *Angew. Chem. Int. Ed.*, 2011, **50**, 2773; (c) X. Huang, Z. Zhao, J. Fan, Y. Tan, N. Zheng, *J. Am. Chem. Soc.*, 2011, **133**, 4718.
- [3] K. Sasaki, H. Naohara, Y. M. Choi, Y. Cai, W. F. Chen, P. Liu, R. R. Adzic, *Nat. Commun.*, 2012, **3**, 1115.
- [4] (a) Y. Jia, Y. Jiang, J. Zhang, L. Zhang, Q. Chen, Z. Xie, L. Zheng, *J. Am. Chem. Soc.*, 2014, **136**, 3748; (b) S. Chen, H. Su, Y. Wang, W. Wu, J. Zeng, *Angew. Chem. Int. Ed.*, 2015, **54**, 108; (c) Z. Zhang, Y. Yang, F. Nosheen, P. Wang, J. Zhang, J. Zhuang, X. Wang, *Small*, 2013, **9**, 3063; (d) Y. Wu, D. Wang, G. Zhou, R. Yu, C. Chen, Y. Li, *J. Am. Chem. Soc.*, 2014, **136**, 11594.
- [5] (a) K. A. Kuttiyiel, K. Sasaki, D. Su, L. Wu, Y. Zhu, R. R. Adzic, *Nat. Commun.*, 2013, **52**, 5185; (b) S. Liu, Q. Zhang, Y. Li, M. Han, L. Gu, C. Nan, J. Bao, Z. Dai, *J. Am. Chem. Soc.*, 2015, **137**, 2820.
- [6] (a) V. Mazumder, M. Chi, M. N. Mankin, Y. Liu, Ö. Metin, D. Sun, K. L. More, S. Sun, *Nano Lett.*, 2012, **12**, 1102; (b) S. Ha, R. Larsen, R. I. Masel, *J. Power Sources*, 2005, **144**, 28.
- [7] C. Hu, X. Zhai, Y. Zhao, K. Bian, J. Zhang, L. Qu, H. Zhang, H. Luo, *Nanoscale*, 2014, **6**, 2768.
- [8] (a) S. Guo, S. Dong, E. Wang, *ACS Nano*, 2010, **4**, 547; (b) J. Xie, Q. Zhang, W. Zhou, J. Y. Lee, D. I. C. Wang, *Langmuir*, 2009, **25**, 6454; (c) Y. B. He, G. R. Li, Z. L. Wang, Y. N. Ou, Y. X. Tong, *J. Phys. Chem. C*, 2010, **114**, 19175.
- [9] (a) B. Y. Xia, H. B. Wu, N. Li, Y. Yan, X. W. Lou, X. Wang, *Angew. Chem. Int. Ed.*, 2015, **54**, 3797; (b) B. Lim, Y. Xia, *Angew. Chem. Int. Ed.*, 2011, **50**, 76; (c) X. Yu, D. Wang, Q. Peng, Y. Li, *Chem. Eur. J.*, 2013, **19**, 233; (d) H. S. Chen, Y. T. Liang, T. Y. Chen, Y. C. Tseng, C. W. Liu, S. R. Chung, C. T. Hsieh, C. E. Lee, K. W. Wang, *Chem. Commun.*, 2014, **50**, 11165.
- [10] (a) M. Rauber, I. Alber, S. Müller, R. Neumann, O. Picht, C. Roth, A. Schökel, M. E. Toimil-Molares, W. Ensinger, *Nano Lett.*, 2011, **11**, 2304; (b) N. C. Bigall, A. K. Herrmann, M. Vogel, M. Rose, P. Simon, W. Carrillo-Cabrera, D. Dorfs, S. Kaskel, N. Gaponik, A. Eychmüller, *Angew. Chem. Int. Ed.*, 2009, **48**, 9731; (c) F. Yu, W. Zhou, R. M. Bellabarba, R. P. Tooze, *Nanoscale*, 2014, **6**, 1093.
- [11] B. Y. Xia, W. T. Ng, H. B. Wu, X. Wang, X. W. Lou, *Angew. Chem. Int. Ed.*, 2012, **51**, 7213.
- [12] (a) M. Bersani, L. Conte, A. Martucci, M. Guglielmi, G. Mattei, V. Bello, R. Rosei, M. Centazzo, *Nanoscale*, 2014, **6**, 1560; (b) C. Xu, Q. Hao, H. Duan, *J. Mater. Chem. A*, 2014, **2**, 8875; (c) J. J. Lv, L. P. Mei, X. Weng, A. J.

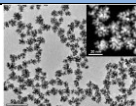
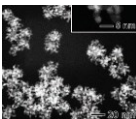
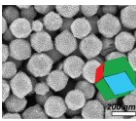
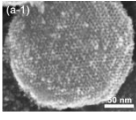
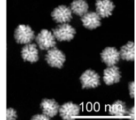
- Wang, L. L. Chen, X. F. Liu, J. J. Feng, *Nanoscale*, 2015, **7**, 5699; (d) Y. W. Lee, M. Kim, S. W. Kang, S. W. Han, *Angew. Chem. Int. Ed.*, 2011, **50**, 3466.
- [13] S. F. Ho, A. Mendoza-Garcia, S. Guo, K. He, D. Su, S. Liu, Ö. Metin, S. Sun, *Nanoscale*, 2014, **6**, 6970.
- [14] (a) L. Ma, C. Wang, M. Gong, L. Liao, R. Long, J. Wang, D. Wu, W. Zhong., M. J. Kim, Y. Chen, Y. Xie, Y. Xiong, *ACS Nano*, 2012, **6**, 9797; (b) S. Maksimuk, X. Teng, H. Yang, *J. Phys. Chem. C*, 2007, **111**, 14312.
- [15] (a) Y. H. Chen, H. H. Hung, M. H. Huang, *J. Am. Chem. Soc.*, 2009, **131**, 9114; (b) B. Jiang, C. Li, M. Imura, J. Tang, Y. Yamauchi, *Adv. Sci.*, 2015, **2**, 1500112.
- [16] (a) Y. Zheng, S. Zhao, S. Liu, H. Yin, Y. Y. Chen, J. Bao, M. Han, Z. Dai, *ACS Appl. Mater. Interfaces*, 2015, **7**, 5347; (b) H. H. Li, C. H. Cui, S. Zhao, H. B. Yao, M. R. Gao, F. J. Fan, S. H. Yu, *Adv. Energy Mater.* 2012, **2**, 1182; (c) B. Jiang, C. Li, V. Malgras, Y. Yamauchi, *J. Mater. Chem. A*, 2015, **3**, 18053.
- [17] (a) Z. Y. Shih, C. W. Wang, G. Xu, H. T. Chang, *J. Mater. Chem. A*, 2013, **1**, 4773; (b) C. Xu, Y. Liu, J. Wang, H. Geng, H. Qiu, *J. Power Sources*, 2012, **199**, 124.
- [18] (a) K. Zhang, D. Bin, B. Yang, C. Wang, F. Ren, Y. Du, *Nanoscale*, 2015, **7**, 12445; (b) L. Zhang, S. I. Choi, J. Tao, H. C. Peng, S. Xie, Y. Zhu, Z. Xie, Y. Xia, *Adv. Funct. Mater.*, 2014, **24**, 7520; (c) M. Chen, B. Wu, J. Yang, N. Zheng, *Adv. Mater.* 2012, **24**, 862.
- [19] F. Wang, C. Li, L. D. Sun, C. H. Xu, J. Wang, J. C. Yu, C. H. Yan, *Angew. Chem. Int. Ed.*, 2012, **51**, 4872.
- [20] (a) J. Y. Wang, Y. Y. Kang, H. Yang, W. B. Cai, *J. Phys. Chem. C*, 2009, **113**, 8366; (b) D. Sun, L. Si, G. Fu, C. Liu, D. Sun, Y. Chen, Y. Tang, T. Lu, *J. Power Sources*, 2015, **280**, 141; (c) M. Breiter, *J. Electroanal. Chem. Interfacial Electrochem.*, 1977, **81**, 275.
- [21] (a) Q. S. Chen, Z. N. Xu, S. Y. Peng, Y. M. Chen, D. W. Lv, Z. Q. Wang, J. Sun, G. C. Guo, *J. Power Sources*, 2015, **282**, 471; (b) H. Wu, H. Li, Y. Zhai, X. Xu, Y. Jin, *Adv. Mater.* 2012, **24**, 1594.

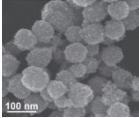
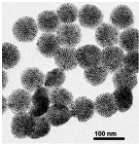
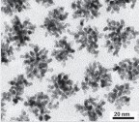
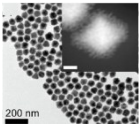
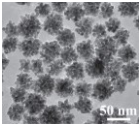
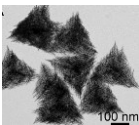
Chapter 7. General Conclusions and Future Perspective

7.1. Overview of the Achievements

Many synthetic methods have been developed for the fabrication of nanoporous noble metal materials, such as platinum (Pt), palladium (Pd), and gold (Au) materials with well-controlled morphologies and pore structures. Recently, a wide range of dendritic nanoporous structures were successfully fabricated by various strategies, please refer to **Table 7.1**. Although great progress has been made in nanoporous metals, the methods often require multiple steps and specialized synthetic techniques, making them challenging to scale up. In addition, the porous architectures obtained in previous reports are mainly limited to dendritic pores, possessing tiny and random interspaces. A soft-templating approach, specifically, one based on diluted surfactant/polymer solutions, has been considered as a more versatile, flexible, and effective strategy. In principle, the pore sizes are basically determined by the hydrophobic volume of the template molecules. By using various template molecules with different hydrophobic chains, the pore structures can be easily controlled. Generally, the use of nanoporous catalysts with large-sized pore for electrochemical applications is expected for higher catalytic performance owing to the short diffusion path lengths for both electronic and reagent transport. Accordingly, in my Ph.D. study, I have focused on the preparation of large-pore metals with various compositions based on diluted surfactant and polymer solutions.

Table 7.1 A few examples of nanoporous metal particles prepared by different methods.

Product	Method	Morphology	Reference
Dendritic Pt	Soft template		<i>J. Am. Chem. Soc.</i> , 2009, 131 , 9152.
Dendritic PtPd	Seed-mediated growth		<i>Science</i> , 2009, 324 , 1302.
Mesoporous Pt	Hard template		<i>J. Am. Chem. Soc.</i> , 2011, 131 , 14526.
Mesoporous Pt-Au alloys	Lyotropic liquid crystal		<i>J. Am. Chem. Soc.</i> , 2012, 134 , 5100.
Porous Pd	Seed-mediated growth		<i>Angew. Chem. Int. Ed.</i> 2012, 51 , 4872.

Porous PtRh	Solvent thermal		<i>Adv. Funct. Mater.</i> , 2012, 22 , 3570.
Porous Pd	Soft template		<i>Angew. Chem. Int. Ed.</i> , 2013, 52 , 2520.
Porous Pt ₃ Ni	Solvent thermal		<i>Adv. Mater.</i> , 2013, 25 , 2974.
Nanoporous Au@PdPt	Co-reduction method		<i>ACS Nano</i> , 2013, 7 , 7945.
Dendritic PtCu nanoparticle	Solvent thermal		<i>Small</i> , 2013, 9 , 3063.
Bipyramid PtCu nanoframes	Solvent thermal		<i>Angew. Chem. Int. Ed.</i> , 2015, 54 , 108.

(I) Mesoporous Pt Nanospheres with Designed Pore Surface as Highly Active Electrocatalyst (shown in Chapter 2)

In this chapter, I reported a novel strategy for the large-scale synthesis of shape- and size-controlled mesoporous Pt nanospheres through a slow reduction reaction in the presence of a surfactant. In this route, bromides ions are added to the precursor solution containing $[\text{PtCl}_6]^{2-}$ salts and Pluronic F127 for reducing the reduction rate. The presence of bromide ions can shift the redox potential of the Pt ions toward a more negative potential through ligand exchange reactions to form $[\text{PtBr}_6]^{2-}$ with a redox potential is more negative (0.61 V vs. SHE) than that of $[\text{PtCl}_6]^{2-}$ (0.73 V vs. SHE). The slow reduction reaction exclusively results in well-defined mesoporous architectures distinctly different from the dendritic constructions reported previously. More importantly, abundant catalytically active sites are created on the highly accessible mesoporous surfaces by the selective adsorption of bromide ions. The mesoporous Pt nanospheres prepared using the new synthetic route not only show superior electrochemical performance toward methanol oxidation reaction and oxygen reduction reaction but also exhibit extremely high structural thermostability, which makes them promising catalysts for industrial applications.

(II) Tunable-Sized Polymeric Micelles and Their Assembly for Preparation of Large Mesoporous Pt Nanoparticles (shown in Chapter 3)

Different from the low-molecular-weight block polymers or surfactants (*e.g.*, P123, F127, CTAB, and CTAC), which usually lead to a small pore size because of the limitation of the chain length of hydrophobic segments, high-molecular-weight block polymers have advantages for the preparation of large-sized mesoporous metals. However, high-molecular-weight block polymers do not dissolve in water, leading to difficulty in the formation of micelle structures in aqueous solution. In this study, I described a facile and one-step polymeric micelle approach for the synthesis of Pt nanoparticles with continuously tunable porous structures, which are highly accessible by the reagent due to the large-pore sizes. The key to successful generation of the mesoporous structure is the use of high-molecular-weight diblock polymers poly(ethylene oxide)-*b*-poly(methyl methacrylate) (PEO-*b*-PMMA) as pore-directing agent. By changing the solvent compositions in the precursor solutions, the micelle sizes can be continuously tuned. With the increase in micelles sizes, the resultant pore sizes are also linearly varied. Comprehensive studies on catalytic activity based on the various mesoporous structures illuminate that all of the porous Pt materials exhibited enhanced electrocatalytic activity toward methanol oxidation reaction in comparison with the commercially available catalysts (Pt black and activated carbon with Pt nanoparticles (Pt/C)). This novel polymeric micelle approach will surely provide a new concept for design of the next generation of metallic catalysts with superior catalytic activity.

(III) Multicomponent Metallic Mesoporous Pt-based Spheres through Surfactant-Directed Synthesis (shown in Chapters 4-5)

In view of strong social demand, the development of low-content Pt-based catalysts with high performance is extremely important. Multicomponent metallic nanostructures with a large spectrum of compositions represent an emerging class of catalysts, because their properties can be effectively adjusted by the manipulation of compositions and/or nanostructural features. As described in **Chapter 4**, bimetallic Pd@Pt nanostructures have been successfully synthesized by manipulating the reduction rates of the metal species because the kinetic controlled reduction is an effective method for the preparation of mesoporous metals with various morphologies. Owing to a combination of the high surface area of mesoporous architecture in addition to the bimetallic synergetic effect, mesoporous Pd@Pt nanoparticles exhibited greatly enhanced electrocatalytic performance toward methanol oxidation reaction.

I extend the above method to synthesize the trimetallic mesoporous PtPdRu and PtPdCu nanospheres (**Chapter 5**). Because the neighboring Ru atoms can provide oxygen-containing species for reaction

intermediates to complete, the PtPdRu alloy shows improvement of the tolerance for CO poisoning, thus enhancing electrocatalytic performance compared to bimetallic PtPd and commercial available catalysts. By replacing the Ru precursor with Cu precursor, the trimetallic PtPdCu nanospheres can be also obtained without changing the porous structures and morphologies. Owing to the electronic effect arising from *d*-band shift alloying with Cu, trimetallic PtPdCu nanospheres also exhibit enhanced catalytic activity.

(IV) Synthesis of Pt-free Electrocatalysts with Different Nanostructures (shown in chapter 6)

In Chapters 2-5, I demonstrated that the mesoporous Pt, bimetallic core-shell Pd@Pt, and trimetallic Pt-based alloys with high electrochemical performances. However, Pt is one of the most expensive and rarest metals in the world. These approaches only reduce the usage of Pt and do not fully solve the problem of Pt requirements. Therefore, the development of less expensive and more abundant Pt-free electrocatalysts with improved catalytic activity and durability is still an urgent matter to be solved. This chapter shows a demonstration of non-Pt electrocatalysts. Mesoporous Pd films with perpendicularly aligned mesochannels are synthesized to provide fascinating electrocatalytic properties due to their low diffusion resistance and the full utilization of their high surface area. To the best of my knowledge, there have been no studies on such mesoporous metal films, because it is really difficult to align the molecular templates in perpendicular direction to the substrate. The present approach is not only highly reliable and effective for creating vertically aligned mesoporous Pd electrocatalysts, but also paves the way for other metals and alloys towards achieving a superior catalytic activity. In order further obtain the higher electrocatalyst, another Pt-free electrocatalyst branched PdCu alloy prepared by using kinetically controlled reduction is described.

7.2. Future Prospects

Currently, fuel cell technology is believed to play a key role in the next generation of environmentally friendly energy systems. Over the past decade, significant progress has been made toward meeting the performance and cost targets necessary for commercializing proton exchange membrane fuel cells (PEMFCs). One major technical challenge in PEMFC technology is the development of anodes and cathodes with improved catalytic activity. The current standard industrial catalyst, Pt nanoparticles supported on activated carbon, is still not optimal. Recent reports have demonstrated that the catalytic properties of Pt catalysts can be improved by further modifying their composition and morphology. The hollow structure, such as the frame, cage, is one of the most promising designs that can achieve high electrocatalytic performance and utilization efficiency by

exposing the interior surface and three-dimensional molecular accessibility. For electrocatalytic reactions, the Pt nanocrystals with different facets exhibited various activities in electrochemical application. For example, Pt octahedral nanocages with $\{111\}$ bounded facets is more active than the Pt cubic nanocage with $\{100\}$ bounded facets. Thus, rational design of hollow Pt structures with $\{111\}$ bounded facets are expected to have good electrocatalytic activity toward the oxidation reduction reaction. Recently, considerable improvements can also be observed in the catalytic properties of Pt catalysts by introducing additional metals (*e.g.*, Ru, Pd, and Ni). Based on these ideas, mesoporous multi-layered hollow particles consisting of different metallic layers are believed to be a promising alternative that can provide a high surface area and high catalytic activity due to the electronic landscape reconfiguration originating from the bimetallic hetero-interfaces. Such a unique structure can be prepared through a layer-by-layer deposition of different mesoporous metals on silica particles, carbon particles or metal particles followed by the removal of the template, as shown in **Figure 7.1a**. Furthermore, hierarchical porosity can effectively improve the diffusion rate of guest molecules and increase the catalytic performance, in which large-sized mesopores facilitate the transport of reactants and products across the porous catalyst, while smaller pores (micropores and mesopores) provide a highly active surface area. Different soft templates consist of different micelle sizes can be employed to achieve such a hierarchical porosity, as shown in **Figure 7.1b**.

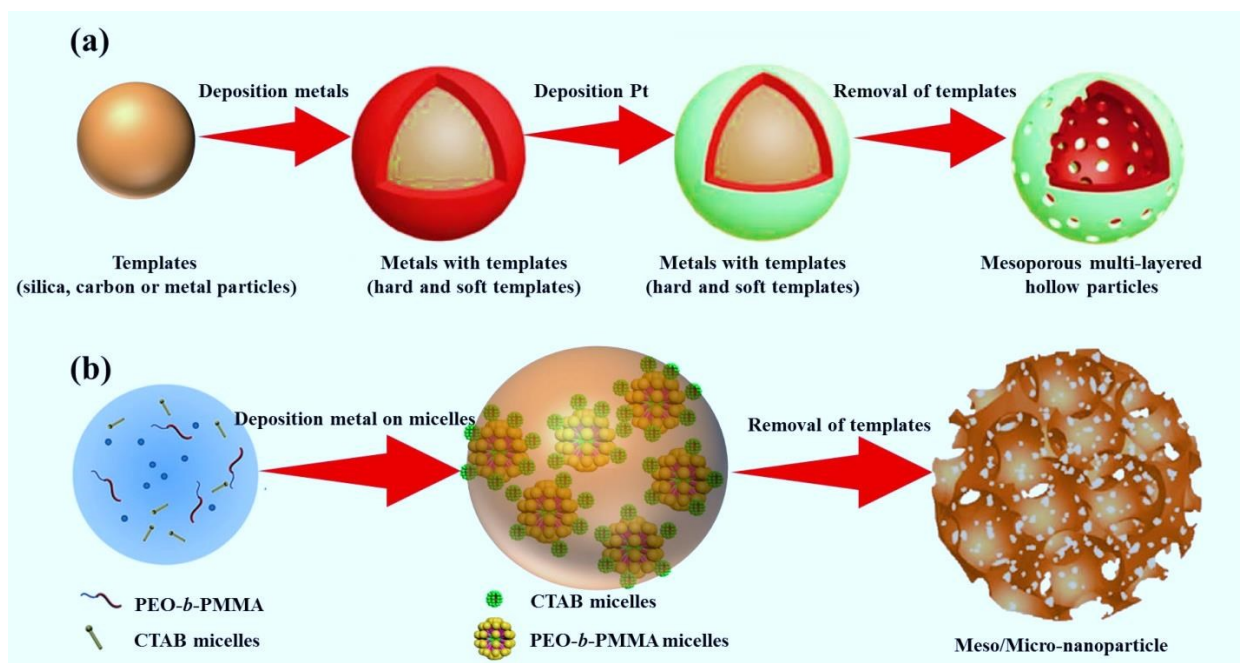


Figure 7.1 Formation process of (a) mesoporous multi-layered hollow particles and (b) metal nanoparticles with hierarchical porosity.

List of Publications

Original Papers

1. Tunable-Sized Polymeric Micelles and Their Assembly for the Preparation of Large Mesoporous Platinum Nanoparticles

Angewandte Chemie International Edition, **2016**, 55, 10037-10041.

Bo Jiang, Cuiling Li, Jing Tang, Toshiaki Takei, Jung Ho Kim, Yusuke Ide, Joel Henzie, Satoshi Tominaka, Yusuke Yamauchi

2. Mesoporous Pt Nanospheres with Designed Pore Surface as Highly Active Electrocatalyst

Chemical Science, **2016**, 7, 1575-1581.

Bo Jiang, Cuiling Li, Victor Malgras, Masataka Imura, Satoshi Tominaka, Yusuke Yamauchi

3. Mesoporous Trimetallic PtPdRu Spheres as Superior Electrocatalysts

Chemistry-A European Journal, **2016**, 22, 7174-7178.

Bo Jiang,[#] Hamed Ataee-Esfahani,[#] Cuiling Li, Joel Henzie, Yusuke Yamauchi (#Contributed equally)

4. Morphosynthesis of Nanoporous Pseudo Pd@Pt Bimetallic Particles with Controlled Electrocatalytic Activity

Journal of Materials Chemistry A, **2016**, 4, 6465-6471.

Bo Jiang, Cuiling Li, Joel Henzie, Toshiaki Takei, Yoshio Bando, Yusuke Yamauchi

5. Three-dimensional Hyperbranched PdCu Nanostructures with High Electrocatalytic Activity

Chemical Communication, **2016**, 52, 1186-1189.

Bo Jiang, Cuiling Li, Victor Malgras, Yoshio Bando, Yusuke Yamauchi

6. Multimetallic Mesoporous Spheres Through Surfactant-Directed Synthesis

Advanced Science, **2015**, 2, 1500112.

Bo Jiang, Cuiling Li, Masataka Imura, Jing Tang, Yusuke Yamauchi

7. Synthesis of Ternary PtPdCu Spheres with Three-dimensional Nanoporous Architectures toward Superior Electrocatalysts

Journal of Materials Chemistry A, **2015**, 3, 18053-18058.

Bo Jiang, Cuiling Li, Victor Malgras, Yusuke Yamauchi

8. Surfactant-Directed Synthesis of Mesoporous Pd Films with Perpendicular Mesochannels as Efficient Electrocatalysts

Journal of the American Chemical Society, **2015**, 137, 11558-11561.

Cuiling Li, **Bo Jiang**, Nobuyoshi Miyamoto, Jung Ho Kim, Victor Malgras, Yusuke Yamauchi

9. Nanoarchitectures for Mesoporous Metals

Advanced Materials, **2016**, 28, 993-1010.

Victor Malgras, Hamed Atae-Esfahani, Hongjing Wang, **Bo Jiang**, Cuiling Li, Kevin C-W Wu, Jung Ho Kim, Yusuke Yamauchi

10. Oxygen-Assisted Synthesis of Mesoporous Palladium Nanoparticles as Highly Active Electrocatalysts.

Chemistry-A European Journal, **2015**, 21, 18671-18676.

Cuiling Li, **Bo Jiang**, Masataka Imura, Naoto Umezawa, Victor Malgras, Yusuke Yamauchi

11. Mesoporous Pt Hollow Cubes with Controlled Shell Thicknesses and Investigation of Their Electrocatalytic Performance

Chemical Communication, **2014**, 50, 15337-15340.

Cuiling Li, **Bo Jiang**, Masataka Imura, Victor Malgras, Yusuke Yamauchi

12. Superior Electrocatalytic Activity of Mesoporous Au Film Templated from Diblock Copolymer Micelles

Nano Research, **2016**, 9, 1752-1762.

Cuiling Li, **Bo Jiang**, Hungru Chen, Masataka Imura, Liwen Sang, Victor Malgras, Yoshio Bando, Tansir Ahamad, Saad M. Alshehri, Satoshi Tominaka, Yusuke Yamauchi

13. Mesoporous Palladium-Copper Bimetallic Electrodes for Selective Electrocatalytic Reduction of Aqueous CO₂ to CO

Journal of Materials Chemistry A, **2016**, 4, 4776-4782.

Mu Li, Junjie Wang, Peng Li, Kun Chang, Cuiling Li, Tao Wang, **Bo Jiang**, Huabin Zhang, Huimin Liu, Yusuke Yamauchi, Naoto Umezawa, Jinhua Ye

14. Self-construction from 2D to 3D: One-pot Layer-by-Layer Assembly of Graphene Oxide Sheets Held together by Coordination Polymers

Angewandte Chemie International Edition, **2016**, 55, 8426-8430.

Mohamed Barakat Zakaria, Cuiling Li, Qingmin Ji, **Bo Jiang**, Satoshi Tominaka, Yusuke Ide, Jonathan P. Hill, Katsuhiko Ariga, Yusuke Yamauchi

15. Hard-templating Synthesis of Macroporous Platinum Microballs (MPtM)

Materials Letters, **2016**, 164, 488-492.

Hiroaki Shirai, Yu-Yuan Huang, Tetsu Yonezawa, Tomoharu Tokunaga, Wei-Chen Chang, Saad M Alshehri, **Bo Jiang**, Yusuke Yamauchi, Kevin C-W Wu

16. First Synthesis of Continuous Mesoporous Copper Films with Uniformly Sized Pores by Electrochemical Soft Templating

Angewandte Chemie International Edition, **2016**, 55, 12746-12750.

Cuiling Li, **Bo Jiang**, Zhongli Wang, Yunqi Li, Md Hossain, A Shahriar, Jung Ho Kim, Toshiaki Takei, Joel Henzie, Ömer Dag, Yoshio Bando, Yusuke Yamauchi

Poster

1. Multimetallic Mesoporous Spheres through Surfactant-Directed Synthesis

The 6th NIMS (MANA)-Waseda International Symposium, Tokyo, Japan, 29 July, 2015.

Bo Jiang, Cuiling Li, Yusuke Yamauchi

Acknowledgements

All these years of study and research at Waseda University and National Institute for Materials and Science (NIMS) have been a wonderful and unforgettable experience for me. I would like to take this opportunity to thank the people who helped me and supported me during this period.

Foremost, I would like to express my most sincere appreciation to my supervisor, Prof. Dr. Yusuke Yamauchi, for giving me an opportunity to study in his group, for continuously supporting my Ph.D. research, for his patience, motivation, enthusiasm, and immense knowledge. His guidance helped me in all the time of research and writing of this thesis.

Besides my supervisor, I would like to thank to Prof. Kazuyuki Kuroda, Prof. Yoshiyuki Sugahara, Prof. Toru Asahi, and Prof. Kiyoshi Shimamura for their encouragement, insightful comments and generous assistance in my defense and my dissertation.

My sincere thanks also go to Dr. Cuiling Li, Dr. Joel Henzie, Dr. Satoshi Tominaka and Dr. Yusuke Ide, for offering me many invaluable advisors and comments.

I really appreciate the support from NIMS-Waseda University Joint Graduate Program and thank to all administrative and technical staff at Research Center for Materials Nanoarchitectonics (MANA), NIMS for their support.

I am grateful to all of the group members in Prof. Yamauchi's group for their kind help, support and stimulating discussions.

Last but not the least, I would like to thank my parents whose unconditional love and supporting me spiritually throughout my life.

Bo Jiang